Sol-gel studies of the Yb_2O_3-Al_2O_3 system and alumina garnets with ytterbium.

WANG, Heming.

Sol-gel studies of the Yb_2O_3-Al_2O_3 system and alumina garnets with ytterbium

Heming Wang

A thesis submitted in partial fulfilment of the requirements of Sheffield
Hallam University for the degree of Doctor of Philosophy

August 2003

Abstract

Sol-gel science and techniques have mainly been used to synthesize inorganic oxides. Thousands of inorganic oxides or mixed oxides have been manufactured by the sol-gel method. They can take the form of thin films, powders, monolithic, and fibres. Many sol-gel oxides systems have been studied. One of the most important systems is the Y_2O_3-Al_2O_3 system which has been studied for many years by sol-gel methods. In this system, there are several phases which have widespread uses in industry such as $Y_3Al_5O_5$, $YAlO_3$, and $Y_4Al_2O_9$. For example, Nd doped $Y_3Al_5O_5$ is presently the most widely used solid-state laser material. Yb doped YAG is one of the most promising laser active materials and is more suitable for diode pumping than the traditional Nd-doped YAG. In fact, the rare earth aluminium garnet family is one of the most active areas of activities in recent years because of their optical, mechanical, and thermodynamical properties.

In this thesis, the production and properties of the sol-gel Yb_2O_3-Al_2O_3 system are studied using sol-gel science and techniques. Ytterbium is a rare earth element in the lanthanide series and belongs to the same group as yttrium in the periodic table and hence, the oxides that they form often have very similar properties and applications in industry. The research focuses on the sol-gel synthesis, sol-gel processing, crystallisation, and structures of alumina garnets in the Yb_2O_3-Al_2O_3 system. The thermal behaviour of the sol-gel Yb_2O_3-Al_2O_3 system was studied by DTA and TG. The crystallisation characteristics were investigated in the pure Yb_2O_3-Al_2O_3 system. The effects of the crystallisation were also studied after other elements were doped in this system. Thin films, thick coatings, and nanosize powders of the pure and doped alumina garnets were produced by the sol-gel method. Their morphologies and structures were studied and consideration was given to their potential uses in industry.

In this thesis, novel Mo doped YbAG garnets were synthesised for the first time by the sol-gel technique. Their application depends on the existing state of Mo (VI) cations in the YbAG matrix. Laser materials, Yb doped YbAG garnets, were successfully produced for the first time using the sol-gel method and their structural changes have been studied. The host crystal structures deform after doping with various concentrations of Yb^{3+}. However, this deformation does not show a linear relationship with the doped Yb^{3+} concentration, which could, in part, explain why around 20 atomic % doped Yb:YAG generally exhibits good properties in laser or scintillator applications.

Acknowledgements

I am extremely grateful to my supervisor Professor John M. Rodenburg, for entirely supporting me to continue doing research in the area of sol-gel science and technique, and for providing me with continuous feedback and encouragement during the entire Ph.D program. I also thank him for many fruitful discussions and suggestion related to this work.

I would like to acknowledge the support of this research from the Materials Research Institute at SHU.

I would like to thank Dr Mike C Simmond, Dr Hywel Jones, and Dr Neil Bricklebank at SHU for their kind help and discussions during the course of this research.

I would like to thank all my friends at Sheffield Hallam University for making me stay here an enjoyable one.

Finally, I am indebted to my wife, my daughter, and my parents for their emotional support. I extremely thank my wife, Xiaoning, for her total support during the whole Ph.D program.

Dedication

To my wife, my daughter, and my parents.

TABLE OF CONTENTS

List of Abbreviations

AFM	Atomic force microscopy
Aquo	$-(OH_2)$
Aquo-cations	$[MO_nH_{2n}]^{z+}$
Aquo-hydroxo	$-(OH_2)(OH)$
At.	Atomic
BE	Binding Energy
CN	Coordination number
CRT	Cathode-ray tube
CZ	Czochralski
DTA	Differential thermal analysis
EuGG	$Eu_3Ga_5O_{12}$
FED	Field emission display
FWHM	Full width at half maximum
GGG	$Gd_3Ga_5O_{12}$
GSGG	$Gd_3Sc_2Ga_3O_{12}$
Hex	Hexogonal phase
H_v	Vicker's hardness
Hydroxo	$-OH$
IR	Infrared
JMA	John-Mehl-Avrami
LIQ.	Liquid
LY	Light yield
M	Metal elements
$M(OR)_z$	Metal alkoxide, where 'R' is an alkyl group
Mo:YbAG	Mo doped $Yb_3Al_5O_{12}$
NdGG	$Nd_3Ga_5O_{12}$
Nd:YAG	Nd doped $Y_3Al_5O_{12}$
NMR	Nuclear magnetic resonance

Ortho	Orthorhombic phase;
Oxo	=O
Oxy-ions	$[MO_n]^{(2n-z)-}$
Oxo-hydroxo	=O(OH)
PVA	Polyvinyl alcohol
R	alkyl group
RE	Rare earth elements
SCE	Saturated calomel reference electrode
SEM	Scanning electron microscopy
TBC	Thermal barrier coating
TbGG	$Tb_3Ga_5O_{12}$
TEM	Transmission electron microscopy
TEOS	Tetraethoxysilane, $Si(OC_2H_5)_4$
TG	Thermogravimetric analysis
T-T-T or 3T	Time – temperature – transformation
Wt.	Weight
XPS	X-ray photoelectron spectroscope
XRD	X-ray diffraction analysis
YAG	$Y_3Al_5O_{12}$
YAP	$YAlO_3$
YbAG	$Yb_3Al_5O_{12}$
YbAM	$Yb_4Al_2O_9$
YbAP	$YbAlO_3$
Yb:YAG	Yb doped $Y_3Al_5O_{12}$
YGG	$Y_3Ga_5O_{12}$
YIG	$Y_3Fe_5O_{12}$
YSZ	8% Y_2O_3 stabilised cubic ZrO_2 phase

Chapter I

Introduction

I.1 Subject of the thesis

The first use of sol-gel synthesis was to form silica as described by Ebelmen in 1844. The first commercial application of sol-gel coatings onto glass appeared in the early sixties of last century. However, the development of sol-gel science only really started twenty years ago with the "First International Workshop on Glasses and Ceramics from Gels" in 1981. Yoldas's work [1] [2] in the late seventies of last century led to the explosion of activity that continues today. In this very short time, sol-gel science and technique has advanced rapidly. Sol-gel processes are now widely used for the synthesis of multicomponent ceramics and nanophase materials. More than 10000 papers have been published during the past twenty years. Especially with the development of hybrid organic-inorganic materials in recent years, the area of sol-gel applications has been expanded significantly [3]. It seems that sol-gel technique has been used in every area of industry.

Generally, sol-gel techniques include several basic steps such as hydrolysis, condensation, and crystallisation. The sol-gel science in these processes has been widely studied by numerous researchers. Two basic routes were divided according to the chemical nature of the precursors, namely: the aqueous route and the metal-organic route. The most common sol-gel products are SiO_2, TiO_2, Al_2O_3, ZrO_2, and multicomponent systems in which at least one or more of these components are included. The characteristics of these components in sol-gel processes are quite well known due to their valences and their binding energies which make it easy to form the network structure. Many useful materials have been produced from these components; e.g. TiO_2 thin films and Al_2O_3 supported catalysts.

The first purpose of this thesis is to study the binary $Yb_2O_3 – Al_2O_3$ system by sol-gel methods. Ytterbium is rare earth element in the lanthanide series and belongs to the same group as yttrium in the periodic table. It has almost the same properties with yttrium apart from a slightly smaller effective radius. Thus, the Yb_2O_3-Al_2O_3 system and the Y_2O_3-Al_2O_3 system are very similar. In fact, our interest in this system really comes from the Y_2O_3 - Al_2O_3 system. Many sol-gel studies on the Y_2O_3-Al_2O_3 system have been reported. There are three widely utilized phases in the Y_2O_3-Al_2O_3 system, i.e. $YAlO_3$, $Y_4Al_2O_9$ and $Y_3Al_5O_{12}$. $Y_3Al_5O_{12}$ is the most important phase in this system and belongs to the rare earth alumina garnet family. Rare earth alumina garnets such as $Y_3Al_5O_{12}$ and $Yb_3Al_5O_{12}$ have many important applications. Rare earth alumina garnets are corrosion resistant because of their chemical inertness even at high temperature and recently are chosen as one of the promising candidates for next generation thermal barrier materials [4] [5] due to their low thermal conductivity and phase stability with the change of temperature. However, it is generally required to fully crystallise under 800^0C or even much lower than 800^0C if the use of rare earth alumina garnets involves application of the coating to a substrate, and in particular a thermally sensitive substrate, for example metals. Many of these substrates suffer irreversible and detrimental changes in their properties if they are heated at very high temperature. Thus, a fully crystallised alumina garnet produced at under 800^0C will be very useful in industry. One possible such application is an alumina garnet coated on stainless steel as a corrosion resistance coating. Rare earth alumina garnets such as YAG powders are conventionally manufactured via the solid-state reaction at very high temperature (up to 1600^0C). Recently, rare earth alumina garnets have been prepared by low temperature sol-gel techniques, but the reported lowest sintering temperature for producing fully crystallised pure or doped yttrium aluminum garnets by sol-gel methods is currently about 900^0C. Thus, whilst the sol-gel processing route offers a considerably lower sintering temperature than that associated with conventional ceramic processing technique, a significant problem still exists if alumina garnets are used as coatings on metal substrates by sol-gel methods. Thus, the second purpose of this thesis is to synthesize rare earth alumina garnets in the $Yb_2O_3 - Al_2O_3$ system by sol-gel methods and lower their crystallisation temperature by doping.

Rare earth alumina garnets can be used as corrosion resistant or thermal barrier coatings on various substrates. However, the most important applications of rare earth alumina garnets are currently used as laser materials and phosphors. By doping different cations into alumina garnets, many useful properties can be achieved through the change of their structures. For example, Nd^{3+}, Cr^{3+}, or Yb^{3+} doped YAG are very useful laser materials; Tb^{3+}, Ce^{3+} or Eu^{3+} doped alumina garnets are important phosphors used in the colour display devices. The most widely used solid-state laser material is the Nd^{3+} doped YAG that can only commercially be produced via single crystal growth (Czochralski [6] method). It is well known that the process of single crystal growth is very sluggish and it is very difficult to dope more than 1 at. % Nd homogeneously in a YAG single crystal. Nd heavily doped YAG single crystals (< 5 at. %) are necessary for obtaining high-power output laser, but they cannot be produced by the single crystal growth method. Thus, in recent years ceramic laser materials have received much attention [7-10]. Especially with the development of nanomaterials, transparent high quality ceramics of YAG have become possible by the isostatically pressed method. Very recently, a high optical quality Nd:YAG ceramic prepared from nano-size powders by sol-gel methods presented almost the same laser properties as the single crystal rod [9]. Compared to single crystal growth, the technique of manufacturing ceramics offers many advantages for the application of solid-state laser materials such as inexpensive, easily high-doped concentrations, mass production, large size, and graded ceramic structure. However, it is still quite difficult to obtain high quality single-phase polycrystalline YAG. The reason for this is attributed to the complicated crystallisation pathway of YAG from the amorphous phase in sol-gel or other techniques. $YAlO_3$ or other phases often crystallise and appear as impurities in YAG phases.

Very recently, heavily ytterbium doped YAG has been found to be potentially good scintillators for solar neutrino detection and can be optimised in terms of efficiency and lifetime [11-14]. Moreover, especially, heavily ytterbium doped YAG (>> 5 at. %) is a new-generation laser material [15] [16]. It is attractive for Q-switching operations to obtain a higher peak power optical pulse compared with those of Nd-doped YAG. We are aware that there are no reports about the synthesis of Yb doped YAG by sol-gel techniques. Sol-gel chemistry and rare earth alumina structures will change after ytterbium cations with various concentrations are heavily doped into yttrium aluminum garnets. We also find that formation of $YbAlO_3$ perovskite in the Yb_2O_3–Al_2O_3 system corresponding to $YAlO_3$ in the Y_2O_3–Al_2O_3 system is not observed in the high temperature phase diagram of the Yb_2O_3–Al_2O_3 system [17] and YbAP is an unstable phase. This advantage will be very beneficial for preparing single phase YbAG or heavily Yb doped YAG because it decreases the chance of forming one of the most common crystallised impurities (i.e. perovskite phase) and makes it easier to obtain high-quality single-phase heavily Yb doped YAG than for Nd:YAG by sol-gel methods.

Hence, the third purpose of this thesis is to extend our studies to the synthesis of heavily Yb doped YAG by sol-gel methods.

I.2 Organization of the thesis

The thesis is organized as follows. In this first chapter, we present an overview of the thesis, i.e. the study of a novel Yb_2O_3-Al_2O_3 system and rare earth alumina garnets by sol-gel techniques. We are interested in the crystallisation process of this system. The most important phase in the system is YbAG which belongs to rare earth alumina garnet family. Since rare earth alumina garnets currently and potentially have many important applications in industry, we further extend our research to the sol-gel synthesis of rare earth alumina garnets related to ytterbium, i.e. YbAG, Mo:YbAG, and Yb:YAG. Our objective is to lower the crystallisation temperature of rare earth alumina garnets and to synthesize novel doped alumina garnets using sol-gel techniques. We also consider extensions to the novel applications of rare earth alumina garnets by sol-gel methods.

In Chapter 2, we present a literature review about sol-gel science, sol-gel system, sol-gel synthesis of rare earth alumina garnets, and their applications. In Chapter 3, we describe the experimental process of preparing samples by our sol-gel techniques. The preparation of characteristic samples is also presented in this chapter.

In Chapter 4, we describe the techniques which were used to characterise our samples. In Chapter 5, we present our sol-gel studies of the pure and doped Yb_2O_3–Al_2O_3 system. The phase development of this system is investigated by choosing three typical compositions in the system and by doping other elements.

In Chapter 6, we describe our sol-gel synthesis of pure or doped YbAG garnets on the basis of sol-gel studies of the Yb_2O_3–Al_2O_3 system. Especially, a novel MoO_3 doped YbAG garnet is described in this chapter. This discovery could bring us some new applications for rare earth alumina garnets. A fully crystallised Mo doped ytterbium aluminium garnet was obtained at a very low temperature heat treatment. Crystallisation kinetics of the pure and doped YbAG were studied. In Chapter 7, the morphologies of rare earth alumina garnet coatings are described. We also consider some possible applications for rare earth alumina garnet coatings; e.g. corrosion resistance in this chapter.

In Chapter 8, we present our sol-gel synthesis of Yb doped YAG. When Yb^{3+} with different concentration is doped into the host YAG crystal, it causes different crystal structural deformations and the adjustment of the crystal lattice constant. These changes will have some effects on the optical properties. Finally in Chapter 9, we conclude our work with a summary of the thesis and directions for future work.

Several of research achievements in this thesis have been published, patented, submitted or prepared for publication during the course of this research. Part of the work about sol-gel studies of the Yb_2O_3–Al_2O_3 system was published in [18]. Rare earth alumina garnet coatings were introduced in [19]. Mo doped YbAG was patented pending in [20] and will be submitted for publication in [21]. Sol-gel synthesis of Yb:YAG was accepted for publication in [22]. A paper about crystallisation kinetics of rare earth alumina garnets is in preparation.

Chapter II

Literature review

In this background chapter, we describe the normal sol-gel processing in Section II.1. Then, sol-gel studies of some important cations and their relevant systems are described in section II.2, specifically for the Y_2O_3-Al_2O_3 and Yb_2O_3-Al_2O_3 systems. In section II.3 and II.4, we describe the most important phase in these two systems, i.e. the rare earth alumina garnets YAG and YbAG. Structures, properties, and sol-gel studies of YAG and YbAG were given in section II.3 and current or potentially extensive applications of rare earth alumina garnets are described in section II.4.

II.1 Processes of sol-gel technique

II.1.1 Hydrolysis

Hydrolysis is the first step in sol-gel processing. Generally, there are two routes used to produce the sol according to the chemical nature of the precursors, i.e. the aqueous route and the metal-organic route. The aqueous route is based on inorganic salts dissolved in water whereas the metal-organic route uses alkoxides dissolved in organic solvents. A lot of research work is being carried out now on both types of sol-gel chemistry, but alkoxides are much more expensive and difficult to handle than aqueous solutions. Thus, the aqueous route is more suitable for industrial applications.

In the aqueous route, when a metal cation is solvated in pure water, it forms a complex or a solvated cation according to:

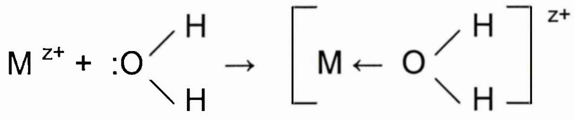

$$M^{z+} + :O\begin{smallmatrix} H \\ H \end{smallmatrix} \rightarrow \left[M \leftarrow O\begin{smallmatrix} H \\ H \end{smallmatrix} \right]^{z+} \qquad (2.1)$$

The formation of M-OH_2 bonds with the metal cation draws electrons away from the O-H bond of the water molecule toward the empty orbitals of the metal ion. This electron transfer weakens O-H bonds and makes coordinated water molecules behave as stronger acids than solvent water molecules. The magnitude of the charge transfer is attributed to the water acidity. The equilibra are established in the following equation, which is defined as hydrolysis:

$$[M(OH_2)]^{z+} \leftrightarrow [M{-}OH]^{(z-1)+} + H^+ \leftrightarrow [M{=}O]^{(z-2)+} + 2H^+ \qquad (2.2)$$

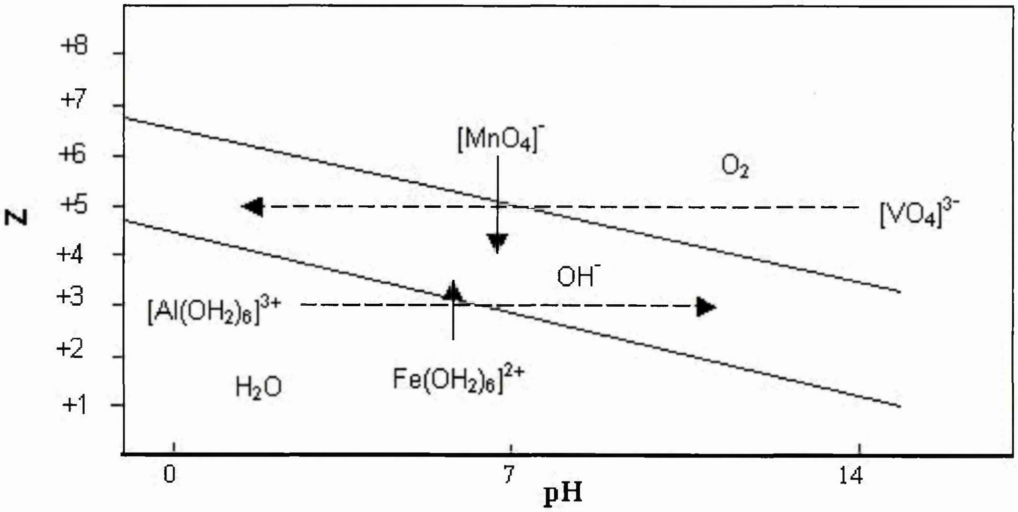

Fig.2.1. pH-charge diagram showing two lines corresponding to h=1 and h=2n-1 separating three domains in which H_2O, OH^- or O^{2-} ligands are formed. From ref. [25].

Spontaneous deprotonation for any aquo-cations may take place as follows:

$$[M(OH_2)_n]^{z+} + hH_2O \leftrightarrow [M(OH)_h(OH_2)_{n-h}]^{(z-h)+} + hH_3O^+ \qquad (2.3)$$

where n is the coordination number of water molecules around M and h can be defined as the hydrolysis ratio. It corresponds to the number of protons that have been removed from the solvation sphere of the aquo-cation.

A partial charge model [23] [24] was developed by Livage and coworkers to quantify the pH-charge relationship. The hydrolysis ratio usually increases with the pH of the

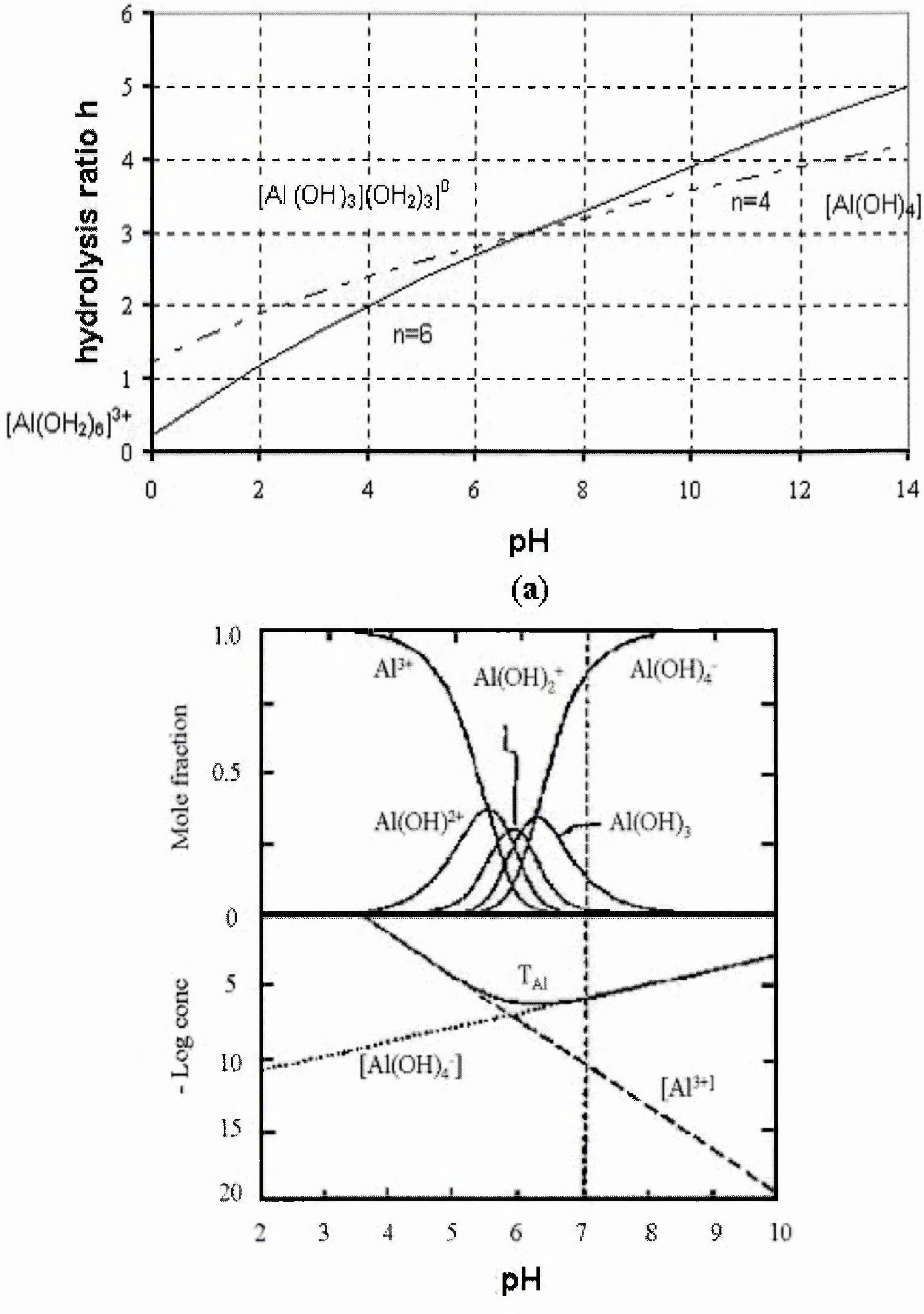

(a)

(b)

Fig.2.2. Hydrolysis of Al^{3+} in dilute aqueous solutions (a) from the partial charge model, and (b) from thermodynamic data. From ref. [23] [24] and [27].

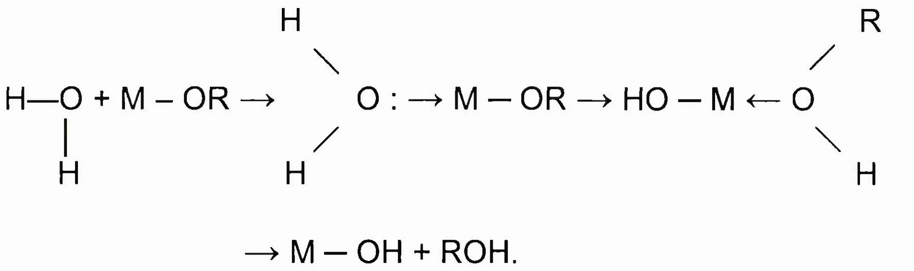

$$H-\underset{\displaystyle H}{\underset{|}{O}} + M-OR \rightarrow {}^{H}_{H}\!\!>O: \rightarrow M-OR \rightarrow HO-M \leftarrow O<^{R}_{H}$$

$$\rightarrow M-OH + ROH. \qquad (2.6)$$

For example, aluminium alkoxide, $Al(OR)_3$, normally [$Al(OC_4H_9)_3$ or $Al(OBu^s)_3$], was hydrolysed in a large of excess of water at 80 ~ 100^0C, resulting in the precipitation of fibrillar boehmite, followed by condensation with a mineral acid (HNO_3) to yield a stable sol [1] [29]. Some research has found that lower hydrolysis temperature ($\leq 80^0C$) and /or higher acid concentrations ($\geq 0.28\ HNO_3/Al$) result in substantial concentration of tetrahedral aluminum atoms relative to aqueous solution of $AlCl_3$ or $Al(NO_3)_3$ [30] [31]. At a lower acid concentration, the octahedrally coordinated Al species: $[Al(OH_2)_6]^{3+}$, can easily be formed [32]. High-temperature (90^0C) hydrolysis resulted in alumina sols containing only octahedrally coordinated Al species for all acid ratios.

II.1.2 Condensation

Monomeric species can generally be observed in very dilute solution only ($< 10^{-4}$ mol/l). At higher concentration, condensation reactions often occur. It can proceed by either of two nucleophilic mechanism (substitution and addition) via the nuleophilic attack of $HO^{\delta-}$ groups onto metal cations $M^{\delta+}$, depending on the coordination of the metal. In all cases, at least one nucleophilic OH group has to be present in the coordination sphere of the hydrolyzed precursor. When the preferred coordination is satisfied, condensation occurs by nucleophilic substitution

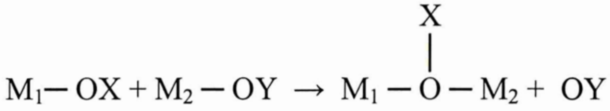

$$M_1-OX+M_2-OY \rightarrow M_1-\overset{\displaystyle X}{\overset{|}{O}}-M_2+OY \qquad (2.7)$$

When the preferred coordination is not satisfied, condensation can occur by nucleophilic addition with an attendant increase in the coordination number of the metal cation

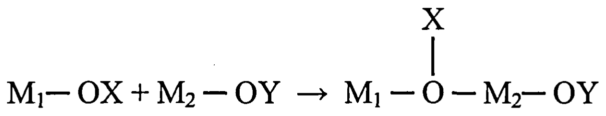

$$M_1-OX+M_2-OY \rightarrow M_1-\overset{\overset{\displaystyle X}{|}}{O}-M_2-OY \qquad (2.8)$$

The size of condensed species depends on many parameters such as pH, concentration or temperature, the main being the hydroxylation ratio 1 = OH/M.

The "charge-pH" diagram is then a very useful guide for sol-gel chemistry as condensation only occurs within the OH domain (Figure 2.1). Condensation is generally initiated via acid-base reactions by adding a base to low-valent aquo-cations or an acid to high-valent oxy-anions.

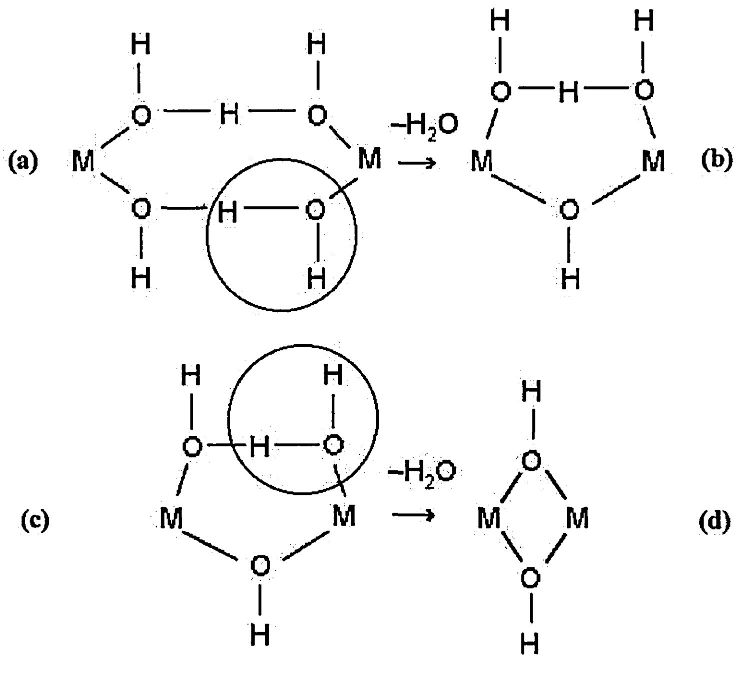

Fig.2.3. A schematic diagram of olation.

The two main mechanisms for condensation are called olation and oxolation. In both cases polynuclear species are formed via the elimination of water molecules from the coordination sphere of the metal cation containing at least one M-OH group [33]. Olation is a condensation process in which a hydroxy bridge ('ol' bridge) is formed between two metal centres. According to Ardon et al [34] [35], olation occurs via a intermediate reaction involving H_3O_2 bridging ligands. It is shown in Figure 2.3.

Since H_2O is the leaving group, the kinetics of olation are related to the lability (ability to dissociate) of the aquo ligand, which depends on size, electronegativity [36] [37], and the electronic configuration of M [38]. In general, the smaller the charge and the larger the size, the greater the rate of olation.

Oxolation is a condensation reaction in which an oxobridge (—O—) is formed between two metal centres. For the co-ordinately unsaturated metal, the oxolation occurs according to:

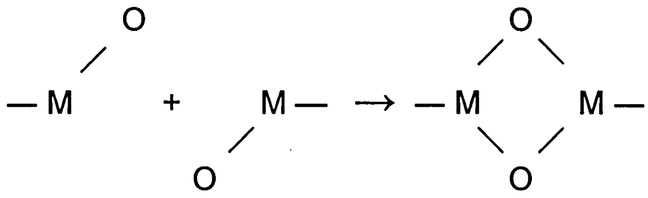

Edge-shared polyhedra (2.9)

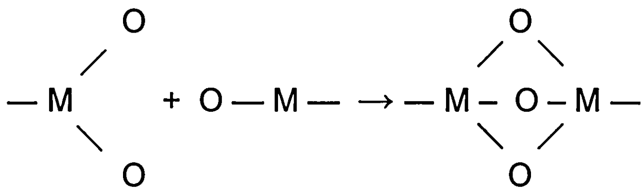

Face-shared polyhedra (2.10)

For the co-ordinately saturated metal, oxolation occurs by two-steps in the following:

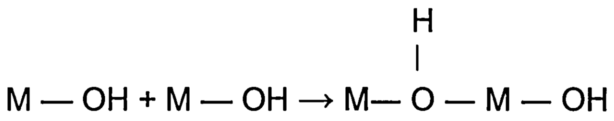

$$M—OH + M—OH \rightarrow M—\overset{\overset{H}{|}}{O}—M—OH \tag{2.11}$$

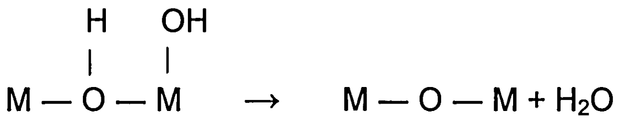

$$M—\overset{\overset{H}{|}}{O}—\overset{\overset{OH}{|}}{M} \rightarrow M—O—M + H_2O \tag{2.12}$$

The first step (Eq. 2.11) is catalysed by bases (Eq.2.13 & 2.14).

$$M—OH + OH^- \rightarrow M—O^- + H_2O \tag{2.13}$$

$$M—O^- + M—OH \rightarrow M—O—M + OH^- \tag{2.14}$$

The second step (Eq. 2.12) is catalyzed by acids (Eq. 2.15 & 2.16):

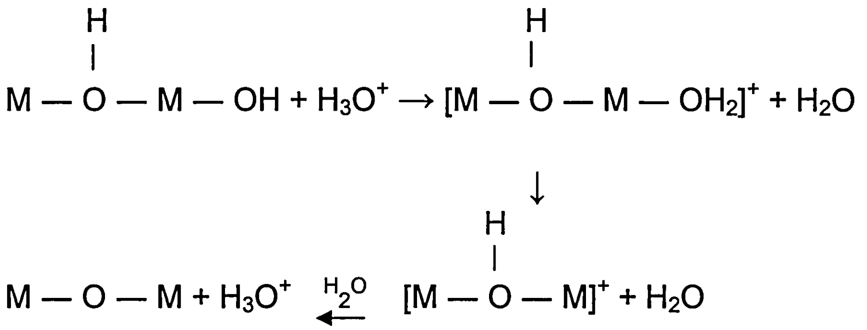

$$M - \overset{H}{\overset{|}{O}} - M - OH + H_3O^+ \rightarrow [M - \overset{H}{\overset{|}{O}} - M - OH_2]^+ + H_2O \qquad (2.15)$$

$$\downarrow$$

$$M - O - M + H_3O^+ \xleftarrow{H_2O} [M - \overset{H}{\overset{|}{O}} - M]^+ + H_2O \qquad (2.16)$$

Compared to olation, oxolation occurs over a wide range of pH, but due to the two-step process, kinetics is slower and never diffusion-controlled.

As an example, Figure 2.4 shows early stages of the hydrolysis and olation of Al^{3+} which could be expressed as the following [39]:

1). The dimerization of the h=1 $[Al(OH)(OH_2)_5]^{2+}$ precursor leads to edge sharing dimers.

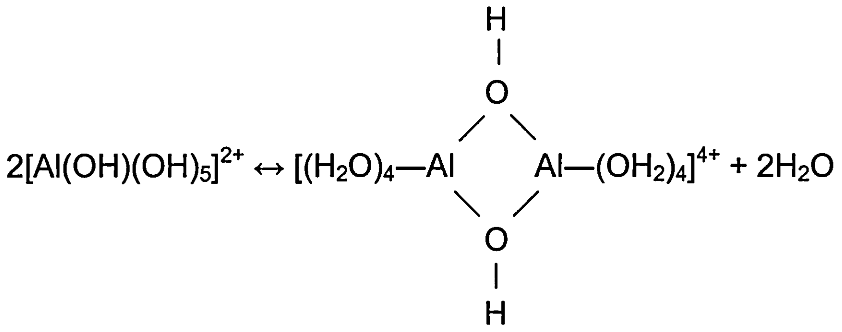

(2.17)

2). Further hydrolysis leads to trimeric species formed by adding one hydrolysed monomer (h=2) to the previous dimer.

$$[Al_2(OH)_2(OH_2)_8]^{4+} + [Al(OH)_2(OH_2)_4]^+ \rightarrow [Al_3(OH)_4(OH_2)_9]^{5+} + H_2O \qquad (2.18)$$

Olated polycations are formed during the first steps of condensation [40] [41]. Only a few polycations are known for Al^{3+}. The first hydroxylation stages (l=OH/Al < 2) leads to the formation of $[Al(OH)(OH_2)_5]^{2+}$ and $[Al(OH)_2(OH_2)_4]^+$. Olation then leads to oligomeric species in equilibrium with monomers. Some Al polycations have been evidenced [27]; such as $[Al_2(OH)_2(OH_2)_8]^{4+}$ dimer, $[Al_3(OH)_{4+x}(OH_2)_{9-x}]^{(5-x)+}$ as well as the well known Al_{13} polycation $[Al_{13}O_4(OH)_{24}(OH_2)_{12}]^{7+}$ [27] by X-ray crystallography of the corresponding sulphate salts, SAXS, and a narrow ^{27}Al NMR resonance. It is made of one tetrahedral $[AlO_4]$ surrounded by four groups of three octahedral $[AlO_6]$. The trimeric species $[Al_3(OH)_4(OH_2)_9]^{5+}$ is easily deprotonated by:

$$[Al_3(OH)_4(OH_2)_9]^{5+} + H_2O \rightarrow [Al_3O(OH)_3(OH_2)_9]^{4+} + H_3O^+ \quad (2.19)$$

Then a nucleophilic oxygen atom is formed, which can react with $[Al(OH_2)_6]^{3+}$ species. The nucleophile addition of four deprotonated trimers onto a single aqui-ion leads to the formation of the $[Al_{13}O_4(OH)_{24}(OH_2)_{12}]^{7+}$ polycations.

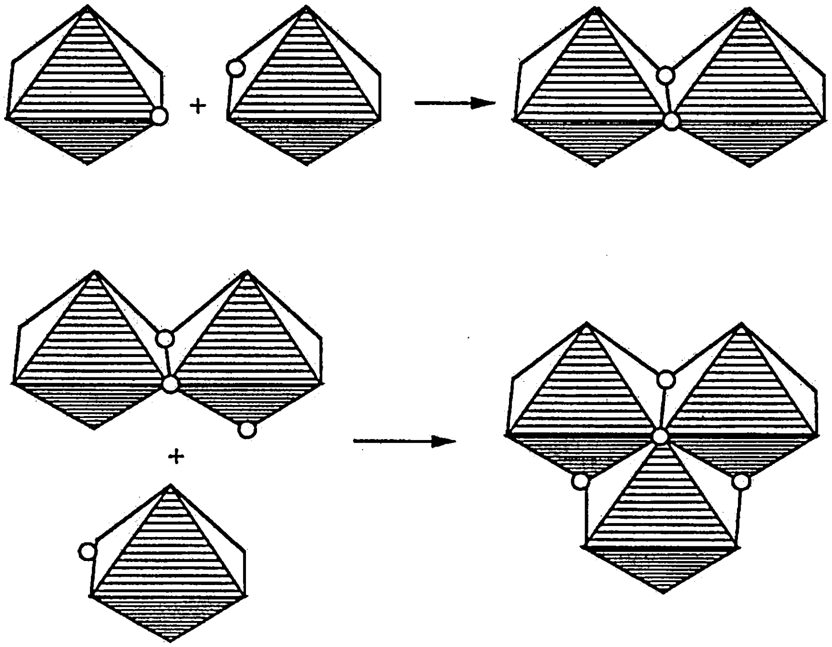

Fig.2.4. Early stages of the hydrolysis and olation of Al^{3+}; o=OH group. From ref. [39].

Hydrolysis and condensation are actually affected by many other factors such as temperatures, anions [42-44], and catalysts [45]. Heating allows a faster diffusion of solute species. The dielectric constant of water decreases drastically when the temperature increases and water looses its properties as a good solvent toward ionic species. Ionic dissociation becomes less important so that ion-pairs and neutral complexes are more often observed.

II.1.3 Gelation, aging and drying

The hydrolysis and condensation lead to the growth of clusters that eventually collide and link together into a gel. Some models have been set up to explain the process of gelation [46-48]. However, most of these models must generally be studied by computer simulations and are not very good when compared with experimental observations. Due to the complicated nature of the gelation process, there is no model that can wholly describe the process of the gelation.

The processes of change during aging after gelation are classified as polymerisation, coarsening and / or phase transformation.

The typical polymerisation process is demonstrated in a SiO_2 gel. The increase in connectivity of the network is produced by condensation reactions, such as

$$\equiv Si - O - H + H - O - Si \equiv \rightarrow \equiv Si - O - Si \equiv + H_2O \qquad (2.20)$$

Apart from condensation, aging can result in other reactions such as further hydrolysis:

$$\equiv Si - O - R + H_2O \rightarrow \equiv Si - O - H + ROH \qquad (2.21)$$

Shrinkage is the most important phenomena in the aging process, which results in the expulsion of liquid from pores. Aging a gel before drying helps to strengthen the network and thereby reduces the risk of fracture [49].

After aging, the gel is heated to around 200^0C and the absorbed water or structured water or other organic solvents are evaporated from the gel. This process is called drying. Drying produces a pressure gradient in the liquid phase of a gel, which leads to differential shrinkage of the network when the exterior of the gel tries to shrink faster than the interior, tensile stresses arise that lead to fracture the network at the exterior as shown in Figure 2.5.

The classic work of Griffith [50] has given the mechanism of fracture of brittle materials. The theory of linear elastic fracture mechanics (LEFM) [51-53] indicates that catastrophic crack propagation occurs when

$$\sigma_x \sqrt{\pi c} \geq K_{IC} \tag{2.22}$$

where K_{IC} is a material property called the critical stress intensity factor; c is the crack size; and σ_x represents the applied stress (see Figure 2.6).

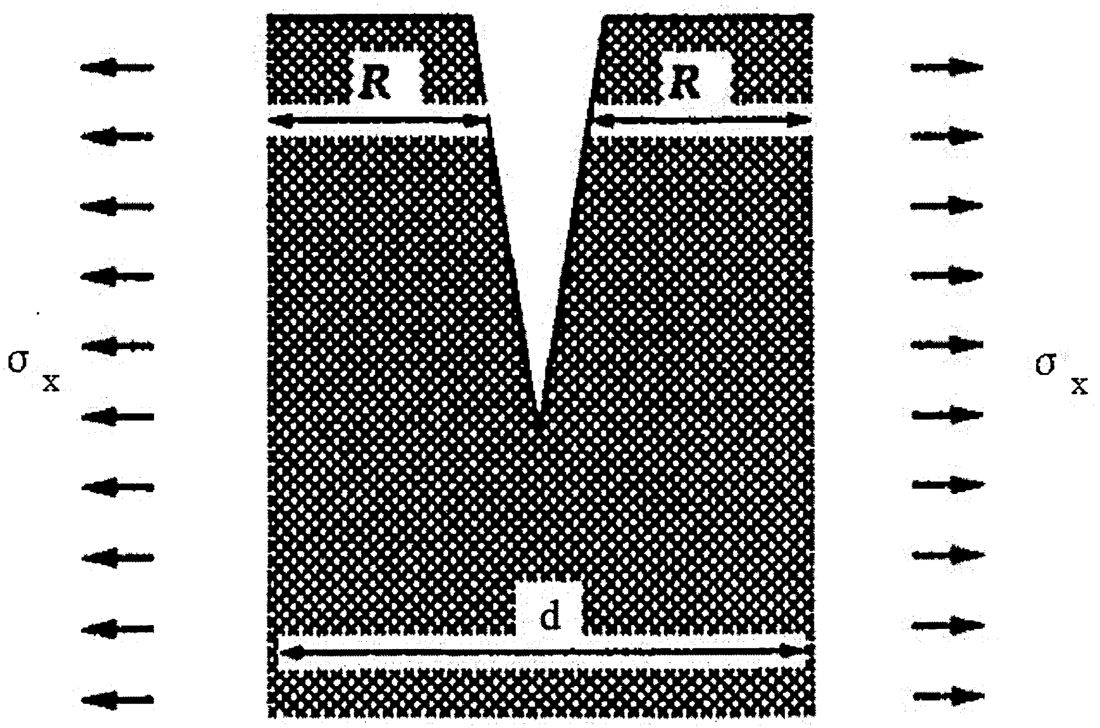

Fig.2.5. Schematic illustration of stress relief by cracking at the drying surface of a gel. From ref. [55].

Crack growth is called 'catastrophic', because the stress intensity (the left side of Eq. (2.22)) increases with the size of the crack, so the bigger the crack gets, the faster it goes until it reaches the speed of sound.

Cracking is sometimes attributed to the existence of pore size distribution in the gel [54] as is indicated in Figure 2.7. The higher tension in the smaller pore creates stress that cracks the 'wall' between the pores. This provides a simple explanation for the observation that cracking often occurs at the critical point, as the pores begin to empty.

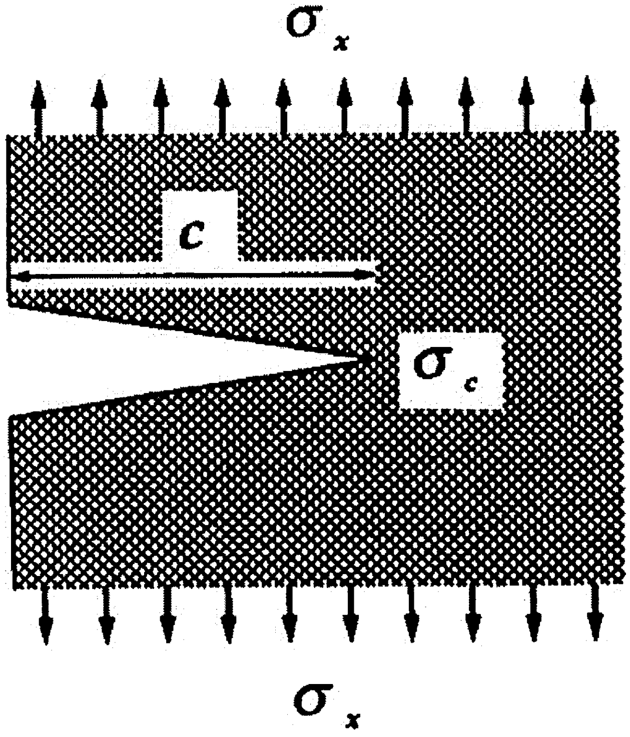

Fig.2.6 Illustration of applied stress on sample containing cracks. The stress at the tip of the crack, σ_c, is greater than the stress applied to the body, σ_x, and increases with the crack size according to $\sigma_c \propto \sigma_x \sqrt{c}$. From ref. [55].

It does not explain cracking in the drying process when there is slower evaporation. The process of slow drying is very complicated, accompanying with continuous hydrolysis and condensation. Some modified models have been selected to explain the mechanism of cracking during the drying process, especially in the process of slow drying.

Many techniques have been developed to prevent cracking during drying such as chemical additives, supercritical drying and freeze-drying.

For thin films, the problem is very interesting. In general, inorganic films thinner than ~0.5 μm do not crack, regardless of the drying rate, whereas films thicker than ~ 1.0 μm are virtually impossible to dry without cracks [55-58]. The drying stresses due to shrinkage of films in the drying process lead to the cracking. This behaviour may be analogous [59] [60] to crack growth in composites containing inclusions, where the thermal expansion mismatch causes cracks to appear near large inclusions, but not near small ones.

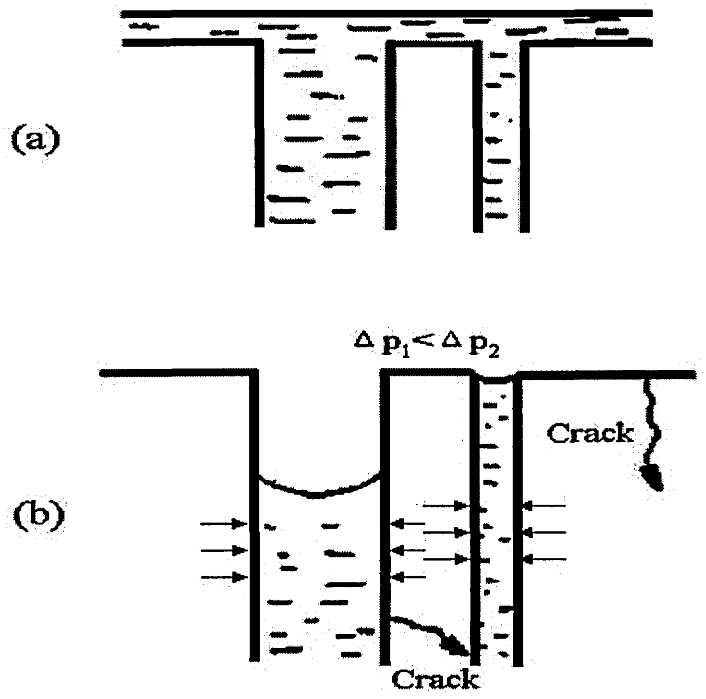

Fig.2.7. Schematic illustration of cracking resulting from draining of nonuniform pores (a) Liquid covers surface before drying starts; (b) larger pores empty first, after critical point. The higher tension in the smaller pore creates stress that cracks the "wall" between the pores. From ref. [59].

II.1.4 Heat treatment

The dried gels are further heated at a higher temperature and a series of structure changes occur during this heat treatment process.

In general, between 200^0C ~ 600^0C heating, concurrent weight loss and contraction are attributed primarily to the removal of organics (principally weight loss), polymerisation (shrinkage and weight loss) and structure relaxation (shrinkage only). For example, structure changes of silicate xerogels prepared from TEOS using an acid-catalyzed process with a large excess of water are shown in Figure 2.8a and b [61], where IR and Raman spectra are respectively compared to the corresponding spectrum of the silicate precursor, TEOS. The major features of the Raman spectra associated with network vibrational modes are the 430, 800, and 980 cm^{-1} bands. Corresponding IR bands are observed at 460, 800, and 1080 cm^{-1}. The 980 cm^{-1} (Raman) and the 1080 cm^{-1} (IR) bands are assigned to Si-O-Si anti-symmetric stretching modes, respectively. The ~800 cm^{-1} vibration is associated with symmetric Si-O-Si stretching or vibrational modes of ring structures. Bertoluzza et al [62] assigned the 430 (Raman) and 460 (IR) cm^{-1} vibrations to Si-O-Si bending modes. The removal of organics is attributed to the weight loss, but it occurs with little associated shrinkage [63] [64]. Shrinkage in this process is caused by continuing condensation reactions, which occur both within and on the surface of the inorganic skeleton. The network is further densified through structural relaxation, an irreversible process in which the free energy decreases through bond restructuring or rearrangement with no associated weight loss [65]. Structural relaxation occurs by diffusive motions of the network. Both condensation and structural relaxation contribute to skeletal densification.

In the crystalline system, the conversion of amorphous to crystallisation [66] is occurred. Structural evolution may be dominated by the effects of phase transformation [67], which often occurs in conjunction with dehydration or when metastable transitional phases are involved. The changes of the coordination numbers of the network species (e.g. Al^{3+} or Ti^{4+}) may happen during both phase transformation and crystallisation of amorphous system. The addition of "seeds" can be used as a viable approach to control the microstructure during nucleation and crystal growth.

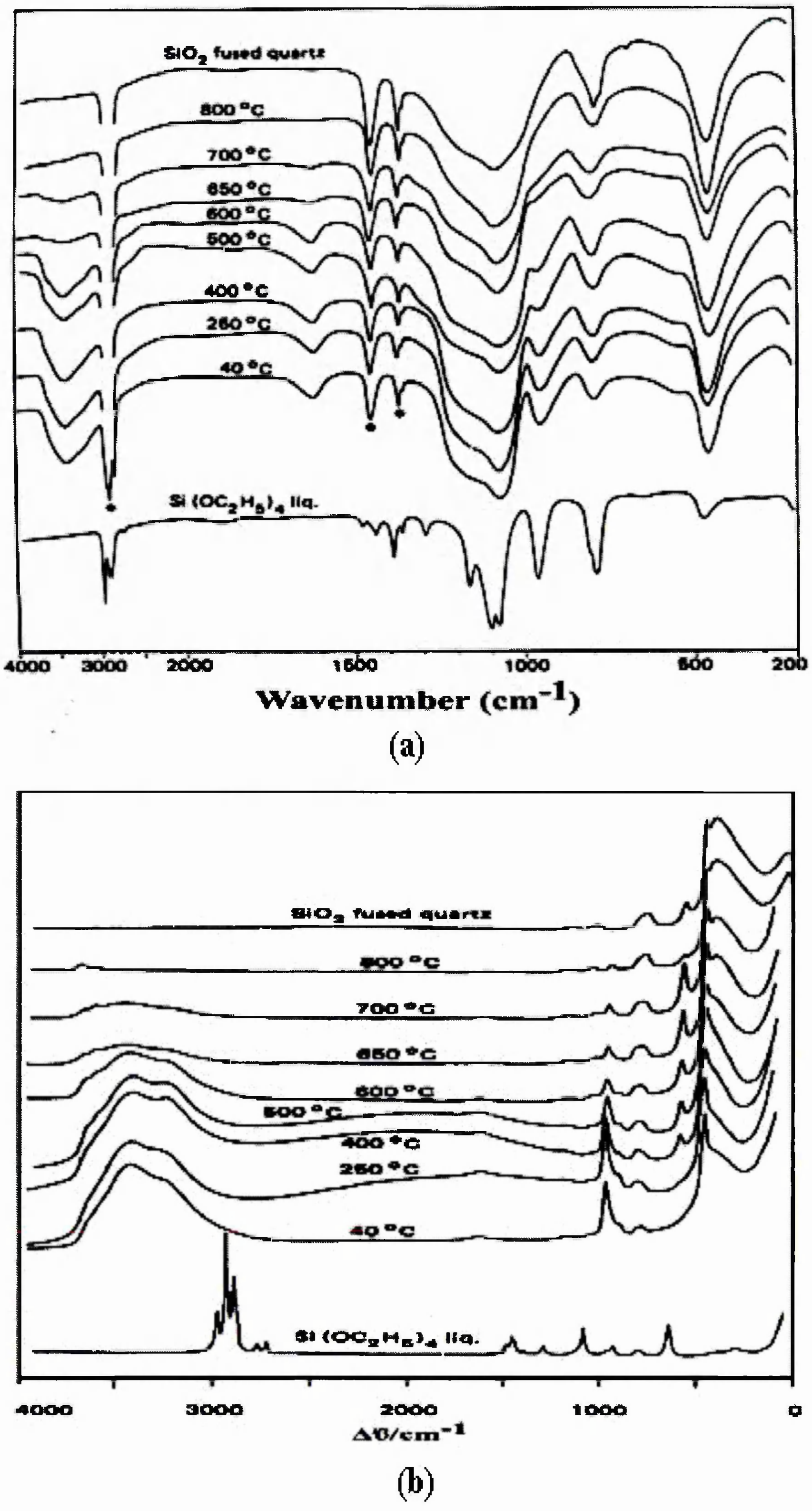

Fig.2.8. Structure changes of silicate xerogels prepared from TEOS using an acid-catalyzed process with a large excess of water; (a) IR spectra; (b) Raman spectra. From ref. [61].

One of the most thoroughly studied crystalline gel system is alumina, in which structural and morphological changes accompanying phase conversions have been investigated by many researchers [1] [29] [68-72]. A typical sequence of crystallisation deduced from XRD [68-70] is the following:

$$AlOOH \xrightarrow{300^0C} \gamma\text{-}Al_2O_3 \xrightarrow{850^0C} \delta\text{-}Al_2O_3 \xrightarrow{1100^0C} \theta\text{-}Al_2O_3 \xrightarrow{\geq 1200^0C} \alpha\text{-}Al_2O_3 \qquad (2.24)$$

or

$$Al(OH)_3 \xrightarrow{400^0C} \eta\text{-}Al_2O_3 \xrightarrow{1150^0C} \theta\text{- and } \alpha\text{-}Al_2O_3 \qquad (2.25)$$

Heating causes dehydration and rearrangement leading to a series of transitional aluminas and finally $\alpha\text{–}Al_2O_3$.

II.1.5 Crystallisation kinetics

Crystallisation is the final stage of sol-gel processing for a crystalline system, in which it is very important to control the crystallisation process. In general, allowing for nonspherical crystals and time-dependent nucleation rates, the amount of transformed crystals can be expressed by the John-Mehn-Avrami equation [73-76] as the following:

$$x = 1 - \exp[-(kt)^n] \qquad (2.26)$$

where x is the ratio of transformed crystals, k is a temperature-dependent function related to viscosity and the rate of crystal growth, n is a constant. Eq.(2.26) applies only for isothermal phase transformation.

A common method of analysis of nonisothermal crystallisation data is to assume that k in Eq.(2.26) can be represented by the Arrhenius equation,

$$k = k_0 \exp(Q / RT) \qquad (2.27)$$

where k_0 is a constant and Q is an activation energy for crystallisation.

II.2 Sol-gel studies of some important systems

II.2.1 Sol-gel processing of Si^{4+}, Zr^{4+}, Ti^{4+}, and Al^{3+}

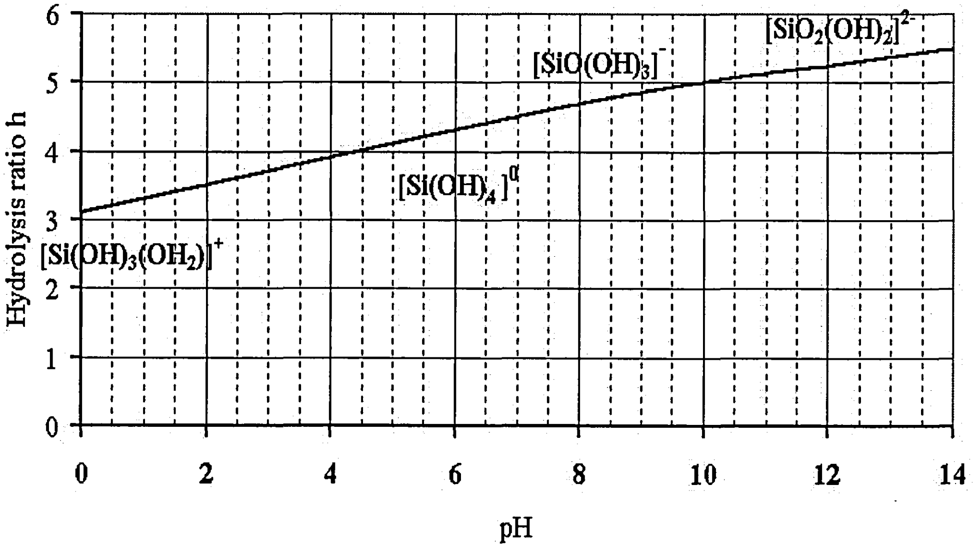

Fig.2.9. Hydrolysis of Si $^{4+}$ in dilute aqueous solutions from the partial charge model. From ref. [23] [24].

Numerous sol-gel systems have been studied. The systems, including SiO_2, Al_2O_3, ZrO_2, or TiO_2 components, are widely studied due to their structures, properties and widespread applications in various industries.

The polarising power of tetravalent cations (Si^{4+},Ti^{4+},Zr^{4+}) is too strong for aquo-species to be formed, even at low pH. They usually give aquo-hydroxo, hydroxo, or oxospecies in aqueous solution [77].

II.2.1.1 For Si^{4+}, the partial charge model [23] [24] leads to four different hydrolyzed precursors $[H_nSiO_4]^{(4-n)}$, ranging from $\{Si(OH)_3(OH_2)\}^+$(h=3) at pH=0 to $[SiO_2(OH)_2]^{2-}$ (h=6) at pH=14 as shown in Figure 2.9. Si^{4+} remains tretrahedrally coordinated over the whole range of pH. Condensation occurs via oxolation due to the lack of any coordinated water molecules in the tetrahedral $[H_nSiO_4]^{(4-n)}$ precursors.

The amorphous hydrated silica gels are formed from the major precursor neutral $[Si(OH)_4]^0$ via oxolation in the pH range of 3~9 as following:

$$Si(OH)_4 \leftrightarrow SiO_2 + 2H_2O \tag{2.28}$$

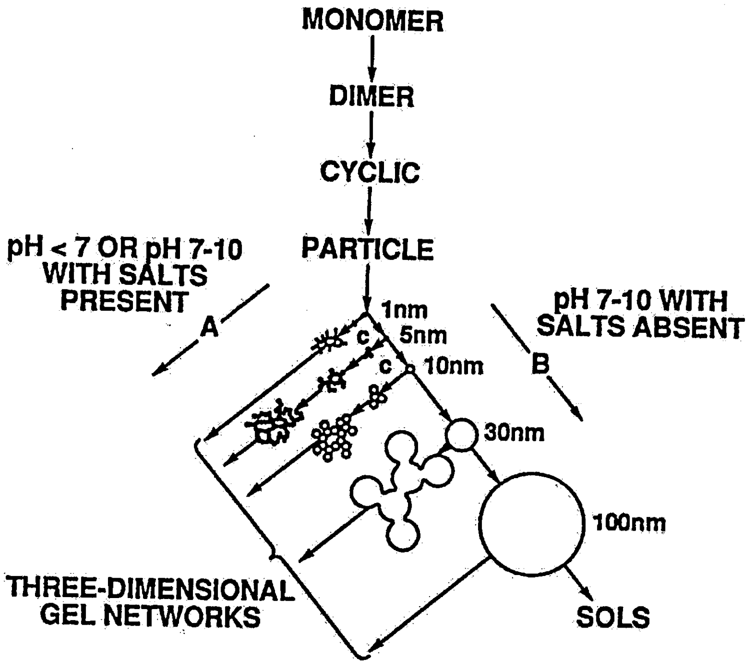

Fig.2.10. Polymerization of silica in basic and acid conditions. From ref. [60].

Gelation is very slow and goes through a minimum around pH~3, but the reaction rates can increase significantly after adjusting the pH. The oxolation reactions are significantly affected by the catalysis. At pH>3, base catalysis occurs. Anionic precursors $[SiO(OH)_3]^-$ are better nucleophiles than $[Si(OH)_4]^0$ increasing the rate of the nucleophilic addition. Gelation occurs readily around pH 7~8. Large colloidal particles are formed and dense opaque gels are obtained. Condensation between surface OH groups then leads to fast aggregation and the formation of unstable gels. Upon drying, these gels give highly porous silica. Below pH ~3, acid catalysis leads to the protonation of the leaving silanol groups and the chain polymers are formed.

Crystalline phases (quartz or crisobalite) can be formed after very high-temperature heat treatment. The processes are shown in Figure 2.10.

One of the most useful multicomponent systems including SiO_2 is the Al_2O_3-SiO_2 system. When the silica and alumina sources are mixed, a gel is formed. Silicate anions react with Al^{3+} precursors to give alumino-silicate compounds [78]. The well-known zeolites can be produced by these reactions.

II.2.1.2 For Zr^{4+}, when $ZrCl_4$ is dissolved in water, it is readily hydrolysed to form the species $[Zr(OH)_2(OH_2)_6]^{2+}$ (h=2). Then, olation leads to the well-known cyclic tetramer, $[Zr_4(OH)_8(OH_2)_{16}]^{8+}$ in which Zr atoms are eightfold coordinated by four bridging OH groups and four terminal water molecules as shown in Figure 2.11.

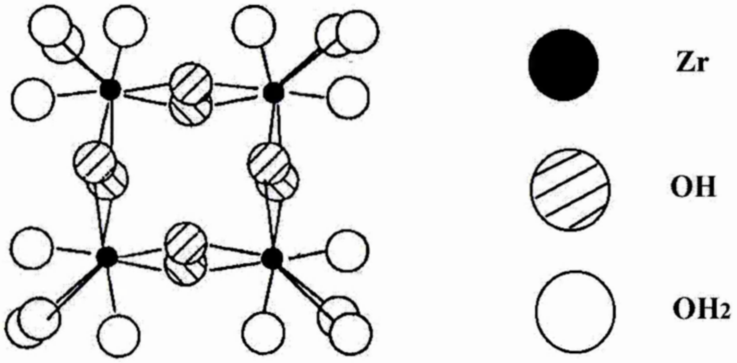

Fig.2.11. Solid phases formed via the precipitation of Zr^{4+} precursor: $ZrOCl_2.8H_2O$. From ref. [60].

The precipitation of amorphous hydrous zirconia $ZrO_2.nH_2O$ occurs by adding ammonia. The change in the final pH from 8 to 10 can alter the crystallisation temperature by 200^0C and the tetragonal-monoclinic transformation temperature by more than 1000^0C. The variation of the final pH is attributed to Cl^- anions. Cl^- anions become complexing between pH 5~9. They are then released at higher pH but a considerable amount of anions remain absorbed in the amorphous oxide. Many other precursors with non-complexing Cl^- anions have been used to produce zirconia and pure crystalline monoclinic zirconia can be obtained.

In the metal alkoxide route, $Zr(OPr^i)_4$ is often used as the precursor in the ZrO_2 sol-gel technique. However, such precursors are highly reactive. This arises mainly from their tendency to increase the coordination number of zirconium up to 7 or 8 as in crystalline zirconia. Coordination expansion occurs as soon as water is added to the alkoxide solution leading to the uncontrolled precipitation of polydispersed powders. Therefore, complexing ligands such as acetylacetone (acacH = $CH_3COCH_2COCH_3$) have to be added to the alkoxide solution prior to hydrolysis in order to decrease its reactivity [79].

One of the most important multicomponent systems including ZrO_2 is the well-known Y_2O_3-ZrO_2 system which is used as thermal barrier materials at high temperature [80]. Generally, 8% Y_2O_3 is doped in ZrO_2 to stabilise the cubic ZrO_2 phase (YSZ). YSZ has a very low thermal conductivity at 1000^0C.

II.2.1.3 For Ti^{4+}, a lot of Ti alkoxides are used to produce TiO_2 using the sol-gel techniques. The hydrolysis and condensation rate of $Ti(OR)_4$ at pH=7 is more than five orders of magnitude greater than that of $Si(OR)_4$ [81]. TiO_2 sol-gel science has been widely studied due to its various applications in recent years.

Sol-gel processing of the multicomponent TiO_2-SiO_2 system is of significant technological interest for the low-temperature formation of refractory, ultralow thermal expansion glasses as well as the preparation of graded refractive index optics. A hetercondensation reaction is as following:

$$(R'O)_3Si\text{-}OH + RO\text{-}Ti(OR)_3 \rightarrow (R'O)_3Si - O - Ti(OR)_3 + ROH \qquad (2.29)$$

where R' in this case could be H, or an alkyl group. But, on the other hand, $Ti(OR)_4$ catalyses silanol condensation [82], promoting homocondensation of the silicate species rather than uniform incorporation of Ti at the molecular level.

II.2.1.4 Finally, the hydrolysis and condensation of Al^{3+} have been presented in section II.1. Alumina based systems are very useful, which are extensively studied by many researchers such as the MgO-Al_2O_3, Li_2O-Al_2O_3, and Y_2O_3-Al_2O_3 systems.

II.2.2 Sol-gel studies of the Y_2O_3 -Al_2O_3 system

In this section, we will describe sol-gel studies of the Y_2O_3-Al_2O_3 system. As mentioned in Chapter I, our research interests in the Yb_2O_3-Al_2O_3 system initially came from this system. Although a lot of research work on this system by sol-gel techniques has been done, the study of the hydrolysis and condensation of this system, typically for Y^{3+}, were actually reported very rarely. Almost all research work focuses mainly on the final stage of sol-gel processing, i.e. crystallisation. The reason is that there are three important transition compounds in this system, i.e. $Y_3Al_5O_{12}$, $YAlO_3$, and $Y_4Al_2O_9$. These three phases have many important applications in industry, especially in optics. The phase diagram of the Y_2O_3-Al_2O_3 system is shown in Figure 2.12 [83].

In general, sol-gel processing of the Y_2O_3-Al_2O_3 system can be divided into five stages as following:

$$\text{Sol} \rightarrow \text{Gel} \xrightarrow{200^0\text{C}} \text{Xerogel} \xrightarrow{600^0\text{C}} \text{Amorphous} \xrightarrow{\text{Above } 900^0\text{C}} \text{Crystallites} \qquad (2.30)$$

The sol is prepared, and then it becomes gel either as a bulk, particles or films. After carefully heating at about 200^0C, the wet gel transforms to xerogel. By further heat treatment below the temperature 600^0C, an amorphous metal oxide is formed. Finally, this amorphous phase converts to a crystalline structure by calcination at above 900^0C.

J.R. Lo and T.Y. Tseng [84] studied the phase development of the Y_2O_3 -Al_2O_3 system by a modified sol-gel process. Aluminium butoxide [$Al(OBu^s)_3$] and yttrium nitrate dissolved in 2-methoxyethanol were used as starting materials. The chemical inhomogeneity of yttrium caused by their sol-gel processing could exist in the prepared gel-derived powders. Three compositions for YAG, YAM, and YAP respectively were studied in this report. For the YAG composition, a considerable amount of $Y_3Al_5O_{12}$ crystallites appeared at about 1000^{0}C. For $Y_4Al_2O_9$ composition, the formation of Y_2O_3 began at 650^{0}C and there were three phases (YAP, YAM, and Y_2O_3) that co-existed at 1300^{0}C. Finally pure YAM was achieved at 1500^{0}C. For YAP composition, the phase development was quite complicated. Y_2O_3 and YAG initially crystallised at 650^{0}C, but a relatively large amount of Y_2O_3 and YAG appeared only at 1000^{0}C. At this temperature, YAM initially crystallised, which coexisted with Y_2O_3 and YAG. Then YAP began to grow at 1300^{0}C. The high purity perovskite phase YAP can only

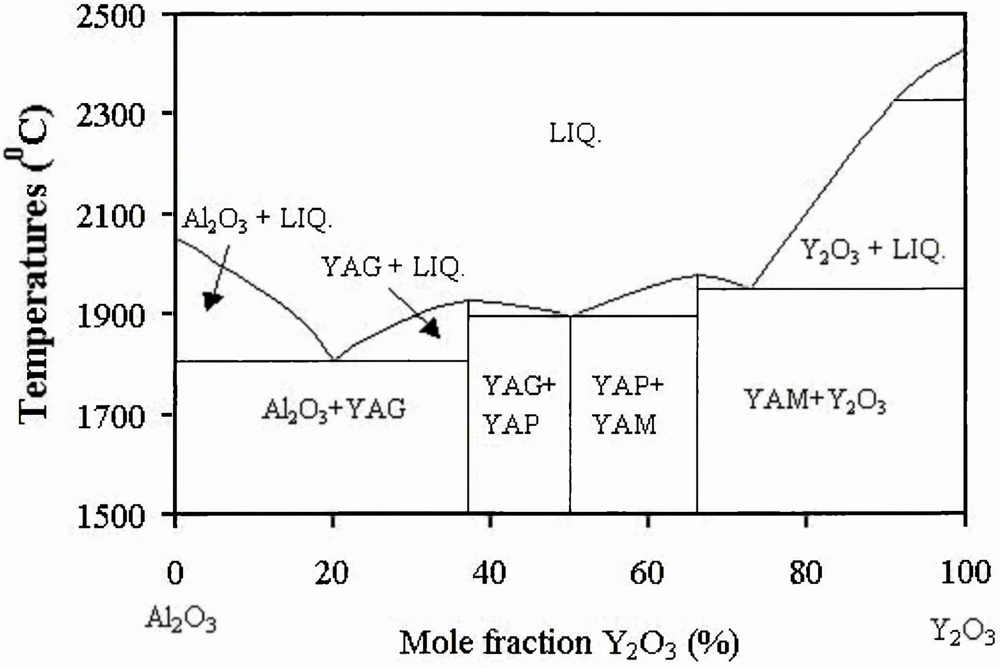

Fig.2.12. Phase diagram of the Y_2O_3 -Al_2O_3 system. From ref. [83].

be obtained at 1500^0C for 40 hours heat treatment. Thus, the formation of YAP was deduced by the reaction YAG + YAM → YAP.

R.S. Hay [85] studied a phase transformation in sol-gel-derived yttrium-aluminium-garnet films. In the report, the yttria sol and the alumina sol were prepared separately from yttrium and aluminium isopropoxide. The films were formed on nickel or platinum grids for TEM studies. In this system, hydrated Y_2O_3 and Al_2O_3 particles formed first as the sol-gel films were heated; consequently, mixing was not on an atomic level. The phase evolution of the bulk gel with a Y: Al mole ratio of 3:5 during heat treatment was also observed. There were four phases that appeared in the study. The transition alumina phase crystallised at 800^0C and $Y_4Al_2O_9$ appeared at 850^0C. The YAG phase nucleated between 800^0C-950^0C and then the pure YAG appeared at 1050^0C. Nucleation was weakly correlated with the transient presence of $YAlO_3$ (YAP). The crystallisation pathway with several intermediate phases before YAG finally crystallised was quite complicated. Hay [85] postulated that the nucleation of YAM before YAG was due to lower yttria mobility combined with influence of strain energy effects. The nucleation of YAG from the matrix was reported to be site saturated, and crystal growth occurred by consumption of the parent phases. Crystallisation was described as being a cellular transformation with spherulitic growth and with a constant number of nuclei. Crystal growth was essentially two dimensional due to very thin film thickness in comparison to spherulite size.

Yamaguchi et al. [86] [87] used an alkoxy-derived stoichiometric precursor for synthesizing $YAlO_3$, $Y_4Al_2O_9$, and YAG. For YAG and YAP composition precursors, the formation of an intermediate hexagonal YAP phase was observed at approximately 800-900^0C. For YAG composition precursors, the hexagonal $YAlO_3$ phase converted to YAG and was single phase at 1050^0C. For YAP composition, the crystallisation pathway was more complicated. Hexagonal YAP crystallised between 870 and 900^{0}C and transformed into an intermediate cubic solid solution phase [$Y_3AlY(AlO_4)_3$] from 1000-1060^{0}C. The cubic $YAlO_3$ phase then decomposed to a YAG + YAM mixture between 1080 and 1200^{0}C, which subsequently underwent a solid-state reaction to form single-phase orthorhombic YAP by 1650^{0}C.

In the Y_2O_3-Al_2O_3 system, it is said that synthesizing the pure $YAlO_3$ single phase has been difficult because of preferential formation of other phases by sol-gel methods or other wet chemical processes. M. Harada et. al. [88] used a polymerised complex method to produce the doped $YAlO_3$. The most important feature of this method is the formation of a mixed metal citric acid complex with a stoichimetric ratio stabilised in a polyester based resin. In this study, yttrium nitrate and aluminium nitrate as well as a combination of aluminium isopropoxide and yttrium acetate were the starting materials. The crystallisation temperature of the $YAlO_3$ phase was 1100^{0}C. T. Tachiwaki et. al [89] manufactured $YAlO_3$ using the sol-gel method. $YAlO_3$ solid solution phase crystallised at 880-935^{0}C from amorphous materials which were prepared in the mole ratio Y^{3+}/Al^{3+}=1:1 or 3:5 using yttrium chloride ($YCl_3.6H_2O$), aluminium chloride, ($AlCl_3.6H_2O$), and hydrazine monohydrate [$(NH_2)_2.H_2O$] as starting materials. The hexagonal $YAlO_3$ phase transformed to YAG for the Y^{3+}/Al^{3+}=3:5 composition at 1005-1075^{0}C.

Rao [90] reported the preparation of YAG, YAM and YAP doped with rare earth elements using the sol-gel process. In the experiment, yttrium hydroxide and aluminium hydroxide xerogels were used as the precursors and the samples were found to be fully crystallised at 1000^{0}C. Hess et al [91] studied the formation of YAG, YAP and YAM via combustion synthesis of aqueous glycine-nitrate solutions with stoichiometric yttrium-to-aluminum cation ratios. This process produced amorphous powders that were crystallised by subsequent heat treatment. The heat treatment temperature has affected the crystallisation pathway; e.g. for YAG composition, at temperature 800^{0}C YAG initially crystallised directly from the amorphous precursors. At higher temperatures, hexagonal YAP formed as a metastable intermediate product. Since the fuel concentration could possibly affect the ultimate temperature reached during combustion synthesis, the crystallisation pathway is related to the fuel concentration and the initial heat treatment process.

S.L Liu [92] et al synthesized doped $Y_4Al_2O_9$ by the sol-gel method. Yttrium and aluminium citrate complexes were used as starting materials. The single-phase $Y_4Al_2O_9$ was crystallised at 900^{0}C as opposed to the conventional solid-state reaction, which led to the formation of other impurity phases.

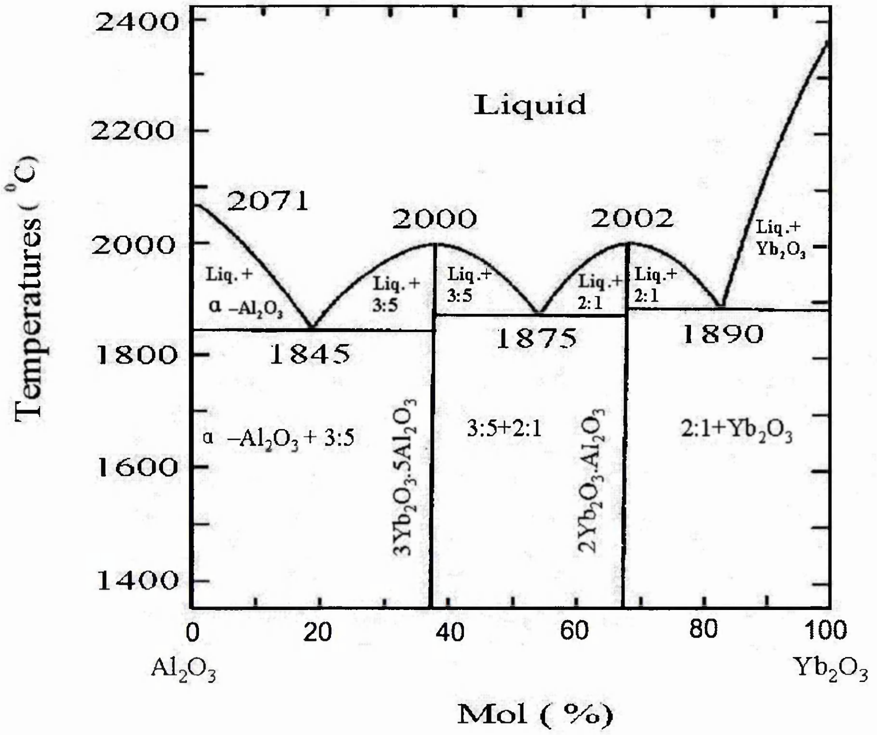

Fig.2.13. A phase diagram of the Yb_2O_3-Al_2O_3 system. From ref. [17].

II.2.3 Sol-gel studies of the Yb_2O_3-Al_2O_3 system

In the above section, we described the extensive sol-gel studies of the Y_2O_3-Al_2O_3 system due to its widespread applications in industries. The Yb_2O_3-Al_2O_3 system described in this section is a novel system for sol-gel science. To the best of our knowledge, there have been no published papers about sol-gel studies of the Yb_2O_3-Al_2O_3 system besides our research work in this thesis. Although the Yb_2O_3-Al_2O_3 system is very similar to the Y_2O_3-Al_2O_3 system, there are some differences that existed between them. This is evident by comparing phase diagram of the Yb_2O_3-Al_2O_3 system (shown in Figure 2.13) [17] to that of the Y_2O_3-Al_2O_3 system (Figure 2.12). According to phase diagram of the Yb_2O_3-Al_2O_3 system, there are only two transition compounds, i.e. $Yb_3Al_5O_{12}$ and $Yb_4Al_2O_9$, whereas formation of $YbAlO_3$ perovskite phase corresponding to $YAlO_3$ in the Yb_2O_3-Al_2O_3 system is not observed. The reason is that Yb^{3+} has a smaller radius (0.86Å) than that of Y^{+3} (0.89Å) [26]. Thus, it is unsuitable for any site of the perovskite structure. It is too large for the octahedral positions (CN=6) and too small for the sites with coordination number (twelve). Thus, $YbAlO_3$ perovskite is an unstable phase. This is an advantage when preparing pure-phase ytterbium aluminium garnet because it decreases the chance of forming the perovskite impurity phase.

II.3 Rare earth alumina garnets

II.3.1 Crystal structures of rare earth alumina garnets

As we mentioned in II.2.2, there are three important transition compounds in the Y_2O_3-Al_2O_3 system, i.e. $Y_3Al_5O_{12}$, $YAlO_3$, and $Y_4Al_2O_9$. However, the most important phase among them is the well-known yttrium aluminium garnet. YAG is host materials for a number of phosphor systems and typically famous as a host laser material. YAG belongs to the rare earth alumina garnet family. It is a body-centred cubic structure with the space group Ia3d, the most symmetric space group of the cubic system. Natural garnets are silicates and they are known as beautiful precious stones. They have a general formula $[A]_3[B]_2[C]_3O_{12}$ (for silicate garnets, C is Si and B is Al; for alumina garnets, B and C are Al). A, B, C cations occupy particular sites, depending on cation radii. In most cases of natural garnets, and also in artificial obtained crystals with the garnet structure, the same sites of A, B, or C cations can be occupied in a statistical manner by more than one type of ion.

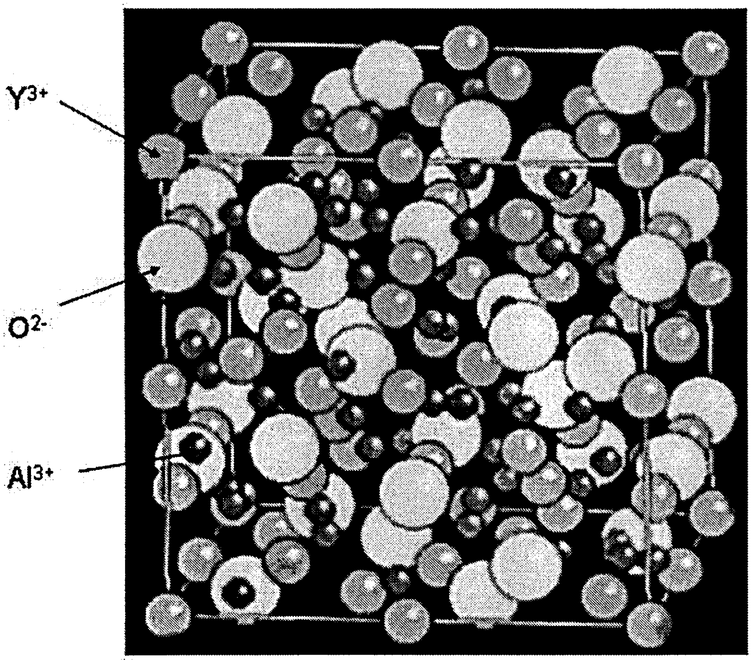

Fig.2.14. A schematic diagram of yttrium aluminium garnets.

Figure 2.14 shows the structure of yttrium aluminium garnets. There are eight molecules per unit cell and 160 atoms. 3/5 aluminum atoms occupy the $[AlO_4]$ tetrahedral, 2/5 aluminum atoms occupy the $[AlO_6]$ octahedral and yttrium atoms exist in $[YO_8]$ dodecahedron. F. Euler et. al. [93] studied the oxygen coordinates with alumina garnet structures. Each oxygen belongs to two dodecahedra, one tetrahedron, and one octahedron. Thus, the alumina garnet crystal structure consists of a 3D network of oxygen polyhedra.

Y^{3+} cations in alumina garnets can be replaced partly or completely not only by rare earth elements in the lanthanide series, but also by other transition metals that have similar radii of atoms. Al^{3+} cations also can be substituted by other metal cations. All these substitute ions may cause the structure deformation and the adjustment of the crystal cell constant. When Yb^{3+} cations replace Y^{3+} ions totally, it is ytterbium aluminium garnet in the Yb_2O_3-Al_2O_3 system. YbAG theoretically has a smaller crystal lattice constant (11.93Å) than that of yttrium aluminum garnet (12.01Å) [94]. This is attributed to the fact that Yb^{3+} has a smaller radius (0.86Å) than that of Y^{+3} (0.89Å) [26]. When Yb^{3+} cations partly replace Y^{3+} ions, it is ytterbium doped yttrium aluminium garnet which has very recently shown promise as a novel laser material and potentially good scintillator. The unit cell constant becomes 11.978 Å [95] after 30 at. % Yb atoms substitute for yttrium. Many of the optical properties of alumina garnets are achieved by doping other rare earth or transition metal elements in their structures, which lead to additional energy levels on their energy band structures such as Yb:YAG and Nd:YAG.

Generally, the sites (rare earth ions) of the oxygen dodecahedra in alumina garnets are substituted by the cations with the +2 or +3 chemical valence whereas the oxygen tetrahedral or octahedral sites (Al^{3+} cations) are replaced by other cations with the +3, or +4 chemical valence. The chemical valence and the radius of the doped elements are very sensitive to form solid solution alumina garnets. To the best of our knowledge, nothing has been published on alumina garnets doped by transition metal with the +6 chemical valence and especially where the substituted cations occupy the dodecahedron sites of alumina garnets.

N. Gautier et. al [96] investigated aluminium-gallium substitution in yttrium garnets via the sol-gel method by NMR and X-ray absorption. J. Carda et al. [97] studied the cation substitution between uvrovite and yttrium aluminium synthetic garnets obtained by sol-gel methods and the cation distribution in dodecahedral, octahedral and tetrahedral sites and bond distances in these garnets using the Rietveld method. The work shows the incomplete substitution in small sites. The smaller site the smaller substitution that is possible.

II.3.2 Basic properties of rare earth alumina garnets

There is an enormous volume of literature on the physical properties of rare earth alumina garnets. In this section, we only describe some elementary important properties of YAG and YbAG as a comparison. They present many similar properties which can be extrapolated on the basis of their being iso-structured.

Rare earth alumina garnets are very stable from room temperature to their melting points (about 2000^0C). They keep the body-centred cubic structure regardless of the change of temperature. The melting point of YAG is 1970^0C and that of YbAG is 2000 ± 20^0C. The density of YbAG can be calculated as 6.6 g/cm^3 whereas the density of YAG is 4.6 g/cm^3.

The reported H_v hardness values of YAG are in the range of 1100 ~1700 kg/mm^2 [98]. Doping of a garnet crystal generally leads to a greater hardness [99]. Within a group of related crystals, the lattice constant is a measure of the strength of bonding. The larger the lattice constant, the weaker the bonding. Research results have indicated decreasing hardness with increasing lattice constant for alkali halides [100], divalent and tetravalent crystals [101] with NaCl structure by plotting the hardness against the lattice constant. Since the lattice constant of YbAG is smaller than that of YAG, it is extrapolated that the H_v hardness of YbAG is in the range of 1100 ~1700 kg/mm^2 too. The relationship between garnet hardness and lattice constant can be seen in Figure 2.15 [98].

The thermal expansion coefficient of YAG is 9.1 x 10^{-6} (1/^{0}C) [102]. YbAG possesses almost the same thermal expansion coefficient as YAG [103].

The elastic modulus of YAG is 280 GPa. YbAG should have a similiar elastic modulus as YAG.

Oxygen diffusivity in YAG is appoximately 10^{-20} m^2/s (1100^{0}C) [104]. Oxygen diffusivity in YbAG is of the same level as it is in YAG [104].

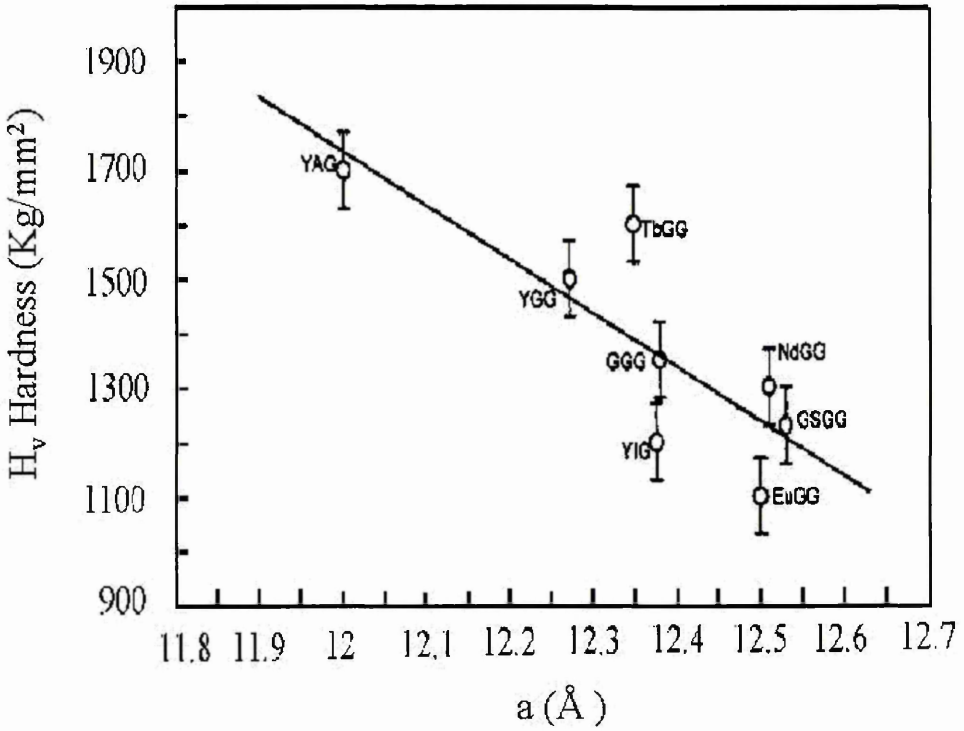

Fig.2.15. Plot of hardness (Hv) against lattice constant a. From ref. [98].

The thermal conductivity of YAG is 3.2 W/m.K [5] at the temperature of 1000^{0}C. The relationship between the thermal conductivity of YAG, the temperature and the grain size is shown in Figure 2.16 [5]. It can be extrapolated that YbAG has lower thermal conductivity than YAG because atomic masses of Yb is heavier than that of Y.

Generally, the heavier the atomic masses in one cell, the lower the thermal conductivity. When Yb is doped into YAG garnets, the thermal conductivity decreases greatly at room temperature, especially at high doping levels [95]. The thermal conductivity of Yb:YAG single crystals decreases with the increase in temperature shown in Figure 2.17 [95]. The reduction of thermal conductivity at a higher doping concentration is regarded as the result of possible changes of phonon modes [95]. In Yb doped YAG crystals, there are no free electrons, so the main mechanism of heat transfer is heat transfer by phonons. Therefore, the change of lattice vibration directly influences the thermal conductivity of Yb doped YAG.

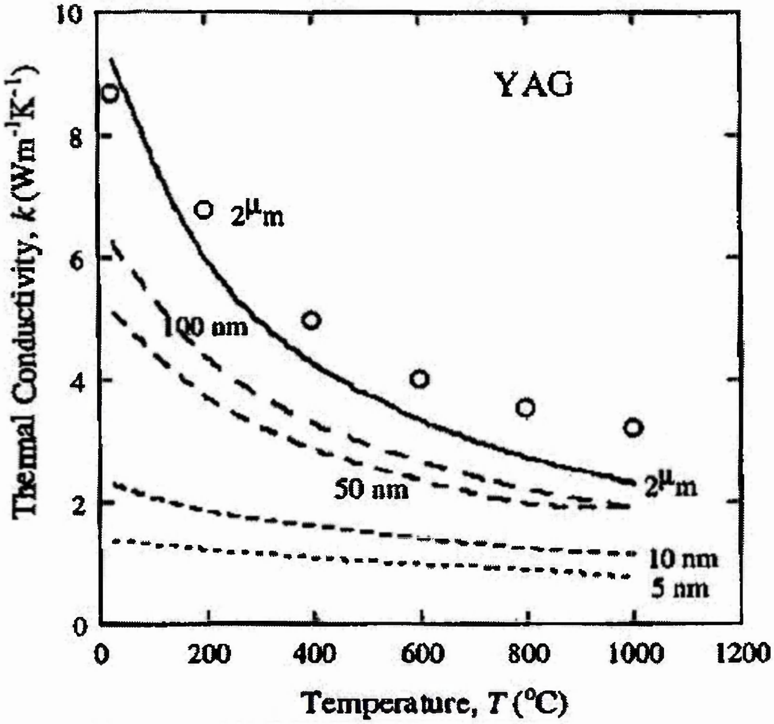

Fig.2.16. Theoretical relationship of the thermal conductivity of YAG, the temperature, and the grain size. Circles are measured values for 2 μm grain size. From ref. [5].

II.3.3 Sol-gel studies of YAG garnets

More and more papers on the synthesis of YAG and doped YAG by sol-gel or other low-temperature chemical methods have been published in recent years [105~109].

Some of them have been described in section II.2.2. The interest in the synthesising YAG by sol-gel methods is due to the need for high-quality powders and transparent ceramics. Synthesis by the sol-gel method has many advantages such as atomic level mixing of high purity precursors and low processing temperature compared with the conventionally sintering method. Most work on sol-gel synthesis has shown that YAG does not transform directly from an amorphous precursors. In general, crystallisation of YAG by the sol-gel method occurred at approximate to 900~1000^{0}C and can be densified to transparency under 1600^{0}C. The crystallisation pathways of a selected YAG synthesis via different precursors are listed in Table 2.1.

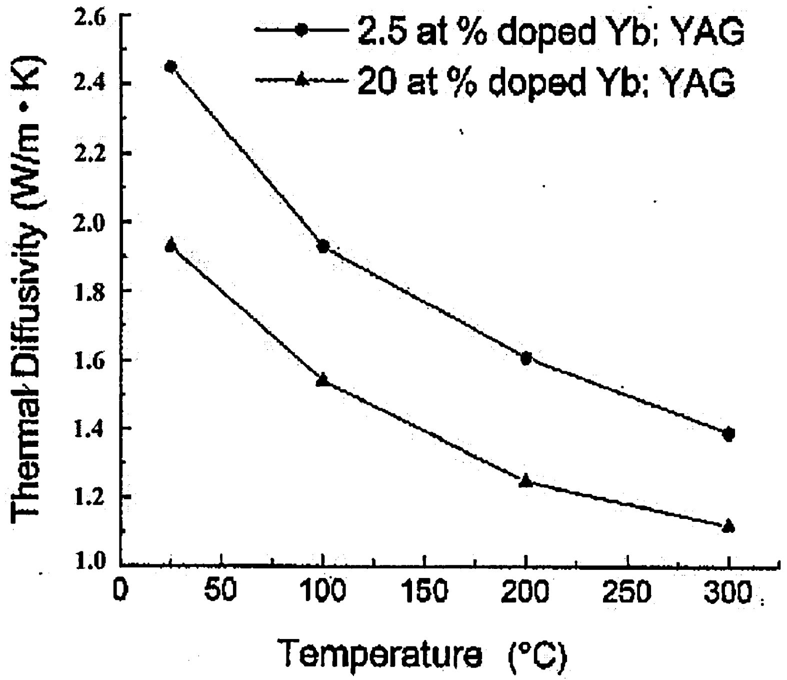

Fig.2.17. Thermal conductivity of 2.5 at. % and 20 at. % doped Yb:YAG. From ref. [95].

Many authors [110-114] have reported sol-gel studies of YAG: RE (RE = Eu, Ce, Tb or other elements) in recent years. J.Y. Choe et. al [115] studied the cathodoluminescencs of sol-gel derived Tb doped YAG powders and thin films using alkoxide organic precursors: yttrium isopropoxide, Al butoxide, and Tb acetyl acetonate. Fully crystallised pure single phase YAG was obtained at 900^0C.

D. Ravichandran et al [116] prepared Eu doped YAG thin films and powders for field emission display application using sol-gel methods. D. Hreniak [117] reported synthesis and optical properties of Nd doped YAG semitransparent nanoceramics by sol-gel methods. It was found that with increasing the temperature of heat treatment, the size of grains increased. The size of polycrystallites had significant effects on luminescence properties of Nd doped YAG.

Table 2.1 Crystallisation pathways for YAG synthesis via different precursors.

Precursors	Pathway	Reference
$Al(NO_3)_3$ and $Y(NO_3)_3$	→ YAG (~900^0C)	P. Vaqueiro et al.[109]
Alkoxy precursors	$YAlO_3$ (hex) → $YAlO_3$ (ortho) →YAG (1050^0C)	Yamaguchi et al [86], [87]
Organometallic (nitrates)	$YAlO_3$ (hex) → YAG (1100^0C)	Vietch [106]
Glycine- nitrate	$YAlO_3$ (hex) → YAG (~ 875^0C)	Hess et al [91]
Diphasic sol-gel	θ-Al_2O_3 + $YAlO_3$ → YAG (900^0C)	Hay [85]
Y & Al Isobutyrate	→YAG (910^0C)	Y. Liu et al. [107]
PVA + Y & Al nitrates	→YAG (940^0C)	Nguyen et al. [108]

J.R. Lo and T.Y. Tseng [118] studied the effects of crystallisation behaviour when a LiCl flux was used in heat treatment of single-phase Tb or Cr doped YAG sol-gel-derived powders. It was found that the 20 wt. % addition of LiCl increased the crystalline size of powders and lowered the crystallisation temperature.

YAG fibers produced by sol-gel techniques have also been reported [119-122]. Rare earth aluminium garnet ceramic fibers were found to be able to be used as reinforcements in ceramic matrix composites [123], which are high-temperature structure materials. The alumina is often added as seeds in the preparing process of YAG fibres by the sol-gel method to promote crystallisation and to form the composite fibre materials [124-126].

II.3.4 Activation energy of YAG crystallisation

B.R. Johnson et al. [127] studied crystallisation kinetics of yttrium aluminum garnet. In this report, YAG powders were prepared from the starting materials; yttrium nitrate hexahydrate [$Y(NO_3)_3.6H_2O$] and aluminium nitrate hexahydrate [$Al(NO_3)_3.6H_2O$]. They were dissolved in hydrolysed polyvinyl alcohol [PVA] [108] [128]. The direct crystallisation temperature was at 940^0C, which was similar to the 910^0C crystallisation temperature reported by Y. Liu [107] from the metalorganic system they used. The powders were then heated and melted at high temperature 2200^0C and rapidly quenched (at approximately $250^0C/s$) to form an amorphous phase with some YAG nanocrystallites. The material crystallised directly into stoichiometric YAG at temperature as low as 840^0C; no intermediate phases were observed. Crystallisation most likely occurred with a constant number of sites due to pre-existent crystals. Isothermal crystallisation kinetics were studied by DTA. Several different kinetic models were examined and were applied to the data to determine which one best described the amorphous to crystallisation transition. The model that best described the data was the JMA equation [73-76]. The activation energy for YAG crystallization was then obtained as 437 kJ/mol and the measured Avrami exponent was 2.47, which corresponded to three dimensional crystal growths with a constant number of nuclei.

E.A. Aguilar studied the rapidly solidified Al_2O_3-Y_2O_3 fibres [129]. Crystallisation activation energy calculated from scan-rate dependence of DTA peaks was 390 kJ/mol for the Kissinger method and 352 kJ/mol by the Augis-Bennett method.

R.S. Hay [85] reported the activation energy for YAG formation from hydrated Y_2O_3 and Al_2O_3 particles as 280 kJ/mol. This was considered to be related to YAG -YAM boundary diffusion or surface diffusion due to the microstructural and microchemical phase composition of the parent intermediate phases.

J.R. Lo and T.Y. Tseng [84] estimated the activation energy of YAG crystallisation at about 289 kJ/mol by the isothermal process as fitted with the John-Mehl-Avrami equation [73-76] and this result is very similar to Hay's result [85]. The morphology exponent is about 0.8, which is related to the mechanism of crystal growth. However, the activation energy is about 929±8 kJ/mol by the continuous heating method as fitted with Kissinger and Sotgiu plots [130] [131]. The difference in activation energies between the two methods was explained by the different phase-transformation mechanisms of YAG for the methods. From the continuous heating method, it includes surface nucleation and crystal growth in the system they studied.

Zhukovskaka et al. [132] estimated the activation energy of YAG using the Zhuravlev equation and studied the quantitative effect of Y_2O_3. They found that the composition with a mole ratio of Y:Al = 3:5 possessed the lowest activation energy of 96 kJ/mol. Kumar et al. [133] studied the thermodynamics and nucleation behaviour in the YAG system using the regular solution model. They reported that the free energy barrier of a YAG critical nucleus was high under homogeneous conditions.

Chapter III

Experimental procedure

In this chapter, we describe the preparation and processing of samples by our sol-gel techniques. Characterisation of samples is presented in the corresponding sections. In section 1, we present the process of preparing sols of the pure and doped Yb_2O_3-Al_2O_3 system. In section 2, the sol-gel process of preparing thin films and thick coatings is described. In section 3, we present the preparation of nano-size powders by our sol-gel methods.

III.1 Preparation of sols

Aluminium chloride ($AlCl_3$, 99.99%) was used as the starting material. Aluminium chloride was dissolved in distilled water to prepare aluminium chloride solution with the concentration 10 wt. %. Then, 10 wt. % aqueous ammonia solution was added dropwise into the stock aluminium chloride solution, while stirring using a magnetic stirring rod. A precipitate of $Al(OH)_3$ was formed according to the following reaction:

$$AlCl_3 + 3\ NH_4OH \quad \leftrightarrow \quad Al(OH)_3 \downarrow + 3\ NH_4Cl \qquad (3.1)$$

The precipitate was then filtered and washed for 3 times using distilled water and then dried overnight. An organic solvent (e.g. ethanol, methanol and/or isopropanol) and water were mixed with the precipitate and stirred for at least 10 mins at room temperature in a three-necked flask which was equipped with a reflux condenser, a dropping funnel, a stirring rod, a thermometer, and a thermocontroller. The schematic diagram is shown in Figure 3.1. Then, 10 wt. % aqueous acetic acid was added dropwise to the mixed suspension at temperature 60~80^{0}C with continuous stirring for at least 2 hours. The as-prepared alumina sol was sealed in a glass bottle and allowed to age for 2 ~ 3 days.

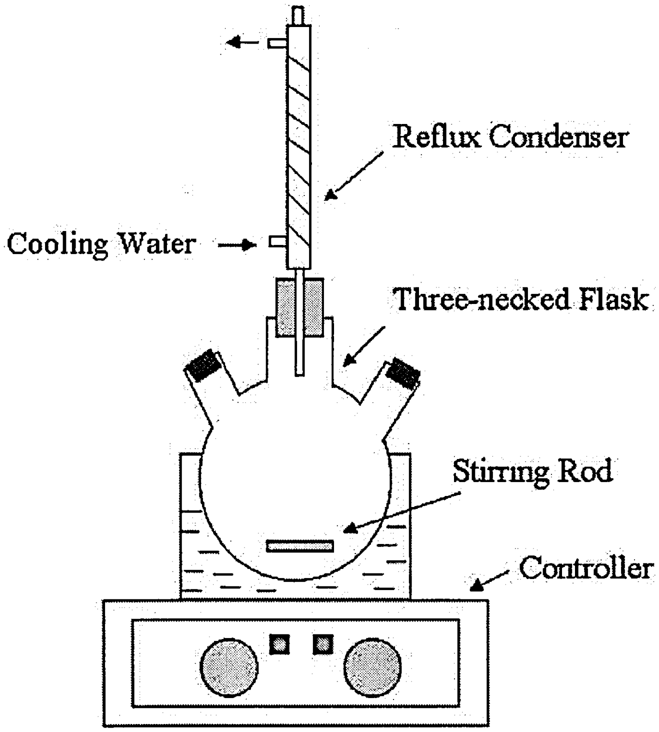

Fig.3.1. The schematic diagram of manufacturing devices in sol-gel methods.

Sample sols of the pure Yb_2O_3-Al_2O_3 system were prepared by adding Yb chemicals that were dissolved in the distilled water and allowed to hydrolyse. The pH value was controlled in the range of 3~5 to allow the sol further hydrolysis and condensation. Sample sols of the doped Yb_2O_3-Al_2O_3 system were obtained by adding the doping chemical according to the desired mole ratio into the as-prepared sol of the pure Yb_2O_3-Al_2O_3 system.

Figure 3.2 shows a schematic representation of the processing steps. The prepared sample sols of the pure and doped Yb_2O_3-Al_2O_3 system with their compositions are shown in Table 3.1. All sample sols were prepared for further use to produce thin films, coatings, or nano-size powders. Samples #1~7 were prepared to study sol-gel processing of the pure and doped Yb_2O_3-Al_2O_3 system. Sol-gel synthesis and crystallisation kinetics of the pure and Mo doped YbAG were investigated using samples #5, #7, and #8. Samples #9~12 were prepared to manufacture phase-pure Yb doped YAG nano-size powders and thin films.

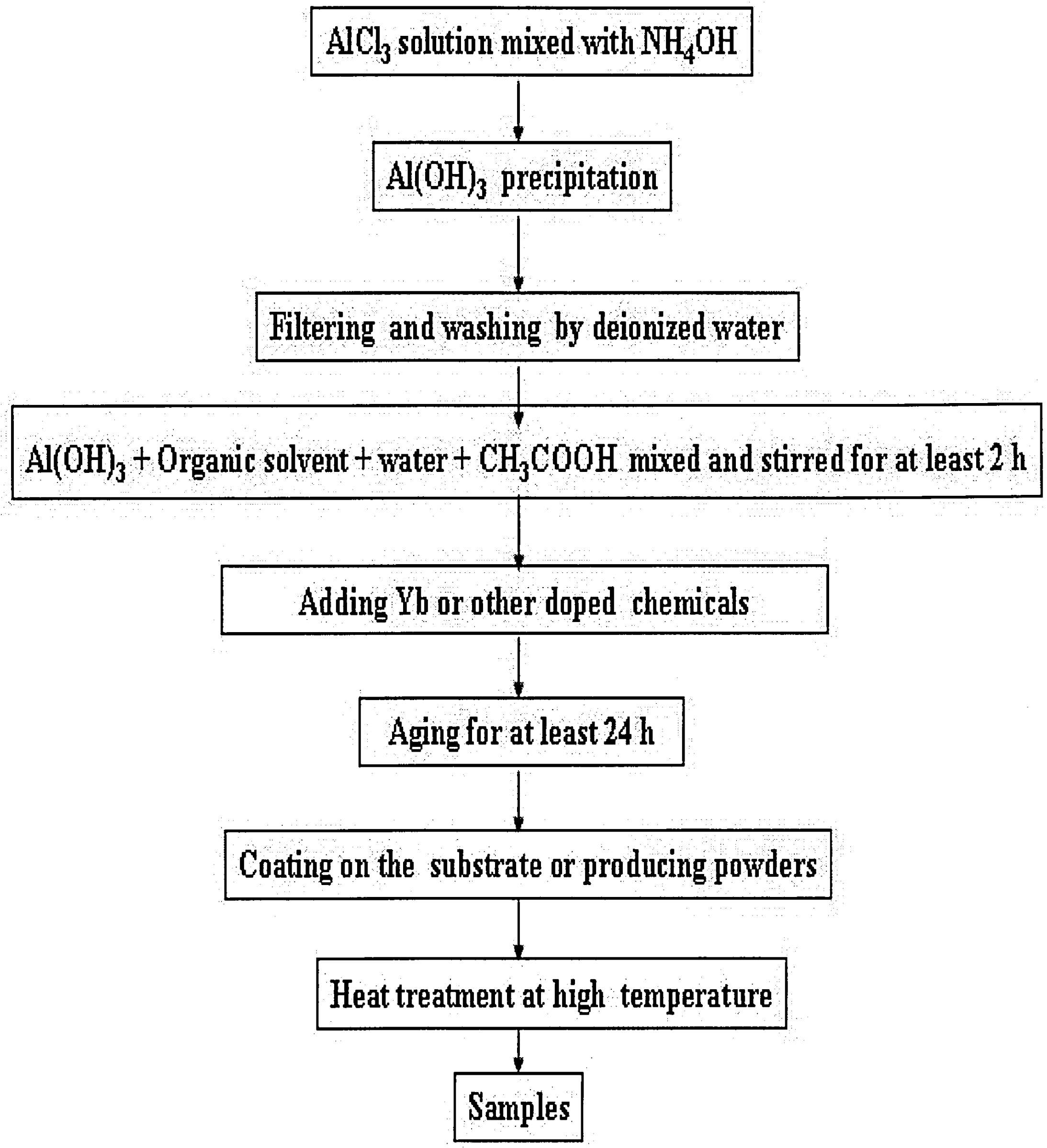

Fig.3.2. A schematic representation of the steps of preparing samples.

Table 3.1 Sample sols with their compositions.

Samples	Compositions	Doping
Sample #1	Yb^{3+}/Al^{3+}=2:1	No doping
Sample #2	Yb^{3+}/Al^{3+}=1:1	No doping
Sample #3	Yb^{3+}/Al^{3+}=1:1, Li^{+}/Yb^{3+}= 8 at. %	8 at. % Li^{+} doping
Sample #4	Yb^{3+}/Al^{3+}=1:1, Li^{+}/Yb^{3+}= 8 at. %, Mo^{6+}/Yb^{3+}=4 at. %	8 at. % Li^{+} & 4 at. % Mo^{6+} doping
Sample #5	Yb^{3+}/Al^{3+}=3:5	No doping, Pure YbAG
Sample #6	Yb^{3+}/Al^{3+}=3:5, Li^{+}/Yb^{3+}= 4 at. %, Mo^{6+}/Yb^{3+}=4 at. %	4 at. % Li^{+} & 4 at. % Mo^{6+} doping
Sample #7	$(2Mo^{6+}+Yb^{3+})/Al^{3+}$=3:5 Mo^{6+}/Yb^{3+}=10 at. %	10 at. % doped Mo^{6+}:YbAG
Sample #8	$(2Mo^{6+}+Yb^{3+})/Al^{3+}$=3:5 Mo^{6+}/Yb^{3+}=30 at. %	30 at. % doped Mo^{6+}:YbAG
Sample #9	$(Yb^{3+}+Y^{3+})/Al^{3+}$=3:5 Yb^{3+}/Y^{3+}=10 at. %	10 at. % doped Yb:YAG
Sample #10	$(Yb^{3+}+Y^{3+})/Al^{3+}$=3:5 Yb^{3+}/Y^{3+}=20 at. %	20 at. % doped Yb:YAG
Sample #11	$(Yb^{3+}+Y^{3+})/Al^{3+}$=3:5 Yb^{3+}/Y^{3+}=50 at. %	50 at. % doped Yb:YAG
Sample #12	$(Yb^{3+}+Y^{3+})/Al^{3+}$=3:5 Yb^{3+}/Y^{3+}=100 at. %	100 at. % doped Yb:YAG

III.2 Preparation of coatings

III.2.1 Thin films

The prepared sols were spin or dip coated on Si or stainless steel substrates. Si substrates were single crystals with the surface normal orientation [100] and were cut to 1 x 2 cm. Prior to coating, substrates were cleaned with soap, water and then distilled water, and finally ultrasonically cleaned in ethanol and acetone. After each coating, the substrates were annealed at 400^0C for 30 minutes. The coated samples were then heated at various temperatures at the heating rate of 10^0C/min to study the crystallisation process. The coated samples were also heated at very fast heating rate (100^0C/min) to investigate the crystallisation kinetics with various calcination times at the designated crystallisation temperature. This very fast heating rate was used to avoid the effects on the crystallisation during the heating process. All samples that were used to study the crystallisation kinetics were prepared under the same conditions.

For the sake of clearly describing our research, thin film samples on Si (100) coated by the prepared sols listed in Table 3.1 were divided into four groups as following:

Group 1: TFL1-GP1.

Group 2: TFL2-GP2, TFL3-GP2, and TFL4-GP2.

Group 3: TFL5-GP3, TFL6-GP3, TFL7-GP3, and TFL8-GP3.

Group 4: TFL9-GP4, TFL10-GP4, TFL11-GP4, and TFL12-GP4.

where the abbreviation "TFL" stands for the thin film; the "number" following the "TFL" means that this thin film was coated by the corresponding "number" of the sample sols listed in Table 3.1; the abbreviation "GP" represents the group; and the "number" following the "GP" is the group number.

Polished 304 stainless steel substrates were prepared for the study of corrosion resistance. The prepared sample #7 sol in Table 3.1 was dip coated 4 times on the stainless steel substrates at the dip speed rate of 3 cm/min. After each coating, the substrates were annealed at 400^0C for 30 minutes. The final heat treatment was 600^0C and 750^0C for 1 hour, respectively. We assign this is Group 5 as follows:

Group 5: TFL7-GP5-a (600^0C calcination) and TFL7-GP5-b (750^0C calcination)

All samples in Group 1, 2, 3, and 4 were annealed at various temperatures for different times and then characterised by XRD.

Thin film thermal behaviour of samples TFL2-GP2, TFL3-GP2, TFL4-GP2, and TFL6-GP3 in the sol-gel processing was studied by DTA. DTA samples were prepared by scratching off the gel thin films which had been dip coated on Si substrates.

Thin film samples TFL3-GP2 and TFL7-GP3 after heating respectively at 850^0C were analysed by XPS.

The xerogel thin film thickness of the sample TFL5-GP3 was measured by SEM. The sample was prepared by carefully dropping 3.0 wt. % aqueous ammonia solutions onto the one-time dip coated xerogel thin film surface, which made the thin film corrode and roll up on the substrate. The thin film surface morphology of samples TFL5-GP3 and TFL7-GP3 after full crystallisation at 850^0C annealing was characterised by AFM.

The electrochemical polarisation of thin film samples TFL7-GP5-a and TFL7-GP5-b as well as the stainless steel were tested. After testing, the surface morphologies were observed by SEM.

III.2.2 Thick coatings

In general, it is very difficult to make thick coatings with the thickness of more than ten microns directly by the conventional sol-gel method. However, a modified sol-gel coating technology may be a way to overcome this problem. Fine powders can be added into the sol as the so-called filler to form the mesastable slurry. The slurry is then coated on substrates either by dip coating or by spray coating. Thick coatings can be obtained. The shrinkage of the coatings is reduced dramatically because there is no shrinkage of the added particles. However, the bonding between the coatings and the substrate or among particles is weak and it is necessary to modify the coatings to strengthen the bonding. Adding an organic polymer such as PVA into the slurry could be very useful, which can be used to stabilize the suspension and to enhance the bonding.

Ni superalloy substrates were prepared by polishing the surface to within one micron, and then were ultrasonically cleaned in ethanol and acetone. YAG powders with the particle size about 1 μm were added and mixed ultrasonically with the prepared 10 atomic. % Mo doped YbAG sol (sample #7 in Table 3.1) for at least 2 hours. The slurry was then dip coated on the Ni superalloy substrate for 4~5 times. After each slurry coating, the sample #7 sol without the YAG powder filler was dip coated on the sample to fill in the spaces or pores in order to enhance the bonding of particles. After each coating, the substrate was annealed at 400^0C for 30 minutes. Finally, the coated sample was heated to crystallise at 750^0C for 8 hours at the heating rate of 10^0C/min and the thick composite coatings of Mo:YbAG and YAG were produced. Surface and cross section morphologies of the thick composite coatings were observed by SEM.

III.3 Preparation of nano-size powders

The prepared sol was added dropwise to the 10-30 wt. % aqueous ammonia solution with continuous vigorous stirring. Urea $[(NH_2)_2CO]$ [167], Polyacrylamide (PAM) [168], or other polymers can be added into the sol before dropping it into the ammonia solution. The added organics serve as a dispersing medium to limit the agglomeration of particles.

The precipitate was filtered and allowed to dry in an air oven at 80^0C. The dried powders were then heated at various temperatures at the heating rate of 10^0C for the required time to obtain xerogel powders, amorphous powders, and finally calcined at the required temperature to realise the full crystallisation. Finally, nano-size powders were produced.

The prepared powders are divided into two groups as following:

Group 6: POW5-GP6, POW7-GP6.

Group 7: POW9-GP7, POW10-GP7, POW11-GP7, and POW12-GP7.

where the abbreviation "POW" stands for powders; the "number" following the "POW" means that the powders were prepared by the corresponding "number" of the sample sols listed in Table 3.1; the abbreviation "GP" represents the group; and the "number" following the "GP" is the group number.

Thermal behaviour of samples POW5-GP6 and POW7-GP6 using the wet gel powders was analysed by DTA and TG, separately.

Samples POW5-GP6 and POW7-GP6 were heat-treated at 200^0C, 300^0C, 400^0C, 500^0C, 600^0C, 750^0C or 850^0C for 30 minutes, respectively. The heated powders were directly used as the samples for IR spectra and Raman spectra. After 850^0C for 30 minutes heat treatment, samples POW5-GP6 and POW7-GP6 were characterised by XRD, respectively. IR transmittance spectra were also carried out by using disk samples which were prepared by mixing and pressing POW5-GP6 and POW7-GP6 samples after 850^0C for 30 minutes annealing with KBr in the mass ratio 10:100.

Samples POW9-GP7, POW10-GP7, POW11-GP7, and POW12-GP7 were heat-treated at 800^0C for 3 hours and 850^0C for 11 hours, respectively. The heated powders were characterised by XRD and Raman spectra. IR transmittance spectra were also performed by using disk samples which were produced by mixing and pressing the samples after 850^{0}C 11 hours heat treatment with KBr in the mass ratio 10:100.

The morphologies of samples in Group 7 after 850^{0}C 11 hours heat treatment were observed by SEM. Nanosize powders of the sample POW12-GP7 were characterised by TEM. Specimens for TEM observation were prepared by briefly and ultrasonically dispersing the nanosize powders in acetone. One drop of the solution was then placed on a copper grid coated with an evaporated amorphous carbon film.

Chapter IV

Techniques

In this chapter, we describe the techniques which are used to characterise our samples. These techniques were DTA, TG, XRD, IR and Raman spectra, XPS, SEM, AFM, and TEM. The electrochemical polarization tests of coatings are also included in this chapter.

IV.1 Differential thermal analysis and thermogravimetric analysis

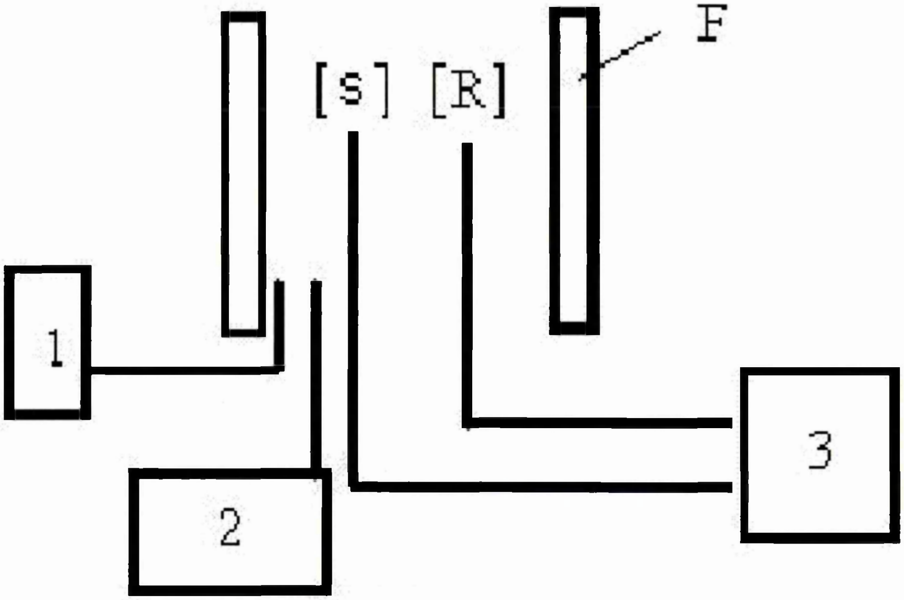

Fig.4.1. A schematic diagram of differential thermal analysis. F: Heating Furnace; 1: Temperature controller; 2: Gas controller; 3: Differential thermal recording equipment; S: Sample; R: Passive material.

A schematic diagram of a typical DTA apparatus is shown in Figure 4.1. Temperature differences between the sample material, heated at a controlled rate to a pre-determined temperature, and alumina are recorded. Any physical or chemical emissions of heat or absorption of heat from the sample appear in the curve as exothermic or endothermic peaks. The precise temperature at which a reaction takes place is determined or a phase change or reaction product is identified.

Thermogravimetric analysis (TG) is a precise measurement of the weight change of a solid as it is heated at a controlled rate to a pre-determined temperature. For example, TG can be used to determine the amount of chemically attached water or the organic content of an otherwise inorganic substance.

DTA thermal analysis was performed with a Perkin-Elmer thermal analyser. DTA curves were recorded over a wide range of temperatures (up to 1000^0C) at a heating rate of 10^0C in an air atmosphere. TG analysis was performed with Mettler TG50. TG curves were recorded in an air atmosphere at a heating rate of 10^0C over a wide range of temperatures from 30^0C to 900^0C.

IV.2 X-ray diffraction analysis

The high voltage maintained across the electrodes draws electrons toward a metal target (the anode). X-rays are produced at the point of impact, and radiate in all directions. Metal copper is commonly used as a target. It produces the strongest characteristic radiation (Kα1) at a wavelength of about 1.5 angstroms (Å).

Bragg's law describes the situation when an incident X-ray beam encounters a crystal lattice (shown in Figure 4.2) in the following equation:

$$2d(\sin\theta) = \lambda_0 \tag{4.1}$$

where d is the lattice interplanar spacing of the crystal; θ is the X-ray incidence angle (Bragg's angle); and λ_0 is the wavelength of the characteristic X-rays.

In general, X-ray are scattered and most scattering interferes with itself and is eliminated (destructive interference). However, a peak in X-ray intensity occurs when scattering from one set of X-ray planes is in phase with scattered rays from other atomic planes. Under this condition the reflections combine to form new-enhanced wave fronts that mutually reinforce each other (constructive interference). The position of these peaks in intensity corresponds to the d-spacing of the crystal lattice. This diffraction pattern of intensity v.s 2θ is unique for each crystalline material like a fingerprint and material can be identified by comparison with a database of known materials. XRD can be used as research tool for confirming the presence of crystalline phases, rapid identification of unknown materials, the study of thin films or powders, etc.

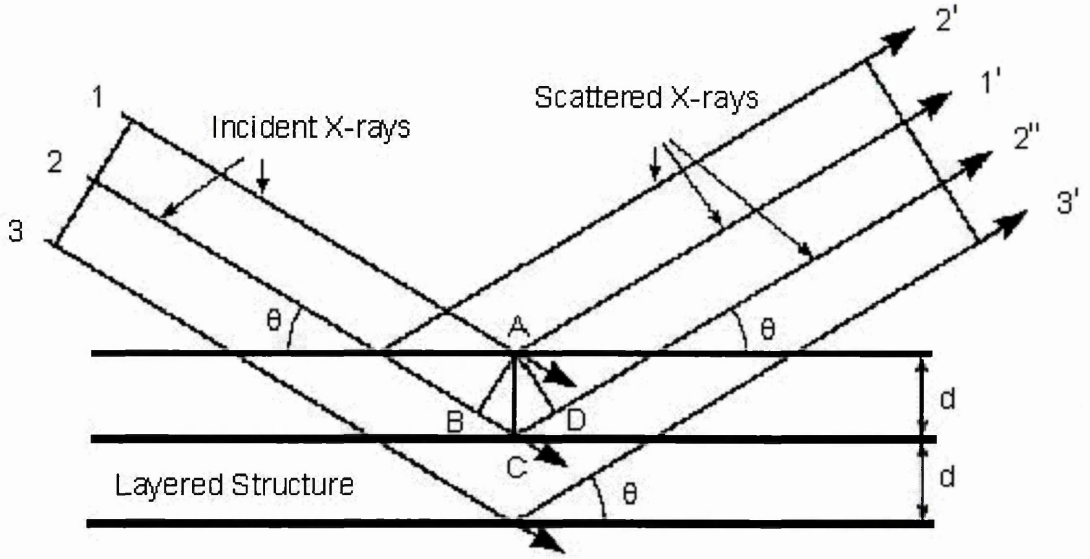

Fig.4.2. A schematic diagram of X-ray diffraction with a crystal lattice.

The basic geometry of an X-ray diffractometer is shown in Figure 4.3. A source of monochromatic radiation and an X-ray detector are situated on the circumference of a graduated circle centred on the powder specimen. Divergent slits, located between the X-ray source and the specimen, and receiving slits, located between the specimen and the detector, limit scattered (non-diffracted) radiation, reduce background noise, and collimate the radiation. The detector and specimen holder are mechanically coupled with a goniometer so that a rotation of the detector through 2x degrees occurs in conjunction with the rotation of the specimen through x degrees, a fixed 2:1 ratio.

The X-ray patterns of all samples were collected in the mode of a Philips PW3710 diffractometer using Cu Kα radiation. The tube current and voltage were 35 mA and 40 kV, respectively. The scan step time was 4s and the step size was 0.02^0. Usually, the 2θ range examined was $15 \sim 60^0$.

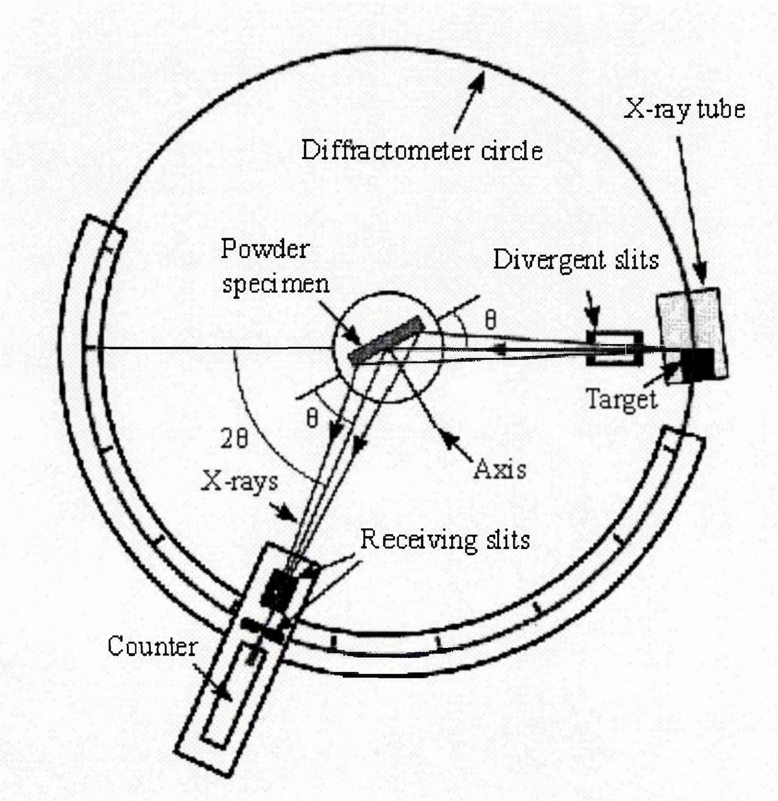

Fig.4.3. The basic geometry schematic of an X-ray diffractometer.

IV.3 Infrared and Raman spectra

IV.3.1 Infrared spectra

Infrared spectroscopy includes far (400~10 cm^{-1}), mid (4000~400 cm^{-1}) and near (10000~4000 cm^{-1}) infrared regions. However, most vibrational transitions (of the chemical bonds in materials) are generally within the mid-infrared spectroscopy range. When infrared radiation is incident on the sample, it will only be absorbed under certain conditions even if resonance occurs with the vibrational frequency of a given vibration. Thus, a change in dipole moment with molecular vibration is required for a vibrational transition to be seen in IR absorption spectroscopy. The rules determining optical activity are known as selection rules. For example, the symmetric stretch in a linear heteroatomic molecule is IR active, but for a homonuclear diatomic, it is not. Obviously, the more symmetric the molecule, the fewer transitions are IR active.

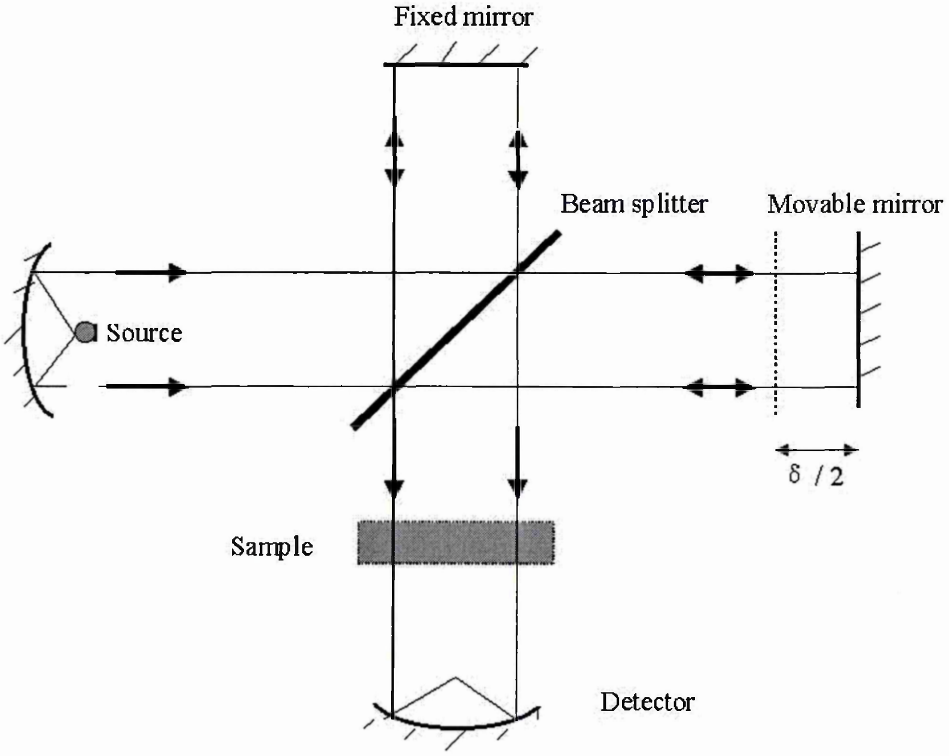

Fig.4.4. A schematic technique for obtaining the Fourier transform infrared spectroscopy using a Michaelson Interferometer.

Basic infrared spectroscopy can be interpreted in terms of normal modes of vibration. The number of normal modes available to a molecule depends upon the number of atoms, N, it contains. There are 3N-6 normal modes for non-linear molecules and 3N-5 for linear molecules. And generally there are 3N-4 normal modes for polymer molecules.

A schematic technique for obtaining the Fourier transform infrared spectroscopy using a Michaelson Interferometer is shown in Figure 4.4. An interferogram is obtained from two light beams by the beamsplitter. One beam is from the fixed mirror and another is from the movable mirror. The interferogram intensity can be expressed as the following:

$$I(x) = B(\upsilon)cos(2\pi\upsilon x) \qquad (4.2)$$

where I(x) is the intensity as a function of mirror position, x; and B(v) is the radiance of the source as a function of frequency, υ.

The modulation frequency is affected by two factors in the following:

$$f_\upsilon = 2 * v * \upsilon \qquad (4.3)$$

where f_υ is the modulation frequency, v is the speed of the movable mirror.

For a polychromatic source, the interferogram intensity is the sum of all amplitudes of all monochromatic radiation.

Thus, it can be expressed as:

$$I(x) = \int_{-\infty}^{\infty} B(\upsilon)\cos(2\pi\upsilon x)d\upsilon \qquad (4.4)$$

This is one half of a Fourier Transform pair. The other half is

$$B(\upsilon) = c\int_{-\infty}^{\infty} I(x)\cos(2\pi\upsilon x)dx \qquad (4.5)$$

We can measure the interferogram, I(x), and obtain the spectrum B(v) by taking the Fourier transform.

IR spectra were performed in Magna-IR 860 spectrometer made by Nicolet and the examined wavenumber range was from 4000 to 500 cm^{-1}. IR transmittance spectra were recorded in Genesis Series FTIR™ made by ATI Mattson and the examined wavenumber range was from 1000 to 200 cm^{-1}.

IV.3.2 Raman spectra

Raman spectroscopy is based on light scattering phenomena. When a photon strikes a molecule, and is scattered with no transfer of energy, i.e. at the same wavelength, this is elastic scattering or called Rayleigh scattering. Conversely, there can be an interaction that changes the energy of the scattered radiation. This is inelastic in nature and is called Raman scattering. If the ground state molecules gain the energy between excited states by the interaction with the photons, this gives rise to Stokes lines. The Raman scattered light is at lower energies (longer wavelengths) than the incident radiation. Interaction with excited states also produces scatter at wavelengths shorter than the excitation line. This gives rise to anti-Stokes lines. They are shown in Figure 4.5.

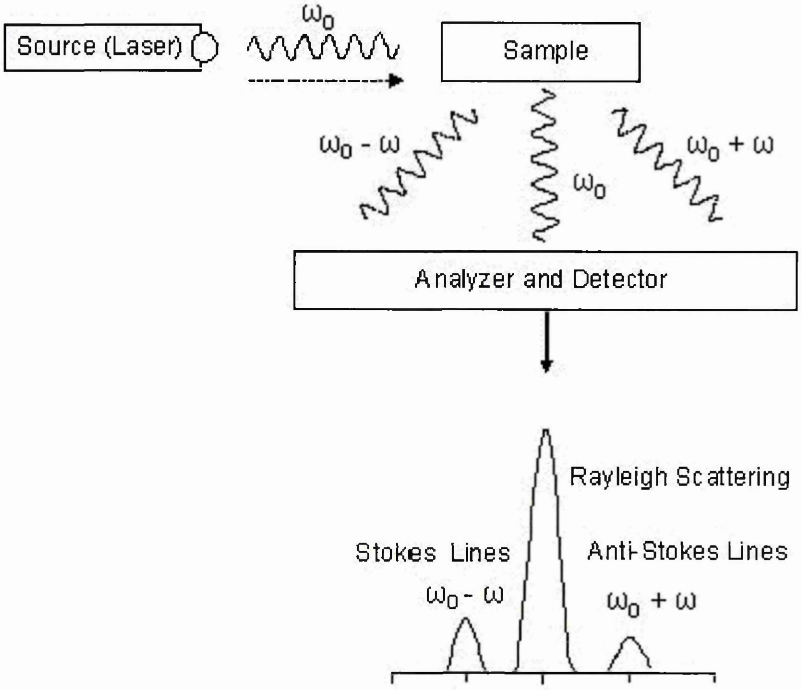

Fig.4.5. A schematic diagram of Raman spectra.

For Raman activity the selection rules are different from Infrared absorption and there must be a change of polarisability with molecular vibration. If a molecule has a centre of symmetry, vibrational modes active in the infrared will be Raman inactive and vice versa. If a molecule has no a centre of symmetry, the infrared and Raman spectra are sometimes very similar.

Raman spectra were obtained using a Renishaw Ramanscope system 2000 spectrometer using the helium/neon laser with the laser wavelength 633 nm and 25 mW power. The examined vibrational frequency range was from 1000 to 200 cm^{-1}.

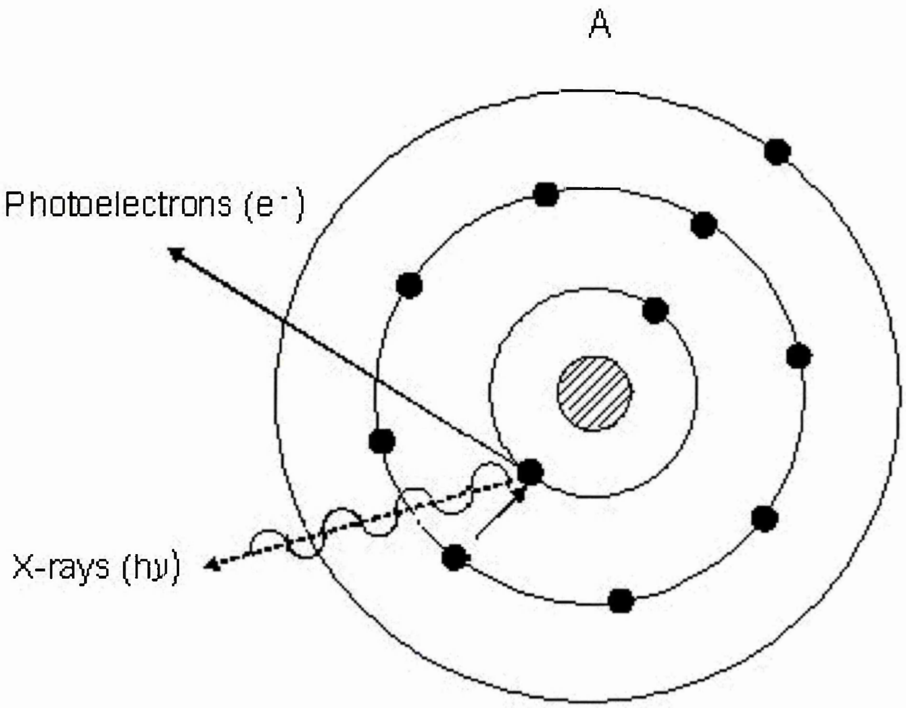

Fig.4.6. Schematic diagram of the interaction process of photons and atoms.

IV.4 X-ray Photoelectron Spectroscopy

When photons with energy hυ interact with atoms of a material, the atom gains an energy amount equal to hυ by absorbing a photon. Incident X-ray photon results in the ejection of a single photoelectron. The released photoelectron obtains all the energy from the striking photon. It can then escape from the atom, and even further from the matter and kinetic energy keeps it moving. The atom is ionised. Incident photons usually carry an energy ranging from 1 to 2 KeV. This process is expressed as (Figure 4.6):

$$h\upsilon + A \rightarrow A^{*+} + e^- \qquad (4.6)$$

where A is the neutral atom, hυ is the energy of a photon, A^{*+} is the atom in the ionised state. e^- is the ejected photoelectron.

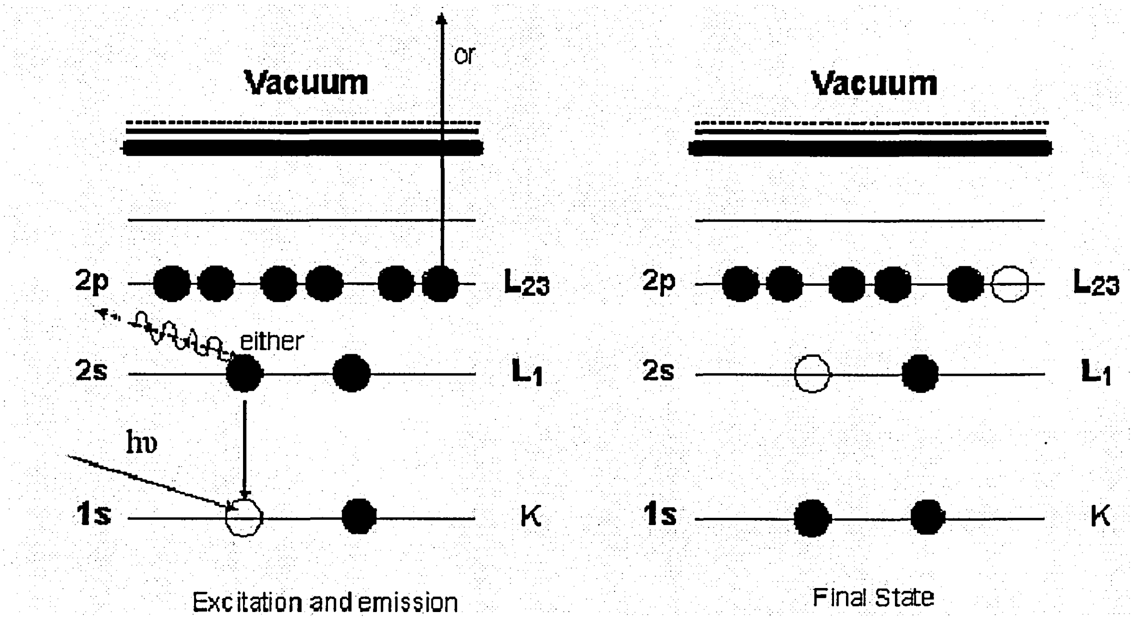

Fig.4.7. Schematic diagram of the process of Auger and X-ray photoelectrons.

Consequently, there will be some atoms lacking electrons in the shells from which photoelectrons have been released. To recover from this ionised state, an electron from a higher orbital descends to fill the vacancy created by the photoelectron resulting in an energy release, which in turn, ejects a second (Auger) electron. It is shown in Figure 4.7. The principle of the conservation of energy allows us to write the energy balance equation, valid for the absorption of a photon carrying energy of hυ:

$$h\upsilon = E_{\text{Kinetic}} + E_{\text{Binding}} + W_{\text{Work function}} \qquad (4.7)$$

where $h\upsilon$ is X-ray beam incident energy; E_{Kinetic} is the electron kinetic energy when leaving the specimen; E_{Binding} is the electron binding energy inside the atom.

From equation 4.7, we can obtain:

$$E_{\text{Binding}} = h\upsilon - E_{\text{Kinetic}} - W_{\text{Work function}} \qquad (4.8)$$

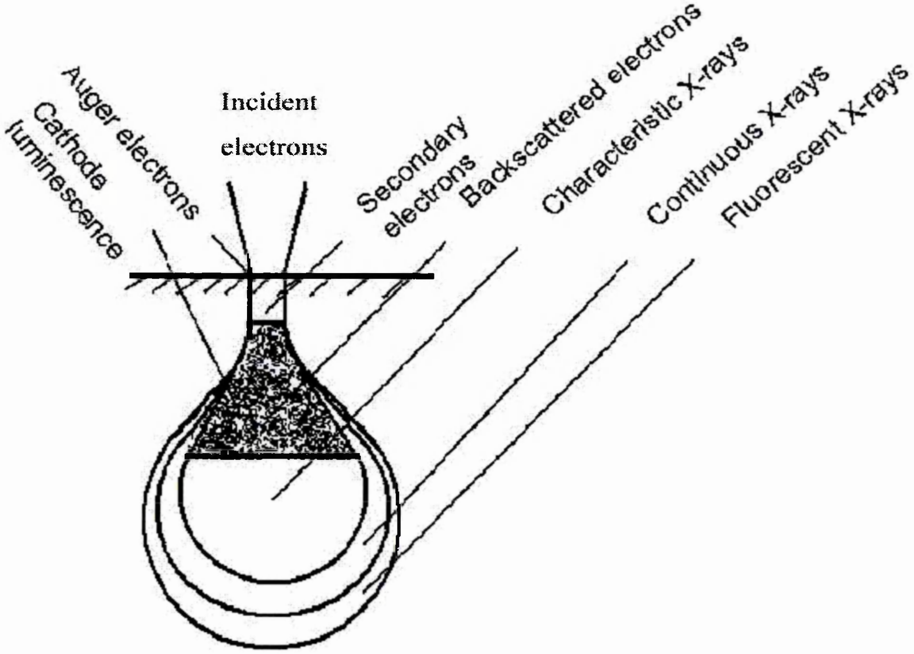

Fig.4.8. The schematic diagram of the interactions of the incident electrons and the surface of the sample.

Since $h\upsilon$ is known from X-ray beam incident energy and $W_{\text{Work function}}$ is a constant for the instrument under same conditions (generally 4 eV), E_{Binding} will be dependent on E_{Kinetic}.

Chemical analysis was performed via XPS using a Kratos AXIS 165 instrument with monochromatic Al Kα radiation (1486.6 eV). Survey scans were taken at pass energy of 80 eV. High-resolution scans were taken at pass energy of 20 eV. In the latter configuration the Ag 3d $_{5/2}$ peak has measured FWHM of around 0.6 eV. The spectra were analysed and the background subtraction was carried out using XPSPEAK software. All the curve fitting was done with 80% Lorentzian and 20% Gaussian curves.

IV.5 Scanning Electron Microscopy

The well-known results are shown in Figure 4.8 after the incident electrons strike the sample and interactions occur inside the sample. Morphologies of SEMs are patterned from the secondary electrons, or part of background electrons. A typical SEM functions is shown in Figure 4.9.

A stream of monochromatic electrons is produced from the electron gun. The stream is condensed by the first condenser lens. This lens is used to both form the beam and limit the amount of current in the beam. The second condenser lens forms the electrons into a thin, tight, coherent beam. The condenser apertures work to eliminate the high-angle electrons from the beam. A set of coils then "scan" or "sweep" the beam in a grid fashion, dwelling on points for a period of time determined by the scan speed. The final lens, the Objective, focuses the scanning beam onto the part of the specimen desired. The signals from the sample are detected with various instruments.

SEM samples were observed using XL30 ESEM-FEG or Joel-800 at 20 kV work voltage. Gold thin films are coated on the samples to make them as good conductors if samples are examined by SEM Joel-800.

IV.6 Transmission Electron Microscopy

The incident electrons strike the sample and elastic or inelastic scattering interactions occur. When the sample is very very thin, part of the electrons are transmitted and projected onto a phosphor screen to form TEM patterns. A typical TEM working is shown in Figure 4.10.

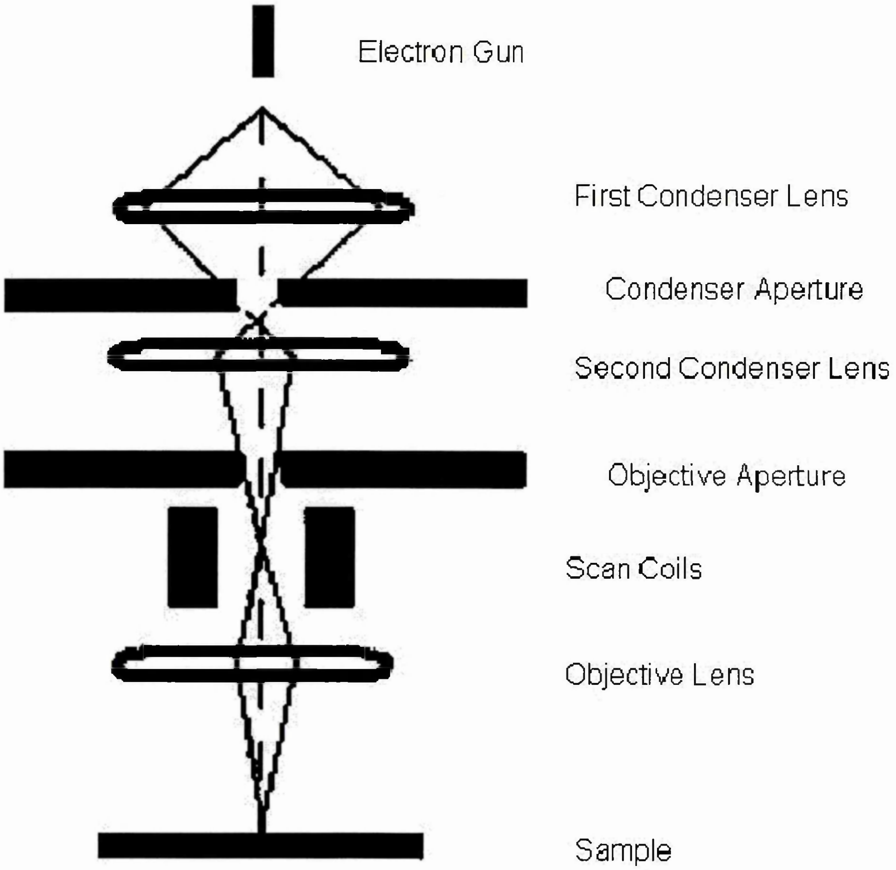

Fig.4.9. A typical SEM functions diagram.

A stream of monochromatic electrons is produced from the electron gun. This stream is focused to a small, thin, coherent beam by the use of condenser lenses 1 and 2. The first lens largely determines the "spot size", i.e. the general size range of the final spot that strikes the sample. The second lens (intensity or brightness) actually changes the size of the spot on the sample, changing it from a wide dispersed spot to a pinpoint beam. The beam is restricted by the condenser aperture (selectable), knocking out high angle electrons. The beam strikes the specimen and parts of it are transmitted. This transmitted portion is focused by the objective lens into an image. Optional Objective and Selected Area metal apertures can restrict the beam. The Objective aperture enhances contrast by blocking out high-angle diffracted electrons and the Selected Area aperture enables the user to examine the periodic diffraction of electrons by ordered arrangements of atoms in the sample. The image is passed down the column through the intermediate and projector lenses, being enlarged all the way.

TEM characterisation was performed on Phillips CM20 at 200 kV.

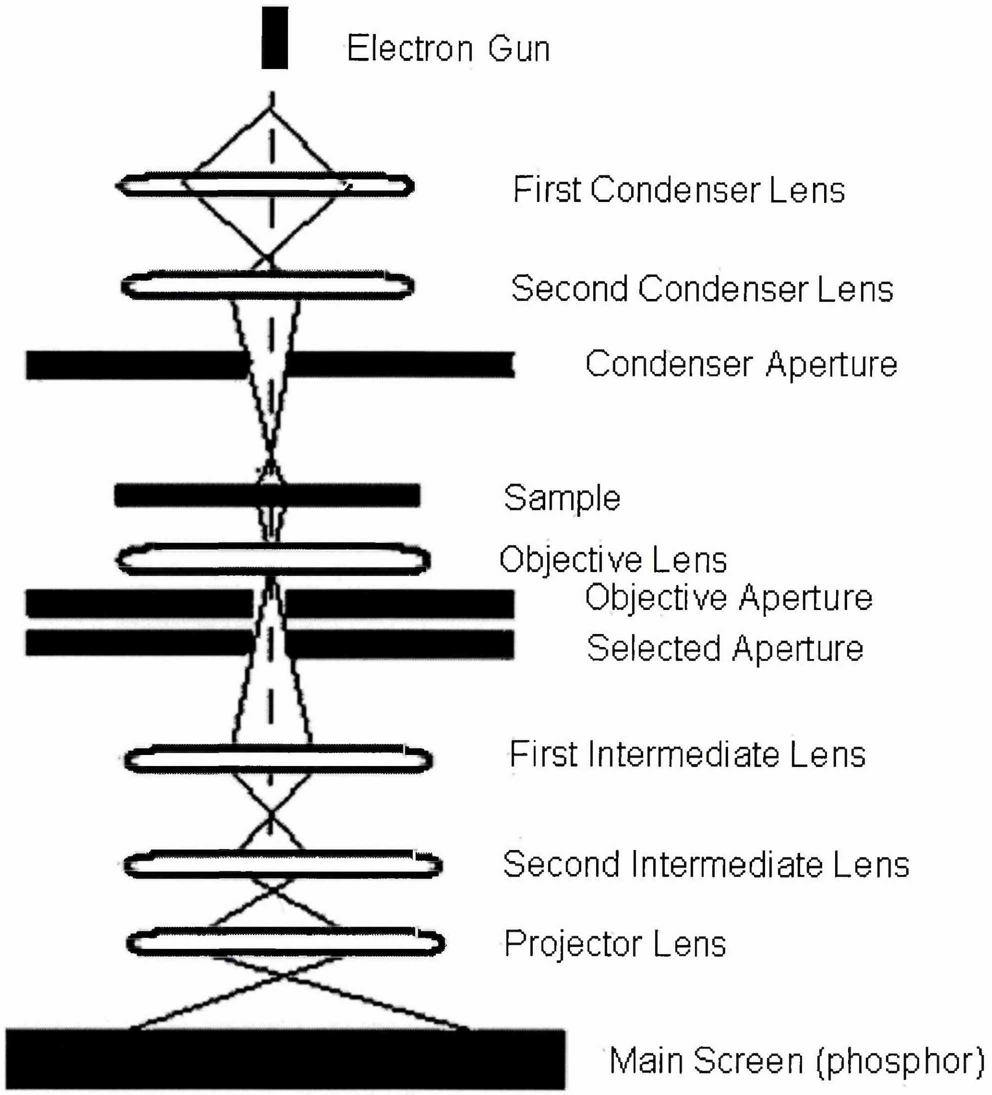

Fig.4.10. A typical TEM schematic diagram.

IV.7 Atomic Force Microscopy

A sharp tip (approximately radius ~ 20 nm) formed on soft cantilever is used to probe the interaction (force) between the tip and surface. There is a small attraction force that can be calculated around a separation distance of 0.4 nm between two atoms. When the separation distance gets smaller and smaller the repulsive force increases steeply.

For practical AFM probe tip and the sample surface, attraction force between them could be much larger than that of a two-atoms system. This is because, at least, the size of the tip is much larger than an atom. Also, much longer-range forces could occur in practice.

The interaction between the tip and sample surface is measured through the deflection of the cantilever using a laser beam and photodetector in today's commercial AFMs. There are two types of AFM: contact mode and dynamic force (tapping, non-contact) mode AFMs.

In the contact mode AFM, after a mechanical contact between the tip and the sample surface, there is a repulsive force between them. The force is used as the feedback parameter (by maintaining a constant force through adjustment of the sample height while the tips scans the surface) to obtain AFM images.

Dynamic force mode AFM was developed to measure soft surfaces where the contact mode AFM could result in degradation on the surface due to a large applied force. This mode is operated with a stiff cantilever with a typical spring constant of ~ 40 N/m, which is oscillated at around its resonant frequency. The amplitude decreases when the tip 'feels' attraction and/or repulsive forces as the tip is brought closer to the sample surface. The decrease of the oscillation magnitude when the tip is approaching toward to the sample surface is used as the feedback parameter to obtain surface morphology. The main point for using dynamic force mode AFM is that the lateral force during scanning is tremendously reduced comparing to the contact mode AFM.

AFM was performed on a Nanoscope IIIa in tapping mode using a standard silicon nitride tip.

IV.8 Electrochemical Polarization Tests

The test procedure is widely used in corrosion studies and employs a potentiostat in combination with a three-electrode cell arrangement as shown in Figure 4.11.

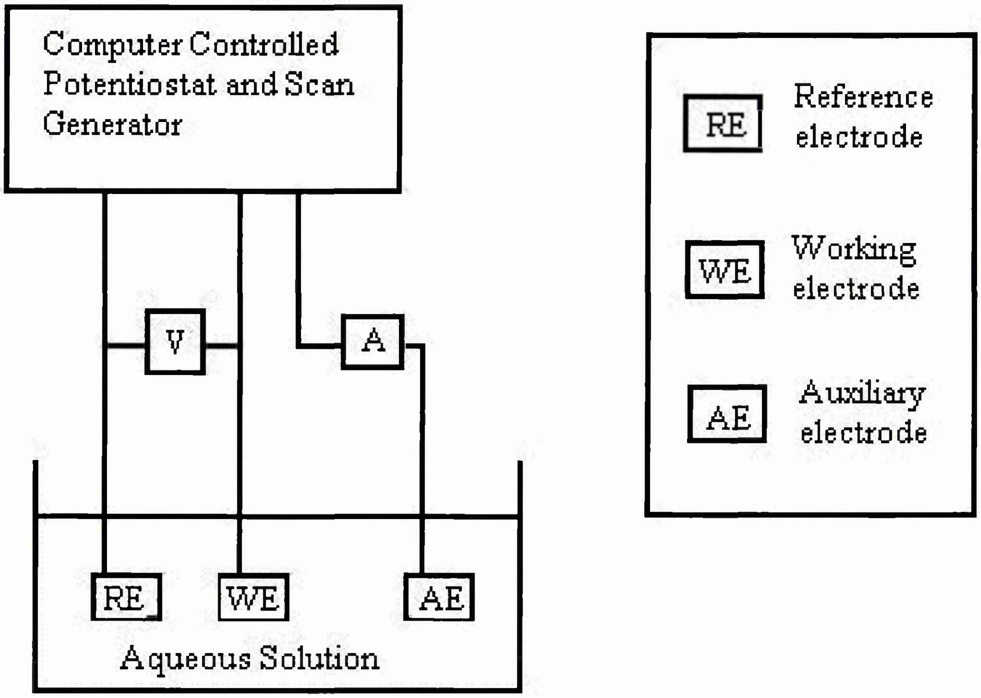

Fig.4.11. Three-electrode cell arrangement for electrochemical measurements.

In DC-Anodic polarisation tests, the sample under investigation is forced to become the net anode in an electrochemical cell and therefore the specimen corrosion is accelerated. This is achieved by forcing the electrode potential of the sample in the positive direction from the free corrosion potential (E_{corr}). As the potential is shifted away from E_{corr} there is a driving force for the electrochemical anodic reaction to occur at an accelerated rate on the sample and by monitoring the current flowing in the external circuit, as a function of potential, the corrosion kinetics can be determined. Thus, accelerated DC polarization test data for a material which is actively corroding can be plotted as an E – Log I plot.

All measurements were performed under the conditions consisting of an aqueous, air-exposed, sodium chloride (3.5%) NaCl solution. Each sample was sealed with resistance adhesive tape in order to prevent premature corrosion along the edges of the substrate. A 7.0 mm x 7.0 mm area within the centre of each sample was exposed to the solution during testing. Polarization measurements were carried out potentiostatically at room temperature using a saturated calomel reference electrode (SCE) and a platinum counter electrode. Prior to the measurements, each sample was immersed in 3.5% NaCl solution for at least 15 mins.

Chapter V

Phase conversion of the Yb_2O_3-Al_2O_3 system

V.1 Introduction

In this chapter, we will present the phase transformation in the sol-gel processing of the pure and doped Yb_2O_3-Al_2O_3 systems. As we already highlighted in Chapter II, there are no published papers on the study of this system by sol-gel methods. The phase diagram of the Yb_2O_3-Al_2O_3 system (Figure 2.13) shows that only two stable transition phases exist in this system, i.e. $Yb_3Al_5O_{12}$ and $Yb_4Al_2O_9$. According to the phase diagram in the Yb_2O_3-Al_2O_3 system, we chose three typical compositions to investigate their phase transformation in the sol-gel processing. We also doped two oxides into this system to investigate their effect on the phase conversion. One of them was Li_2O with valence one, and the other one is MoO_3 with six-coordination number.

V.2 Results

V.2.1 Thermal behaviour of the pure and doped Yb_2O_3-Al_2O_3 system

Thermal behaviour of the pure and doped Yb_2O_3-Al_2O_3 systems in sol-gel processing was studied by DTA. The experimental procedure was presented in Chapter III. The investigated samples were TFL2-GP2, TFL3-GP2, TFL4-GP2, TFL6-GP3, POW5-GP6, and POW7-GP6, where the former four samples were gel powders from thin films (see page 56 in Chapter III) and the latter two are directly from wet gel powders (see page 59 in Chapter III). The latter two samples are designed the pure and doped garnet compositions i.e. YbAG and Mo:YbAG, which will be further specifically present in chapter VI, their weight losses during the sol-gel processing were studied by TG.

V.2.1.1 DTA traces of samples TFL2-GP2, TFL3-GP2, and TFL4-GP2 are shown in Figure 5.1a, b, and c. These three samples have the same matrix composition i.e. Yb_2O_3/Al_2O_3 = 1:1. Characterisation of the thermal processes can be divided into three stages as follows:

Processes I (below 200^0C): There are two endothermic peaks for sample TFL2-GP2 (Figure 5.1a) under 200^0C. The endothermic peak that is attributed to the removal of organic solvents is overlapped in the first peak centered at about 125^0C, which is possibly due to the existence of residual excess acetic acid [169] [170] in the wet gel. The second peak centered at 160^0C is attributed to the removal of absorbed structural water. The characteristics of the thermal process in samples TFL3-GP2 and TFL4-GP2 below 200^0C are different from the sample TFL2-GP2. For sample TFL3-GP2 (Figure 5.1b), the centers of two endothermic peaks shifted to 140^0C and 180^0C. For sample TFL4-GP2 (Figure 5.1c), there are two endothermic peaks. A small one centered at 100^0C and a very large one centered at 170^0C. These changes are possibly due to the effects of the doped Li^+ or Mo^{6+}.

Processes II (between 200^0C and 500^0C): Endothermic peaks for sample TFL2-GP2 are located at 240^0C, 280^0C, and 370^0C. For sample TFL3-GP2, there are three endothermic peaks centered at 300^0C, 337^0C, and 418^0C. Two peaks centered at 300^0C and 337^0C are much smaller than the one centered at 418^0C. Sample TFL4-GP2 has three endothermic peaks in the processes II, which centered at 229^0C, 330^0C and 467^0C. In sol-gel chemistry, the endothermic peaks between heating temperature

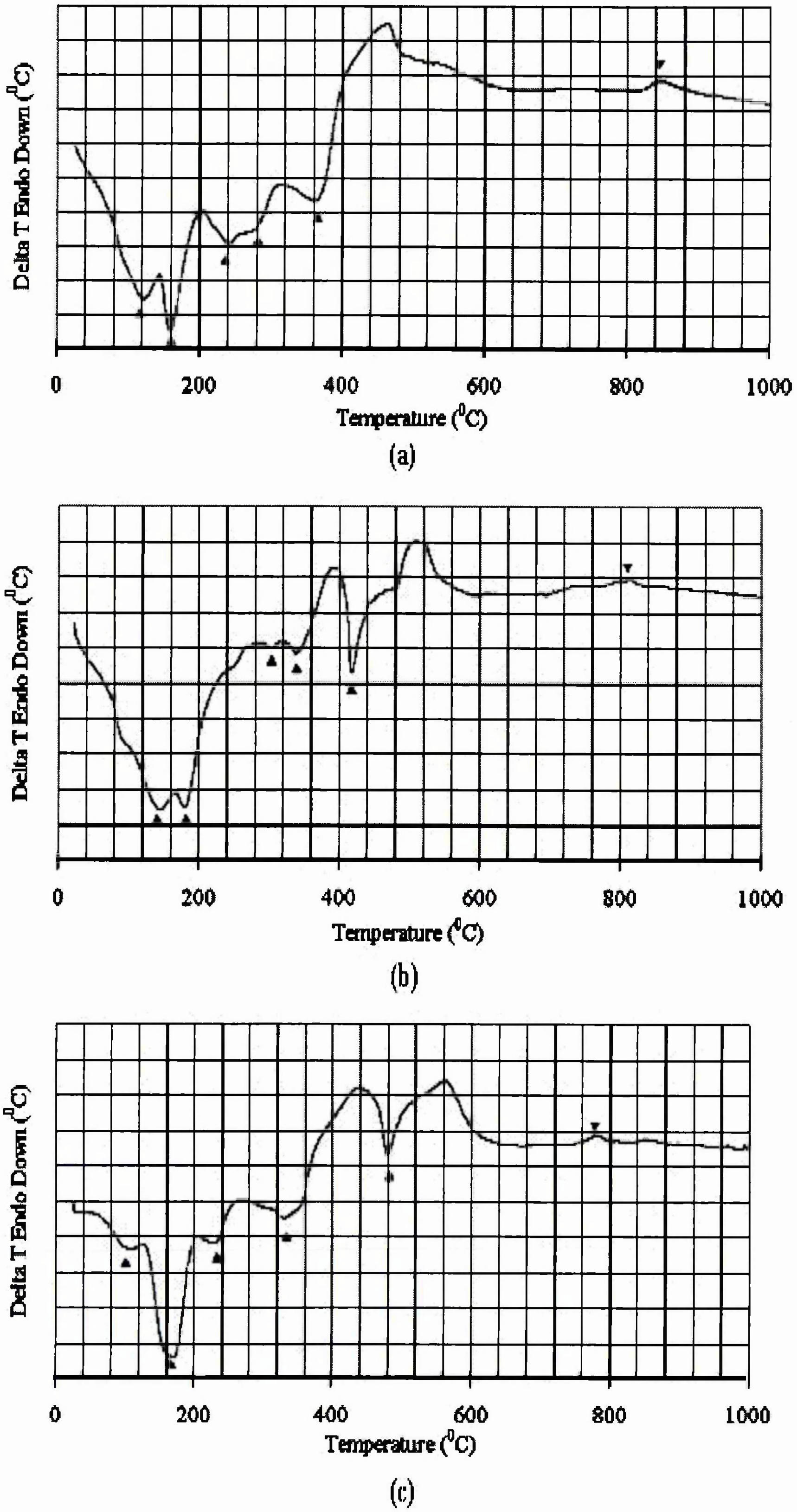

Fig.5.1. DTA traces of samples; (a) TFL2-GP2; (b) TFL3-GP2; (c) TFL4-GP2.

200^0C and 500^0C are generally attributed to carbonization or dehydroxylation. These three samples all show three endothermic peaks in the process II region which indicates a very complicated process.

After the process II, the gels have formed the amorphous network or glass structures. The amorphous oxides will transform to polycrystalline structures by further annealing at temperatures higher than 500^0C. This is the process III.

Processes III (above 500^0C): In sample TFL2-GP2, a small exothermic peak is observed at 850^0C. For samples TFL3-GP2 and TFL4-GP2, the small exotherms are at around 805^0C and 780^0C, respectively. These exothermic peaks correspond to the characteristics of crystallisation. It is expected that the corresponding temperatures of these exothermic peaks have a relationship with the crystallisation temperature. XRD results below show that the sample TFL2-GP2 has the highest initial crystallisation temperature in these three samples, followed by the sample TFL3-GP2. The sample TFL4-GP2 has the lowest initial crystallisation temperature in these three samples.

V.2.1.2 DTA traces of samples POW5-GP6, POW7-GP6, and TFL6-GP2 are shown in Figure 5.2a, b, and c, respectively. Thermogravimetric curves of samples POW5-GP6 and POW7-GP6 are also presented in Figure 5.2a and b together with their corresponding DTA curves. These three samples have very similar matrix compositions i.e. (1) POW5-GP6, the pure garnet composition Yb_2O_3 / Al_2O_3=3:5; (2) POW7-GP6, 10 at. % Mo:YbAG and $(2MoO_3+Yb_2O_3)/Al_2O_3=3:5$; (3) TFL6-GP2, $Yb_2O_3/Al_2O_3=3:5$ and dopants 4 at.% MoO_3 and 4 at. % Li_2O.

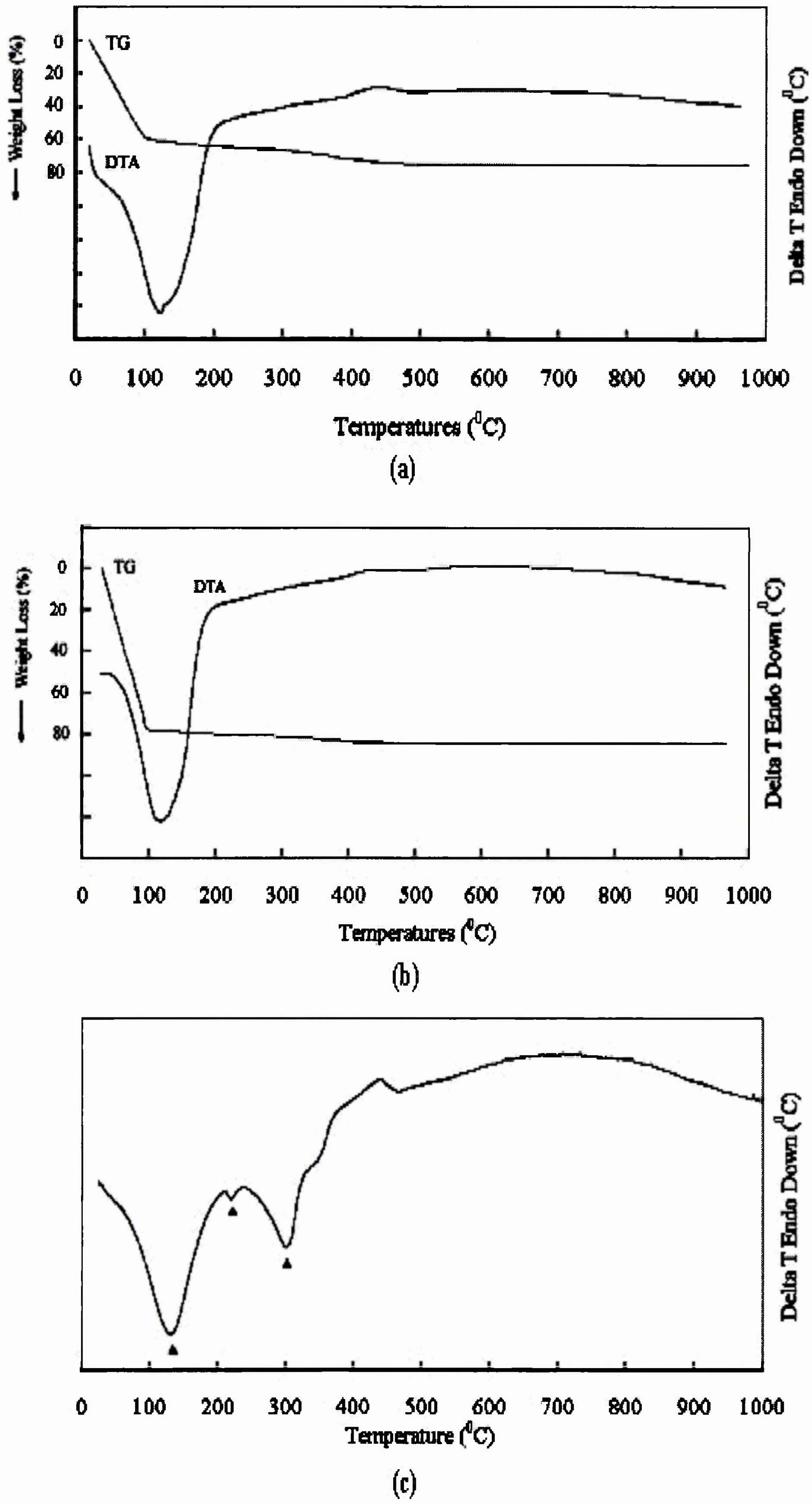

(a)

(b)

(c)

Fig 5.2. DTA and TG curves of samples; (a) POW5-GP6; (b) POW7-GP6; (c) TFL6-GP2.

Processes I (below 200^0C): Figure 5.2a, b, and c are all very similar; i.e. only one strong endothermic peak. It is centered at about 120~130^0C. This strong peak is mainly attributed to the removal of organic solvents and the absorbed structural water. Most of the weight losses (about 60% ~ 80%) occurred below 150^0C.

Processes II (between 200^0C and 500^0C): Figure 5.2a and b show no peaks in this region. However, Figure 5.2c presents two endothermic peaks; the very small one is centered at 220^0C and the large one is centered at 300^0C, which are possibly due to the effect of the doped Li_2O.

In this process, there was a continuous weight loss (about 5 ~ 10%) for samples POW5-GP6 and POW7-GP6 although DTA traces did not show any endothermic peaks. It is attributed primarily to carbonisation or dehydroxylation.

Processes III (above 500^0C): No sharp exothermic peaks related to the crystallisation temperature are found in all three cases. They present a broad and smooth exothermic process. This is an interesting result. The former two DTA traces are very similar to a sol-gel processing of SiO_2 prepared from TEOS [171]. XRD results below show that only one single-phase ytterbium alumina garnet appeared in this crystallisation process for all three samples.

V.2.2 Phase conversion of the Yb_2O_3 –Al_2O_3 system

V.2.2.1 Sample TFL1-GP1 with a composition Yb_2O_3 / Al_2O_3=2:1 in the Yb_2O_3-Al_2O_3 system was investigated by XRD. Combined plots of XRD spectra are shown in Figure 5.3. The single-phase $Yb_4Al_2O_9$ was crystallised after 950^0C heat treatment, which was identified by JCPDS #34-0368 [94].

V.2.2.2 Samples TFL5-GP3, TFL6-GP3, and TFL7-GP3 (see page 55 and 56 in Chapter III) with a matrix composition Yb_2O_3/ Al_2O_3=3:5 in the Yb_2O_3-Al_2O_3 system were investigated by XRD. Combined plots of their XRD spectra are shown in Figure

5.4 a, b, and c, separately.

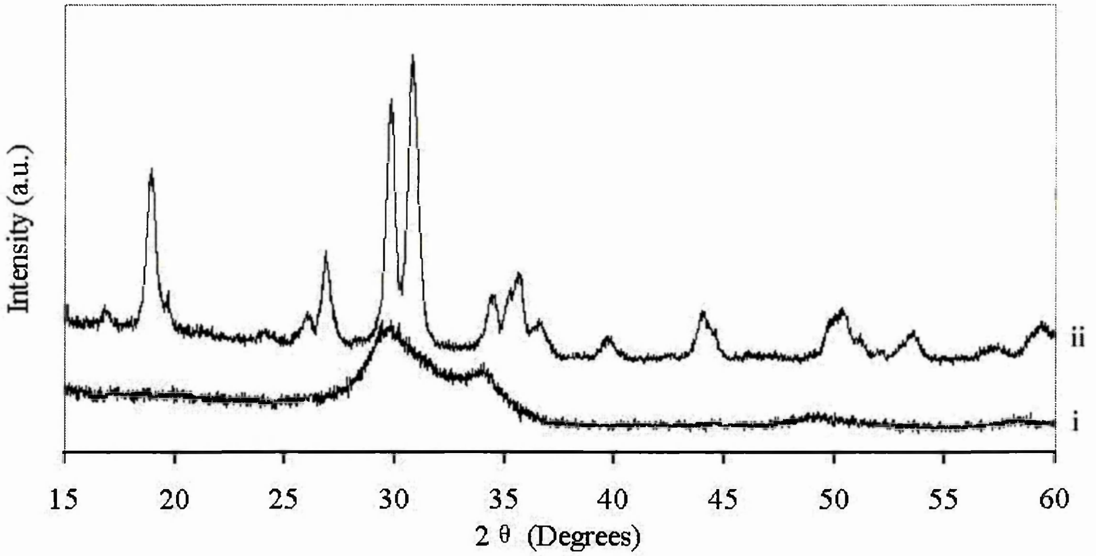

Fig.5.3. XRD patterns of sample TFL1-GP1; (a). i: 850^{0}C, 1h; ii: 950^{0}C, 1h.

For sample TFL5-GP3 (Figure 5.4a), the peaks are attributed to the only crystallised phase i.e. $Yb_3Al_5O_{12}$, identified as JCPDS #73-1369 [94]. The initial garnet phase appeared at 850^{0}C. Fully crystallised YbAG garnets can be obtained after a long time heat treatment at 850^{0}C or a relatively short time annealing at higher temperature than 850^{0}C, e.g. 950^{0}C. It must be emphasized that this is the first time that single-phase YbAG garnets have been produced by sol-gel techniques.

For sample TFL6-GP3 (Figure 5.4b), single phase YbAG garnet was obtained at 700^{0}C and no other phase was detected. This crystallisation temperature was about 150^{0}C lower than sample TFL5-GP3. The doped Li^+ or Mo^{6+} has significantly lowered the crystallisation temperature of single-phase ytterbium aluminium garnets.

For sample TFL7-GP3 (Figure 5.4c), the temperature for the onset of crystallisation of single-phase YbAG garnets was found to be 700^{0}C. This temperature is the same with sample TFL6-GP3 and 150^{0}C lower than that of sample TFL5-GP3.

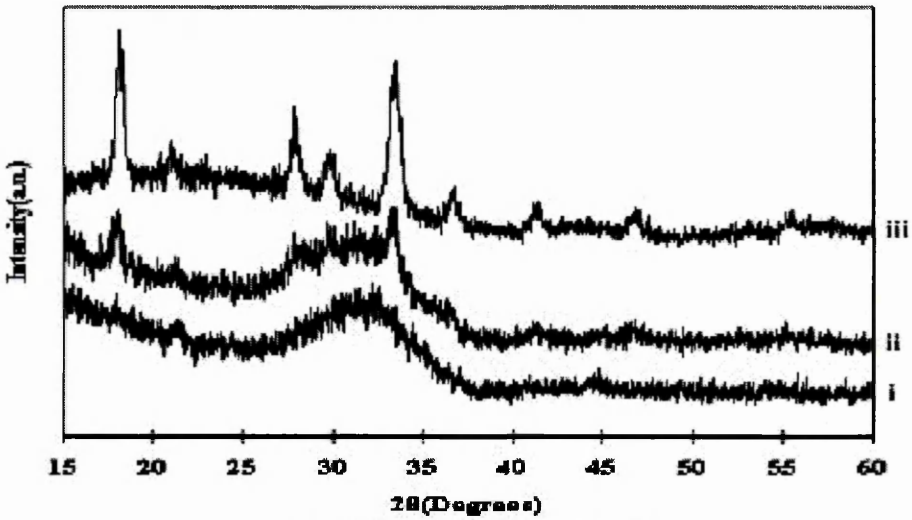

(a). i: 800⁰C; ii: 850⁰C; iii: 950⁰C.

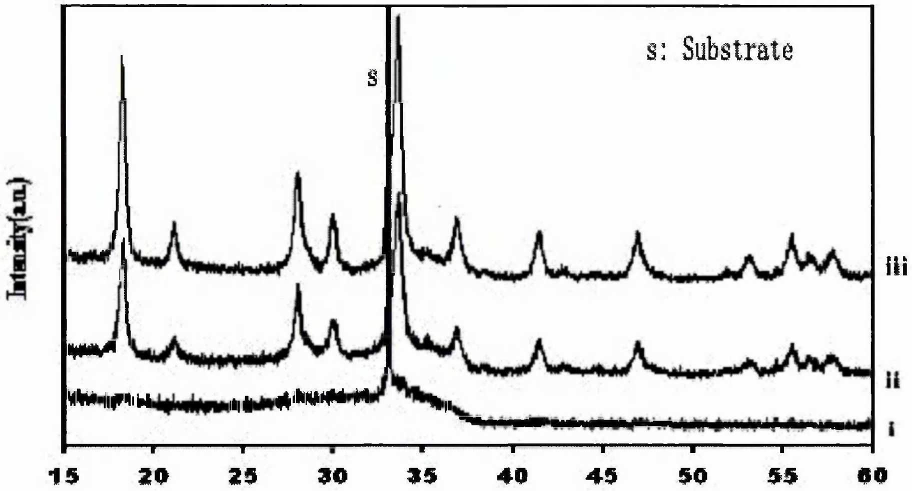

(b). i: 600⁰C; ii: 700⁰C; iii: 800⁰C.

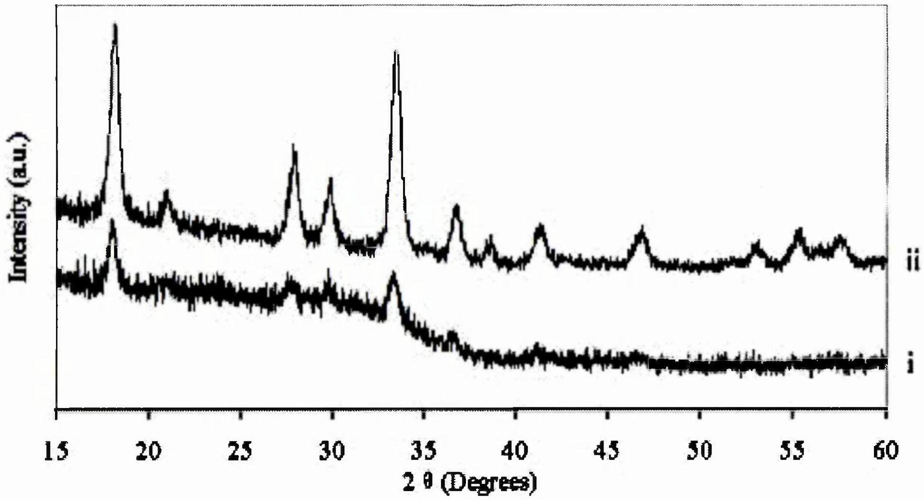

(c). i: 700⁰C; ii: 850⁰C

Fig.5.4. XRD patterns of samples; (a) TFL5-GP3;(b) TFL6-GP3;(c) TFL7-GP3.

In summary, phase transformations of Group 3 in the Yb_2O_3-Al_2O_3 system are listed in Table 5.1, from which we can find that MoO_3 has significantly lowered the crystallisation temperature of YbAG garnets when it is doped into the Yb_2O_3-Al_2O_3 system.

Table 5.1 Crystallisation of Group 3 in the Yb_2O_3-Al_2O_3 system

Samples	Heat treatment conditions				
	600^0C	700^0C	800^0C	850^0C	950^0C
TFL5-GP3	Amorphous	Amorphous	Amorphous	YbAG	YbAG
TFL6-GP3	Amorphous	YbAG	YbAG	YbAG	YbAG
TFL7-GP3	Amorphous	YbAG	YbAG	YbAG	YbAG

V.2.2.3 Samples TFL2-GP2, TFL3-GP2, and TFL4-GP2 (see page 55 and 56 in Chapter III) with a matrix composition Yb_2O_3/ Al_2O_3=1:1 in the Yb_2O_3-Al_2O_3 system were investigated by XRD. They present a more complicated phase transformation than that of Group 1 and Group 3 materials. Their XRD patterns at different heating temperatures and various times are shown in Figure 5.5a, b, and c, respectively.

For sample TFL2-GP2, two phases were found in XRD patterns in Figure 5.5a. They are the cubic–Yb_2O_3 (#43 – 1037 from the JCPDS database [94]) and the $Yb_3Al_5O_{12}$ garnet (JCPDS #73-1369 [94]). Cubic-Yb_2O_3 is easier to crystallise than YbAG garnets from the amorphous oxides. It initially appeared at 700^0C and YbAG garnets began to crystallise at 800^0C.

Sample TFL3-GP2 was amorphous at 500^0C. Cubic-Yb_2O_3 crystallised at about 600^0C.

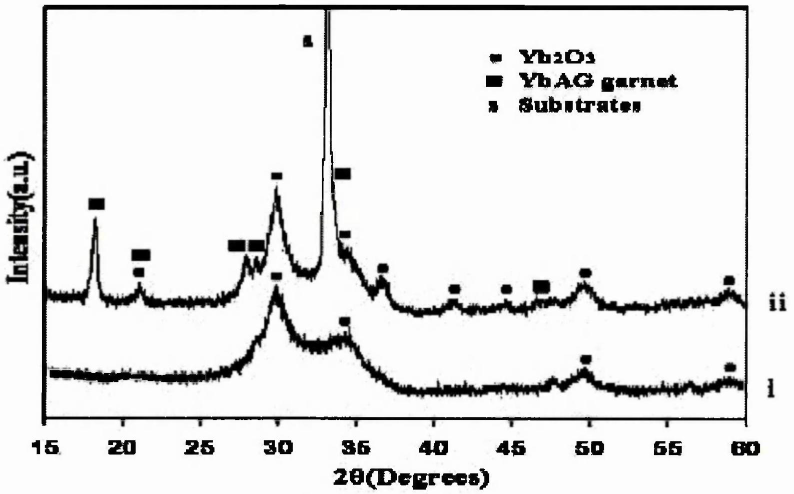

(a). i: 700°C; ii: 800°C.

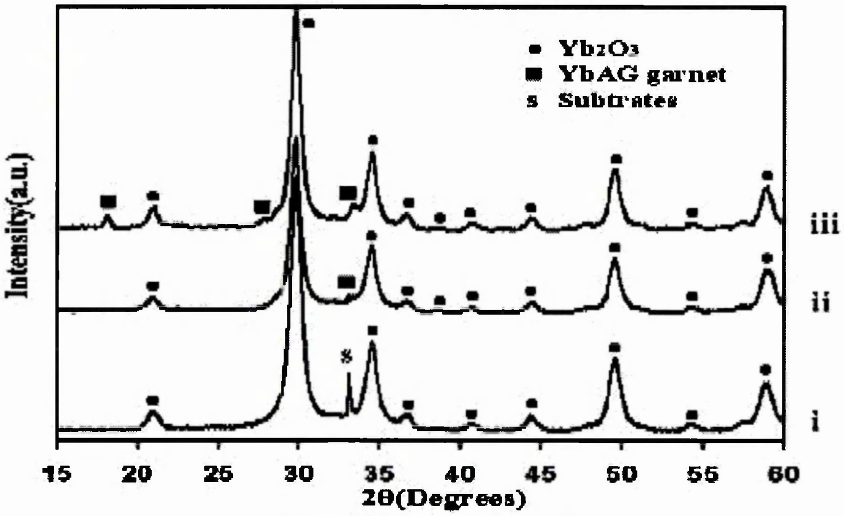

(b). i: 600°C; ii: 700°C; iii: 800°C.

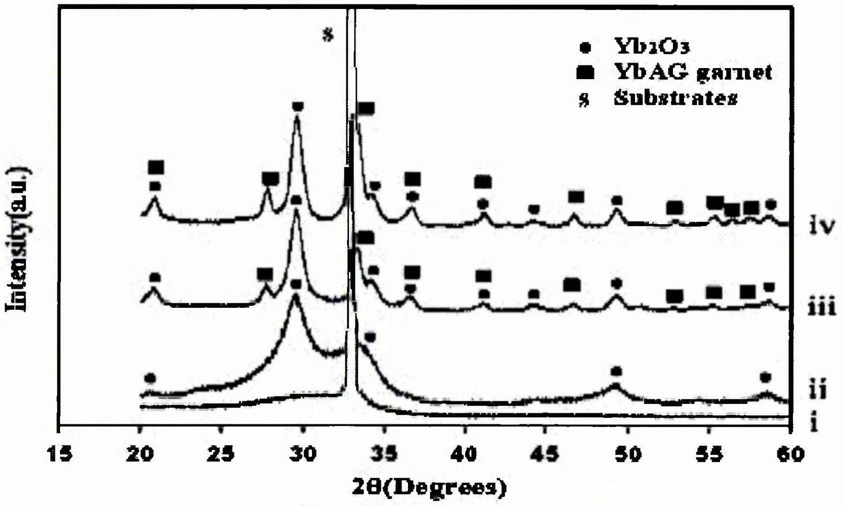

(c). i: 450°C; ii: 500°C; iii: 700°C; iv: 800°C.

Fig.5.5. XRD patterns of samples; (a) TFL2-GP2; (b) TFL3-GP2; (c) TFL4-GP2.

Table 5.2 Crystallisation of Group 2 in the Yb_2O_3-Al_2O_3 system

Samples	500^0C	600^0C	700^0C	800^0C
TFL2-GP2	Amorphous	Amorphous	c-Yb_2O_3	c-Yb_2O_3 YbAG
TFL3-GP2	Amorphous	c-Yb_2O_3	c-Yb_2O_3	c-Yb_2O_3 YbAG
TFL4-GP2	c-Yb_2O_3	c-Yb_2O_3	c-Yb_2O_3 YbAG	c-Yb_2O_3 YbAG

This crystallisation temperature is 100^0C lower than that of sample TFL2-GP2 with the same matrix composition but no dopants. The initial appearance of YbAG garnet was at about 800^0C (the same as that of sample TFL2-GP2). Two phases, cubic-Yb_2O_3 and YbAG garnet, were obtained at 800^0C.

For sample TFL4-GP2, there were no crystallised phases until cubic-Yb_2O_3 appeared at 500^0C. It is 200^0C lower than sample TFL2-GP2. Garnet YbAG crystallised about 700^0C. This is 100^0C lower than that of sample TFL2-GP2.

In summary, phase transformations of Group 2 materials in the Yb_2O_3-Al_2O_3 system are listed in Table 5.2, from which we can observe that doped Li_2O lowers the crystallisation temperature of c-Yb_2O_3 phase while doped MoO_3 promotes the crystallisation of YbAG garnet.

V.2.3 Chemical analysis (XPS)

Sample TFL3-GP2 had the matrix composition Yb_2O_3/ Al_2O_3=1:1 and was only doped by Li_2O oxides. The XPS wide scan spectrum of sample TFL3-GP2 (after heating at

800°C) in the range of 0 ~ 1200 eV was obtained, and is shown in Figure 5.6. The major features were identified. The most intense peak at 530 eV corresponds to the O 1s peak. The Li 1s and Al 2p peaks appear at 48 – 62 and 70 – 80 eV, respectively. The Yb 4d peaks occur at 176 – 213 eV. High-resolution spectra were performed for all elements and the deconvoluted Al, Yb and Li peaks spectra for sample TFL3-GP2 are shown in Figure 5.7a, b and c. The binding energy (BE) data are shown in Table 5.3. The Al 2p in Figure 5.7a has been deconvolved into two peaks (73.6 eV and 74.4 eV for $p^{3/2}$ and $p^{1/2}$ respectively), which show reasonable in agreement with that expected for an oxidized form which has reported values of around 74.0 eV [172]. There is no obvious evidence of the aluminium occupying tetrahedral and octahedral sites in the garnet structures. The differences in binding energies are probably too small to result in separate peaks. The Yb 4d spectra in Figure 5.7b have five peaks between 180 ~ 210 eV which can be attributed to an ytterbium oxidation state. Five complicated peaks are due to the configuration of the d and f electrons, which results in the satellite peaks [173]. The binding energy of the principal $4d^{5/2}$ peak is 185.0 eV which is very close to that reported values of 185.2 for Yb_2O_3 by Uwamino et al [174]. The Li 1s spectrum (Figure 5.7c) has a well-resolved peak at around 55.7 eV which

Table 5.3 XPS core level binding energies (BE ± 0.1eV) of sample TFL3-GP2 (values have been charge corrected for C 1s = 284.8 eV)

O 1s	Al $2p_{3/2}$	Al $2p_{1/2}$	Yb $4d_{5/2}$	Li 1s
530.1	74.4	73.6	185.0	55.7

shows in good agreement with reported value of 55.6 eV for Li_2O [175]. Doped Mo^{6+} was confirmed too from XPS analysis of the fully crystallised sample TFL7-GP3 at 850^{0}C heat treatment. Sample TFL7-GP3 is 10 at. % MoO_3 doped YbAG. The result will be described in next chapter.

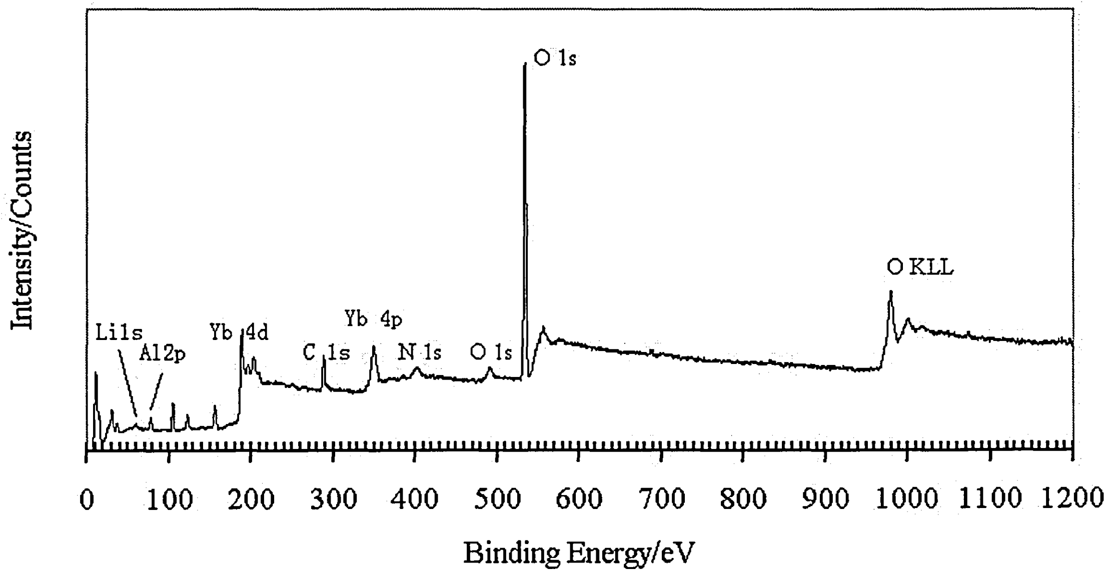

Fig.5.6. The XPS wide scan spectrum of sample TFL3-GP2.

V.3. Discussion

V.3.1 Crystallisation characteristics of the pure Yb_2O_3-Al_2O_3 system

Crystallisation characteristics in the pure Yb_2O_3-Al_2O_3 system are dependent on the compositions (the molar ratio of Yb_2O_3/Al_2O_3) when produced by sol-gel techniques. When the crystallisation temperatures are compared in samples TFL1-GP1, TFL2-GP2, and TFL5-GP3, it is evident that the amorphous phase having the $Yb_3Al_5O_{12}$ or $Yb_4Al_2O_9$ composition is a more stable structure than that possessing the composition Yb_2O_3/Al_2O_3=1:1. In the sample TFL2-GP2 (Yb_2O_3/Al_2O_3=1:1), cubic-Yb_2O_3 appeared at 700^{0}C followed by the crystallisation of $Yb_3Al_5O_{12}$ at 800^{0}C. There are

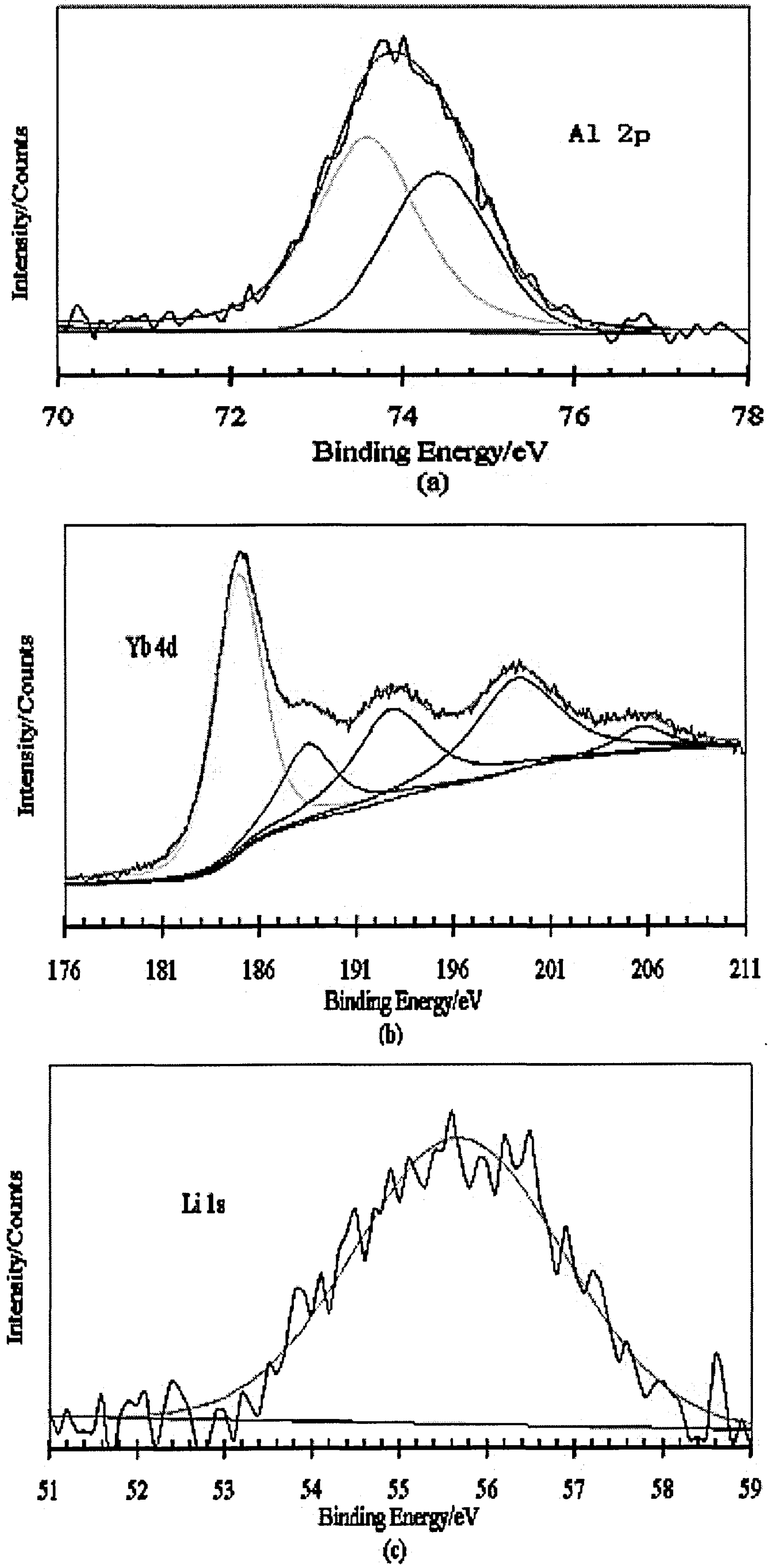

Fig.5.7. High resolution XPS spectra of Al, Yb and Li.

four possible phases that can crystallise from the amorphous oxides in the pure Yb_2O_3-Al_2O_3 system; i.e. Al_2O_3, Yb_2O_3, $Yb_3Al_5O_{12}$, and $Yb_4Al_2O_9$. The cubic-Yb_2O_3 has the lowest crystallisation temperature. The YbAG garnet crystallises at a higher temperature. The $Yb_4Al_2O_9$ phase presents the highest crystallisation temperature. The Al_2O_3 is very difficult to form in our investigated compositions by sol-gel methods. Al_2O_3 did not appear below the temperature 950^0C.

V.3.2 The effect of dopants on the crystallisation temperature

In Table 5.1, it is clear that doping with MoO_3 has lowered the crystallisation temperature of $Yb_3Al_5O_{12}$ by about 150^0C when compared with undoped compositions (TFL5-GP3). Sample TFL6-GP3 has the same crystallisation temperature with sample TFL7-GP3 even though both MoO_3 and Li_2O were doped in the sample TFL6-GP3.

Furthermore, it is evident that the doped Li^+ has lowered the crystallisation temperature of cubic-Yb_2O_3 when we compare the sample TFL2-GP2 to the sample TFL3-GP2 in Table 5.2. In the sample TFL2-GP2, cubic-Yb_2O_3 appeared at 700^0C whereas it crystallised at 600^0C in sample TFL3-GP2. The same effect of lowering the crystallisation temperature can be confirmed in the sample TFL4-GP2 that has the lowest crystallisation temperature at 500^0C for the transition of the cubic-Yb_2O_3 phase. It can also be seen that the transition temperature of $Yb_3Al_5O_{12}$ in sample TFL4-GP2 is correspondingly 100^0C lower than that in sample TFL3-GP2. This again confirmed that doping with MoO_3 promotes the crystallisation of $Yb_3Al_5O_{12}$.

V.3.3 The mechanism of lowering the crystallisation temperature

It is well known that a xerogel has an amorphous network structure after hydrolysis and condensation. It behaves as a disordered structure in the long-range and as an ordered structure in the short-range. The basic central cations here are Al^{3+} and Yb^{3+} ions. In the xerogel, the cations Al^{3+} can exist in the oxygen or hydroxyl group of octahedral or tetrahedral sites in the Yb_2O_3-Al_2O_3 system due to its small ionic radius (0.51 Å) [26]. However, the radius of the Yb^{3+} ion (0.86 Å) [26] is much larger than that of the Al^{3+} ion. Thus, it generally occupies the oxygen or hydroxyl group of octahedral or dodecahedron sites.

Yb^{3+} ions can easily form the basic crystal growth units [YbO_6] octahedral with oxygen and hydrogen. In this case, the chain consists of these octahedral units that are bonded through the corner, the edge and the face. The bonding between the chains is by the hydroxyl group OH^-. Thus, the crystallisation of cubic-Yb_2O_3 is actually the convergence and order arrangement process of ytterbium oxygen coordination octahedral. The greater the number of basic octahedral growth units [YbO_6] linked together by OH^-, the easier the crystallisation of Yb_2O_3. With the increase of heat treatment temperature, the motion of atoms was enhanced in the structure and the viscosity will decrease in the amorphous structure. This will be beneficial to overcome the energy barrier for the crystallisation. However, the problem here is that the hydroxyl group will be lost due to heat treatment and lead to the change of the cation coordination status and the decrease in the number of basic growth units. When the small radius lithium ions are doped in the material, they may substitute some hydrogen positions during the process of heat treatment. The replacement will keep the basic growth units of Yb_2O_3 at the same number density during the firing process and hence be beneficial to the formation of cubic-Yb_2O_3. Hence, doped Li^+ ions in the structure catalyse the Yb_2O_3 crystallisation. Furthermore, it may form a very unstable intermediate phase Yb_2O_3.X Li_2O that can then decompose very quickly to yield Yb_2O_3 and Li_2O. Although our X-ray diffraction patterns did not identify the existence of Li_2O due to the very small amount present, a high molar concentration of Li_2O on the very top surface of the sample TFL3-GP2 has been confirmed by the XPS chemical analysis in section V.2.3. The appearance of Yb_2O_3 polycrystallites will promote the YbAG crystallisation via heterogeneous nucleation that will lower the energy barrier of YbAG nucleation. This is shown in the crystallisation process of the sample TFL2-GP2.

However, the cubic-Yb_2O_3 does not crystallise from the amorphous phase when the xerogel has the composition of YbAG or YbAM. The crystallised phase is YbAG or YbAM after annealing at high temperature. The reason is that the aluminium oxygen and ytterbium oxygen amorphous polyhedra network structures in these two cases are very stable. Hence, it limits the convergence and order arrangement of Yb oxygen coordination octahedron and leads to the formation of YbAG or YbAM directly at high temperature because of the change of the cation coordination status.

Doped Mo^{6+} has lowered the crystallisation temperature of YbAG garnets in our sol-gel techniques. The reason is that doped Mo^{6+} has significantly decreased the activation energy of YbAG crystallisation. Doped Mo^{6+} has very high valence that promotes the convergence and order arrangement of aluminium oxygen and ytterbium oxygen polyhedra and lowers the activation energy of crystallisation. A detailed discussion about the activation energy of crystallisation is given in Chapter VI.

V.4 Summary

Crystallisation in the pure and doped Yb_2O_3-Al_2O_3 system produced by the sol-gel method was widely studied in this Chapter. Three phases appeared in the crystallisation process in different samples, i.e. cubic-Yb_2O_3, YbAG and YbAM. This is the first time that single phase YbAG and YbAM were synthesized by the sol-gel method. Doping with Li_2O and MoO_3 significantly lowered the crystallisation temperatures of cubic-Yb_2O_3 and YbAG, respectively.

Chapter VI

Synthesis of the pure and Mo doped YbAG

VI.1 Introduction

$Yb_3Al_5O_{12}$ belongs to the crystal family of rare earth aluminium garnets with the space group Ia3d and crystallises in the body-centred cubic lattice. The most well known crystal in this family is the YAG garnet that has been described in Chapter II. YAG has widespread applications especially in near-infrared solid-state lasers and in phosphors as a host material. Rare earth aluminium garnets have also been chosen as promising high-temperature thermal barrier and corrosion resistance materials based on their stable phases and complicated crystal structures. Very recently, rare earth aluminium garnets with ytterbium have attracted much attention because of the simple and proper electronic structure of Yb^{3+}.

Conventionally, YbAG single crystals are grown by the Czochraski technique [6] at the melting temperature (about 2000^0C). The process is very sluggish. Polycrystalline materials are manufactured by sintering methods at about 1600^0C. The sol-gel techniques offer us a considerably low temperature route to produce the YbAG garnet compared to the conventional methods. However, it is still a problem to realise the full crystallisation by heat treatment below about $850{\sim}900^0C$ when the use of YbAG garnets involves application of the coating to a substrate such as metals. In this chapter, we describe the pure and Mo doped YbAG by sol-gel methods. As we discovered in Chapter V, doped Mo^{6+} can significantly lower the transition temperature of YbAG garnets.

VI.2 Results

VI.2.1 Crystallisation of the pure and doped YbAG garnet thin films

The preparation of the pure and doped YbAG garnet thin films has been described in Chapter III. Coated samples were heated to the desired crystallisation temperature very quickly (at 100^0C/min) and then were taken out of the furnace immediately after the required holding time. After each crystallisation under isothermal condition, the samples were quantitatively analyzed by X-ray diffraction.

XRD spectra of the samples TFL5-GP3 (pure YbAG garnets) at 850^0C, 875^0C, 900^0C and 950^0C with various crystallisation times are shown in Figure 6.1a, b, c, and d, respectively. With the increase in heating time, the amorphous phase gradually transformed into the YbAG garnet phase. The samples were converted to the well-crystallised single phase YbAG when the heat treatment time was long enough. Two peaks at about $2\theta=18^0$ and 34^0 have approximately the same intensities. An unidentified peak at $2\theta \approx 16.9^0$ was sometimes found after the initial crystallisation process. This is possibly due to the fast heating rate. However, the peak disappeared after further annealing and the thin films transformed to the single phase YbAG garnet. In Figure 6.1, it is found that the crystal growth in the thin films has a highly preferred orientation. Comparing XRD spectra in Figure 6.1 to that of YbAG powders in JCPDS #73-1369 or those we produced by the sol-gel method below in VI.2.2, typically, the peak (211) at $2\,\theta \approx 18^0$ in the thin film XRD pattern has the relative intensity almost equal to that of the maximum intensity peak (420) at $2\theta \approx 33.4\,^0$ when it reached a

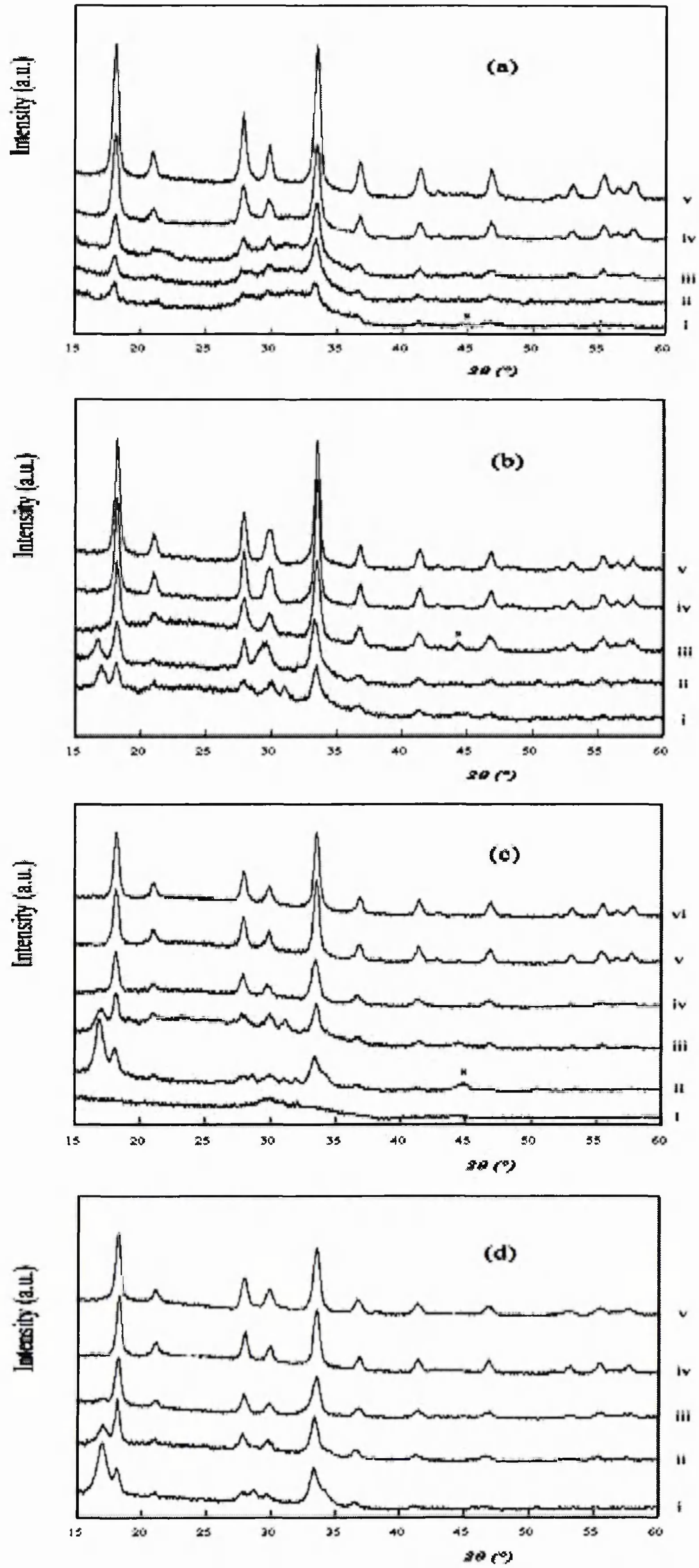

(i): 1 h; (ii): 3 h; (iii): 8 h; (iv): 16 h; (v): 50 h.

(i):1 h; (ii): 3 h; (iii): 8 h; (iv): 16 h; (v): 32h.

(i): 5 mins; (ii): 30 mins; (iii): 1 h; (iv): 3 h; (v) 8 h; (vi): 16h.

(i): 5 mins; (ii): 1 h; (iii): 3 h; (iv): 8 h; (v): 16 h.

Fig.6.1. XRD patterns of sample TFL5-GP3 with the varying time and temperature; (a): 850^0C; (b): 875^0C; (c): 900^0C; (d): 950^0C.

saturation level. While the peak (211) at $2\theta \approx 18^0$ in the powder XRD pattern has the relative intensity equal to that of 30~50% of the maximum intensity peak (420) at $2\theta \approx 33.4^0$. Thus, the YbAG garnet thin films are of textured growth. The maximum texture is the orientation in the plane (211). The relative intensity of the (211) peak increased much faster with increasing the annealing time than other increasing peaks in the corresponding XRD spectra. The higher the isothermal heating temperature, the shorter the crystallisation time of reaching the saturation level.

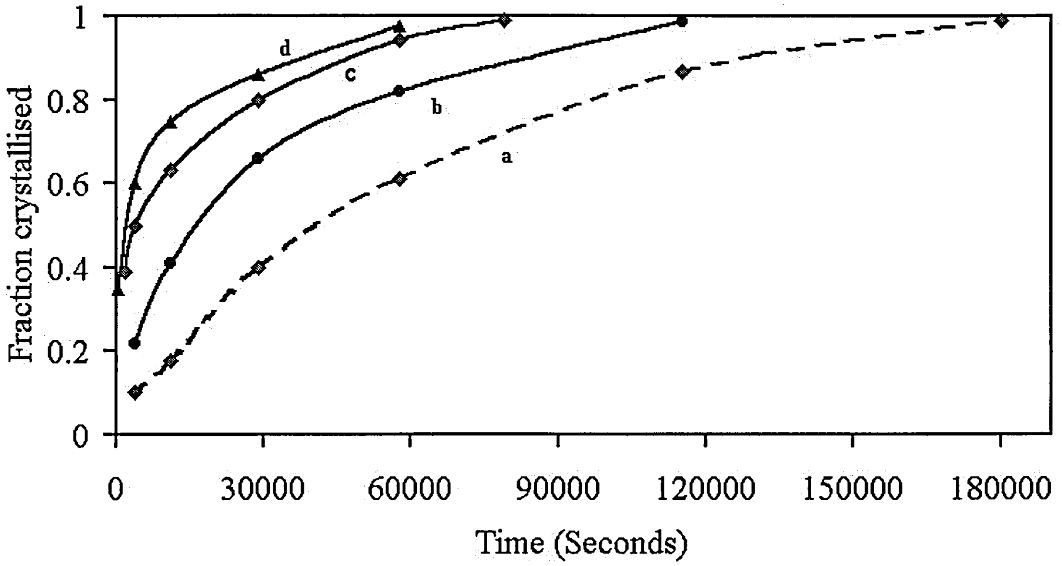

Fig.6.2. The combined plot of the crystallised fraction via the change of time for the sample TFL5-GP3. (a) 850⁰C; (b) 875⁰C; (c) 900⁰C; (d) 950⁰C.

Hence, the combined plot of the crystallised fraction versus time (and hence temperature) is shown in Figure 6.2 for the samples TFL5-GP3. The figure was built up as follows. Because the peak 211 shows a strong (211) texture and its intensity changes with time for a given isothermal treatment and reached a saturation value, it can be used to express the amount of crystallised garnet. The quantitative phase development was estimated by calculation of the integrated intensity of this peak after

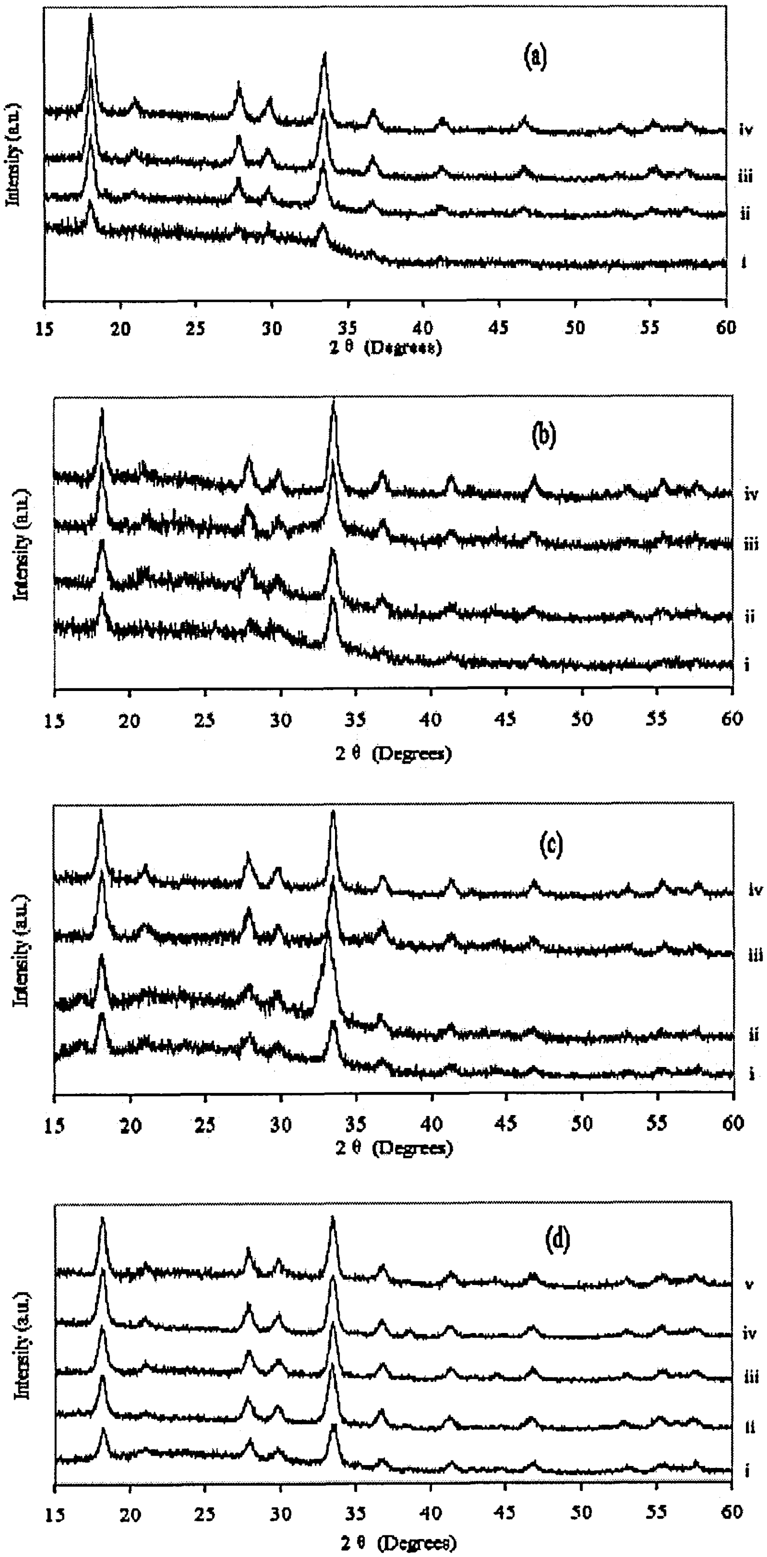

(i): 1 h; (ii): 2 h; (iii): 5 h; (iv): 8 h.

(i):1 h; (ii): 2 h; (iii): 5 h; (iv): 8 h.

(i): 30 mins; (ii): 1h; (iii): 3 h; (iv): 5 h.

(i): 5 mins; (ii): 30 mins; (iii):1h; (iv): 3 h; (v): 5 h.

Fig.6.3. XRD patterns of sample TFL7-GP3 with the varying time and temperature; (a): 750^{0}C; (b): 775^{0}C; (c): 800^{0}C; (d): 850^{0}C.

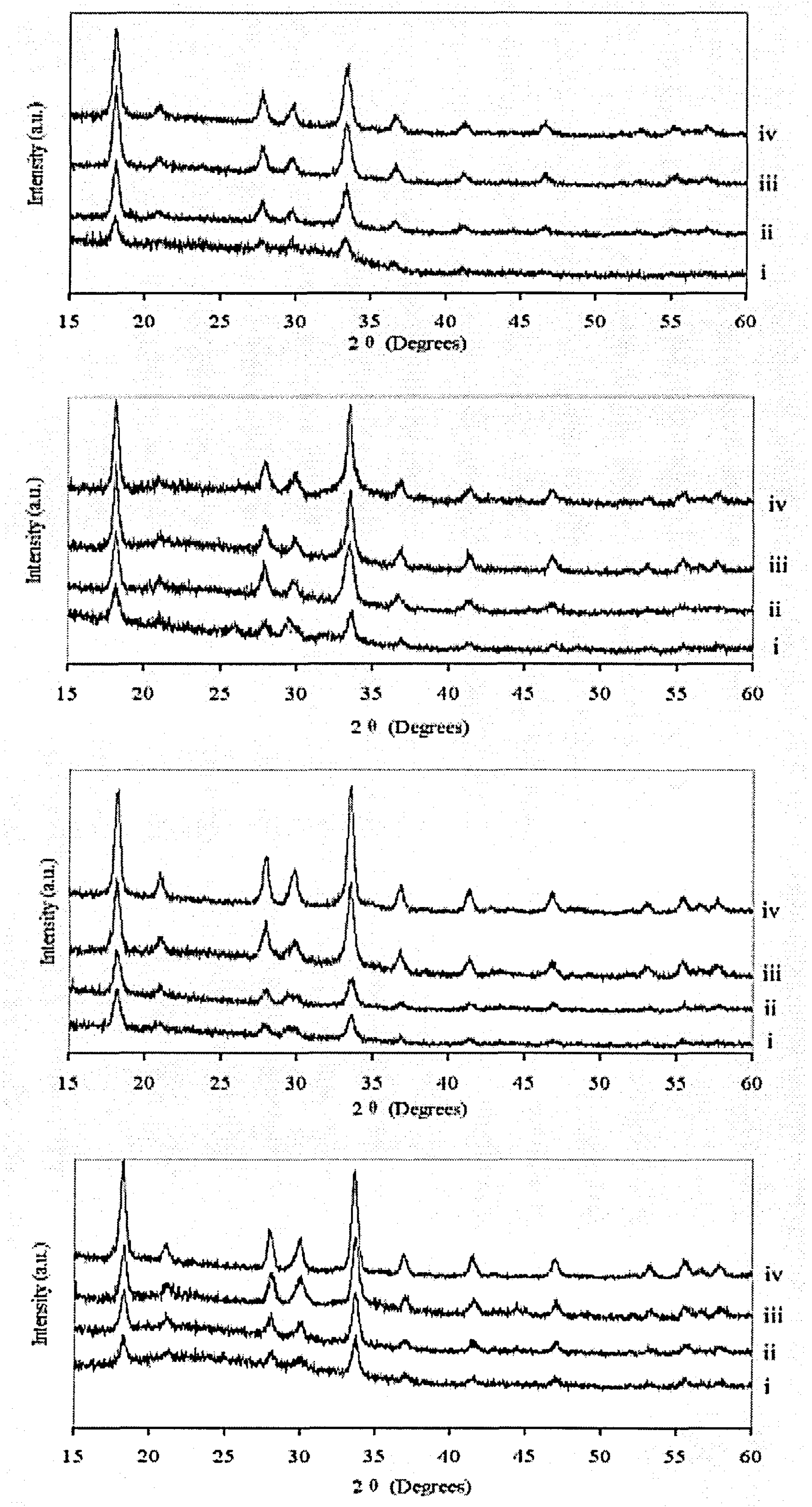

(i): 1h; (ii): 2 h; (iii): 5 h; (iv): 8 h.

(i): 1h; (ii):2 h; (iii): 5 h; (iv): 8 h.

(i): 15 mins; (ii): 1 h; (iii): 3 h; (iv): 5 h.

(i): 15 mins; (ii): 1 h; (iii): 3 h; (iv): 5 h.

Fig.6.4. XRD patterns of sample TFL8-GP3 with the varying time and temperature; (a): 750^{0}C; (b): 775^{0}C; (c): 800^{0}C; (d): 850^{0}C.

utilizing 100% symmetry Gaussian curves fitting. The use of a maximum profile intensity technique was not adopted here because of decreased sensitivity in the case of diffuse and broad profiles. The integrated intensity of the (211) peak, normalised to the saturation value, was used to monitor the crystalline fraction of the film, x. Thus, each curve point corresponds to the integrated intensity of the (211) line, at that time and temperature, divided by this saturation value. Thus, a direct and quantitative crystallisation characteristics affected by time and temperature are obtained for the sample TFL5-GP3. The disadvantage of this method is in the initial stages of crystallisation. It is difficult to obtain the data from the experiments due to the very fast nucleation and crystallisation rate, especially at the high temperature heat treatment. This method has been used to study the kinetics of the thin film growth by many other researchers [176] [177].

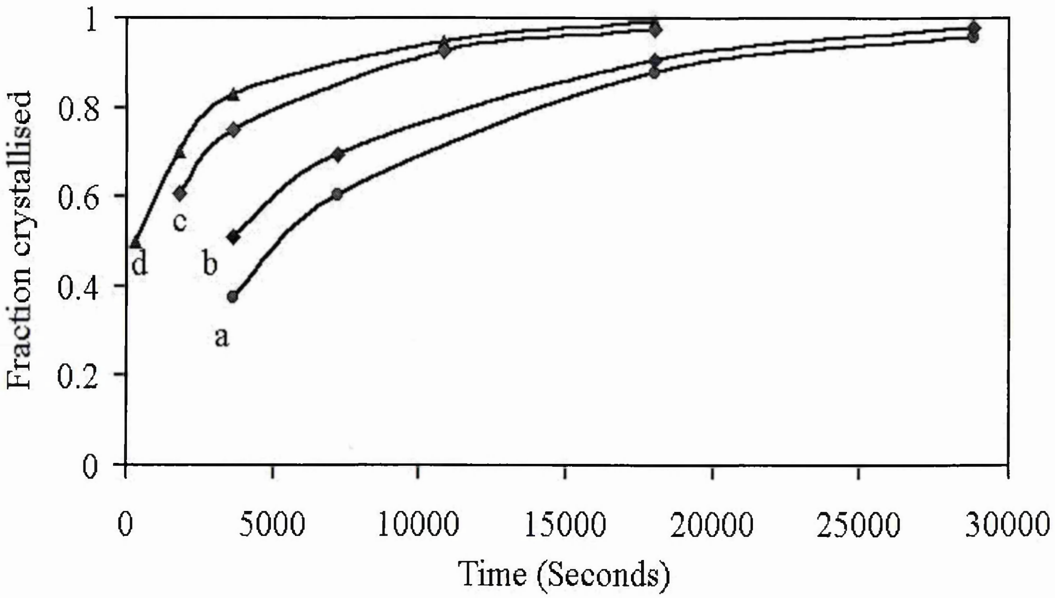

Fig.6.5. The combined plot of the crystallised fraction via the change of time for the sample TFL7-GP3. (a) 750^{0}C; (b) 775^{0}C; (c) 800^{0}C; (d) 850^{0}C.

The same method as above was used in samples TFL7-GP3 and TFL8-GP3 which are 10 and 30 at. % Mo: YbAG, comparatively. Their XRD patterns are shown in Figure 6.3 and Figure 6.4, separately. Only single-phase alumina garnets appeared at 750^{0}C, 775^{0}C, 800^{0}C, and 850^{0}C heat treatments. The combined plots of the crystallised fraction via the change of time and temperature are shown in Figure 6.5 and Figure 6.6 for the samples TFL7-GP3 and TFL8-GP3, separately. A rapid nucleation and crystallisation rate at the initial stage of crystallisation is seen from Figure 6.5 and 6.6.

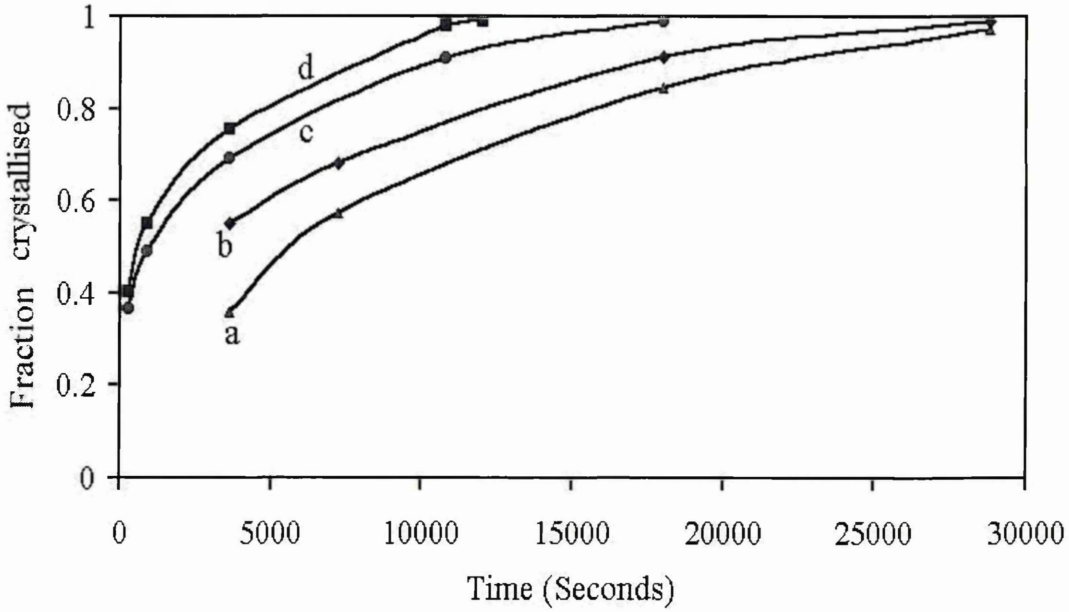

Fig.6.6. The combined plot of the crystallised fraction via the change of time for the sample TFL8-GP3. (a) 750^{0}C; (b) 775^{0}C; (c) 800^{0}C; (d) 850^{0}C.

VI.2.2 Crystallisation of the pure YbAG and Mo: YbAG powders

Two powder samples POW5-GP6 and POW7-GP6 have been prepared in Chapter III. They were heat-treated at various temperatures for half an hour. The same mass of the pure YbAG and 10 at. % Mo: YbAG powders were characterized by XRD. The sample POW5-GP6 was amorphous below heat treatment at 850^{0}C. Its XRD pattern at

850^{0}C half hour calcination is shown in Figure 6.7a, which gives evidence of YbAG and amorphous phase. For the sample POW7-GP6, YbAG crystallised at 750^{0}C. Its XRD pattern at 850^{0}C half hour calcinations, the same treatment as for sample

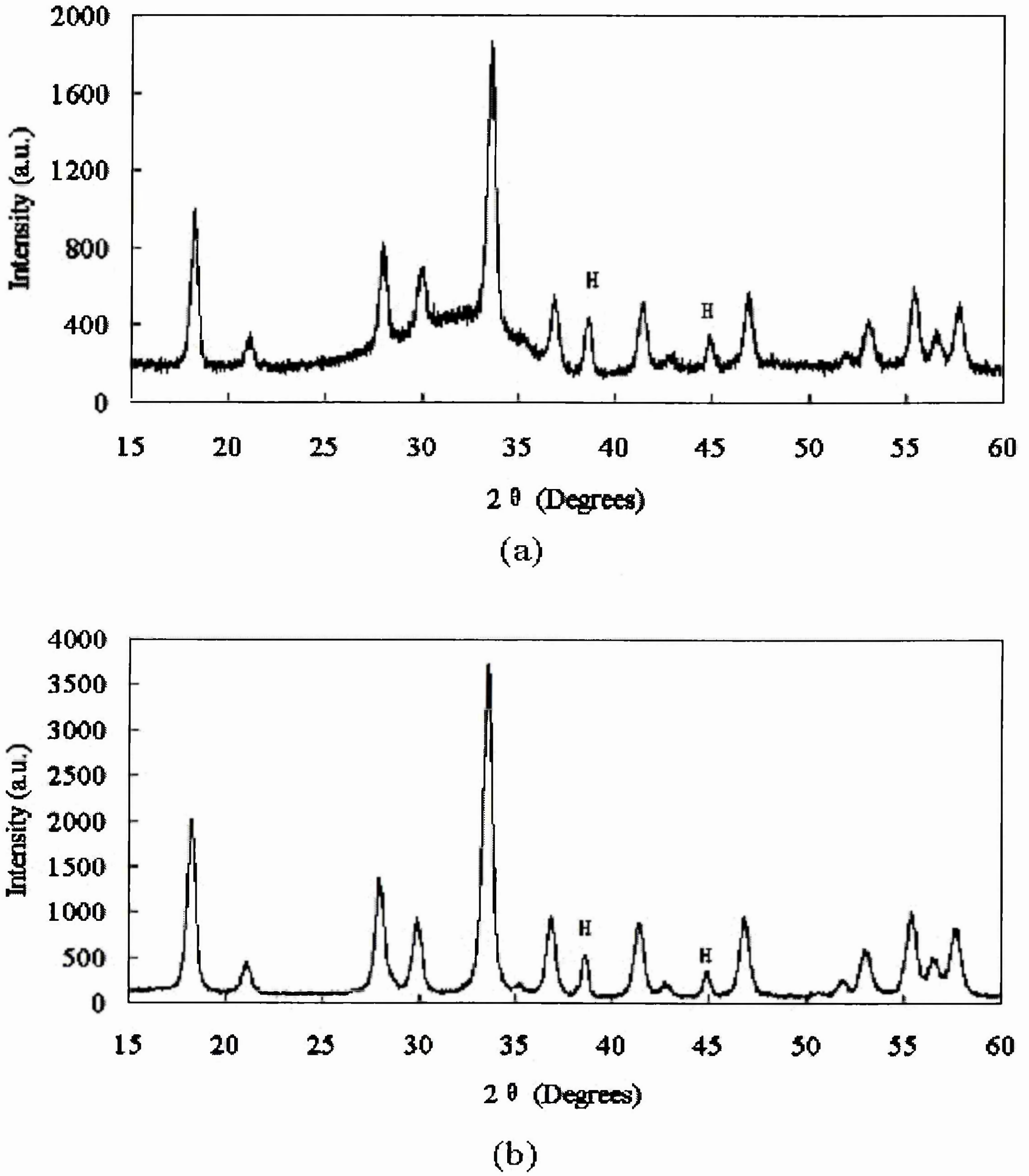

Fig.6.7. XRD patterns of the pure and 10 at. % Mo doped YbAG powders at 850^{0}C half hour heat treatment; (a) POW5-GP6; (b) POW7-GP6; H: Holder of aluminium.

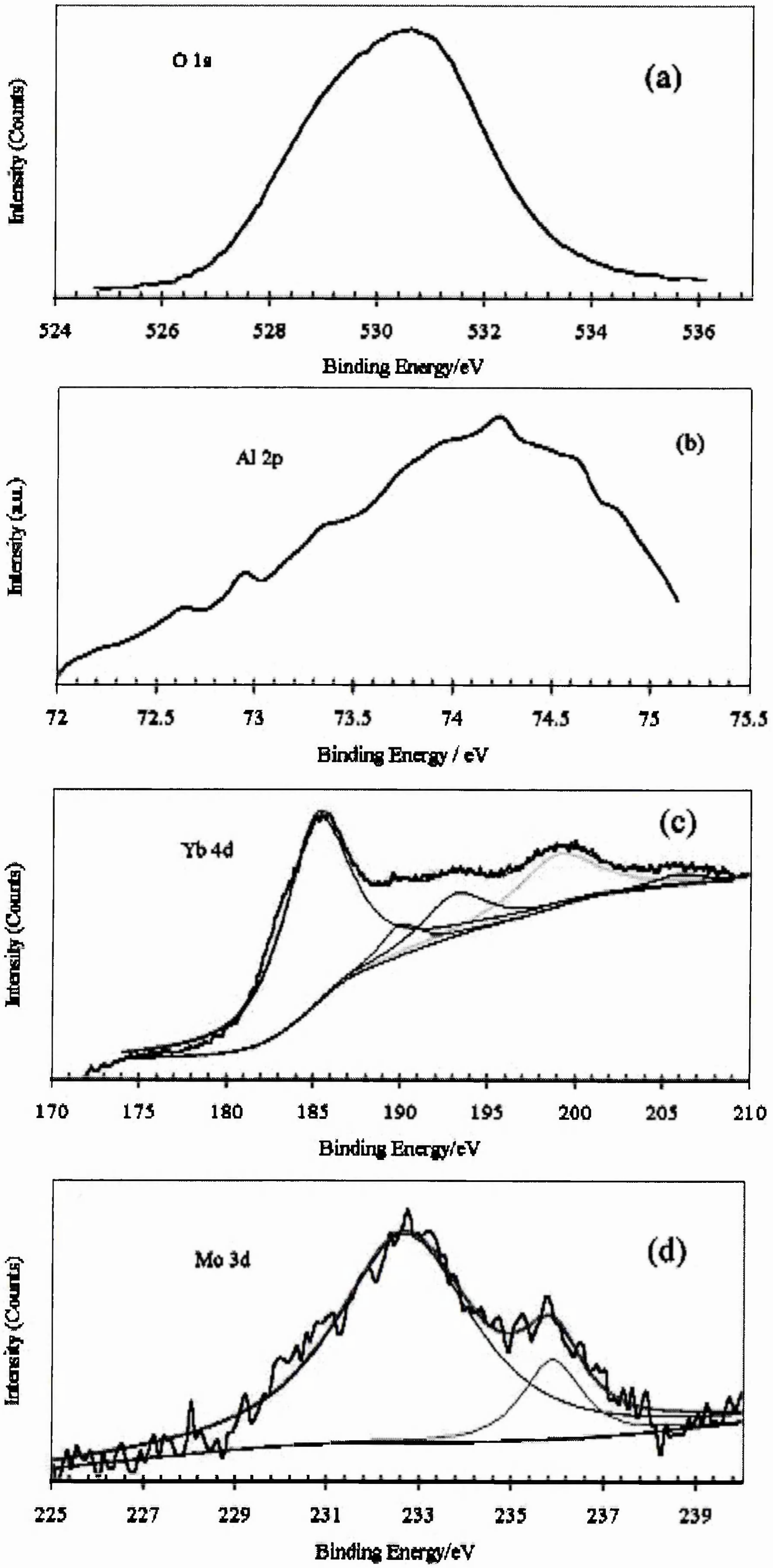

Fig.6.8. High resolution XPS spectra of O, Al, Yb and Mo.

POW5-GP6, is shown in Figure 6.7b, which is well crystallised YbAG. Comparing Figure 6.7a to 6.7b, it is evident that doped Mo(VI) promotes the crystallisation of YbAG garnets.

VI.2.3 XPS surface analysis

The XPS wide scan for the sample TFL7-GP3 (10% Mo doped YbAG thin film) which was heated at 850^0C for 10 hours was taken in the range of 0 ~ 1200 eV. The major features were identified. The most intense peak at 530.6 eV corresponds to the O 1s peak. The Al 2p peaks occurs at 72 ~75 eV. The Yb 4d peaks and the Mo peaks occur at 176 ~ 210 eV and 225 ~ 240 eV, respectively. High-resolution spectra were performed for all elements that are shown in Figure 6.8. The binding energy (BE) data are shown in Table 6.1.

Table 6.1 XPS core level binding energies (BE ± 0.1eV) of the sample TFL7-GP3 (values have been charge corrected for C 1s = 284.8 eV.)

O 1s	Al 2p	Mo $3d_{5/2}$	Yb $4d_{5/2}$
530.6	74.0	232.6	185.11

The O 1s binding energy (Figure 6.8a) is 530.6 eV which is in agreement with that reported value in oxides, e.g. the O 1s binding energy for single oxides TiO_2 and ZrO_2 is 530.1 and 530.4 eV, respectively [178] [179]. The Al 2p in Figure 6.8b show reasonable agreement with that expected for an oxidised form which has reported values of around 74.0 eV [172]. The Yb 4d spectra in Figure 6.8c have five peaks between 176 ~ 210 eV that can be attributed to an ytterbium oxidation state. The binding energy of the principal $4d^{5/2}$ peak is 185.11 eV which is in good agreement with reported values of 185.2 for Yb_2O_3 by Uwamino et al [174]. The Mo 3d spectra in Figure 6.8d has been deconvolved into two peaks at 232.68 and 235.88 eV, characteristic of the two spin-orbit components of Mo (VI) oxidation state, which are well in agreement with reported values of 232.6 and 235.8 eV [180]. XPS analysis of the sample POW7-GP6 also confirms that Mo is in the six valence state or 6+ oxidation state.

VI.3 Discussion

VI.3.1 Crystallisation kinetics of YbAG garnet thin films

VI.3.1.1 Theoretical model

Crystallisation is the process by which the regular lattice of the crystal is generated from the less ordered amorphous, super critical liquid structure.

In its simplest form, crystallisation is observed when a melt of a single pure element or compound is cooled; conversion from liquid to solid state occurs at a fixed temperature for a given pressure and is known as the freezing point. Thus, if a glass (network structure) composition is heated from room temperature to the nucleation temperature zone, a large number of nuclei can be generated within the mass of glass. When the glass is then further heated to the crystallisation temperature, crystals will grow on these nuclei leading to the transformation of the glass into a polycrystalline ceramic material.

The formation of nuclei requires the formation of an interface with a specific energy γ between the two phases. Because of this, the formation of very small particles usually requires an increase in the free energy of the system. Once the particle has reached a sufficiently large size, the interface energy is small compared with the volume energy decrease so that the overall change in free energy on forming the new phase becomes negative. Consider a spherical nucleus of radius r. The free energy change when it forms is [170]

$$\Delta G_r = 4\pi r^2\gamma + \frac{4}{3}\pi r^3\Delta G_v \qquad (6.1)$$

where γ is the interface energy and ΔG_v is the free-energy change per unit volume for the phase transition, neglecting interface energy. The first term on the right is positive, as energy is expended to form the surface of the nucleus, and the second term is negative. An increase in the size of the crystal will decrease the free energy of the system only if $d(\Delta G_r)/dr < 0$, so the critical radius of the nucleus (i.e. the size beyond which it will grow spontaneously) is found by setting $d(\Delta G_r)/dr = 0$ in Eq.6.1. The result is

$$r_c = -\frac{2\gamma}{\Delta G_v} \quad (\text{here } \Delta G_v<0) \qquad (6.2)$$

This means there is a barrier for crystallisation. If this barrier is surmounted, crystallisation will proceed and the system can move directly toward equilibrium by growth of the crystal. The barrier decreases as the temperature drops, because

$$\Delta G_v \approx \frac{\Delta H_v(T_m - T)}{T_m} \qquad (6.3)$$

where ΔH_v is the heat of fusion. T_m is the melting point. At the melting point $T=T_m$, $\Delta G_v = 0$, the nucleation barrier is infinite. At low temperatures ΔG_v is large and the critical nucleus becomes small enough to be formed with ease. However, the rate of formation of nuclei, I_v, depends on the viscosity [170]

$$I_v = \frac{k_1}{\eta}\exp\left(-\frac{k_2\gamma^3}{T(\Delta G_v)^2}\right) \qquad (6.4)$$

where k_1 and k_2 are constants. Thus, nucleation is energetically favorable at lower temperatures, but may be inhibited kinetically by the high viscosity.

The process of formation of a critical nucleus is called homogeneous nucleation, when only the liquid and corresponding crystals are involved. If another substance facilitates nucleation by lowering the energy in creating the surface of the nucleus, the process is called heterogeneous nucleation.

Generally, the total rate of crystal growth is dependent on two processes, i.e. nucleation and crystal growth. It can be expressed by the crystallised fraction, x, dependent on the crystallisation time, t. When an amorphous phase with a volume V is kept at the temperature of crystallisation for a time τ, then

$$N_\tau = I_v V^l d\tau \qquad (6.5)$$

where $N\tau$ is the number of the crystallised new phase during the time $d\tau$, I_v is the rate of formation of nuclei, and V^l is the non-crystallised amorphous volume.

If the crystal growth begins after the time τ, then,

$$V^s = \frac{3\pi}{4} U^3 (t-\tau)^3 \qquad (6.6)$$

where V^s is the volume of the crystallised new phase during the time t, U is the rate of the crystal growth considering a spherical crystal with the same growth rate in all directions. At the initial stage, the size of the new phase is very small, thus, $V^l \approx V$.

Hence, at the moment of time t, the volume of crystallisation, dV^s, is equal to the volume of formation of the new phase in the time interval of τ and (τ + dt).

$$dV^s = N_\tau V^s \approx \frac{4\pi}{3} V I_v U^3 (t-\tau)^3 dt \qquad (6.7)$$

Thus,

$$x = \frac{V^s}{V} = \frac{4\pi}{3}\int_0^t I_v U^3 (t-\tau)^3\, dt \tag{6.8}$$

$$dx = \frac{4\pi}{3} I_v U^3 (t-\pi)^3\, dt \tag{6.9}$$

Considering the impact of particles and the decrease of V with the crystallisation process, a correlation factor (1 - x) is used for Eq.(6.9), hence,

$$dx = (1-x)\frac{4\pi}{3} I_v U^3 (t-\tau)^3\, dt \tag{6.10}$$

When the rate of formation of nuclei and the rate of the crystal growth are independent of the time, Eq.(6.10) will become, after integration as follows,

$$x = 1 - \exp(-\frac{\pi}{3} I_v U^3 t^4) \tag{6.11}$$

This is the well-known Johnson - Mehl - Avrami (JMA) [73-76] equation. Consider the rate of formation of nuclei and the rate of the crystal growth varying with the crystallisation time, thus,

$$x(t) = 1 - \exp[-(kt)^n] \tag{6.12}$$

where x(t) is the volume fraction of the transformed phase, k is the reaction rate, t is the heating time, and n is the Avrami exponent which is related to the crystallisation mechanism and describes the geometry of the crystal growth front. The JMA model is generally used in the isothermal growth data. The reaction rate, k, could itself follow the Arrhenius equation:

$$k(T) = k_0 \exp(-\frac{E}{RT}) \tag{6.13}$$

where k_0 is the pre-exponential factor (units of inverse time), E is the activation energy, R is the gas constant (8.314 J mol^{-1}), and T is temperature.

Equation (6.12) can be rearranged as follows:

$$1 - x(t) = \exp[-(kt)^{n}] \tag{6.14}$$

$$-\ln(1 - x(t)) = (kt)^{n} \tag{6.15}$$

$$\ln[-\ln(1 - x(t))] = n\ln(k) + n\ln(t) \tag{6.16}$$

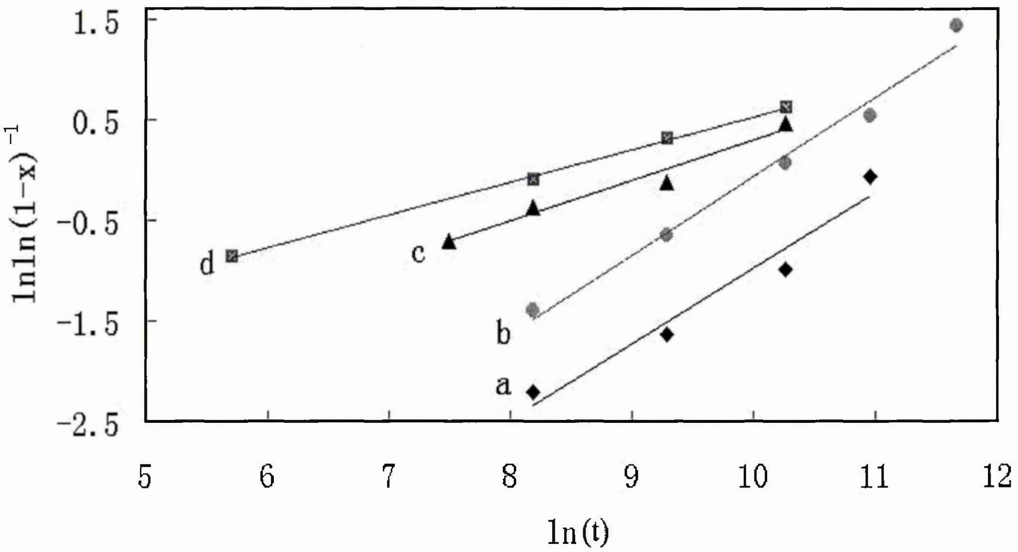

Fig.6.9. The relationship of ln [- ln(1- x)] versus ln(t) of sample TFL5-GP3. (a) 850^{0}C; (b) 875^{0}C; (c) 900^{0}C; (d) 950^{0}C.

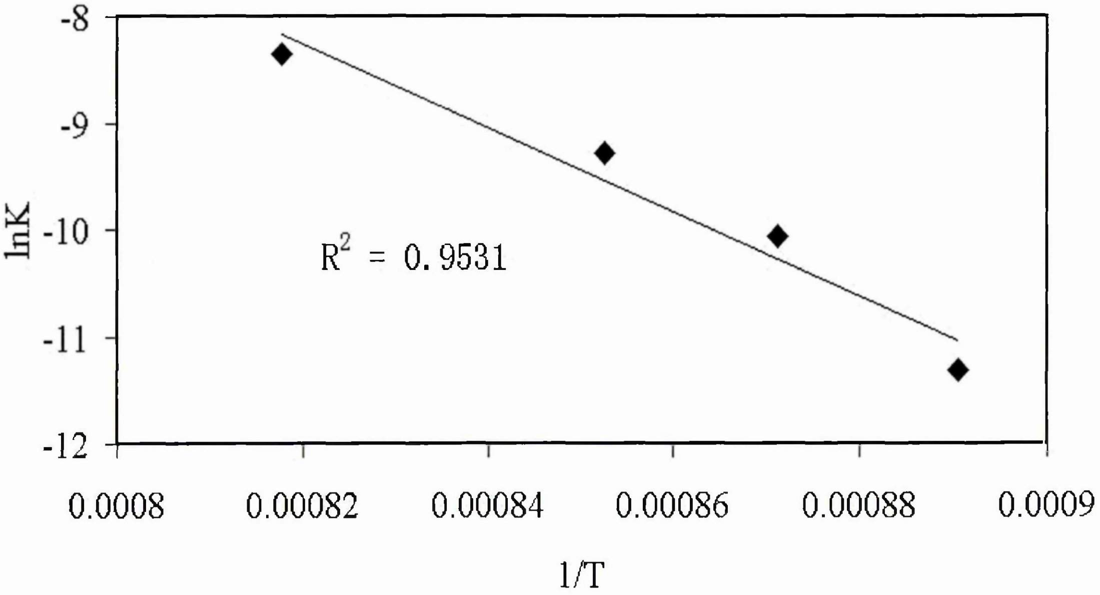

Fig.6.10. The relationship curve of ln(k) and 1/T of sample TFL5-GP3.

Thus, plots are generated of ln [- ln (1-x (t))] verse ln (t) for each hold crystallisation temperature, and values of k and n can be determined from the linear fitting of the data. Furthermore, values of the activation energy and pre-exponential factor can be obtained by rearranging Eq.(6.13) as follows:

$$\ln(k) = \ln(k_0) - \frac{E}{RT} \tag{6.17}$$

A plot is then generated of ln (k) versus 1/T, and a linear fit is applied to the data points to determine the activation energy E and the pre-exponential factor k_0 from the slope and y-intercept of the line, respectively.

All of the pertinent variables (n, k, Ea and k_0) for the JMA equation [Eq.(6.12)] are thus obtained. Time - temperature – transformation (T-T-T) curves which map the phase transformation as a function of time and temperature, are then calculated by rearranging the JMA equation and analytically calculating the temperature required for a fixed fraction of conversion as a function of time:

$$T = \frac{E}{R}\{\frac{1}{\ln(k_0 t)} - \frac{1}{n\ln[-\ln(1-x)]}\} \tag{6.18}$$

VI.3.1.2 Activation energy

From the combined plots of the crystallised fraction variation with time and temperature from the isothermal growth experiments shown in Figure 6.2, 6.5, and 6.6 for the pure and doped garnet thin films, according to Eq.(6.16), a plot of ln [- ln (1-x (t))] versus ln t should yield straight lines with slopes equal to the exponent n and from which the value of k can be derived.

For sample TFL5-GP3 of the pure YbAG thin films, linear regression analysis of the plots ln [- ln(1- x)] versus ln(t) according to Eq.(6.16) is shown in Figure 6.9.

Linear correlation coefficients are 0.9552, 0.9831, 0.9656, and 0.9987 at 850, 875, 900, and 950^{0}C, respectively. The exponent n is provided as 0.7494, 0.4086, 0.7879, and 0.3251 and the average exponent n is calculated as 0.5678.

Four rate constants from Figure 6.9 by the four intercepts with the vertical axis of the plots are also obtained. Hence, using Eq. (6.17), the relationship curve of lnk and 1/T after plotting is shown in Figure 6.10. The correlation coefficient was 0.9531. From the slope of the line, the activation energy can be calculated as 327±10 kJ/mol.

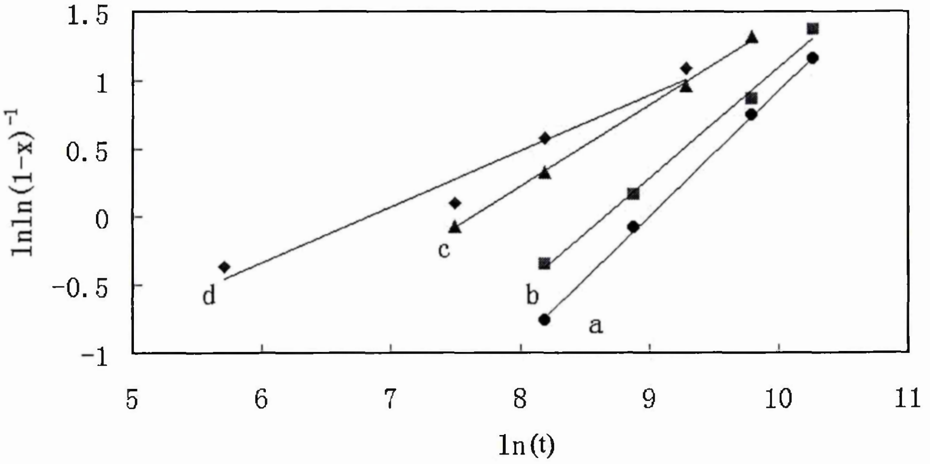

Fig.6.11. The relationship of ln [- ln(1- x)] versus ln(t) of sample TFL7-GP3; (a) 750^{0}C; (b) 775^{0}C; (c) 800^{0}C; (d) 850^{0}C.

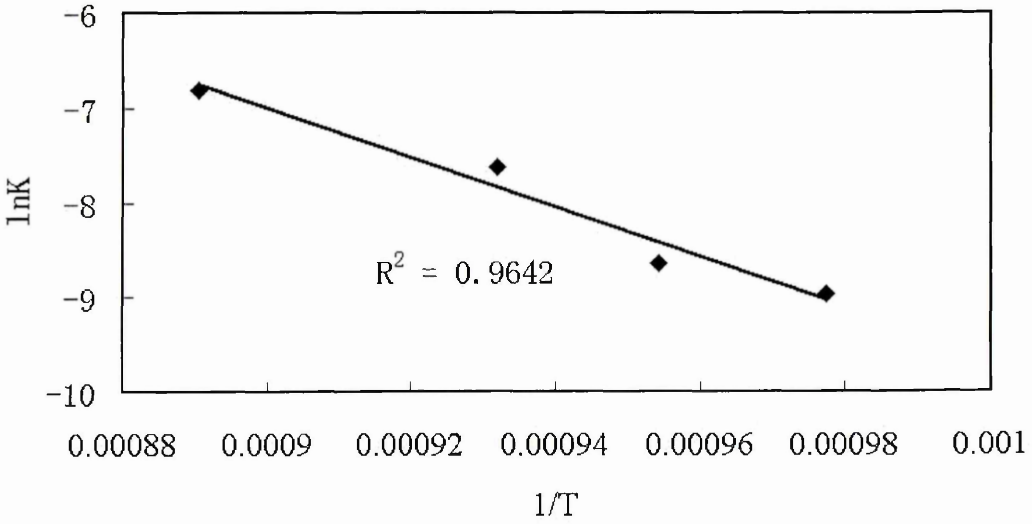

Fig.6.12. The plotting curve of ln(k) and 1/T of sample TFL7-GP3.

The same method was used for samples TFL7-GP3 and TFL8-GP3. Linear regression analysis of the plots ln [- ln(1- x)] versus ln(t) according to Eq. (6.16) is shown in Figure 6.11 and 6.13 and the relationship curves of lnk and 1/T after plotting are shown in Figure 6.12 and 6.14 using Eq. (6.17). The activation energy can be calculated as

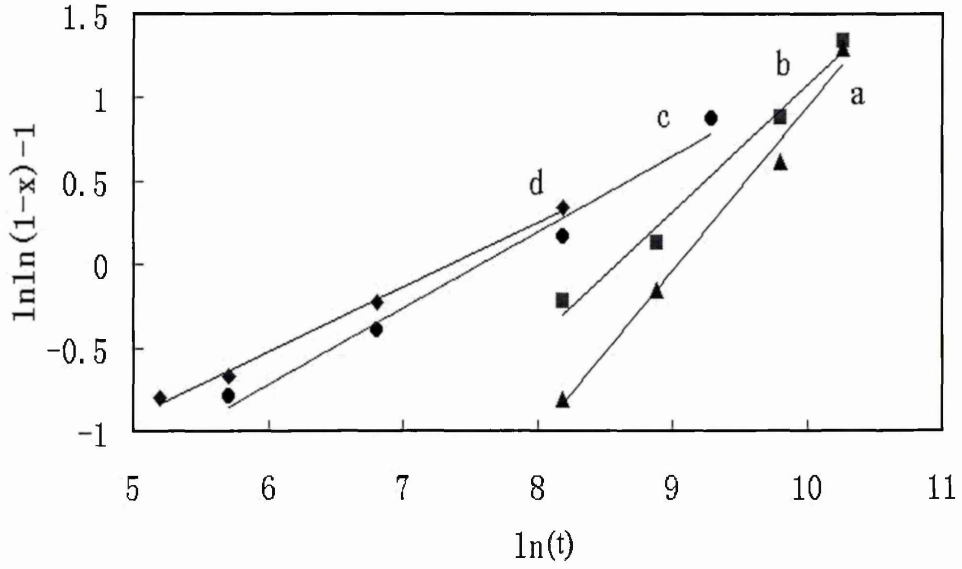

Fig.6.13. The relationship of ln [- ln(1- x)] versus ln(t) of sample TFL8-GP3; (a) 750^{0}C; (b) 775^{0}C; (c) 800^{0}C; (d) 850^{0}C.

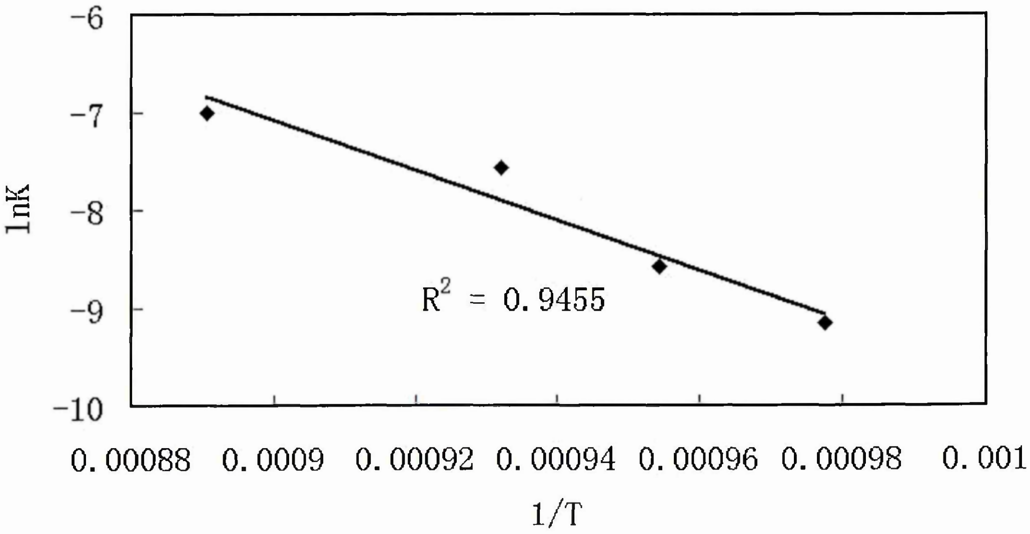

Fig.6.14. The plotting curve of ln(k) and 1/T of sample TFL8-GP3.

217±10 kJ/mol and 212±10 kJ/mol from Figure 6.12 and Fig 6.14 for samples

TFL7-GP3 and TFL8-GP3, respectively. The relative values obtained are all tabulated in Table 6.2.

The calculated activation energy of Mo doped YbAG garnet thin films are about one third lower than that of pure YbAG garnet films. Doping with Mo^{6+} has greatly decreased the energy barrier of crystallisation and thus lowered the temperature of crystallisation. It was also found that the activation energy of samples TFL7-GP3 and TFL8-GP3 were very similar even though the concentration of MoO_3 in the two samples was greatly different. This suggests that only a low level of doping is required for the purpose of lowering the transition temperature of YbAG.

The average exponent n obtained from samples TFL5-GP3, TFL7-GP3 and TFL8-GP3 are between 0.5~0.7. Within the framework of a proposed classification of diffusion-controlled transformations [181], an exponent n greater than 2 indicates that the transformation is nucleation limited and the activation energy can be related to nucleation energy. In contrast, values of n less than 1 indicate that crystal growth dominates. This conclusion is in agreement with our experimental observations by X-ray diffraction that show fast nucleation and crystal growth in the initial stage. Thus, the data obtained from the transformed fraction in Figure 6.2, 6.5, and 6.6 is representative of the crystal growth process.

VI.3.1.3 T – T –T diagram of YbAG garnet crystallisation

Using the data listed in Table 6.2, Eq (6.18) can be deduced as the following equation for sample TFL5-GP3 when the fraction crystallised is equal to 1%,

$$T(K) = \frac{40098}{\ln(t) + 32} \tag{6.19}$$

or

$$T(^{0}C) = \frac{40098}{\ln(t) + 32} - 273 \tag{6.20}$$

Table 6.2 Activation energy and all related parameters.

Samples	n	k	k$_0$	Ea (kJ/mol)
TFL5-GP3	850^{0}C, 0.7494	1.23 X 10^{-5}	2.61X10^{10}	327±10
	875^{0}C, 0.7879	4.25 X10^{-5}		
	900^{0}C, 0.4087	9.31 X 10^{-5}		
	950^{0}C, 0.3251	2.34 X 10^{-4}		
	Average: 0.5678			
TFL7-GP3	750^{0}C, 0.9859	1.27 X 10^{-4}	1.42 X 10^{7}	217±10
	775^{0}C, 0.8093	1.75 X 10^{-4}		
	800^{0}C, 0.5952	4.87 X 10^{-4}		
	850^{0}C, 0.4071	1.10 X 10^{-3}		
	Average: 0.6994			
TFL8-GP3	750^{0}C, 0.8807	1.05 X 10^{-4}	7.76 X 10^{6}	212±10
	775^{0}C, 0.7595	1.88 X 10^{-4}		
	800^{0}C, 0.4550	5.15 X 10^{-4}		
	850^{0}C, 0.6261	9.11 X 10^{-4}		
	Average: 0.6803			

When the fraction crystallised is equal to 99%, Eq(6.18) will be as follows:

$$T(K) = \frac{40098}{\ln(t) + 21} \qquad (6.21)$$

or,

$$T(^0 C) = \frac{40098}{\ln(t) + 21} - 273 \qquad (6.22)$$

For sample TFL7-GP3, Eq(6.18) will be as follows:

$$T(^0 C) = \frac{26691}{\ln(t) + 23} - 273 \qquad (6.23)$$

while the fraction crystallised is equal to 1%, and

$$T(^0 C) = \frac{26691}{\ln(t) + 14} - 273 \qquad (6.24)$$

while the fraction crystallised is equal to 99%.

For sample TFL8-GP3, Eq(6.18) will be as follows:

$$T(^0 C) = \frac{26076}{\ln(t) + 23} - 273 \qquad (6\text{-}25)$$

while the fraction crystallised is equal to 1%, and

$$T(^0 C) = \frac{26076}{\ln(t) + 14} - 273 \qquad (6\text{-}26)$$

while the fraction crystallised is equal to 99%.

Using Eq.(6.20, 6.22 and 6.23 ~ 6.26), T – T –T diagram of YbAG garnet crystallisation can be generated in Figure 6.15a, b, and c. The T – T –T diagrams describe crystallisation as a function of time and temperature. This data may be useful for controlling the microstructure of pure and doped YbAG garnet thin films during crystallisation by sol-gel techniques.

VI.3.2 Crystalline size and lattice constant of the pure and doped YbAG thin films

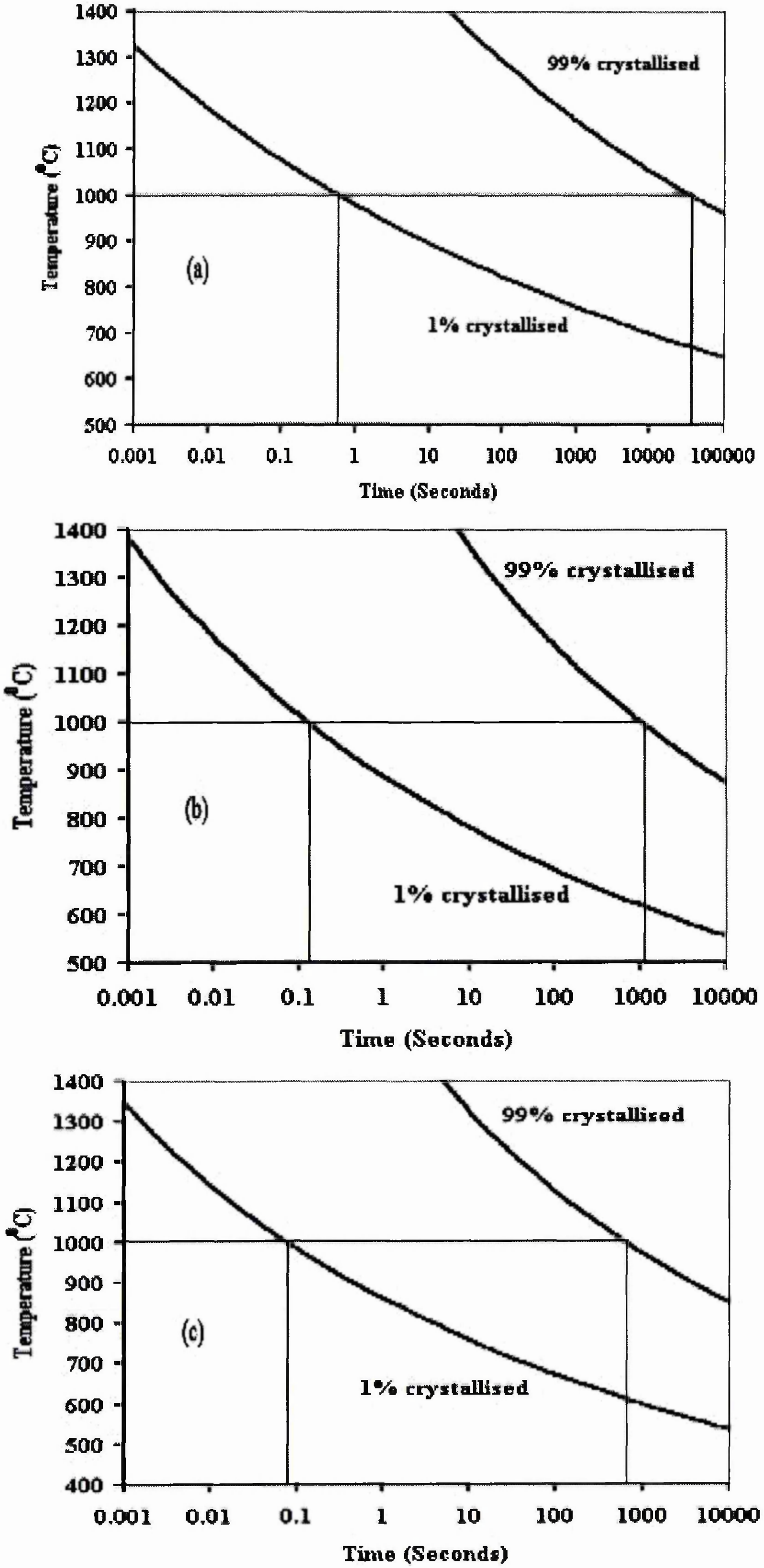

Fig.6.15. T – T –T diagram of YbAG garnet film crystallisation. (a) pure YbAG garnets; (b) 10 at. % Mo: YbAG garnet. (c) 30 at. % Mo: YbAG garnet.

The size of the crystallites are estimated from Debye-Scherrer formula [182], given by

$$L = \frac{0.9\lambda}{B\cos\theta} \qquad (6.27)$$

where L is the coherence length, B is the full width at half maximum (FWHM) of the peak, λ is the wavelength of the X-ray radiation, and θ is the angle of diffraction. In the case of spherical crystallites, the relationship between L and D, the diameter of the crystallite, is given by

$$L = \frac{3}{4} * D \qquad (6.28)$$

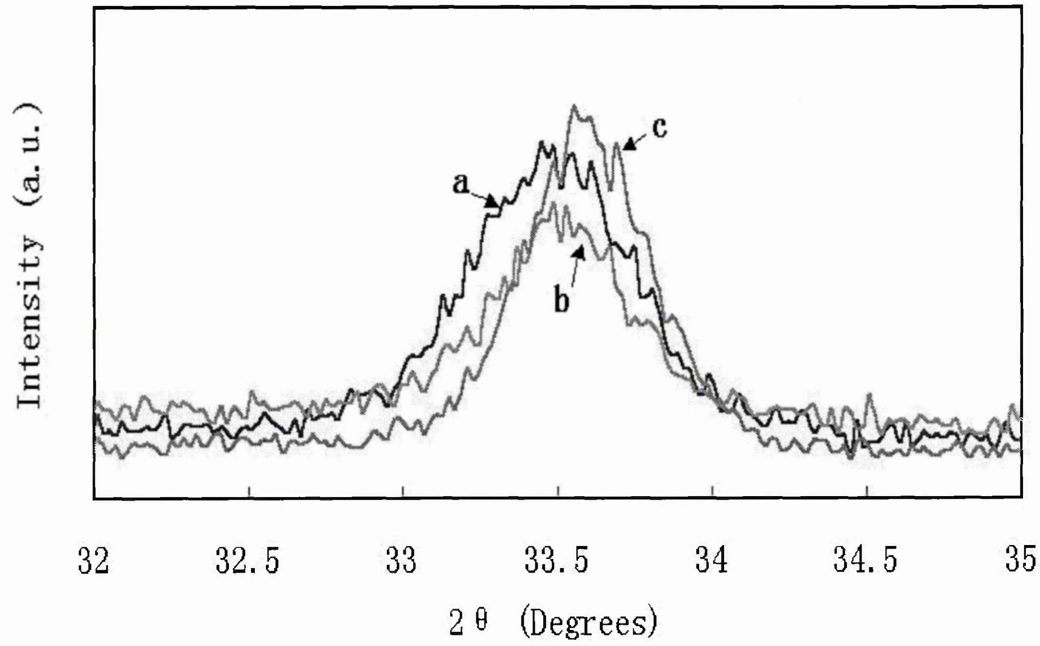

Fig.6.16. XRD peaks at about 33.5^0 (420) of the pure and Mo doped YbAG thin films; (a) pure YbAG; (b) 10 at. % Mo:YbAG; (c) 30 at. % Mo :YbAG.

The estimated size at 850^{0}C or 950^{0}C heat treatment after full crystallization is about 30~40 Å from the FWHM of the maximum texture peak at $2\theta \approx 18.1^0$ in either the pure or doped alumina garnets. This value is smaller than that we observed by AFM in Chapter VII. The difference is possibly contributed by the broadening of the FWHM in XRD patterns due to the strain on small particles.

Lattice constant can be calculated from the 2θ angle position of the strongest intensity (420) about 33.5^0 in XRD patterns by using the equation (32). For cubic crystals, it is expressed as the following:

$$a = d\sqrt{h^2 + k^2 + l^2} = \frac{\lambda_0}{2\sin\theta} * \sqrt{h^2 + k^2 + l^2} \qquad (6.29)$$

where a is the crystal lattice constant and the (h, k, l) is the crystal plane index. The XRD peaks at about 33.5^0 of the pure and Mo doped YbAG are shown in Figure 6.16.

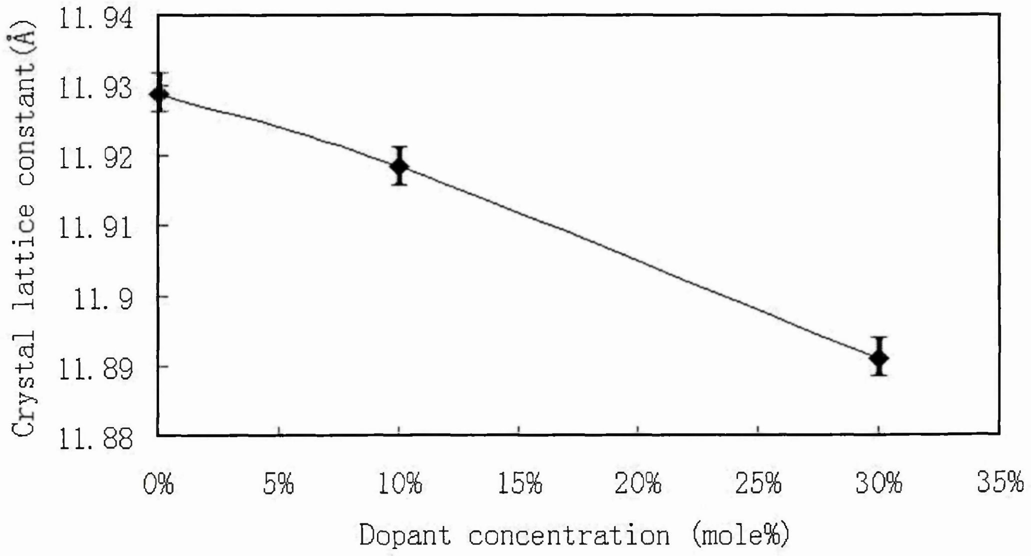

Fig.6.17. The plot of the lattice constant with Mo doping concentrations.

The calculated lattice constants in thin films are 11.93 Å, 11.92 Å, and 11.89 Å for the pure YbAG, 10 and 30 at. % Mo doped YbAG respectively. The value of the pure YbAG is equal to that of JCPDS 73-1369 [94]. The relationship between the lattice parameter and Mo concentration is shown in Figure 6.17. A nearly linear relationship is apparent from Figure 6.17.

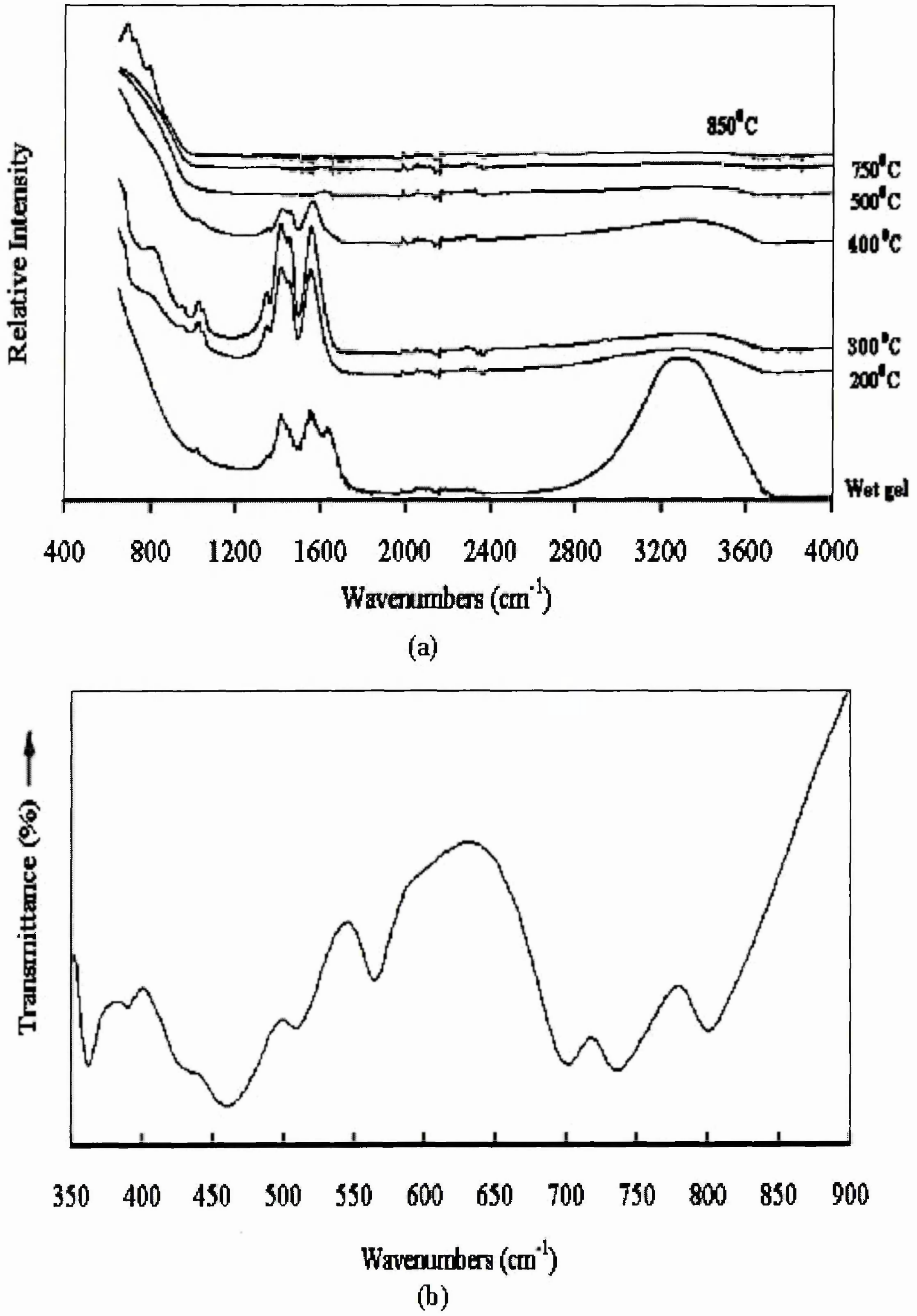

Fig.6.18. Infrared spectra of the pure YbAG powders; (a) structural changes due to 30 minutes heat treatment at various temperatures; (b) 850^0C, 30 mins.

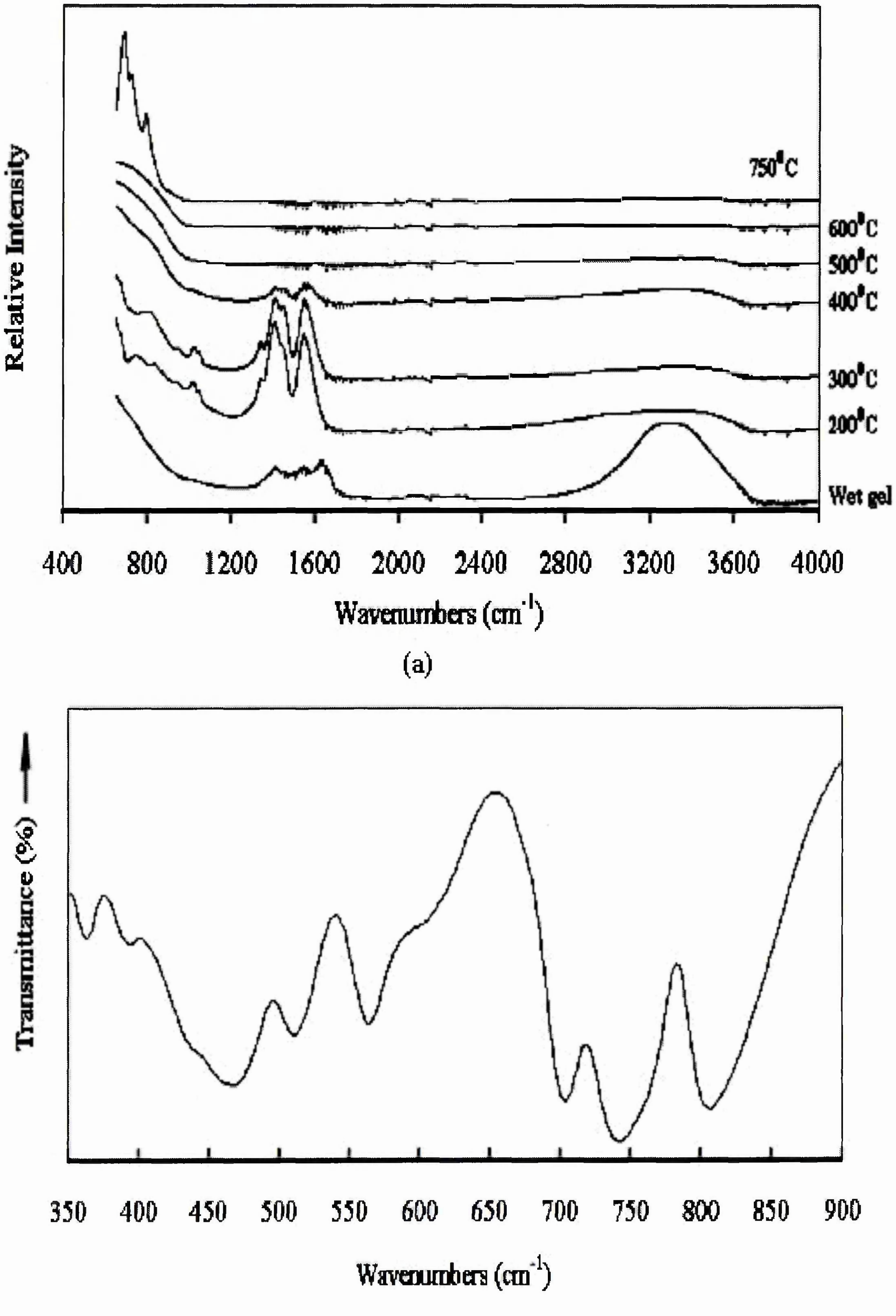

(a)

(b)

Fig.6.19. Infrared spectra of the 10 at. % Mo doped YbAG powders. (A) structural changes due to 30 minutes heat treatment at various temperatures; (B) 850^0C, 30 mins.

VI.3.3 Infrared and Raman spectra of the pure YbAG and Mo: YbAG powders

VI.3.3.1 Infrared spectra

Infrared spectra of the pure and Mo doped YbAG powders at different annealing conditions were recorded. Figure 6.18a shows the infrared spectra in the wavenumber range of 4000~500 cm^{-1} for the sample POW5-GP6. Figure 6.18b is the infrared transmittance spectra of this sample at 850^0C 30 minutes heating in the range of 1000 ~ 400 cm^{-1}. The spectra between 400~200 cm^{-1} were abandoned due to the exited peaks of KBr in this range.

Correspondingly, the infrared spectra of the sample POW7-GP6 (10 at. % Mo:YbAG) in the range of 4000~500 cm^{-1} are shown in Figure 6.19a. The infrared transmittance spectra of this sample at 850^0C 30 minutes heating in the range of 1000 ~ 400 cm^{-1} are shown in Figure 6.19b.

Table 6.3 Comparison of IR vibrational frequencies of the pure YbAG, 10 at. % Mo:YbAG, and reference YbAG powder data.

Pure YbAG (υ / cm^{-1})	Mo: YbAG (υ / cm^{-1})	Reference data [185] (υ / cm^{-1})
800	806	805
737	742	742
702	704	709
565	565	569
510	511	516
461	465	468
431	435	439
390	394	397

There is no significant difference between the pure (Figure 6.18a) and 10 at. % Mo doped YbAG compositions (Figure 6.19a). The wet gel exhibited intense and broad bands at 2800~3600 cm^{-1}. The bands between 3200 ~ 3600 cm^{-1} are due to the ν (O-H) stretching vibration of absorbed H_2O in the sample as well as other broad hydroxyl stretching frequencies. Most of absorbed water was lost after 200^0C heat treatment. The C(O)-OH stretching frequencies can be identified at 3300~2800, 1640~1600, 1340~1290 and 1050~1000 cm^{-1}. Besides, other C-H and C-O stretches can also be assigned in the regions 3000~2800 and 1600~1250 cm^{-1}, respectively, arising from metal-attached alkoxy groups [183]. Nearly all the characteristic peaks had disappeared after 500~750^0C heat treatment for the pure YbAG sample and after 500~600^0C calcination for the Mo doped YbAG sample. The three typical characteristic metal-oxygen vibrations in garnets [184] in the examined range were present at about 692, 728, and 795 cm^{-1} after heat treatment at 850^0C for the pure YbAG samples and at about 689, 725, and 792 cm^{-1} at 750^0C for the 10 at. % Mo:YbAG sample. The pure and 10 at. % Mo:YbAG powders exhibited little difference in colour. The pure YbAG powders were a very white colour while the 10 at. % Mo:YbAG powders were white with a greyish tinge. In comparing IR spectra, it is again confirmed that Mo doped YbAG has a lower crystallisation temperature than the pure YbAG. The structural changes characterised by the infrared spectra of the pure and Mo doped YbAG powders at different annealing conditions are in agreement with that studied in Chapter V by DTA and TG.

Because of the limit in the wavenumber range in our IR instrument, the infrared transmittance spectra were recorded on another instrument using the pressed disk sample to confirm the obtained single-phase alumina garnet. The infrared active vibrations of the pure and 10 at. % Mo:YbAG powders in Figure 6.18b are in good agreement with the experimental [185] and theoretically calculated IR vibrations of YbAG garnets [184]. Comparison of our IR spectra data and the experimental data of YbAG powders from ref. [185] is tabulated in Table 6.3. The infrared spectra, especially emphasis on the 10 at. % Mo:YbAG sample, does not show any IR frequencies corresponding to other phases [e.g. MoO_3, Yb_2O_3, $Al_2(MoO_4)_3$]. Especially in general, the IR band of Mo=O in crystalline MoO_3 appears at 1000 cm^{-1} due to the stretching vibration mode [186-188]. FT-IR spectra have also confirmed that the single phase YbAG garnet was obtained by our sol-gel methods. Comparing the IR spectra of the pure YbAG and 10 at. % Mo:YbAG reveals that the frequencies of all characteristic peaks are the same, apart from some frequency changes due to Mo doping in the YbAG. This observation suggests that Mo is statistically well dispersed in the YbAG lattice, which is also supported by XRD data.

VI.3.3.2 Raman spectra

Raman spectra of the pure and Mo doped YbAG powders at different annealing conditions were recorded. There is no Raman shift for the sample POW5-GP6 that was heat-treated below 850^0C in the range 200~1000 cm^{-1} wavenumbers. Raman vibration lines were observed for the pure YbAG composition after 850^0C heat treatment. Raman spectra of the sample POW5-GP6 powders are shown in Figure 6.20. There exist 25 Raman active modes in rare earth aluminium garnets according to theoretical calculations [189]. 10 Raman active vibrational modes were observed in the range 200-1000 cm^{-1}, most likely because either the samples had not fully crystallised or other experimental causes. The vertical solid lines in Figure 6.20 indicate the observed phonon peaks which are in good agreement with the experimental and calculated Raman mode frequencies of $Yb_3Al_5O_{12}$ or rare earth aluminium garnets [189] [190]. This indicates again that the single-phase ytterbium aluminium garnet was obtained.

In particularly for the sample POW7-GP6 with the 10 at. % Mo doped YbAG composition, the Raman shift can initially be seen in the sample heat treated at 600^0C, 30 minutes in the range of wavenumber 200 ~1000 cm^{-1}. Raman spectra of the sample POW7-GP6 powders are shown in Figure 6.21. This suggests that the initial crystallisation temperature of Mo: YbAG could be as low as 600^0C (Figure 6.21a).

Table 6.4 Comparison of Raman active vibrational frequencies of the pure and 10 at. % Mo doped YbAG powders.

Pure YbAG (υ / cm^{-1})	10% Mo^{6+}:YbAG (υ / cm^{-1})
—	893
860	869
825	—
792	792
723	722
700	—
550	550
378	378
360	360
321	321
256	256

There are 9 Raman active vibrational lines in the range of 200-1000 cm^{-1} that are observed for the 10 at. % Mo:YbAG sample at 750^{0}C, 30 minutes heat treatment in Figure 6.21b. Raman active vibrational frequencies are tabulated in Table 6.4. In comparing the Raman spectra in Figure 6.20 and 6.21, a distinct difference is that there is a strong vibrational line at the frequency of 893 cm^{-1} (shown by the dotted vertical line in Figure 6.21b) in the 10 at. % Mo:YbAG sample. This line does not belong to the vibrational mode in YbAG garnets with the pure composition [189] [190]. Thus, this line is clearly caused by the vibration which is related to Mo^{6+} doping. Furthermore, this line does not belong to any other possible phase such as MoO_3 or $Al_2(MoO_4)_3$. Hence, this strong Raman mode is attributed to the fact of R-site order-disorder in Mo:$Yb_3Al_5O_{12}$ garnets because of the replacement of Yb^{3+} by Mo^{6+}. The Raman spectroscopy of order-disorder has been reported in the structures of many other solid solution ceramic materials; e.g. $Sr(Mg_{1/3}Nb_{2/3})O_3$, $xCaTiO_3$-$(1-x)NdAlO_3$, $Ba(Mg_{1/3}Ta_{2/3})O_3$ [191] [192].

VI.3.4 States of Mo (VI) cations in YbAG garnets

XPS analysis in section VI.2.3 has confirmed that Mo cations are in the six coordination state in the doped YbAG. This raises the question: what position does the dopant Mo (VI) occupy in YbAG garnets? This is a very interesting and important question and is discussed here.

On the one hand, as we highlighted in Chapter II, the formation of solid solutions in the rare earth alumina garnets are very sensitive to the chemical valence and the radius of the doped cations. Rare earth alumina garnets have a general formula $[RE]_3[Al]_2[Al]_3O_{12}$. RE and Al cations occupy particular sites, depending on cation

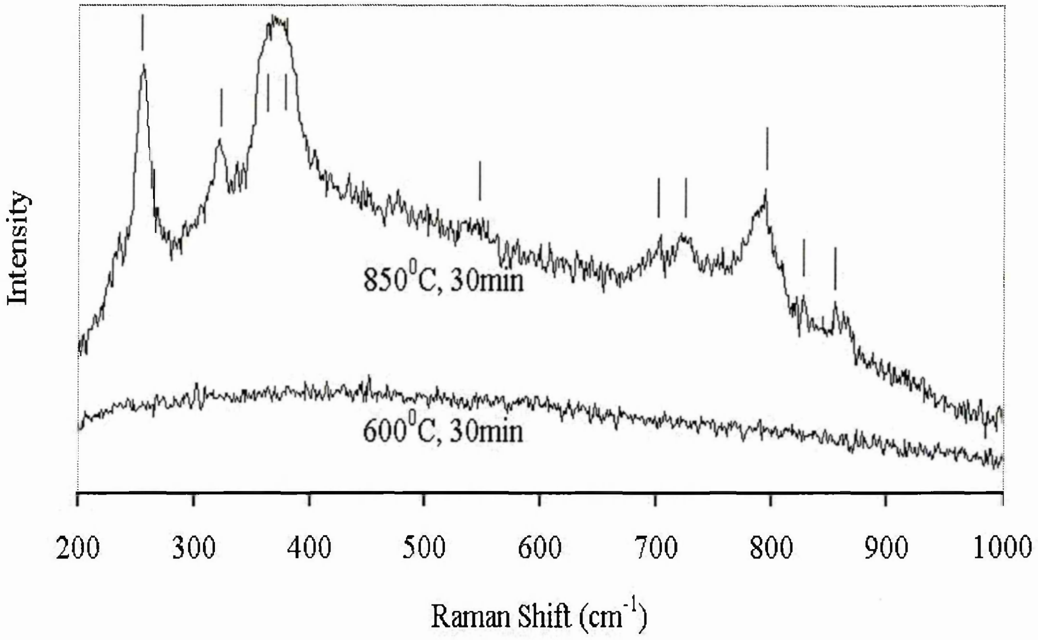

Fig.6.20. Raman spectra of the pure YbAG powders.

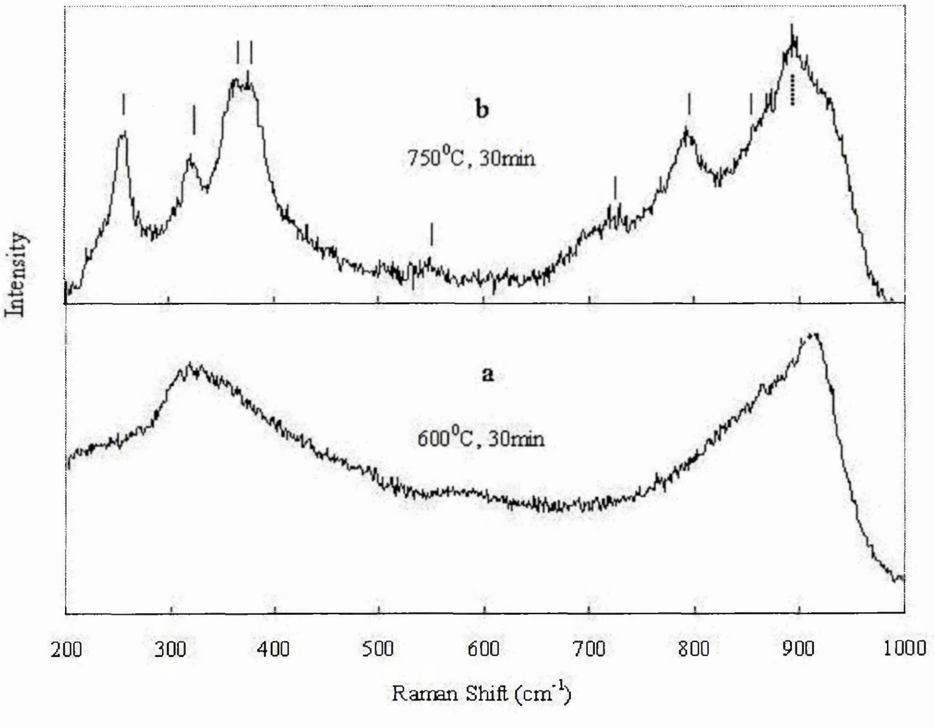

Fig.6.21. Raman spectra of the 10 at. % Mo doped YbAG powders.

radii and their valences; (i) 3 Al^{3+} cations are located at tetrahedral sites; (ii) 2 Al^{3+} cations occupy octahedral sites; (iii)'RE' cations occupy dodecahedral sites; (iv) oxygens are located at normal positions. Therefore, the garnet crystal structure consists of a three-dimensional network of polyhedra (tetrahedra, octahedra, and dodecahedra) having an appropriate cation at their centers and surrounded by the appropriate number of oxygen ions. Each oxygen belongs to two dodecahedra, one tetrahedron, and one octahedron. The radius of Al^{3+} is about 0.51 Å. The radius of RE^{3+} is about 0.9 Å; e.g. Y^{3+} (0.92 Å) and Yb^{3+} (0.86 Å).

On the other hand, it is well known that MoO_3 plays an important role as catalysts in petroleum refining, chemicals production, and environmental protection industries [193-195]. In these applications, MoO_3 is mainly supported by γ- or α-Al_2O_3 [180]. Many other multicomponent supports have also been developed in recent years such as TiO_2-ZrO_2 and La_2O_3-TiO_2 [196] [197]. The dispersed state of supported MoO_3 has been widely investigated from room temperature to 800^0C (the melting point of MoO_3 is 793^0C). In general, it can be divided into two categories: the first suggests that a monolayer of the dispersed ionic compound is formed on the surface of the support, and the second proposes that the dispersed metal cations are incorporated into surface vacancy sites of the support with their accompanying anions staying on top of them for charge neutrality. MoO_3 generally exists as an amorphous phase below 500^0C and above 500^0C, it can transform to its crystalline form or react with other support oxides to form new phases such as $Al_2(MoO_4)_3$ and $ZrMo_2O_8$ [180] [197]. The structure of the dispersed molybdenum species is closely related to the nature of the specific oxide support, the loading amount, the preparation procedure, and the heating temperature.

In our experiments from XRD patterns of Mo:YbAG, there is no crystalline phase transformation below 700^{0}C heat treatment. Only single-phase aluminium garnets appeared above 700^{0}C, even in the fully crystallised sample at 850^{0}C heat treatment. No other crystalline phases were detected by XRD even though the doped concentration of Mo(VI) is very high. Furthermore, IR and Raman spectra also confirm these results. Hence, two possibilities are left to choose for the existence of Mo (VI) species as follows:

VI.3.4.1 Mo (VI) species exists as an amorphous phase similar to that that exists below 500^{0}C, even at temperature up to 950^{0}C heat treatment that have been studied in this thesis. Mo (VI) species may be dispersed as a monolayer on the surface of the YbAG or incorporated into surface vacant sites of the YbAG. In this circumstance, YbAG garnets will be a good support for MoO_3 catalysts due to their phase stability and chemical inertness even at very high temperature. However, one question is why the dispersed Mo (VI) species does not transform into a crystalline phase when it cools down from the heating temperature that is much higher than its melting point.

VI.3.4.2 It is suggested that Mo^{6+} cations are doped into YbAG garnet lattice positions. But, the effective radius of Mo^{6+} is 0.62 Å [26] that is closer to the radius of Al^{3+}(0.51 Å) than that of Yb^{3+} (0.86 Å). In general, the ionic radii of Al^{3+} and Mo^{6+} in the tetrahedral (0.39 Å and 0.41 Å) and octahedral (0.53 Å and 0.6 Å) configuration, respectively, are similar, which means that Mo^{6+} should replace some positions of Al^{3+} in garnets. However, doped Mo here is in a six valence state or 6+ oxidation state that is twice the chemical valence state of Al^{3+}. Thus, it is unlikely that Mo^{6+} cations substitute Al^{3+} because such replacement will result in aluminium vacancies with Mo cation producing one aluminium vacancy for charge neutrality. This means that it will break down the three-dimensional network of oxygen polyhedra in alumina garnets and form other crystalline phases such as $Al_2(MoO_4)_3$, and in fact, there is no evidence of Mo^{6+} cations in the positions of Al^{3+} sites in XRD patterns, which would lead to big changes in the peak positions [96]. The other possibility is that Mo^{6+} cations substitute for the Yb^{3+}cations at the dodecahedral sites of alumina garnets even though the radius of Mo^{6+} (0.62 Å) is much smaller than that of Yb^{3+}(0.89 Å). This will cause the structure deformation and the adjustment of crystal cell constant, decreasing the crystal lattice constant. The decrease of the crystal lattice constant in Mo:YbAG has been confirmed in Figure 6.17. Because the chemical valence of Mo^{6+} is twice greater than that of Yb^{3+}, the replacement of the Yb^{3+} by Mo^{6+} will occur in a 1:2 mole ratio replacement for charge neutrality. That is, for every molybdenum ion included within the garnet structure two Yb^{3+} ions are replaced whereby cationic voids in the dodecahedral are created within the garnet structure. Clearly, such substitution would happen when the replaced Yb^{3+} sites are kept below a limited mole ratio. Our research suggests that this mole ratio of Mo^{6+}/Yb^{3+} generally does not surpass 1/3. Furthermore, if we consider the sample TFL6-GP3 that we described in Chapter V with the ytterbium alumina garnet matrix composition and dopants i.e. Mo^{6+} and Li^{+}, it transformed into the single-phase ytterbium alumina garnet after annealing at 800^0C. Li^{+} cations are likely to occupy the dodecahedral vacancy sites that are caused by the replacement of Yb^{3+} for Mo^{6+}.

To the best of our knowledge, no other reports exist of Mo^{6+} doped aluminium garnets either by naturally occurring or artificial synthesis. Further work is required to confirm the position of Mo^{6+} in the YbAG garnet or Mo (VI) species state when they are doped into YbAG garnets.

VI.4 Summary

The pure and Mo doped YbAG garnet powders and thin films by sol-gel methods have been studied in this Chapter. Fully crystallised single-phase pure YbAG garnets can be produced after 850^0C heat treatment and this transition temperature decreases to at least 750^0C by doping Mo into YbAG. The initial crystallisation temperature of Mo: YbAG is possibly as low as 600^0C according to evidence from Raman spectra. The well-known JMA model was used to investigate the crystallisation kinetics. The results of crystallisation kinetics show that doped Mo has significantly lowered the activation energy when comparing the Mo:YbAG to the pure YbAG. However, only low levels of doping by Mo were needed to lower the crystallisation temperature. The T-T-T diagram from the crystallisation kinetics may be useful to control the structure in the preparation of YbAG garnets by sol-gel methods.

XPS analysis confirmed that Mo existed in the six valence state or 6+ oxidation state in the samples. XRD, FT-IR, and Raman spectra have shown that doped Mo was statistically well dispersed in the matrix of YbAG. Two possibilities for the incorporation of the Mo (VI) species state into the YbAG garnet matrix have been described. We consider that it is more likely that Mo^{6+} cations are doped into the YbAG garnet lattice in the Yb^{3+} positions.

Chapter VII

Morphologies and applications

VII.1 Introduction

YbAG garnets were manufactured by our sol-gel methods. In this Chapter, we present the morphologies of YbAG or Mo:YbAG thin films and thick coatings. As we mentioned in Chapter II, thick films with thicknesses greater than 1 or 2 microns are extremely difficult to produce by the conventional sol-gel method. Some modifications to the conventional sol-gel method are required to achieve this purpose. We will also describe some possible applications for pure or doped YbAG materials in this chapter. Possible applications of ytterbium aluminium garnets are corrosion resistance and thermal insulating coatings which can be coated on various substrates such as ceramics, stainless steels, or Ni superalloys. Many other potential applications are available by further research in the near future.

VII.2 Results and discussion

VII.2.1 Morphologies

VII.2.1.1 Morphologies of thin films

The four-time dip coated xerogel thin film on the stainless steel with the composition of 10 at. % Mo doped YbAG (sample "Group 5" in Chapter III) is shown in Figure 7.1. This had a very smooth surface with a porous structure and the substrate surface was well covered by the thin film. The scratch resulting from polishing is clearly visible on the right top of the image. The xerogel films of the pure YbAG compositions had the same surface morphologies.

After being heated at 600^{0}C, its surface morphology is shown in Figure 7.2. The surface appeared more dense than that of the xerogel thin film in Figure 7.1. This was an amorphous structure and exhibited still an integral surface structure.

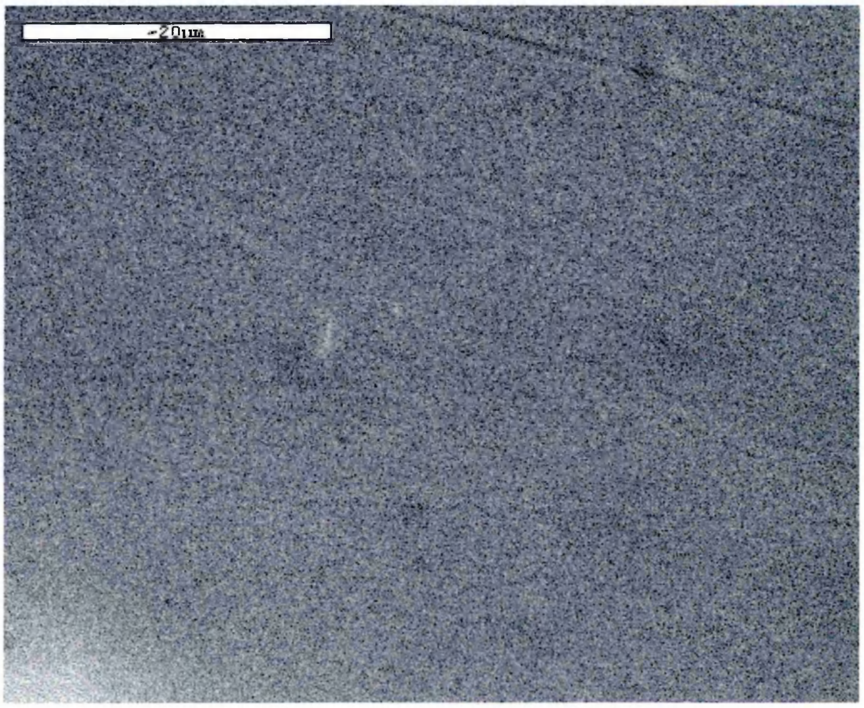

Fig.7.1. Morphologies of the xerogel film with the composition 10% Mo doped YbAG after heating at 200^{0}C. (SEM by Joel-800).

After further heat treatment at 750^{0}C, the surface is shown in Figure 7.3a. The thin film structure transformed from amorphous to YbAG garnets. We can see that the thin film has broken up under these circumstances. A high magnification image is shown in Figure 7.3b. It was found in Figure 7.3b that some parts in the thin film were still interconnected but some parts were pulled away. The film cracked by the stress caused by the mismatch of the thermal expansion coefficient between the YbAG garnet and the stainless steel substrate due to the conversion of the amorphous phase to the

YbAG garnet. The crack width is about half a micron in Figure 7.3b.

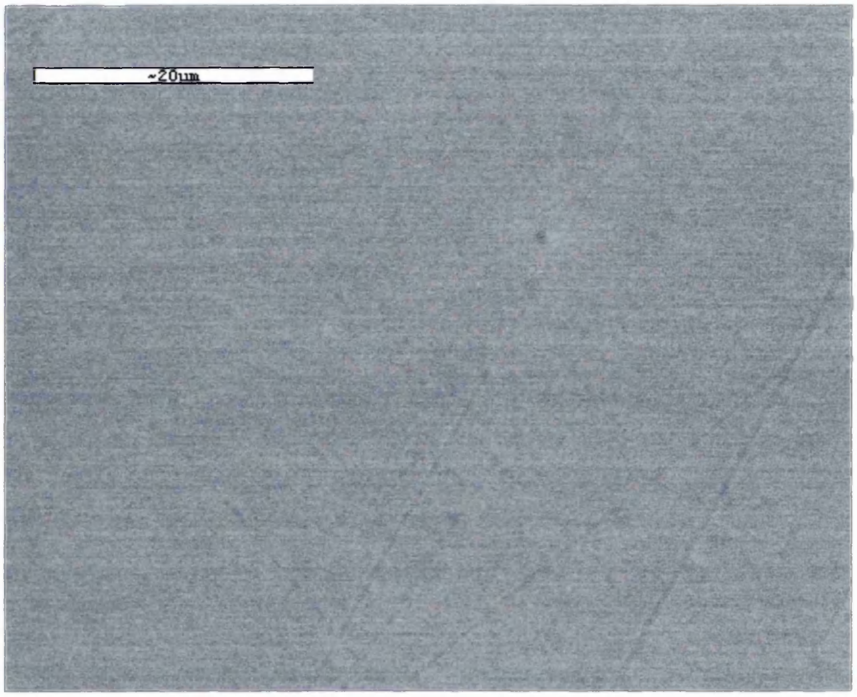

Fig.7.2. Morphologies of the amorphous thin film of sample TFL7-GP5-a.

The film thickness is estimated by the method which we described in Chapter III. We carefully dropped 3 wt. % aqueous ammonia solutions onto the one-time dip coated xerogel thin film surface, which made the thin film corrode and roll up on the substrate. This is shown in Figure 7.4. The film thickness is then measured by choosing an appropriate area as is shown in Figure 7.5 where the thickness is about 700 nm. After further heat treatment at high temperature, the final thickness could be 200 ~ 300 nm after shrinkage.

Thin film surface morphologies of sample TFL7-GP5 were also obtained using AFM and are shown in Figure 7.6a. It consisted of agglomerates of very small grains. The morphological aspects are better seen in Figure 7.6b. The size of nanograins is about 50 ~ 60 nm. This size is larger than calculated using Debye-Scherrer formula [182] by

XRD in Chapter VI. The difference is contributed to the broadening of the FWHM of peaks in XRD patterns because of the strain in the thin film.

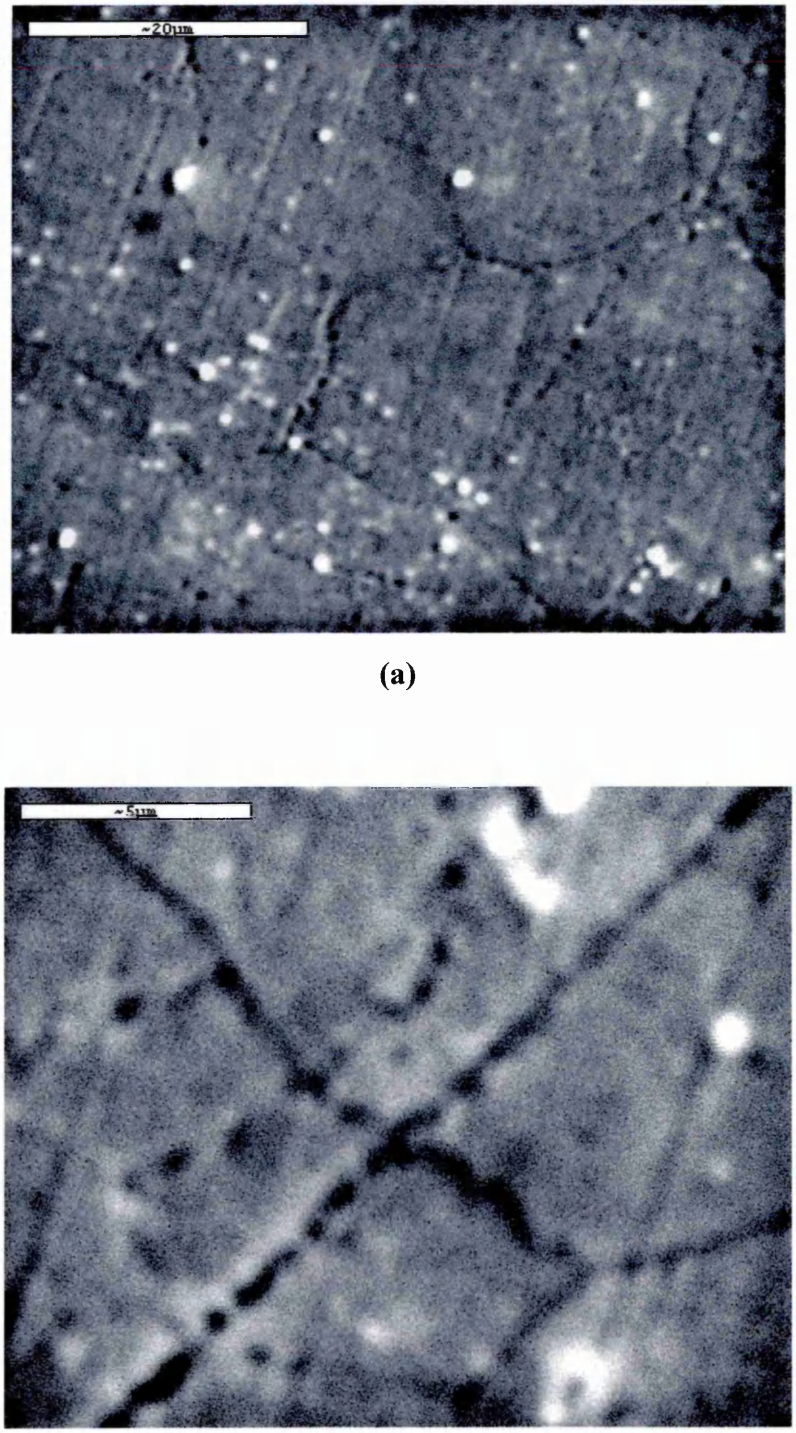

(b)

Fig.7.3. Sample TFL7-GP5-b surface morphologies (SEM by Joel-800).

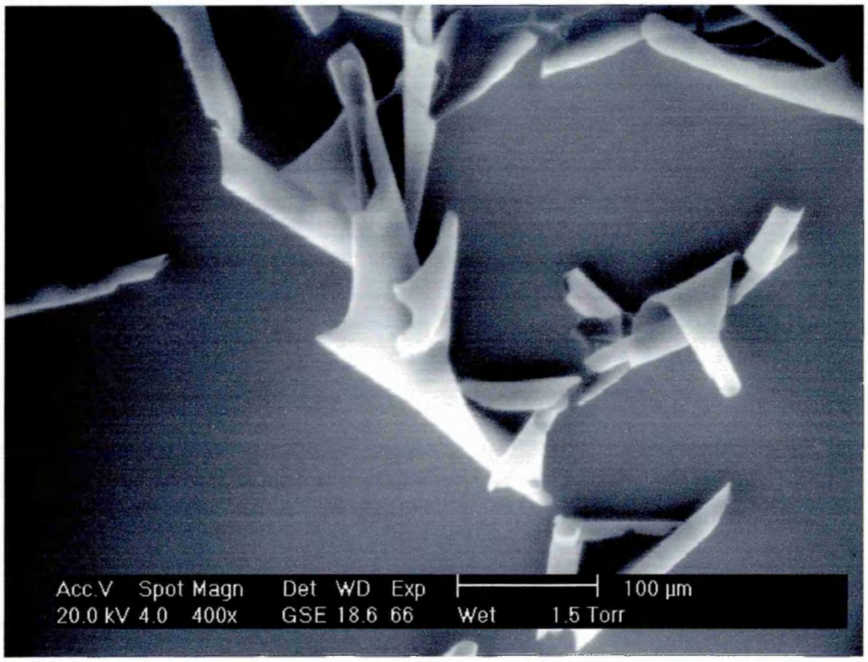

Fig.7.4. Surface of 3.0 wt. % aqueous ammonia solutions treated xerogel thin film.

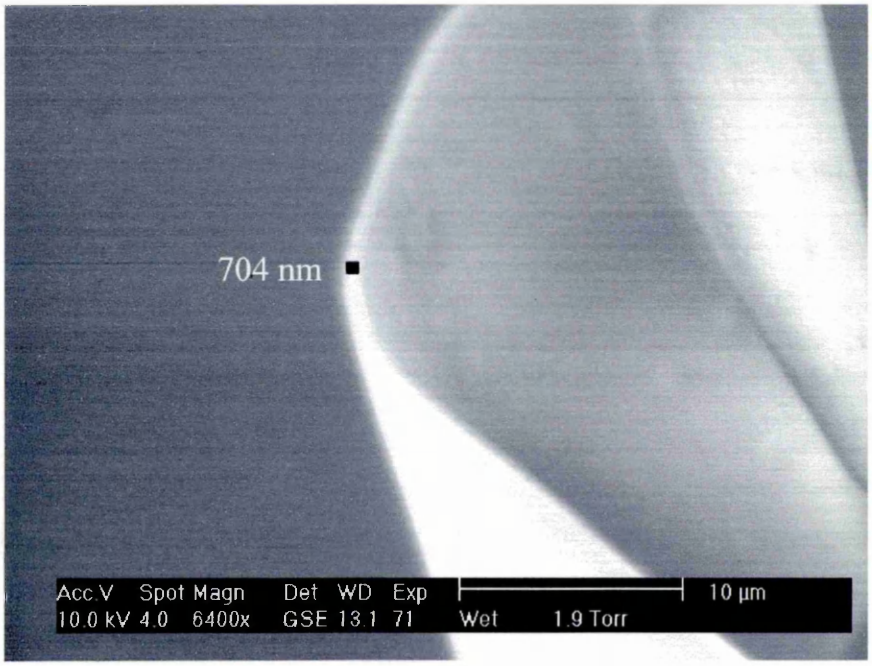

Fig.7.5. A piece of the rolled up xerogel film after 3.0 wt. % aqueous ammonia solutions etching.

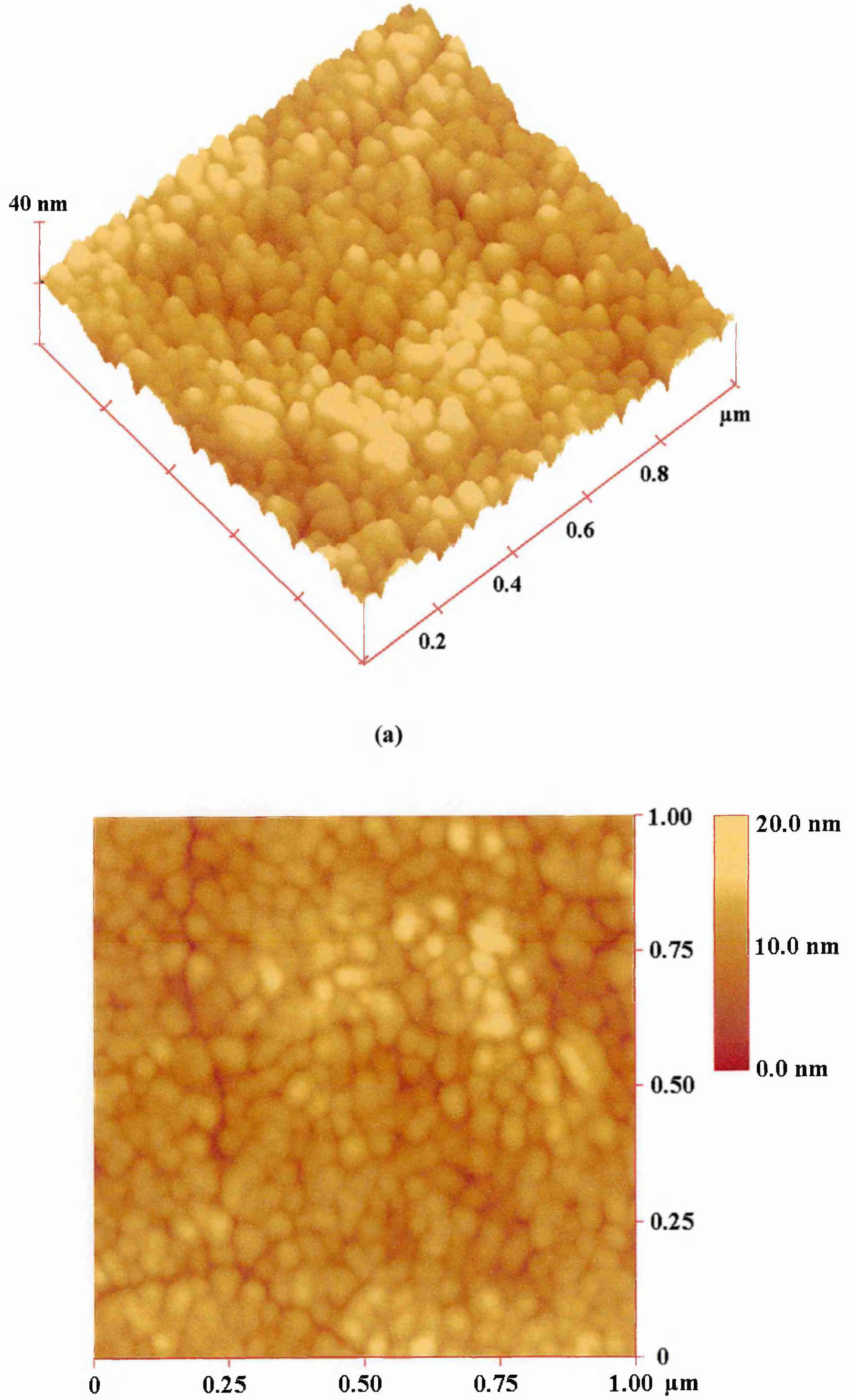

(a)

(b)

Fig.7.6. AFM surface morphologies of sample TFL7-GP3.

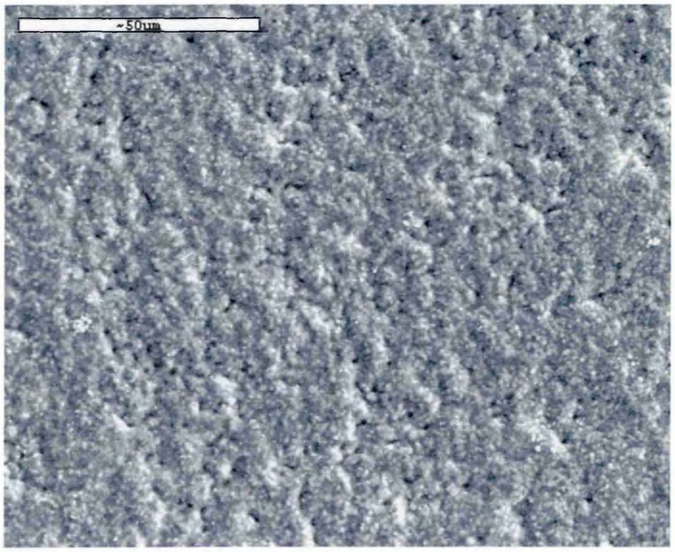

Fig.7.7. A typical surface morphology of the composite thick coatings.

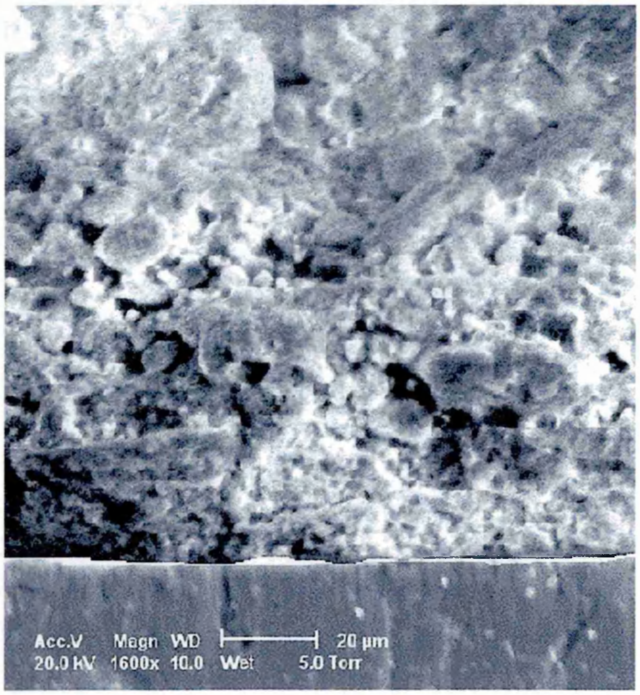

Fig.7.8. A cross-section structure of the composite thick coatings.

VI.2.1.2 Morphologies of Mo:YbAG and YAG composite thick coatings

Figure 7.7 presents a typical scanning electron micrograph of the composite thick coating. It shows agglomerated particles with a porous structure. Particles on the top surface can still be seen in the image. The porous structure could be helpful in lowering the thermal conductivity caused by the radiative contribution at the very high temperature if this coating is used as a thermal barrier coating (TBC).

Figure 7.8 shows a cross section structure of the thick composite coating on Ni superalloys. The sample was heated at 750^0C. The thick coating was prepared 5 times by dip-coating methods using Mo doped YbAG sol and YAG powders. Some layers are seen in Figure 7.8, which were possibly caused by the multicoating process. The diameter of the packed YAG powders is about 1 micron. The thickness of coating is about 80 μm. The density of thick coatings can be improved by packing the nano-size aluminium garnet powders into the sol.

Thick coatings of the composite alumina garnets are prepared on the superalloys by the sol-gel method. This suggests that we could manufacture thermal barrier coatings using sol-gel methods. The sol-gel method offers us a lot of advantages such as low-cost and simple equipment. An anticipated novel thermal barrier coating of rare earth aluminium garnets could be the Mo doped YbAG or YAG.

VII. 2.2 Applications of Mo: YbAG

VII.2.2.1 Potentiodynamic evaluation of thin films with the 10 at. % Mo:YbAG composition

The polarization behaviour of the bare and the coated 304 stainless steel substrates was studied. The polarization curves of the sol-gel coated 304 stainless steel substrate and the bare substrate are compared in Figure 7.9. The film composition is the 10 at. % Mo doped YbAG which was heat-treated at 600^0C and 750^0C, separately. There are two coated samples; TFL7-GP5-a (600^0C calcination) and TFL7-GP5-b (750^0C calcination). Sample TFL7-GP5-a is an amorphous film. The surface morphology was shown in Figure 7.2. Sample TFL7-GP5-b is a crystallised YbAG film. Its surface microstructure was shown in Figure 7.3. Sample ST is the bare 304 stainless steel substrate.

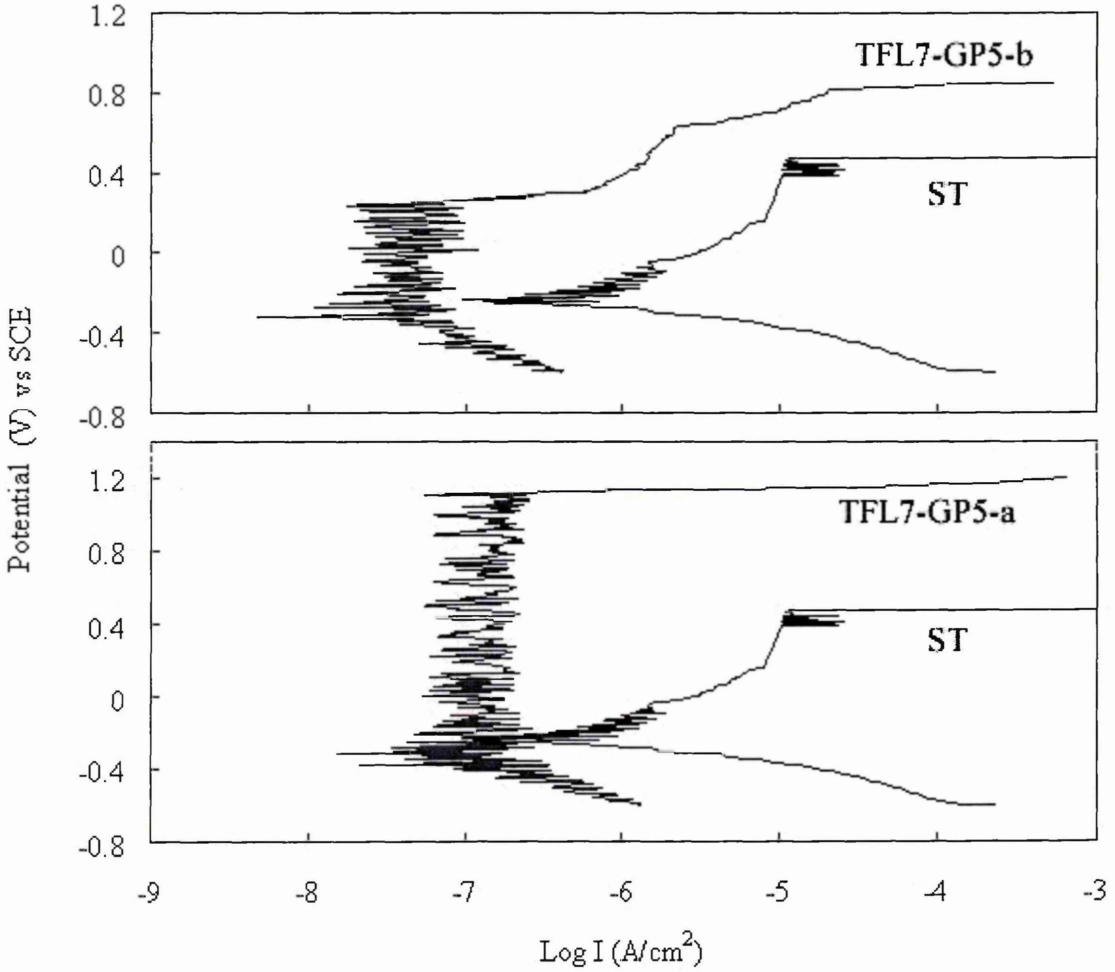

Fig.7.9. Polarisation curves of the bare and the coated 304 stainless steel substrates with the 10% Mo doped YbAG film composition.

A passive region with a low passivation current density of ~ 1 x 10^{-7} A/cm^2 was present in the polarization behaviour of the coated sample TFL7-GP5-a, which implies that the sol-gel coating indeed provided a physical barrier for blocking the electrochemical process. Such a barrier would fail only at a very high electric potential of ~ 1100 mV.

For the coated TFL7-GP5-b, a similar passive region was observed, as evidenced by the very low constant current density of ~ 3 X 10^{-8} A/cm^2 with increasing electrical potential. With this rather low passivation current density, the sol-gel coating resembled a physical barrier for inhibiting the corrosion process. However, this type of barrier would break down at an electric potential of ~ 300 mV. A further increase in the electric potential increased the current density quickly, indicating an active electrochemical reaction. The increase in current density slowed down at a current density of ~ 5.75 X 10^{-7} A/cm^2, indicating the possible formation of a second passive layer. Further increase in electric potential resulted in a rapid increase in the current density.

The bare stainless steel substrate exhibited a significantly different potentio-dynamic polarisation curve. An increase in the electric potential leads to the current density increase. The increase in current density slowed down at a current density of ~ 1 X 10^{-5} A/cm^2, indicating the formation of a passive layer. Further increase in electric potential resulted in a rapid increase in the current density. No obvious secondary passive regions were found.

The polarisation curves of the sol-gel coated substrates were appreciably different from that of the bare stainless steel substrates indicating that the coating had an effect on the corrosion behaviour. The open circuit potential, E_{oc}, of the coated substrates was significantly lower than that of the bare stainless steel. In addition, a distinct passive region was present for the coated substrates, whereas no definitive passive region was found for the bare stainless steel substrates. Furthermore, the samples TFL7-GP5-a and TFL7-GP5-b present a different passive region and passivation current density. The passivation current density of the sample TFL7-GP5-b is smaller than that of sample TFL7-GP5-a but it presents a much lower electric potential of ~ 300 mV for the breakdown of the passive region. Rapid corrosion then occurred. With a further increase in electric potential, the sample TFL7-GP5-b behaves like the uncoated stainless steel substrate. Sample TFL7-GP5-a has a greater passivation current density but presents a much higher electric potential of ~ 1100 mV for the breakdown of its passive region.

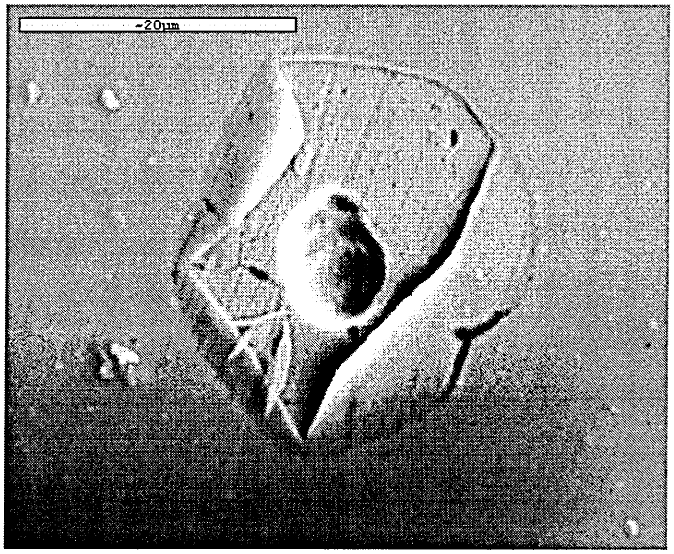

Fig.7.10. SEM images of a pit corrosion on the surface of sample TFL7-GP5-a.

After the electrochemical tests, the samples were carefully analysed by SEM. In sample TFL7-GP5-a, a single pit from the electrochemical reaction on the surface was found. It is this single pit that caused the failure of the coating as shown in Figure 7.10. It is well known that small pores exist in the sol-gel coatings. The diameter of these pores depends on the sol-gel processing. Such pores may be controlled below several nanometers or they could be of a micron scale. The electrochemical test has confirmed the coating as an effective barrier against electrolytic corrosion, and hence these pores must be assumed to be closed and not interconnected. However, the thin film may have some microscopic defects that formed during the sol-gel processing, which allow corrosive ions, such as chloride anions, be able to diffuse through these microscopic pores at the high electric potential and react electrochemically with the metal at the interface between the coating and substrate. This type of reaction led to the breakdown of the coating.

For sample TFL7-GP5-b, no distinctive changes on the surface morphology were found after the electrochemical test. YbAG garnet exhibits good corrosion resistance. It presents a rather low passivation current density in the initial passive region. However, this passive region failed only at a low electric potential. It is clear that the corrosive ions pass through the thin film resulting in attack at the interface between the coating and substrate, which causes the failure of the coating. We have seen in Figure 7.3 that the thin film has broken up but some parts in the thin film were still interconnected. This contributes to the breakdown of the coating at a low electric potential. However, its low open circuit potential still confirms that the YbAG garnet film is a very good corrosion resistance material. To overcome the break-up is the key to enabling this coating to be used on the surface of the stainless steels to protect them from corrosion and wear. Hence, a sublayer coating may be necessary to eliminate the mismatch of the thermal expansion coefficient.

VII.2.2.2 Thermal conductivity of Mo: YbAG garnets

YAG garnets have been reported to be potentially a new-generation of thermal barrier materials [4] [5] because of their low oxygen diffusivity. However, the thermal conductivity of YAG is still a greater than YSZ (YAG=3.2 and YSZ=2.7 W/m.K at 1000°C). Weak binding, large atomic masses, and structural complexity (the number of atoms in one cell) all tend to reduce the intrinsic conductivity. This is why the rare earth alumina garnet has a very low intrinsic conductivity. However, the conductivity is also influenced by lattice defects and grain boundaries. Y_2O_3 doped ZrO_2 (YSZ) is currently the state of the art TBC material and doped Y_2O_3 not only stabilises the cubic phase of ZrO_2 but also greatly affects the thermal conductivity of ZrO_2 by causing point defects; i.e. the solute cations and oxygen vacancies. However, the oxygen diffusivity in YSZ is high due to the oxygen vacancies and leads to the pre-failure of TBCs due to oxygen diffusing to the bonding interface and oxidizing it.

In Chapter VI, we have discussed the possible states of Mo (VI) doped into YbAG garnets. One possibility is that Mo cations substitute for Yb cations which will produce another cation vacancy in the structure. The solute cations and the cation vacancies will further lower the thermal conductivity of the doped aluminium garnets. However, the oxygen diffusivity of Mo:YbAG or Mo doped other rare earth alumina garnets does not increase. Thus, Mo:YbAG or Mo doped other rare earth alumina garnets are potentially promising thermal barrier materials. If Mo (VI) species are dispersed as a monolayer on the surface of the YbAG or incorporated into surface vacant sites of the YbAG, Mo:YbAG has still a low thermal conductivity because of the structural complexity and the low thermal conductivity of MoO_3. In this circumstance,

MoO_3 supported by YbAG garnets is also a promising catalyst.

VII.3 Summary

The morphologies of the thin film of Mo:YbAG and the composite thick coating of Mo:YbAG and YAG have been studied. The xerogel thin film on stainless steel exhibited a porous surface which became dense after being heated at 600^0C. However, the thin film was seen to break up after being annealed at 750^0C. It has been shown that the thin film transformed into the garnet structure, which leads to a large mismatch of the thermal expansion coefficient between the thin film and the substrate. The electrochemical polarisation test showed that the YbAG coating is good corrosion resistance coating but it is necessary to solve the problem of cracking.

Mo:YbAG has a low thermal conductivity and could be a future thermal barrier coating. Sol-gel techniques have been used to produce the 80 μm thick composite coating of Mo:YbAG and YAG. The morphologies of the thick coating show the density of the coating is not very high because the size of the added YAG powders is about 1 μm. However, the density of the composite coating will be improved if nanosize rare earth alumina garnets are used for packing.

Chapter VIII

Synthesis of Yb-doped YAG

VIII.1 Introduction

As we highlighted in Chapter I, Yb doped YAG has become one of the most important microchip laser materials and potential scintillators for neutrino detection in recent years. Synthesis of the high quality single crystal by the Czochralski [6] method is very sluggish, expensive, and difficult. However, the development of nanoceramic techniques recently has made it possible to produce high quality transparent ceramics, which can be less expensive and allow mass production among other advantages. High quality transparent ceramics have shown the potential to achieve the same quality laser as with the single crystals [9]. In this chapter, the nanosize Yb doped YAG produced by sol-gel methods are described. To the best of our knowledge, we are the first to manufacture the Yb:YAG using sol-gel techniques. The properties of Yb doped YAG used as laser and scintillator materials with the doping concentration from 1 to 100% are being widely studied [11] [14] [17] [95] [157] by many other researchers. However, the optical properties of Yb:YAG materials are significantly affected with the increase of the doped Yb^{3+} concentration in Yb:YAG due to the crystal lattice deformation and the change of the lattice constant. This is attributed to the change of the phonon vibration modes. These properties are important to the design of the laser devices. However, very little research about these properties has been published. In this chapter, Yb doped YAG with the doping concentration from 10 to 100 at. % have been produced and the crystallisation kinetics and structural changes have been studied.

VIII.2 Results

VIII.2.1 Crystalline structure conversion of Yb doped YAG

VIII.2.1.1 Yb doped YAG nanosize powders

The procedure of producing the Yb doped YAG powders with typical doping concentrations 10%, 20%, 50%, and 100 at. % respectively has been described in Chapter III. Their XRD patterns are shown in Figure 8.1a, b, c, and d. In Figure 8.1, pattern "i" is the sample at 800^0C 3 hours heat treatment; pattern "ii" is the sample at 850^0C 11 hours heat treatment. The labeled peak "S" belongs to the aluminium holder. All four samples annealed at 800^0C show a very similar structure to that of the rapidly quenched (at approximately 250^0C/s) YAG powders studied by B.R. Johnson et al. [127] from a melting temperature 2200^0C; i.e. the powders were found to be amorphous, with small crystallites whose size was in the nanoscale. Garnet phases were fully crystallised after being heated at 850^0C for 10 ~12 hours. Traditionally, a high synthesis temperature of up to 1600^0C is required by solid state sintering methods. An unidentified peak at $2\ \theta \approx 16.9^0$ in XRD patterns was sometimes found in the initial crystallisation process but this peak disappeared after further heating. The largest peak was located at $2\theta \approx 33.4^0$. The relative intensity of the peak at $2\theta \approx 18^0$ is about 20%. Apparent structural changes can be seen in Figure 8.1 by comparing the patterns. Typically, the relative intensities of two peaks at about 27.8^0 and 29.6^0 are seen. The change is dependent on the doped Yb^{3+} molar ratio from 10% and 20% to 50% and then 100%.

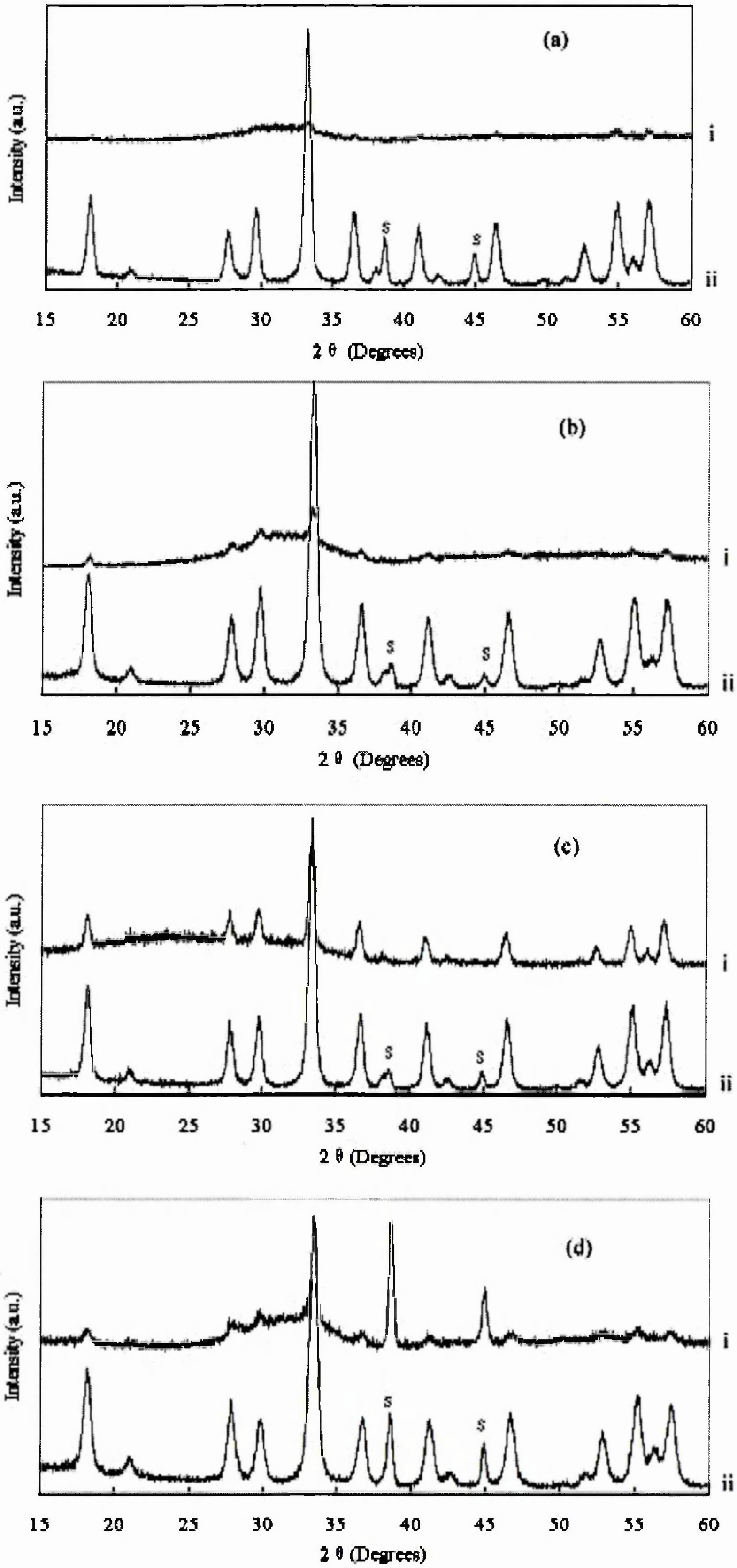

Fig8.1. XRD patterns of Yb:YAG powders; (a) 10%; (b) 20%; (c) 50%; (d) 100%.

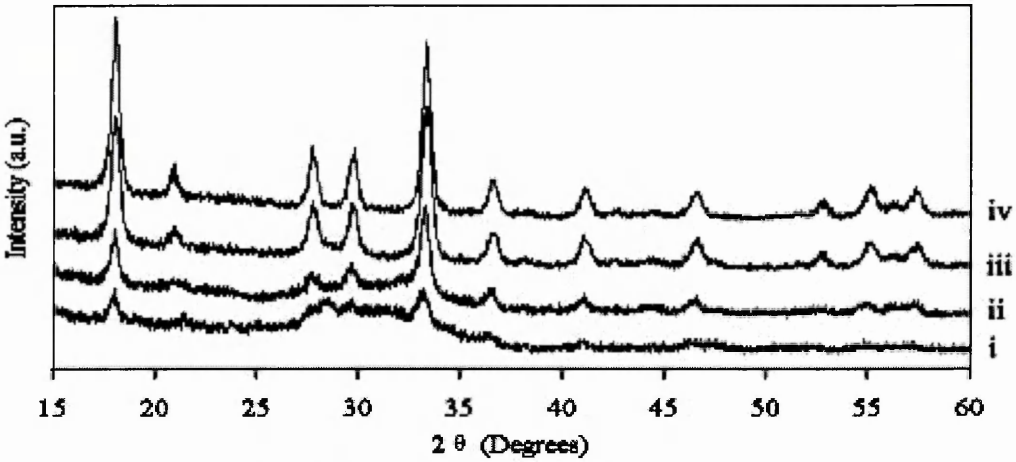

(a). i: 1h; ii: 3 h; iii: 8 h; iv: 23h.

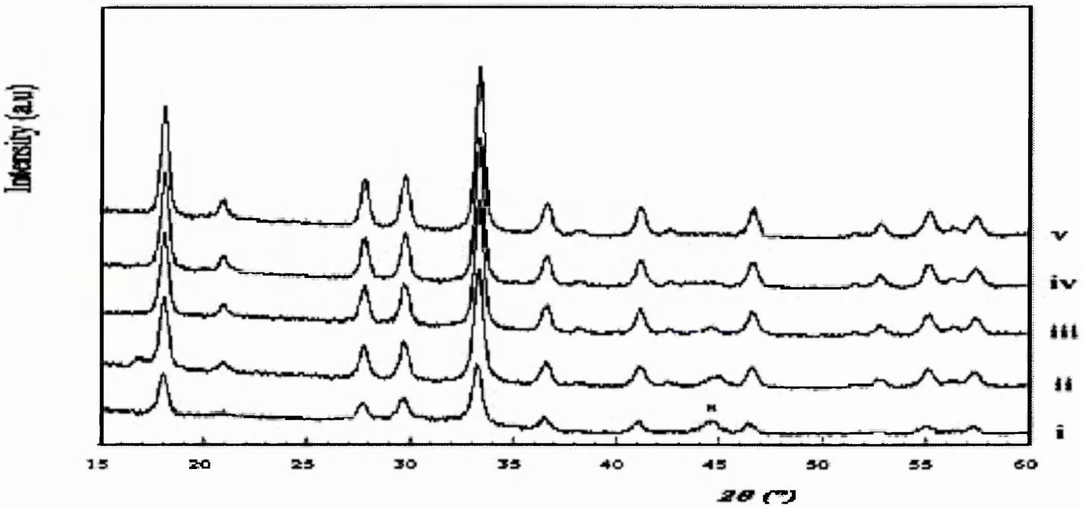

(b). i: 5 mins; ii: 0.5 h; iii: 3 h; iv: 8 h; v: 16 h.

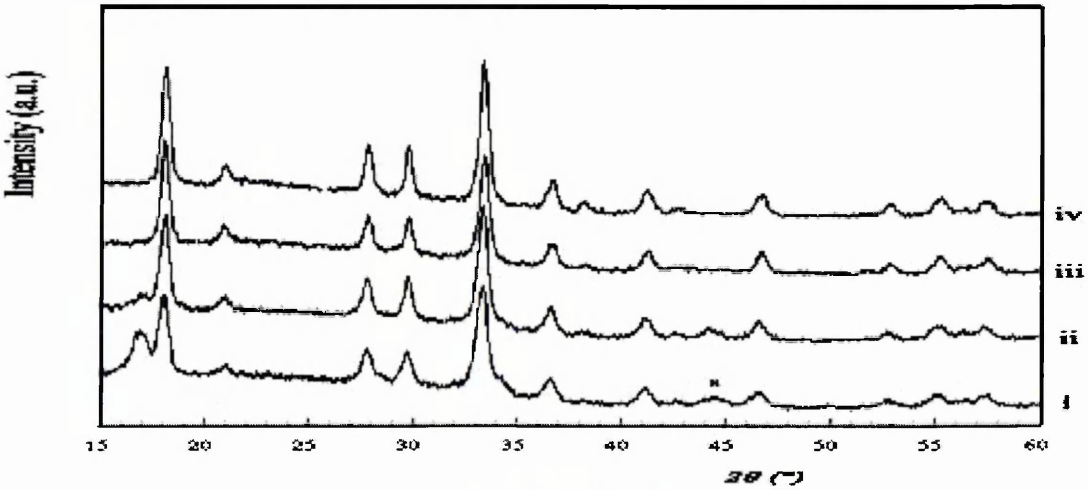

(c). i: 5 mins; ii: 0.5 h; iii:3 h; iv: 16 h.

Fig.8.2. XRD patterns of 100 at. % Yb doped YAG thin films; (a) 850^{0}C; (b) 900^{0}C; (c) 950^{0}C.

The size of the powders was estimated from the Debye-Scherrer formula [182] expressed in Eq.(6.27) and was approximately 60 ~ 80 Å. This size is smaller than was observed by SEM and TEM (see below). The reason for this was attributed to the broadening of the FWHM of peaks because of the microstrain in the particles.

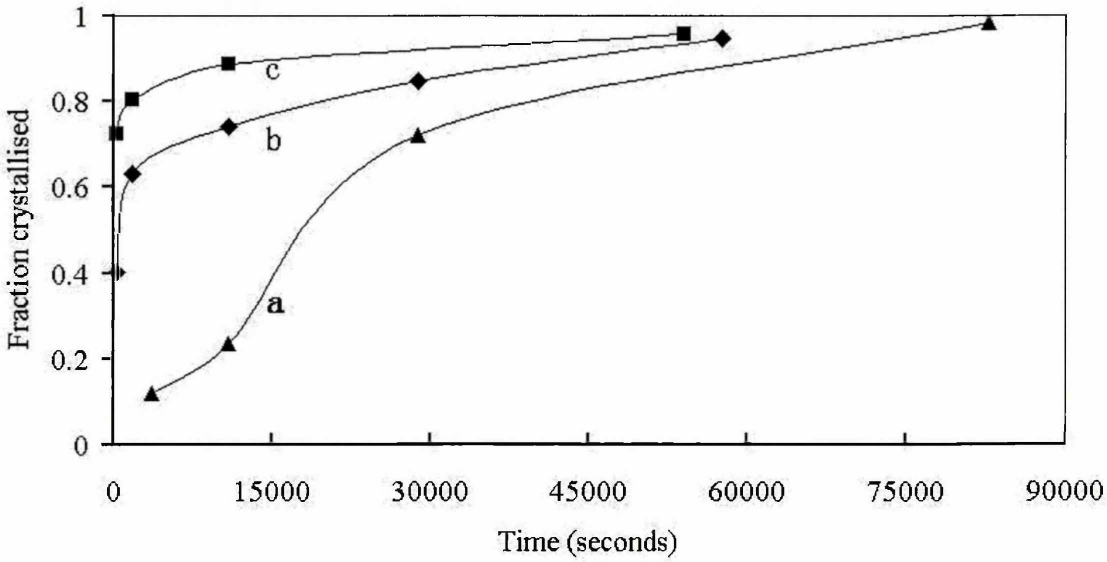

Fig.8.3. The combined plot of the crystallised fraction via the change of time for 100% Yb:YAG thin films. (a) 850^0C; (b) 900^0C; (c) 950^0C.

VIII.2.1.2 Texture growth of Yb doped YAG thin films

Yb doped YAG thin films with the heaviest Yb doping concentration, 100 at. % Yb: doped YAG, were prepared on Si (100) substrates. The crystallisation process was quantitatively analysed by X-ray diffraction under the isothermal conditions. A combined plot of XRD patterns at 850^0C, 900^0C and 950^0C with varying crystallisation times is shown in Figure 8.2a, b, and c, respectively. Only a single phase (garnet) is evident in Figure 8.2. It exhibits the same crystallisation characteristic as the YbAG garnet thin film in Chapter VI. The intensities of all peaks increased with the increase in the calcination time until they reached a saturation level. When the peak intensities of thin film XRD patterns at various heat treatment conditions are compared with that of the powder XRD patterns, e.g. the thin film sample at 850^{0}C for 23 h in Figure 8.2a to that in Figure 8.1, it was found that the crystal growth in thin films exhibits highly preferred orientation growth. The texture maximum is the (211) peak at $2\theta \approx 18^0$, which can be used to represent the amount or degree of thin film crystallisation. After the same method in Chapter VI is used, the combined plot of the crystallised fraction with the change of time and temperature is shown in Figure 8.3 according to the isothermal growth experiments.

VIII.2.2 Morphologies of nanosize Yb doped YAG powders

A scanning electron microstructure of Yb doped YAG powders is shown in Figure 8.4. The morphologies of samples POW9-GP7, POW10-GP7, POW11-GP7, and POW12-GP7 are the same. No difference in morphology was observed with the change in the doped Yb concentration in YAG. It was observed that the particles do not have a very regular shape. They generally exhibited lengthened, rounded, irregular shape. Some particles aggregated but mainly they were still dispersed. The particle size is well distributed and the mean size was about 100 nm.

A bright-field TEM image of the Yb doped YAG is shown in Figure 8.5a. A micro area electron diffraction pattern of a Yb:YAG crystal is shown in Figure 8.5b, correspondingly. The observed shape and the size of particles agree with the results of the scanning electron microscopy. The diffraction patterns in Figure 8.5b characterise the garnet structure. The corresponding crystal plane indexes were all labeled in the picture. The examined axis of the zone is the index $[\bar{2}10]$.

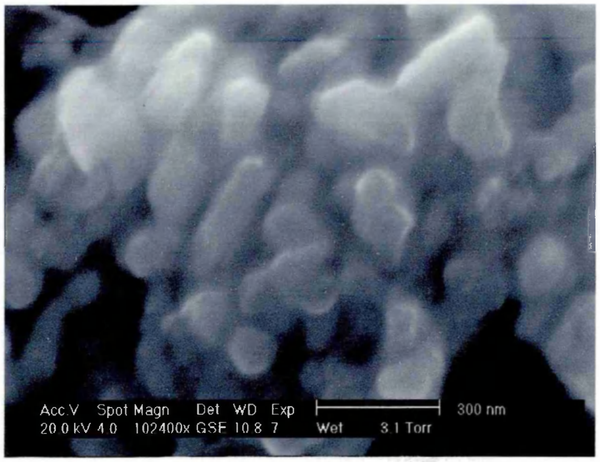

Fig.8.4. A scanning electron image of Yb doped YAG powders.

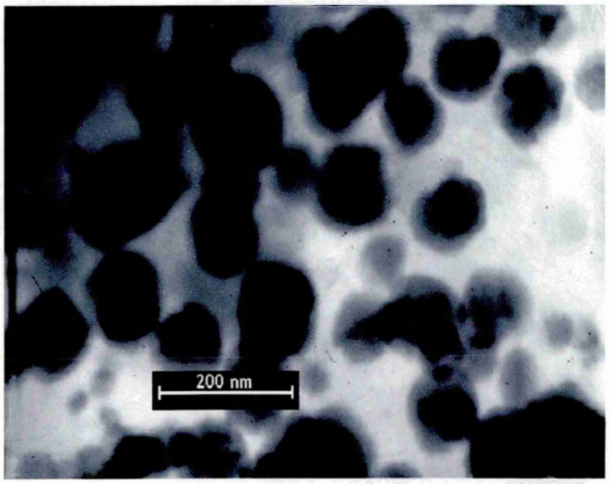

Fig.8.5a. A bright-field transmission electron image of Yb doped YAG powders.

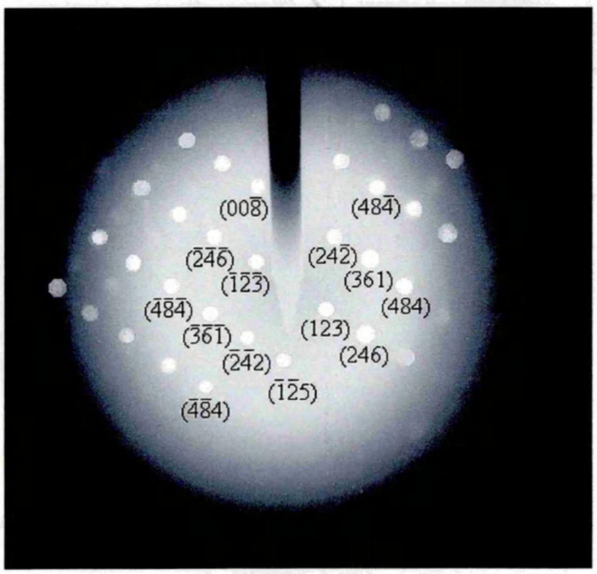

Fig.8.5b. Micro area electron diffraction patterns of 100% Yb:YAG.

VIII.3 Discussion

VIII.3.1 The effect of Yb concentrations on the crystal lattice constant

Yb doped YAG is a new generation laser and scintillator material. The properties of Yb doped YAG are significantly affected by lattice deformation. Thus, the lattice constant change was studied from XRD patterns in Figure 8.1. Because the effective radius of Yb^{3+} (0.86) [26] is smaller than that of Y^{3+} (0.89), it will decrease the crystal lattice constant and lead to the structure deformation after Yb was doped into the host crystal YAG. The maximum peaks (420) of samples POW9-GP7, POW10-GP7, POW11-GP7, and POW12-GP7 at the 2θ angle of 33~34^0 are shown in Figure 8.6. They are $K_{\alpha1}$ X-ray peaks and $K_{\alpha2}$ were stripped from the peaks. The change of the 2θ angle in Figure 8.6 is clearly seen.

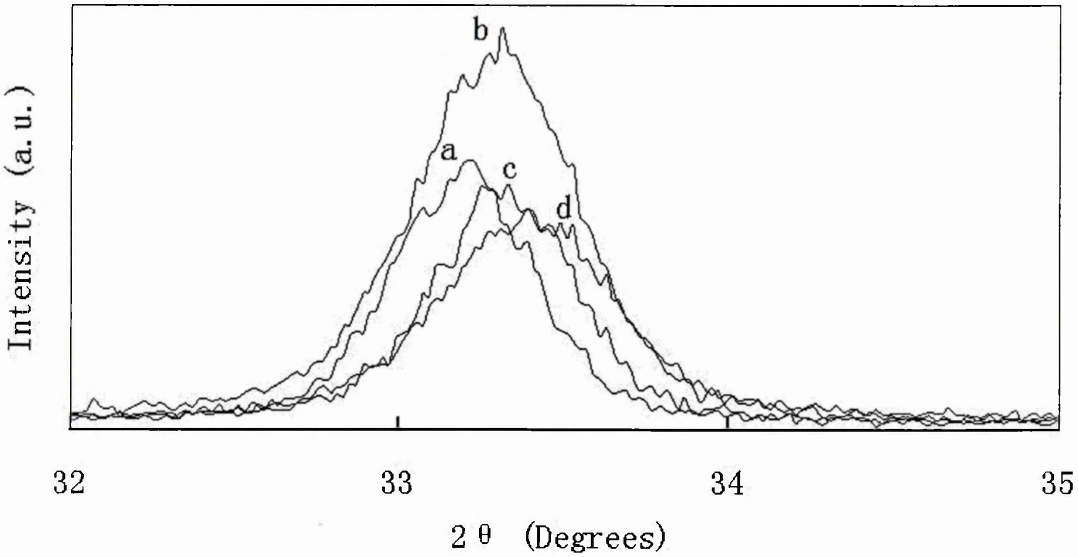

Fig.8.6. The maximum peaks (420) of the Yb doped YAG powders; (a) 10%; (b) 20%; (3) 50%; (d) 100%.

The lattice constants were calculated using Eq (6.7) from the (420) peak position.

They are 12.023Å, 11.991 Å, 11.988 Å, and 11.960 Å for 10%, 20%, 50%, and 100% doped Yb:YAG, respectively. The relationship between the lattice parameter and Yb concentration is shown in Figure 8.7. It does not show a linear relationship. When the Yb doping concentration is below 20%, the lattice constant decreases sharply. There was almost no change of the lattice constant between the doping concentration 20% and 50%. Then, the lattice constant decreases smoothly again with the increase of Yb dopant concentration. Thus, it could be divided into three ranges; i.e. 10 ~ 20%, 20 ~ 50 %, and 50% ~ 100%. Clearly, these changes are dominated by the distribution of the occupied positions of Yb^{3+} in YAG.

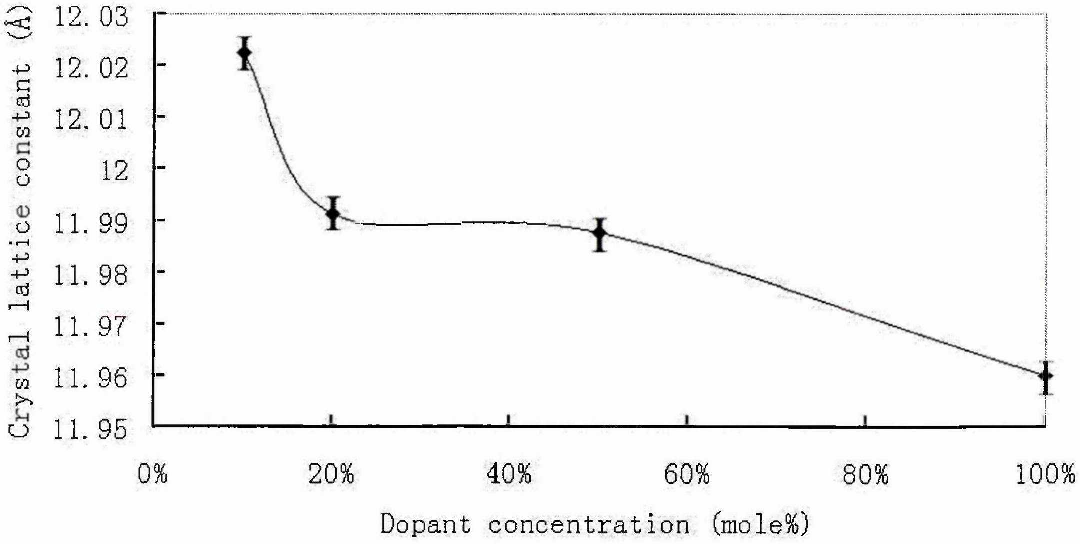

Fig.8.7. The plot of the lattice constant with Yb doping concentrations in YAG.

The fact that the crystal lattice constant decreases with the increase of Yb concentration in YAG is well in agreement with the theoretical prediction. However, the crystal lattice constant of the pure YAG garnet is 12.01 Å [94]. The lattice parameter values of our Yb doped YAG are slightly larger than that it should be. Similar behaviour has

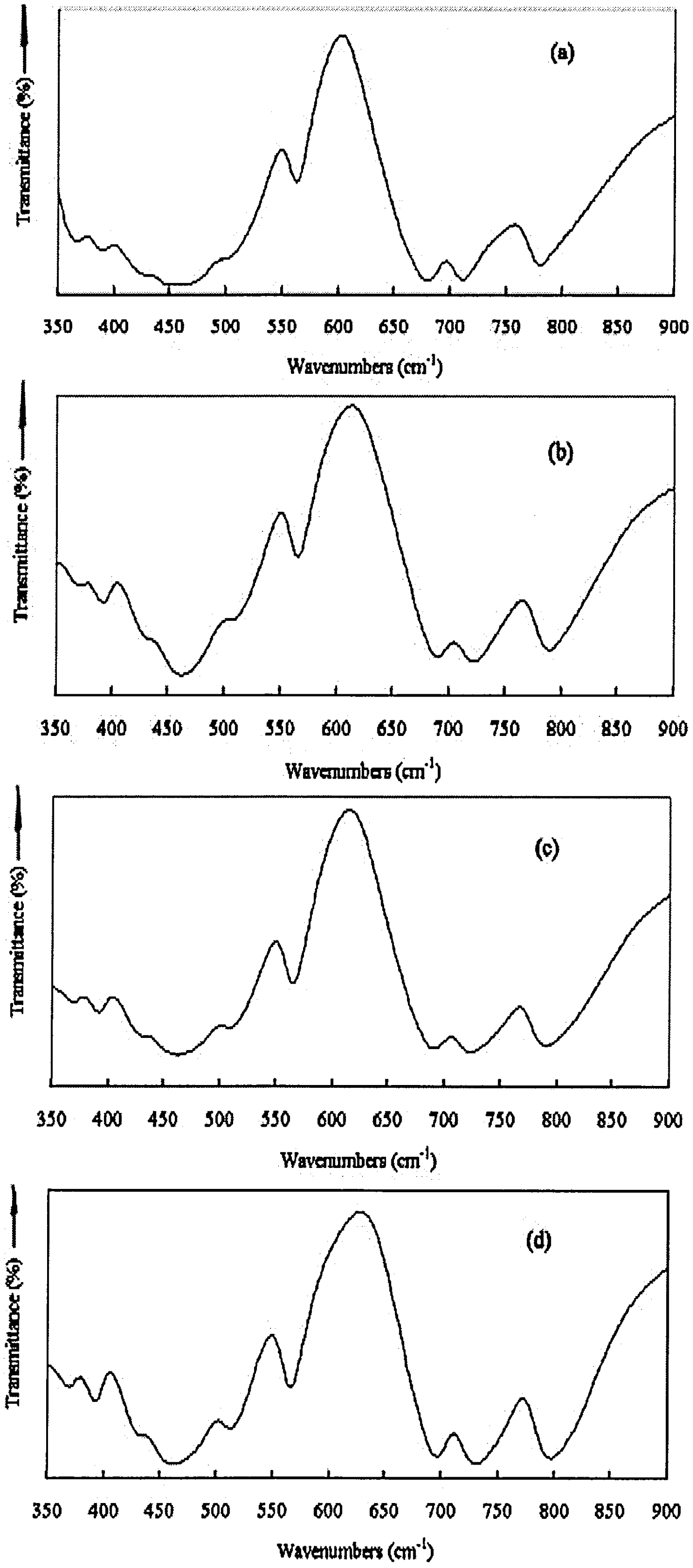

Fig8.8. Infrared spectra of Yb:YAG powders; (a) 10%; (b) 20%; (c) 50%; (d) 100%.

been reported for small particles of the pure YAG or other materials [109] [198-200]. It is said generally that nanoparticles of oxides exhibit a lattice expansion with reduction in particle size while metal particles exhibit a lattice contraction. In oxide particles, the bonds have a directional character and there could exist unpaired electronic orbitals at the outer surface of each particle, which would repulse each other [201]. This contribution from the surface layer increases with decreasing particle size and is attributed to a slightly larger crystal lattice constant than that in the bulk materials.

VIII.3.2 Infrared and Raman spectra

VIII.3.2.1 Infrared spectra of Yb doped YAG powders

Infrared spectra of Yb doped YbAG powders after heating at 850^0C for 11hrs were recorded. Infrared transmittance spectra of samples POW9-GP7, POW10-GP7, POW11-GP7, and POW12-GP7 are shown in Figure 8.8a, b, c, and d. The spectra between 400~200 cm^{-1} were abandoned due to the exited peaks of KBr in this range. They are in good agreement with rare earth aluminium garnets [202]. A comparison of IR spectra of our Yb doped YAG powders with the experimental absorption data of pure YAG powders from ref. [200] is listed in Table 8.1. There were no other phases in the IR spectra apart from ytterbium doped yttrium aluminium garnets (e.g. Y_2O_3, Yb_2O_3, Al_2O_3, or $YAlO_3$). When the vibrational peaks listed in Table 8.1 are compared, we can see that the peak at ~ 566 cm^{-1} is relatively stable and other peaks shift according to the doped Yb concentration in YAG matrix. The similar changes were found in Chapter VI for the pure and Mo doped YbAG. This confirms that Yb cations are statistically well dispersed in the YAG lattice. Furthermore in Figure 8.8, the

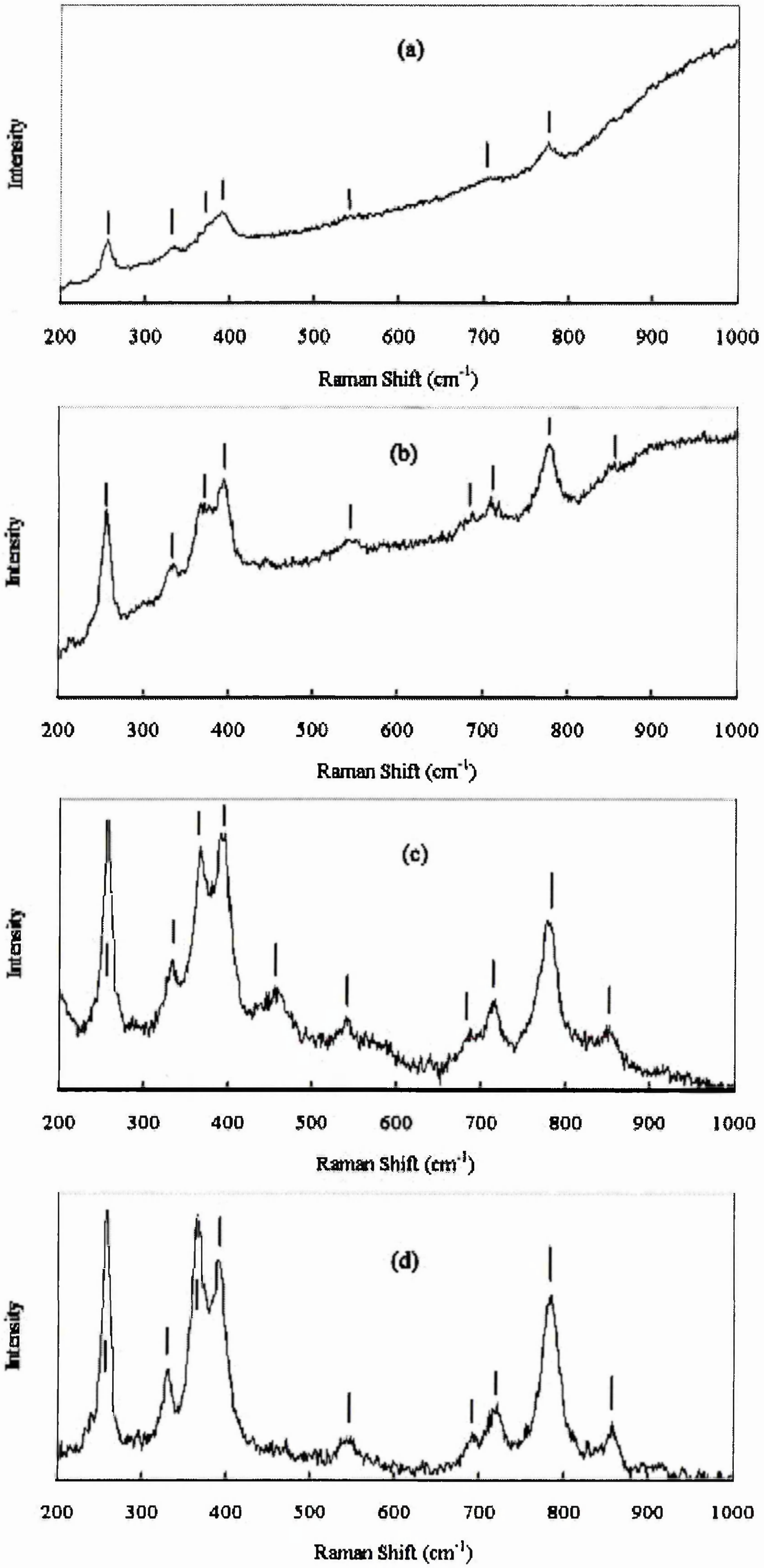

Fig8.9. Raman spectra of Yb:YAG powders; (a) 10%; (b) 20%; (c) 50%; (d) 100%.

wavenumber shift value is very small or no change between 20% and 50% Yb doped YAG garnets (e.g. 790 ~ 790 cm^{-1}, 723 → 725 cm^{-1} and 690 → 692 cm^{-1}). However, the wavenumber change is relatively large from 10 at. % to 20 at. % Yb:YAG and from 50 at. % to 100 at. % Yb:YAG (e.g. 781 → 790 cm^{-1} and 790 → 798 cm^{-1}). This tendency is in agreement with the lattice deformation that was shown in Figure 8.7. Thus, we conclude that the doped Yb^{3+} has caused the crystal deformation but the change does not express a linear relationship with the increase of Yb^{3+} concentration in the YAG matrix.

Table 8.1 Comparison of IR vibrational frequencies of the Yb:YAG and reference YAG powder data.

Yb:YAG (10%)	Yb:YAG (20%)	Yb:YAG (50%)	Yb:YAG (100%)	Reference data [202]
781	790	790	798	794
711	723	725	732	726
680	690	692	698	691
563	566	566	566	567
-	-	-	-	532
501	510	510	513	522
458	462	462	462	463
428	430	430	430	432
390	392	392	392	396

VIII.3.2.2 Raman spectra of Yb doped YAG powders

Raman spectra of Yb doped YbAG powders after being heated at 850^0C for 11 hours were observed. They are shown in Figure 8.9a, b, c, and d. The lines of the observed

Raman active vibrational modes were in the same range of the frequencies when the four samples are compared with each other, which are in good agreement with the experimental and theoretically calculated Raman mode frequencies of YAG or rare earth aluminium garnets [189] [203]. For 10 at. % Yb:YAG particles, 7 Raman active vibrational modes were observed in Figure 8.9a; For 20 at. % Yb:YAG particles, 9 Raman active vibrational modes were found in Figure 8.9b; For 50 at. % Yb:YAG particles, 10 Raman modes were observed in Figure 8.9c; For 100 at. % Yb:YAG particles, 9 Raman modes were seen in Figure 8.9d, which are all indicated by the vertical solid line in the figures. A comparison of Raman vibrational frequencies of the Yb doped YAG powders is listed in Table 8.2. Some frequency changes of the Raman vibrational lines are observed in Figure 8.9. For instance, the frequency of the line in Figure 8.9d at 785 cm^{-1} for 100 at. % Yb:YAG particles becomes 777, 778, and 779 cm^{-1} respectively for the three lower concentrations. The frequency of the line in Figure 8.9a at 391 cm^{-1} for 10% Yb:YAG particles increases to 394 and 393 cm^{-1} at 20 at. % and 50 at. % Yb:YAG powders (in Figure 8.9b and c) and then decreases to 390 cm^{-1} at 100 at. % Yb:YAG powders (in Figure 8.8d). Other Raman vibrational lines also show similar changes. A distinct difference can be observed when comparing the relative intensities of two lines, with frequencies located at 365 and 390 cm^{-1} for the 100 at. % Yb doped YAG. The intensity of the line at about 365 cm^{-1} was smaller than that of the line at ~ 390 cm^{-1} in the former three samples (Figure 8.9a, b and c). However, the intensity of the line at 365 cm^{-1} becomes greater than that of the line at 390 cm^{-1} for the 100 at. % Yb:YAG. Other observed lines in Raman spectra, which can be compared with each other, do not show big changes in the relative intensity. Raman vibrational changes indicate that the doping concentration of Yb in the YAG matrix affects the phonon vibrational modes. But it does not present a linear relationship with the doping concentration. The change of structures is thus confirmed again by the observed Raman spectra. The tendency is in good agreement with that of the crystal lattice constant that was shown in Figure 8.7 and the infrared spectra which are listed in Table 8.1. It explains that the doped Yb^{3+} affects the lattice vibration modes and is related to the doping concentration and the distribution of the occupied sites of Yb^{3+} cations in the host garnet structure.

Table 8.2 Comparison of Raman active vibrational frequencies of the Yb doped YAG powders.

Yb:YAG (10%)	Yb:YAG (20%)	Yb:YAG (50%)	Yb:YAG (100%)
-	850	850	857
777	778	779	785
712	713	714	720
-	688	689	695
541	541	542	548
-	-	459	-
391	394	393	390
372	368	366	365
335	335	333	330
256	257	257	258

The changes in lattice vibrations will influence the interaction between the Yb^{3+} ion and the host YAG. These changes will have some effect on the spectra and the laser performance of Yb:YAG materials when Yb: YAG is used as laser materials.

VIII.3.3 Crystallisation kinetics of the 100% Yb:YAG thin film

The same JMA model and method as that showed in Chapter VI was used to study the crystallisation kinetics of 100% Yb doped YAG garnet films. The combined plot of the crystallised fraction with the change of time and temperature was shown in Figure 8.3.

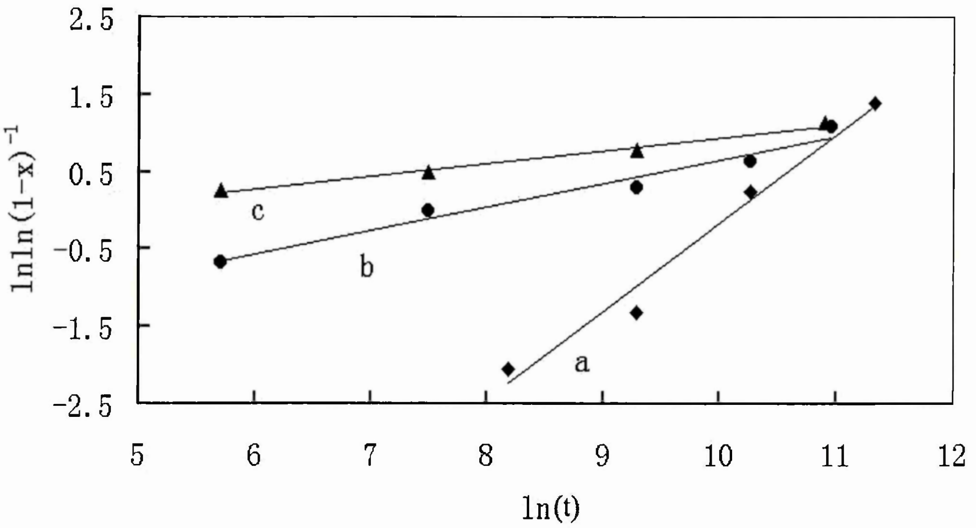

Fig.8.10. The plot of ln [- ln(1- x)] versus ln(t) of 100% Yb:YAG thin films. (a) 850^{0}C; (b) 900^{0}C; (c) 950^{0}C.

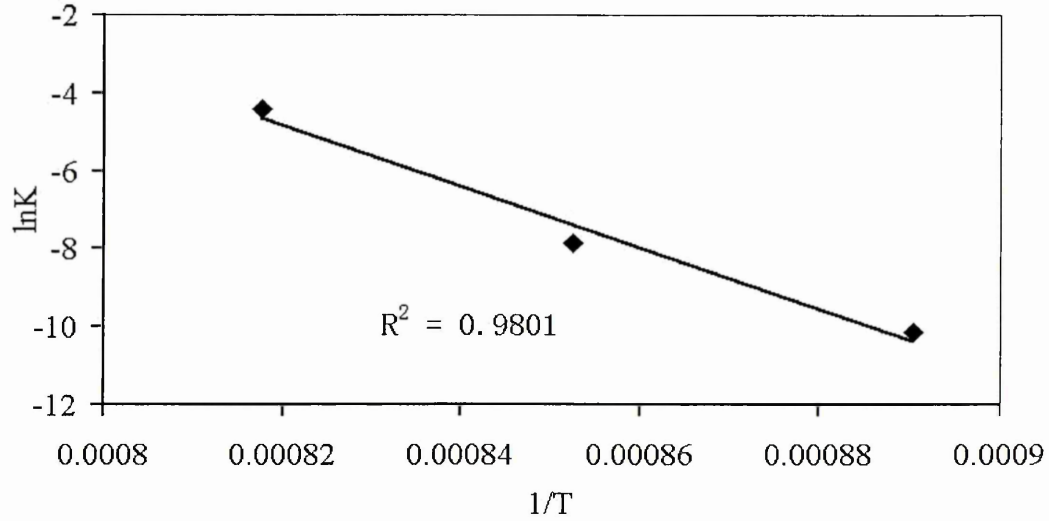

Fig.8-11. The relationship curve of lnk and 1/T for 100% Yb:YAG thin films.

The plot of ln [- ln(1- x)] versus ln(t) for each crystallisation hold temperature according to Eq.(6.16) is shown in Figure 8.10, where x is the crystallised fraction; t is time. We can obtain three rate constants by the three intercepts with the vertical axis of the plots.

Table 8.3 Activation energy and all related parameters for 100% Yb:YAG films

Samples	n	k	k_0	Ea (kJ/mol)
100% Yb	850^{0}C, 1.1428	$3.93 \text{ X } 10^{-5}$	$8.03\text{X}10^{25}$	653±10
doped YAG	900^{0}C, 0.3029	$3.87 \text{ X}10^{-4}$		
garnet films	950^{0}C, 0.168	$1.23 \text{ X } 10^{-2}$		
	Average: 0.5379			

Using Eq.(6.17), the relationship curve of lnk and 1/T after plotting is shown in Figure 8.11. On the basis of the experimental results, the effective activation energy of crystallisation in the thin films was calculated as 653±10 kJ/mol. Other parameters such as the Avrami exponent n and the reaction rate k are all tabulated in Table 8.3. The average exponent n calculated from 100% Yb doped YAG thin films is 0.5379 and this indicates that the crystal growth dominates. However, the three values of the exponents are widely spread. In particular, the exponent value n is 1.1428 (greater than 1) at 850^{0}C. This suggests that the mechanism of crystallisation at this temperature could be nucleation together with the crystal growth limitation. In other words, if the sample is heat-treated at a relatively low temperature (e.g. $\leq$ 850^{0}C), the process of crystallisation is controlled by nucleation and the crystal growth. If it is heated at a higher temperature than at 850^{0}C, overcoming the nucleation barrier becomes easier and the process of crystallisation is dominating the crystal growth.

The calculated activation energy of 100% Yb doped YAG thin films is twice that of the pure YbAG films and three times higher than that of Mo doped YbAG. It indicates that 100% Yb doped YAG has a higher crystallisation barrier than that of YbAG. This is in agreement with the results described in Chapter II. The transition temperature of YAG by sol-gel methods generally is about 900 ~ 1000^{0}C. Thus, this suggests that the YbAG garnet is easier to crystallise than the YAG produced by sol-gel methods.

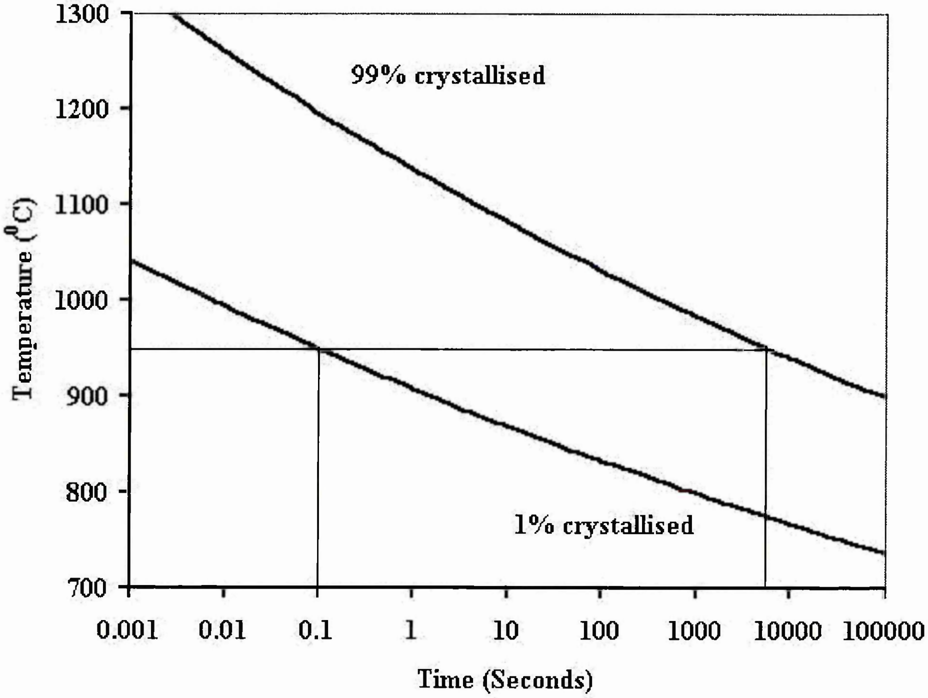

Fig.8.12. T-T-T diagram of 100% Yb doped YAG thin films.

The 3T diagram of 100% Yb doped YAG thin films was obtained and is shown in Figure 8.12. When the fraction crystallised is equal to 1% using Eq(6.18), it will be as follows:

$$T(^0C) = \frac{80319}{\ln(t) + 68} - 273 \qquad (8.1)$$

When the fraction crystallised is equal to 99%, Eq(6.18) will be as follows:

$$T(^0C) = \frac{80319}{\ln(t)+57} - 273 \tag{8.2}$$

The 3T diagram can be used to control the crystallisation process and the microstructures when Yb:YAG garnets are produced by sol-gel techniques.

VIII.4 Summary

To the best of our knowledge, we are the first time to produce Yb doped YAG thin films and nanosize powders by the sol-gel method. Four samples of Yb:YAG nanosize powders from 10% to 100% doping concentrations were synthesized by our sol-gel techniques. The doped Yb^{3+} cations lead to the crystal lattice deformation and phonon vibrational changes of the solid solution rare earth aluminium garnet crystals. The changes could be divided into three ranges according to the doped Yb^{3+} mole concentration (i.e. 0 ~ 20%, 20 ~ 50 %, and 50% ~ 100 at. %). This result is very important in order to understand the properties of Yb:YAG materials when they are used in optics such as laser crystals or scintillators. This could, at least in part, explain why Yb:YAG with about 20 at % dopants generally presents the better laser and scintillation properties that have been studied by many other researchers.

The crystallisation kinetics of 100 at % Yb:YAG thin films have been investigated. The activation energy was calculated as 653±10 kJ/mol, which shows that Yb:YAG garnet has a higher crystallisation barrier than YbAG.

Chapter IX

Conclusions

IX.1 Thesis summary

Yb_2O_3–Al_2O_3 and Y_2O_3–Al_2O_3 systems are very important in industry. YbAG, YbAM, YAG, YAP, and YAM are all very useful materials in many areas. In particular, YbAG and YAG are the most significant of these materials due to their crystal structures. The Y_2O_3 –Al_2O_3 system and rare earth doped YAG has been studied by many authors using sol-gel technologies. In this thesis, the Yb_2O_3 –Al_2O_3 system and rare earth aluminium garnets with ytterbium produced by sol-gel methods have been studied. The sols of the pure and doped Yb_2O_3-Al_2O_3 system and ytterbium doped YAG were successfully prepared. The prepared sols were used to produce thin films, thick coatings, and nano-size powders. This is the first time sol-gel methods have been used in this area. We are the first to synthesize YbAM, YbAG, Mo:YbAG, and Yb:YAG via the sol-gel method. This thesis can be summarised as follows:

IX.1.1 In the Yb_2O_3–Al_2O_3 system, three typical compositions produced by sol-gel methods were studied; i.e. with the mole ratio Yb^{3+}/Al^{3+} = 3:5, Yb^{3+}/Al^{3+} = 2:1, and Yb^{3+}/Al^{3+} =1:1. Sol-gel techniques have successfully produced the sols in the Yb_2O_3-Al_2O_3 system, which can be used to prepare thin films, powders, or other possible applications; e.g. fibers. The structural transformation from gel to polycrystalline was characterised as three stages:

Processes I (below 200^0C): The removal of the absorbed organic solvent or water.

Processes II (between 200^0C and 500^0C): Carbonisation and dehydroxylation.

Processes III (above 500^0C): Transformation from amorphous to crystalline structures. The final phases for the composition of $Yb^{3+}/Al^{3+} = 3:5$, $Yb^{3+}/Al^{3+} = 2:1$, and $Yb^{3+}/Al^{3+} = 1:1$ in the Yb_2O_3–Al_2O_3 system were YbAG, YbAM, and Yb_2O_3 + YbAG, respectively. The crystallisation temperature in the system was significantly affected by doping other elements. In particular, the effects on the Yb_2O_3–Al_2O_3 system were studied when Li^+ and Mo^{6+} cations were doped in them. The chemical analyses by XPS confirmed the existence of Li or Mo in the YbAG garnets. It was found that the doping with Li^+ and Mo^{6+} evidently lowered the crystallisation temperature of the Yb_2O_3–Al_2O_3 system. The mechanism by which doping with Li^+ decreased the crystallisation temperature is likely to be that of promoting the nucleation and crystallisation of c-Yb_2O_3, which further affects the crystallisation of YbAG due to the heterogeneous nucleation. Doping with Mo^{6+} apparently lowered the transition temperature of YbAG by decreasing the activation energy of YbAG crystallisation.

IX.1.2 Thin films of the pure and Mo doped YbAG on various substrates have successfully been produced by the sol-gel method. The YbAG thin film had a maximum texture during the growth process in the orientation of the plane (211). Kinetics studies on the crystallisation process of the pure and Mo doped YbAG have revealed the mechanism of the YbAG thin film crystallisation. It is dominated by crystal growth. The calculated activation energy from the JMA model is 327±10, 217±10, and 212±10 for the pure YbAG, 10 at. %, and 30 at. % Mo doped YbAG, respectively. It is evident that Mo has significantly decreased the activation energy of YbAG crystallisation and it also shows that the concentration of Mo^{6+} does not significantly affect the values of the activation energy. The derived T –T –T diagram of YbAG garnet crystallisation may be useful for controlling the microstructure of amorphous pure and doped YbAG garnet films during crystallisation by sol-gel techniques.

Furthermore, pure and Mo(VI) doped YbAG powders have successfully produced by the sol-gel method. The effect of the crystal lattice constant is linearly dependent on the doped Mo^{6+} concentration. Infrared and Raman spectra have further confirmed the experimental results of single-phase garnet. The infrared characteristic peaks appeared in the samples after 750^0C for Mo doped YbAG powders and after 850^0C heat treatment for the pure YbAG powders. Both Mo doped YbAG or the pure YbAG powders exhibit the single-phase YbAG specta and there were no characteristic peaks belonging to other phases. When the infrared spectra of the pure and Mo doped YbAG were compared, the frequencies of the garnet characteristic peaks changed because of the effect of doped Mo^{6+}. In Raman spectra, the Raman active vibration modes were initially detected in the sample after 600^0C heat treatment. This was considerably lower than the pure YbAG (850^0C). All the observed lines were attributed to the vibration modes in rare earth aluminium garnets. However, a large vibration line in Mo doped YbAG at the frequency of 893 cm^{-1} appeared which did not belong to any other possible phases and thus was very likely caused by the fact of R-site order-disorder in $Mo:Yb_3Al_5O_{12}$ garnets because of the replacement of Yb^{3+} by Mo^{6+}.

The doped Mo in YbAG existed in the six valence state or 6+ oxidation state and was statistically well dispersed in the matrix of YbAG. Two circumstances of Mo(VI) doped in the YbAG garnet matrix are possible. If Mo(VI) species exists as some kind of amorphous phase, then YbAG garnets will be a novel stable support for MoO_3 catalysts. However, it is more likely that Mo^{6+} cations are doped into the YbAG garnet lattice. In this situation, it may result in novel applications of rare earth aluminium garnets.

IX.1.3 The morphologies of the YbAG garnet thin films on stainless steel were observed to change from the xerogel to amorphous phase and then to the polycrystalline. The material presented a porous surface in the xerogel thin film, then a dense amorphous thin film after being heated about 600^0C, and finally the garnet crystalline thin film after 750^0C heat treatment. The thin films consisted of nanograins with the diameter about 50~60 nm by AFM.

IX.1.4 The electrochemical polarisation test showed that the YbAG coating is a very good corrosion resistance coating. The sol-gel coating provided a physical barrier for blocking the electrochemical process. Such a barrier would fail only at a high electric potential. This was 1100 mV for the amorphous film. However, this electric potential was only 300 mV for the Mo doped YbAG polycrystalline. The reason for this is the micro cracking due to the large mismatch of the thermal expansion coefficient between the film and the substrate after the thin film crystallised. Thus, for the use of polycrystalline YbAG garnets on stainless steel, a sublayer may be necessary to eliminate the mismatch of the thermal expansion coefficient between the film and the substrate. The amorphous thin film also presented good corrosion resistance behaviour.

IX.1.5 We prepared the thick composite rare earth aluminium garnet coatings by adding small particles into the sols to decrease the shrinkage. The thick coating was about 80 microns thick. The prepared thick coatings present the possibility of manufacturing novel TBCs by sol-gel methods. Theoretically, Mo doped YbAG will have a very low thermal conductivity and low oxygen diffusivity.

IX.1.6 Nanosize powders and thin films of Yb doped YAG were synthesized by sol-gel methods. Single-phase garnets were obtained directly at significantly lower temperatures than that by the traditional sintering method. Infrared and Raman spectra confirmed the existence of single-phase Yb doped YAG. The garnet structure was also characterised by SEM and TEM. TEM and SEM showed that the nanosize Yb:YAG powders had a generally lengthened, rounded, irregular shape with the mean size about 100 nm.

Yb:YAG has recently been shown to be a promising novel laser material in which the doping Yb concentration is key to obtaining high quality lasers. There is an interaction between the doped Yb^{3+} and the host crystal YAG. The doped Yb^{3+} causes lattice deformation and the change in the phonon vibrations. These changes will affect the laser performance. This research shows that the crystal lattice constant decreased with the increasing concentration of the doped Yb^{3+}, however, the variation of the lattice constant with the doping concentration did not show a linear relationship. The infrared and Raman spectra also confirmed the change of vibrational modes of phonons, which is contributed to the lattice deformation caused by the Yb^{3+} doped in the matrix YAG. The changes in infrared and Raman spectra show the same behaviour as that of the lattice constant. The behaviour could be divided into three ranges according to the doped Yb^{3+} mole concentration (i.e. 0 ~ 20%, 20 ~ 50 %, and 50% ~ 100 at. %). This could, at least in part, explain why about 20 at. % Yb:YAG generally exhibits the better laser and scintillation properties, which have been studied by many other researchers. This result is very useful in designing the laser system when Yb:YAG is used as the laser materials.

The crystallisation kinetics of Yb:YAG were studied by the Avrami model, and the activation energy was 653±10 kJ/mol. This value was twice that of the pure YbAG and three times that of Mo doped YbAG. It indicated that Yb doped YAG had a higher crystallisation barrier than that of YbAG.

IX.2 Future work

The work in this thesis has laid a foundation for future application of these materials based on the Yb_2O_3–Al_2O_3 system, especially rare earth alumina garnets. However, there are several issues that remain to be explored. In the following, some possible areas in which further study is required are discussed.

IX.2.1 Mo doped YbAG garnets

Mo doped YbAG is a novel doped aluminium garnet. The exact sites occupied in the matrix by doped Mo^{6+} cations need to be identified further. NMR may be a useful technique to determine the oxygen environment around Mo^{6+} cations. Furthermore, understanding the basic properties of Mo doped YbAG (such as thermal conductivity, thermal expansion coefficent, electricity conductivity, and so on) is necessary not only for using as TBCs but also in identifying other novel applications.

IX.2.2 Applications of the pure or doped YbAG coatings

YbAG coatings are clearly very useful due to their phase stability, high hardness, good corrosion and oxidation resistance as well as other properties. The substrates could be ceramics or high-temperature superalloys. A possible research area could be to develop the TBC coating on Ni superalloys. Studying the sublayer between the coating and the substrate would be necessary if it is used as a coating on high-temperature metals.

IX.2.3 Yb doped YAG ceramics

Transparent Yb doped YAG ceramics could be achieved using nanosize powders. One of the most important future directions is to study the technique of producing the transparent Yb:YAG ceramics. These materials will have widespread applications as laser optical materials or scintillators.

References

[1] **B.E. Yoldas,** *J. Mater. Sci.* 10, 1975, p1856-1860.

[2] **B.E. Yoldas,** *J. Mater. Sci.* 12, 1977, p1203-1208.

[3] **L. Klein, C. Sanchez,** *Sol-gel Sci. Technol* (Special Issue) 7, 1996, p151-224.

[4] **P. Nitin, P.G. Klemens,** *J. Am. Ceram. Soc.* 80, 1997, p1018~1020.

[5] **P.G. Klemens, M. Gell,** *Mater. Sci. & Eng.* A245, 1998, p143~149.

[6] **J. Kvapil et al.,** *J. Cryst. Growth* 52, 1981, p542.

[7] **T. Tachiwaki, M. Yoshinaka, K. Hirota, T. Ikegami, O. Yamaguchi,** *Solid State Communications* 119, 2001, p603-606.

[8] **D. Hreniak, W. Strek,** *Journal of Alloys and Compounds* 341, 2002, p183~186.

[9] **J.R. Lu, K. Uede, H. Yagi, T. Yanagitani, Y. Akiyama, A.A. Kaminskii,** *J. of Alloys and Compounds* 341, 2002, p220-225.

[10] **A. Ikesue,** *Opt. Mater.* 19, 2002, p183~187.

[11] **N. Guerassimova, N. Garnier, C. Dujardin, A.G. Petrosyan, C. Pédrini,** *Chem. Phys. Letters* 339, 2001, p197~202.

[12] **R. Chipaux, M. Cribier, C. Dujardin, N. Garnier, N. Guerassimova, J. Mallet, J.P. Meyer, C. Pédrini, A.G. Petrosyan,** *Nuc. Instr. and Methods* A 486, 2002, p228~233.

[13] **P. Antonini, S. Belogurov, G. Bressi, G. Garugno, P. Santilli,** *Nuc. Instr. and Methods* A 486, 2002, p220~227.

[14] **P. Antonini, S. Belogurov, G. Bressi, G. Garugno, P. Santilli,** *Nuc. Instr. and Methods* A 488, 2002, p591~603.

[15] **G.J. Spühler, R. Paschotta, M.P. Kullberg, M. Graf, M. Moser, E. Mix, G. Huber, C. Harder, U. Keller,** *Appl. Phys.* B 72, 2001, p285~287.

[16] **J. Saikawa, S. Kurimura, I. Shoji, T. Taira,** *Opt. Mater.* 19, 2002, p169~174.

[17] **M. Mizuno, T. Noguchi,** *Yogyo-Kyokai-Shi* 88, 1980, p322.

[18] **H.M. Wang, M.C. Simmonds, J.M. Rodenburg,** *Mater. Chem. Phys.* 77, 2003, p802-807.

[19] **H.M. Wang and J.M. Rodenburg** "A sol-gel method for growing thick garnet coatings at relatively low-temperature". The international congress Materials Week in Munich, October 2002.

[20] **J.M. Rodenburg and H.M. Wang**, "Molybdenum doped alumina garnets" *UK patent pending* 0315036.4, 2003.

[21] **H.M. Wang, J.M. Rodenburg** et. al., "Synthesis of a novel Mo^{6+} doped YbAG garnet" will be submitted for publishing in 2003.

[22] **H.M. Wang, M.C. Simmonds, Y.Z. Huang, J.M. Rodenburg,** "Synthesis of nano-size powders and thin films of Yb doped YbAG by sol-gel methods". *Chem. Mater.* 15, 2003, p3474-3480.

[23] **J. Livage and M. Henry, and C. Sanchez,** *Progress in Solid State Chemistry* 18, 1988, p259-342.

[24] **J. Livage and M. Henry**, Ultrastructure processing of advanced ceramics, eds.

J.D. Mackenzie and D.R. Ulrich (Wiley, New York, 1988), p183.

[25] **C.K. Jorgensen**, Inorganic Complexes, Academic Press, London, 1963.

[26] **Klein & Hulburt**, Manual of Mineralogy 20th edition, 1985.

[27] **C.F. Baes and R.E. Mesmer**, The Hydrolysis of Cations (Wiley, New York, 1976).

[28] **L.G. Hubert-Pfalzgraf**, *New J. Chem.* 11, 1987, p663.

[29] **B.E. Yoldas**, *Amer. Ceram. Soc. Bull.* 54, 1975, p286-290.

[30] **T. Assih, A. Ayral, M. Abenoza, and J. Phalippou,** *J. Mat. Sci.* 23, 1988, p3326.

[31] **L.F. Nazar and L.C. Klein**, *J. Am. Ceram. Soc.* 71, 1988, C85-C87.

[32] **W.L. Olson**, Better Ceramics Through Chemistry II, Mater. Res. Soc. Symp. Proc. 73, eds. C.J. Brinker, D.E. Clark, and D.R. Ulrich (Mater. Res. Soc., Pittsburgh, Pa., 1986), p611.

[33] **M. Henry, J.P. Jolivet, J. Livage**, *Structure and Bonding* 77, 1992, p153.

[34] **M. Ardon and B. Magyar**, *J. Am. Chem. Soc.* 106, 1984, p3359-3360.

[35] **M. Ardon, A. Bino, and K. Michelson**, *J. Am. Chem. Soc.* 109, 1987, p1986-1990.

[36] **M. Eigen.**, *Pure Appl. Chem.* 6, 1963, p97.

[37] **H. Kruger,** *Chem. Soc. Rev.* 11, 1982, p227.

[38] **R.G. Pearson,** *J. Chem. Educ.* 38,1961, p164.

[39] **H. Stűnzi, L. Spiccia, F.P. Rotzinger, W. Marty**, *Inorg. Chem.* 28, 1989, p66.

[40] **G. Fu, L.F. Nazar,** *Chem. Mater.* 3, 1991, p602.

[41] **G. Sposito**, The Environment Chemistry of Aluminium, CRC press, Boca Raton, 1989.

[42] **R.S. Sapiezsko, R.C. Patel, E. Martijević,** *J. Phy. Chem.* 81, 1977, p1061.

[43] **V. Strahm, R.C. Patel, E. Martijević,** *J. Phys. Chem.* 83, 1979, p1689.

[44] **P.H. Fries, N.R. Jagannathan, F.G. Hering, G.N. Patey,** *J. Phys. Chem.* 91, 1987, p215.

[45] **D.C. Bradley,** *Adv. Chem. Sev.* 23, 1959, p10.

[46] **P.J. Flory,** Principles of Polymer Chemistry (Cornell Univ. Press, Ithaca, New York, 1953) Chapter IX.

[47] **R. Zallen**, The Physics of Amorphous Solids (Wiley, New York, 1983), Chapter IV.

[48] **C. Jeffrey Brinker, George W. Scherer,** Sol-gel Science (Academic Press, San Diego 1990). Chapter V.

[49] **J. Zarzycki, M. Prassas, J. Phalippou,** *J. Mater. Sci.* 17, 1982, p3371-3379.

[50] **A.A. Griffith, Phil.** *Trans. Roy. Soc.* A221, 1920, p163-198.

[51] **B.R. Lawn and T.R. Wilshaw**, Fracture of Brittle Solids (Cambridge Univ. Press, Cambridge, England, 1975).

[52] **H.L. Ewalds and R.J.H. Wanhill,** Fracture Mechanics (Edward Arnold, Victoria, Australia, 1984.)

[53] **G.P. Cherepanov,** Mechanics of Brittle Fracture (McGraw-Hill, New York,

1979).

[54] **L.L. Hench**, Science of Ceramic Chemical Processing, eds., L.L. Hench, D.R. Ulrich (Wiley, New York, 1986) p52.

[55] **H. Schroeder**, Physics of Thin Films, ed. G. Hass (Academic Press, New York, 1969), p87-141.

[56] **H. Dislich**, Sol-gel Technology for Thin Films, Fibers, Preforms, Electronics, and Specialty Shapes, ed. L.C. Klein (Noyes, Park Ridge, N.J., 1988), p50-79.

[57] **S. Sakka, K. Kamiya, K. Makita, and Y. Yamamoto,** *J. Non-Cryst. Solids* 63, 1984, p223-235.

[58] **I. Strawbridge and P.F. James,** *J. Non-Cryst. Solids* 82, 1986, p366-372.

[59] **I. Strawbridge and P.F. James,** *J. Non-Cryst. Solids* 86, 1986, p381-393.

[60] **C.J. Brinker, G.W. Scherer,** Sol-gel Science, Academic Press, San Diego, CA, 1990. Chapter VIII.

[61] **G.W. Scherer**, *J. Non-cryst. Solids* 89, 1987, p217-238.

[62] **A. Bertoluzza, C. Fagnano, M.A. Morelli, V. Gottardi, M. Guglielmi**, *J. Non-cryst. Solids* 48, 1982, p117.

[63] **C.J. Brinker, K.D. Keefer, D.W. Schaefer, C.S. Ashley,** *J. Non-cryst. Solids* 48, 1982, p47.

[64] **M. Yamane, S. Aso, S. Okano, T. Sakaino,** *J. Mat. Sci.* 14, 1979, p607.

[65] **G.W. Scherer**, Relaxation in Glasses and Composites, (Wiley, New York, 1986).

[66] **R.K. Dwivedi, G. Gowda**, *J. Mat. Sci. Lett.* 4, 1985, p331.

[67] **F.W. Dynys, M. Ljungberg, J.W. Halloran**, Better Ceramics Through Chemistry, eds., C.J. Brinker, D.E. Clark, D.R. Ulrich(Elsevier, North-Holland, New York, 1984), p321.

[68] **R.K. Dwivedi, G. Gowda**, *J. Mat. Sci. Lett.* 4, 1985, p331.

[69] **V. Saraswati, G.V.N. Rao**, *J. Mater. Sci.* 22,1987, p2529.

[70] **A.C. Pierre, D.R. Uhlmann**, Better Ceramics Through Chemistry, eds., C.J. Brinker, D.E. Clark, D.R. Ulrich(Elsevier, North-Holland, New York, 1984), p119.

[71] **F.W. Dynys, J.W. Halloran**, Ultrastructure Processing of Ceramic, Glasses, and Composites, eds., L.L. Hench, D.R. Ulrich (Wiley, New York, 1984), p142.

[72] **Y. Yang, A.C. Pierre, D.R. Ulmann**, *J. Non-Cryst. Solids* 100,1988, p371.

[73] **J.W. Christian**, The Theory of the Transformations in Metals and Alloys, part I (Pergamon, New York, 1975), p420-422.

[74] **M. Avrami**, *J. Chem. Phys.* 8, 1940, p212.

[75] **M. Avrami,** *J. Chem. Phys.* 9, 1941, p177.

[76] **A. Marotta, A. Buri, G.L. Valenti,** *J. Mater. Sci.* 13, 1978, p2483.

[77] **J. Livage**, *Catalysis Today* 41, 1998, p3.

[78] **R.M. Barrer,** Hydrothermal Chemistry of Zeolites, Academic Press, London, 1982.

[79] **J. Livage, F. Beteille, C. Roux, M. Chatry and P. Davidson,** *Acta. Mater.* 46, 1998, p743-750.

[80] **D.S. Suhr,T.E. Mitchell and R.J. Keller**, Microstructure and durability of zirconia thermal barrier coatings, Advances in Ceramics, Vol. 3, Ed. A.H. Hueur and L.W. Hobbs, the American Ceramic Society OH 1982, p503-517.

[81] **G. Winter,** *Oil and Colour Chemist's Association* 34, 1953, p30.

[82] **W. Noll,** Chemie and Technologies der Silicone, 2nded, (Verlag Chemie, Weinheim, F.R. Germany, 1968).

[83] **O. Fabrichnaya, H.J. Seifert, T. Ludwig, F. Aldinger, A. Navrotsky,** *Scandinavia J. of Metallurgy* 30, 2001, p175-183.

[84] **J.R. Lo, T.Y. Tseng,** *Mater. Chem. Phy.* 56, 1998, p56-62.

[85] **R.S. Hay,** *J. Mater. Res.* 8, 1993, p578-604.

[86] **O. Yamaguchi, K. Takeoka, and A. Hayashida,** *J. Mater. Sci. Lett.* 10, 1990, p101.

[87] **O. Yamaguchi, K. Takeoka, K. Hirota, H. Takano, and A. Hayashida**, *J. Mater. Sci.* 27, 1992, p1261.

[88] **M. Harada, A. Ue, M. Inoue, X.M. Guo, K. Sakurai,** *Scripta Materialia* 44, 2001, p2243-2246.

[89] **T. Tachiwaki, M. Yoshinaka, K. Hirota, T. Ikegami, O. Yamaguchi,** *Solid State Communications* 119, 2001, p603-606.

[90] **R.P. Rao,** *J. Electrochem. Soc.* 143, 1996, p189.

[91] **N.J. Hess, G.D. Maupin, L.A. Chick, D.S. Sunberg, D.E. McCreedy, and T.R. Armstrong,** *J. Mater. Sci.* 29, 1994, p1873.

[92] **S.L Liu, Q.N. Su,** *Journal of Alloys and Compounds* 255, 1997, p102-105.

[93] **F. Euler and J.A. Bruce**, *Acta Cryst.* 19, 1965, p971.

[94] PCPDFWIN, Version 2.1, JCPDS ICDD International Centre for Diffraction Data, June 2000.

[95] **H.W. Qiu, P.Z. Yang, J. Dong, P.Z. Deng, J. Xu, W. Chen**, *Mater. Lett.* 55, 2002, p1-7.

[96] **N. Gautier, M. Gervais, Landron, D. Massiot, J.P. Coutures,** *Physics Status Solidi A-Applied Research* 165, 1998, p329-336.

[97] **J. Carda, M.A. Tena, G. Monros, V. Esteve, M.M. Reventos, J.M. Amigo**, *Cryst. Res. Tech.* 29, 1994, p387-391.

[98] **D.B. Sirdeshmukh, L. Sirdeshmukh, K.G. Subhadra, K. Kisan Rao, S.B. Laxman,** *Bull. Mater. Sci.* 24, 2001, p469~473.

[99] **K.G. Subhadra, K. Kisan Rao, D.B. Sirdeshmukh,** *Bull. Mater. Sci.* 23, 2000, p147.

[100] **T. Thirmal Rao, D.B. Sirdeshmukh**, *Cryst. Res. Technol.* 26, 1991, k53.

[101] **D.B. Sirdeshmukh, K.G. Subhadra, K. Kisan Rao, T. Thirmal Rao**, *Cryst. Res. Technol.* 30, 1995, 861.

[102] **G. Bayer,** *Proc. Br. Ceram. Soc.* 22, 1973, p39~53.

[103] **D. Ehrentraut**, *J. Crys. Growth* 242, 2002, p375~382.

[104] **I. Sakaguchi, H. Haneda, J. Tanaka, T. Yanagitani,** *J. Am. Ceram. Soc.* 79, 1996, p1627~32.

[105] **R. Manalnert, M.N. Rahaman,** *J. Mater. Sci.* 31, 1996, p3453~3458.

[106] **C.D. Veitch,** *J. Mater. Sci.* 26, 1991, p6527.

[107] **Y. Liu, Z.F. Zhang, B. King, J. Halloran, and R.M. Laine,** *J. Am. Ceram. Soc.* 79, 1996, p385.

[108] **M.H. Nguyen, S.J. Lee, W.M. Kriven,** *J. Mater. Res.* 14, 1999, p3417.

[109] **P. Vaqueiro, M.A. López-Quintela,** *J. Mater. Chem.* 8, 1998, p161~163.

[110] **S.H. Zhou, S.Y. Zhang, J.J. Zhang, W.G. Peng,** *Chem. J. of Chinese Universities - Chinese* 19, 1998, p1826-1828.

[111] **S.K. Ruan, J.G. Zhou, A.M. Zhong et al.**, *Journal of Alloys and Compounds*, 277, 1998, p72-75.

[112] **H.C. Jiang, S.Q. Yang, et al.**, *J. Inorg. Mater.* 16, 2001, p720-722.

[113] **C.H. Lu, R. Jagannathan,** *Appl. Phys. Lett.* 80, 2002, p3608-3610.

[114] **Y.H. Zhou, J. Lin, S.B. Wang, H.J. Zhang,** *Mater. Lett.* 56, 2002, p628-636.

[115] **J.Y. Choe, D. Ravichandran, S.M. Blomquist, K.W. Kirchner, E.W. Forsythe, D.C. Morton,** *J. of Luminescence* 93, 2001, p119~128.

[116] **D. Ravichandran, R. Roy, A.G. Chakhovskoi, C.E. Hunt, W.B. White, S. Erdei,** *J. of Luminescence* 71, 1997, p291~297.

[117] **D. Hreniak, W. Strek,** *Journal of Alloys and Compounds* 341, 2002, p183-186.

[118] **J.R. Lo and T.Y. Tseng,** *Mater. Chem. Phys.*, 57, 1998, p95-98.

[119] **W. Glaubitt, W. Watzka, H. Scholz, D. Sporn,** *J. of Sol-gel Sci. and Tech.* 8, 1997, p29~33.

[120] **Y. Liu, Z.F. Zhang, J. Halloran, R.M. Laine,** *J. Am. Ceram. Soc.* 81, 1998, p629~645.

[121] **R.C. Pullar, M.D. Taylor, A.K. Bhattacharya,** *J. of the Euro. Ceram. Soc.* 18, 1998, p1759-1764.

[122] **Q.M. Lu, W.S. Dong, H.J. Wang, X.K. Wang**, *Journal of Inorganic Materials* 17, 2002, p566~570.

[123] **G.S. Corman**, *Ceram. Eng. & Sci. Proc.* 12, 1991, p1745~1766.

[124] **K. Okada, T. Motohashi, Y. Kameshima, A. Yasumori,** *J. of the Euro. Ceram. Soc.* 20, 2000, p561~567.

[125] **A. Towata, H.J. Hwang, M. Yasuoka, M. Sando, K. Niihara**, *Composites part A-Appl. Sci. and Manufacturing* 32, 2001, p1127~1131.

[126] **A. Towata, H.J. Hwang, M. Yasuoka, M. Sando, K. Niihara,** *J. Am. Ceram. Soc.* 81, 1998, p2469~2472.

[127] **B.R. Johnson, W.M. Kriven,** *J. Mater. Res.* 16, 2001, p1795~1805.

[128] **M.A. Gülgün, M.H. Nguyen, W.M. Kriven,** *J. Am. Ceram. Soc.* 82, 1999, p556.

[129] **J.E.A. Aguilar, R.A.L. Drew, B. Saruhan, C. Milz and B. Hildmann,** *British Ceramic Transactions,* 99, 200 0, p256-259

[130] **K. Matusita, S. Sakka,** *J. Non-Cryst. Solids* 38~39, 1980, p741.

[131] **E. Baiocchi, M. Bettinelli, A. Montenero, L. di Sipio, A. Sotgiu,** *J. Mater. Sci.* 18, 1983, p411.

[132] **A.E. Zhukovskaya, V.I. Strakhov,** *Zh. Prikladnoi Khimii* 48, 1975, p1125.

[133] **J. Kumar, M. Thirumavalavan, R. Dhanasekaran, F.D. Gnanam, P. Ramasamy,** *J. Phys. D.; Appl. Phys.* 19, 1986, p1223.

[134] **S. Hofacker, M. Mechtel, M. Mager, H. Kraus,** *Progress in organic coatings* 45, 2002, p159~164.

[135] **T. Troczynski, Q.Z. Yang,** "Process for making chemically bonded sol-gel ceramics", *US Patent* 6284682, 2001.

[136] **Y. Oishi, K. Ando**, Transport in Nonstoichiometric Compounds, Eds. G, Simkovich, V.S. Stubican. P lenum Pres s, New York, 1985, p189~202.

[137] **T. Yasushi**, Corrosion-resistant composite oxide material, *European Patent*, 1013623, 2000.

[138] **T.L. Metroke, R. L. Parkhill, E. T. Knobbe,** *Progress in organic coatings* 41, 2001, p233~238.

[139] **L.F. Francis,** *Mater. Manufacturing Process* 12, 1997, p963.

[140] **J.S. Abell, I.R. Harris, B. Cockayne, B. Lent,** *J. Mater. Sci.* 9, 1974, p527.

[141] **Shigeo Shionoya,** W.M. Yen (eds.), Phosphor Handbook, CRC Press, Boca Raton, FL, 1998, p515.

[142] **M.F. Yan, T.C.D. Huo and H.C. Ling,** *J. Electronchem. Soc.* 134, 1987,

p493.

[143] **K. Ohno, T. Abe,** *J. Electrochem. Soc.* 133, 1986, p638.

[144] **K. Ohno, T. Abe,** *J. Electrochem. Soc.* 134, 1987, p2072.

[145] **Shigeo Shionoya,** W.M. Yen (eds.), Phosphor Handbook, CRC Press, Boca Raton, FL, 1998, p489-498.

[146] **S. Nakayama, A. Ikesue, M. Sakamoto,** *Nippon Kagaku Kaishi,* 6, 2000, p437~440.

[147] **S. Ramanathan, S.K. Roy, Y.J. Bhat,** *J. Mater. Sci. Letters* 20, 2001, p2119~2121.

[148] **K. Shiroki,** *Solid-state Laser Materials Oyobutsuri* 38, 1969, p117.

[149] **B. Cockayne, B. Lent,** *Journal of Crystal Growth* 46, 1979, p371-378.

[150] **J.L. Caslavsky, D.J. Viechnicki**, *Journal of Materials Science* 15, 1980, p1709-1718.

[151] **M. Gervais, S.L. Floch, J.C. Riflet, J. Coutures,** *J. Am. Ceram. Soc.* 75, 1992, p3166-3168.

[152] **G. De With et al.,** *Mater. Res. Bull.* 19, 1984, p1699.

[153] **M. Sekita, et al.,** *J. Appl. Phys.* 67, 1990, p453.

[154] **C. Honninger, R. Paschotta, F. Morier-Genound, M. Moser, U. Keller**, in: OSA TOPS, *Advanced Solid-State Lasers,* 26, 1999, p397.

[155] **G. Bress, et al.,** *Nuc. Instr. and Methods* A 461, 2001, p361.

P. Antonini, et al., *Nuc. Instr. and Methods* A 460, 2001, p469.

[156] **P. Antonini, S. Belogurov, G. Bressi, G. Garugno, D. Iannuzzi,** *Nuc. Instr. and Methods* A 486, 2002, p799~802.

[157] **R.S. Raghavan,** *Phys. Rev. Lett.* 78, 1997, p3618.

[158] **G.S. Corman,** Final report, Sep. 1987~Sep. 1989, Government Research Announcements and Index, USA , 1990.

[159] **Y. Liu, Z.F. Zhang, J. Halloran, R.M. Laine,** *J. Am. Ceram. Soc.* 81, 1998, p629~645.

[160] **Q.M. Lu, W.S. Dong, H.J. Wang, X.K. Wang,** *J. of Inorganic Mater.* 17, 2002, p566~570.

[161] **R.C. Pullar, M.D. Taylor, A.K. Bhattacharya,** *J. Euro. Ceram. Soc.* 19, 1999, p1747~1758.

[162] **S. Karato, Z. Wang, K. Fujino,** *J. Mater. Sci.* 29, 1994, p6458~6462.

[163] **S. Deng,** *J. Mater. Sci.* 31, 1996, p6077~6083.

[164] **T.A. Parthasarathy, T. Mah, K. Keller,** *J. Am. Ceram. Soc.* 75, 1992, p1756~1759.

[165] **T.A. Parthasarathy, T. Mah, K. Keller,** *Ceram. Eng. & Sci. Proc.* 12, 1991, p1767~1773.

[166] **M. Jimenez-Melendo, H. Haneda, H. Nozawa,** *J. Am. Ceram. Soc.* 84, 2001, p2356~2360.

[167] **P. Pramanik,** *Mater. Sci. Bull.* 18, 1995, p819.

[168] **A. Sin and P. O dier,** *Adv. Mater.* 12, 2000, p649.

[169] **G.A.M. Hussein, A.K.H. Nohman, K.M.A. Attyia**, *J. Thermal Anal.* 42, 1994, p1155.

[170] **W.D. Kingery, H.K. Bowen, D.R. Uhlmann,** "Introduction to ceramics", second edition, 1975; A Wiley – Interscience publication.

[171] **Q.Q. Chen, H.M. Wang, Y.H. Zhu,** *J. Chinese Ceram. Soc.* 20, 1992, p436-441.

[172] See www.srdat.nist.gov/xpsand references therein.

[173] **Akio Kotani,** *J. of Elect. Spectroscopy and Related Phenomena* 100, 1999, p75-104.

[174] **Y. Uwamino, Y. Ishizuka, H. Yamatera,** *J. Electron. Spectrosc.* 34, 1984, p69.

[175] **J.P. Coutour, A. Salesse, M. Froment, M. Garreau, J. Thevenin, D. Warin,** *J. Microsc. Spectrosc. Electron.* 4, 1979, p483.

[176] **C.M. Lopatin, V.B. Pizziconi, T.L. Alford,** *J. Mater. Sci.: Mater. In Medicine* 12, 2001, p767-773.

[177] **M. Es-souni, A. Piorra,** *Mater. Res. Bulletin* 36, 2001, p2563-2575.

[178] **H.J.M. Bosman, A.P. Pijpers, A.W.M.A. Jaspers,** *J. Catal.* 161,1996, p551.

[179] **R. Castillo, B. Koch, P. Ruiz, B. Delmon,** *J. Catal.* 161, 1996, p524.

[180] **F. Barath, M. Turki, V. Keller, and G. Maire,** *J. Catal.* 185, 1999, p1-11.

[181] **C. Rao, K. Rao**, Phase transformation in solids. W & J Mackay Ltd, Chatham, UK, 1978.

[182] **A. Guinier,** X-ray Diffraction; Freeman; San Francisco, CA.

[183] **D.C. Bradley, R.C. Mehrotra and D.P. Gaur**, Metal Alkoxides, Academic Press, London, 1978, p915 ~ 923.

[184] **K. Papagelis, G Kanellis, T. Zorba, S. Ves, G.A. Kourouklis,** *J. Phys.: Condens. Matter* 14, 2002, p915~923.

[185] **N.T. McDevitt,** *J. Opt. Soc. Am.* 59, 1969, p1240.

[186] **B.M. Reddy, B. Chowdhury,** *J. Catal.* 179, 1998, p413.

[187] **R.A. Nyquist, L.L. Putzig, M.A. Leugers,** Handbook of Infrared and Raman Spectra of Inorganic Compounds and Organic Salts, Acedanmic Press, New York, 1997.

[188] **T. Frausen, P.C. Van Berge, P. Mars,** Preparation of Catalysts I, Elsevier, Amsterdam, 1976, p 40001, p343-34 7.

[189] **K. Papagelis, G Kanellis, J. Arvanitidis, S. Ves, G.A. Kourouklis,** *Phy. Status Solidi (B)* 223, 2001, p343~347.

[190] **K. Papagelis, S. Ves,** *J. Phys. Chem.of Solids* 64, 2003, p599~605.

[191] **H. Zheng, G.D.C. Csete de GyÖrgyfalva, R. Quimby, H. Bagshaw, R. Ubic, I.M. Reaney, J. Yarwood,** *J. of the Euro. Ceram. Soc.* 23, 2003, p2653-2659.

[192] **I.G. Siny, R.S. Katiyar, A.S. Bhalla,** *J. of Raman. Spectroscopy,* 29, 1998, pp385-390.

[193] **R. Prins, V.H. de Beer, and G.A. Somorjai,** *Catal. Rev.-Sci. Eng.* 31, 1989,

p1 and references therein.

[194] **H. Knözinger,** in "Proc., 9th Internat. Conr. Catal., Calgary, 1988" (M.J. Philips and M. Ternan, Eds.), V5, p20. Chem. Institute of Canada, Ottawa, 1988.

[195] **K. Bruckman, B. Grzybowska, M. Che., and J.M., Tatibouet,** *Appl. Catal. A:* General 96, 1993, p279 and references therein.

[196] **B. M. Reddy and B. Chowdhury,** *J. Catal.* 179, 1998, p413-419.

[197] **B. M. Reddy, B. Chowdhury, P. G. Smirniotis,** *Applied Catalysis A*: General 219, 2001, p53-60.

[198] **P. Ayyub, M. Multani, M. Barma, V.R. Palkar, R. Vijayaraghavan,** *J. Phys. C: Solid State Phys.* 21, 1988, p2229.

[199] **R. Lamber, S. Wetjen, and N.I. Jaeger,** *Phys. Rev. B* 51, 1995, p10968.

[200] **M.Y. Gamarnik, Y.Y. Sidorin,** *Phys. Status Solidi B* 156, 1989, pK1.

[201] **P. Ayyub, V.R. Palkar, S. Chattopadhyay, M. Multani,** *Phys. Rev.* B51, 1995, p6135.

[202] **A.M. Hofmeister and K.R. Campbell,** *J. Appl. Phys.* 72, 1992, p638.

[203] **J.P. Hurrell, S.P.S. Porto, I.F. Chang, S.S. Mitra, R.P. Bauman,** *Phys. Rev.* 173, 1968, p851.

Chem. Mater. **2003,** *15,* 3474−3480

Synthesis of Nanosize Powders and Thin Films of Yb-Doped YAG by Sol−Gel Methods

H. M. Wang,* M. C. Simmonds, Y. Z. Huang, and J. M. Rodenburg

Materials Research Institute, Sheffield Hallam University, City Campus,
Sheffield S1 1WB, U.K.

Received July 2, 2002. Revised Manuscript Received June 2, 2003

Yb-doped YAG is becoming a very promising optical material. We present a synthesis of single-phase Yb-doped YAG powders and thin films at a significantly lower temperature by sol−gel methods than by other conventional techniques. Yb-doped YAG powders and thin films on Si(100) substrates with a series of different doping concentrations were prepared. The lattice deformation, IR, and Raman vibrations were studied via the change of the doped concentration. This could be one of the reasons why, in general, about 20 atomic % Yb:YAG presents the better laser and scintillation properties. Scanning electron microscopy and transmission electron microscopy were used to investigate the morphology of the structures. A strong preferred orientation of crystal growth in thin films was found during the conversion of the structure from amorphous to crystalline. The Avrami model was used to analyze the isothermal transformation kinetics. On the basis of the experimental results, the effective activation energy of crystallization in the thin films was calculated as 653 ± 10 kJ/mol.

1. Introduction

$Y_3Al_5O_{12}$ (YAG) has excellent thermal properties and is well established as a laser host material.[1] Conventionally, these materials such as Nd- or Cr-doped YAG are single crystals fabricated by the Czochralski (CZ) method.[2] The schematic diagram of the CZ method, also called a "puller", is shown in Figure 1. Such a puller generally has four subsystems, which are the furnace, pulling mechanism, gas control, and control system. The high-purity raw materials are melted at extremely high temperature (2000 °C). The growth of a single crystal is very sluggish. Heavily doped Nd:YAG crystals (<5 atomic %) are necessary for obtaining a high-power output laser. However, in general, it is extremely difficult to dope more than 1 atomic % Nd homogeneously in a YAG single crystal because the effective segregation coefficient[3] of Nd for the YAG single crystals is quite low (~0.2). YAG single crystals doped with more than 2 atomic % of elemental Nd have a relatively inferior optical quality that cannot be used as laser devices. Thus, in recent years, ceramic laser materials have received much attention.[4−8] Especially with the development of nanomaterials, it has become possible to produce transparent high-quality ceramics of YAG by the isostatically pressed method. It has been reported[8] that a high optical quality Nd:YAG ceramic presents almost the same laser property as the single-crystal rod lately. Compared to single-crystal growth, the technique of manufacturing ceramics offers the advantages of being inexpensive and having an easy high-doped concentration, mass production, large size, and gradient ceramic structure. Furthermore, we noticed that Yb-doped YAG has recently been suggested as a new-generation laser medium.[9,10] It is attractive for Q-switching operations to obtain high-peak-power

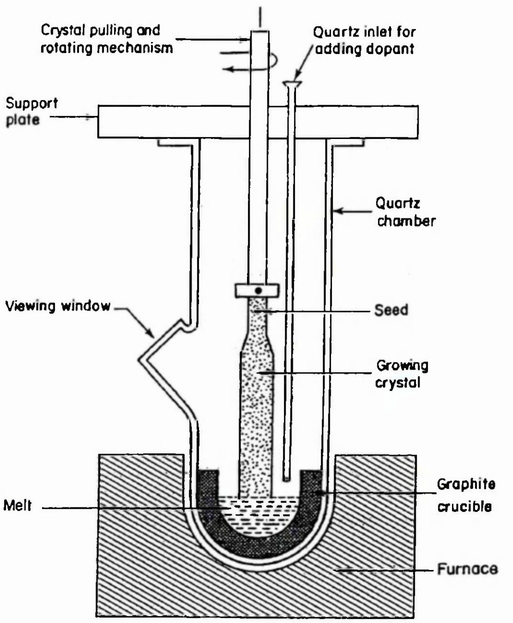

Figure 1. Schematic representation of a CZ crystal pulling furnace.

---

(1) Zayhowski, J. J. *J. Alloys Compd.* **2000**, *303−304*, 393.
(2) Kvapil, J.; et al. *J. Cryst. Growth* **1981**, *52*, 542.
(3) Shiroki, K. *Solid-state Laser Mater. Oyobutsuri* **1969**, *38*, 117.
(4) Sekita, M.; et al. *J. Appl. Phys.* **1990**, *67*, 453.
(5) Ikesue, A.; Furusato, I.; et al. *J. Am. Ceram. Soc.* **1995**, *78* (1), 225.
(6) Ikesue, A. *Opt. Mater.* **2002**, *19*, 183−187.
(7) Hreniak, D.; Strek, W. *J. Alloys Compd.* **2002**, *341*, 183−186.
(8) Lu, J. R.; Uede, K.; Yagi, H.; Yanagitani, T.; Akiyama, Y.; Kaminskii, A. A. *J. Alloys Compd.* **2002**, *341*, 220−225.
(9) Shimokozono, M.; Sugimoto, N.; et al. *Appl. Phys. Lett.* **1996**, *68*, 2177.

10.1021/cm0212481 CCC: $25.00

optical pulses[11,12] because it has relatively low cross-sections that lead to larger pulse energies (4 times higher) compared with those of Nd-doped crystals. Heavily Yb-doped YAG is also found to be a potentially good scintillator for solar neutrino detection very recently and can be optimized in terms of efficiency and lifetime.[13,14] The laser and scintillation properties of Yb-doped YAG with a doped concentration from 1 to 100% are being widely studied.[14–19] However, the optical properties of Yb:YAG materials have been significantly affected with the increase of the doped Yb^{3+} concentration in Yb:YAG due to the crystal lattice deformation and the adjustment of the lattice constant. This is attributed to the change of the phonon vibration modes. These properties are important to the design of the system of laser devices, but very little research about these properties can be found.

Here, we report the manufacturing of Yb:YAG powders with different doping concentrations from low to high by sol–gel methods. The change in the phonon vibration IR and Raman spectra was studied. The sol–gel way has many advantages such as atomic level mixing of high-purity precursors and low processing temperature. Nanosize particles are very significant in preparing high-quality ceramics. Although a lot of sol–gel or similar chemical syntheses of the pure YAG[20–22] and doped YAG (mainly Ce^{3+}, Eu^{3+}, and Tb^{3+}) powders were reported recently, most of them are used as phosphors and the doped concentration is normally lower than 5%. To the best of our knowledge, we are the first to synthesize the heavily Yb-doped YAG material by the sol–gel method.

2. Experimental Section

Al sol was prepared first from $AlCl_3$ (99.985%, Alfa), and then the yttrium and ytterbium chemicals were added to the Al sol. The molar ratio of Yb:Y was controlled to 10%, 20%, 50%, and 100%. The ratio of (Yb + Y):Al was kept as 3:5. After several hours of mixing at 80 °C, a clear transparent sol was obtained. Details can be found in ref 23.

The gel for the preparation of Yb:YAG powders was formed by putting dropwise the clear sol into the 35 wt % NH_4OH solution that is stirred continually. The ammonia solution became opaque because of the formation of gel. Then, the suspension solution was filtered, and the residue gel was dried at 200 °C for about 1 or 2 h to get a white powder and further heat-treated in air at the crystallized temperature with a heating rate of 10 °C min^{-1}.

Thin films were deposited on the substrate of single-crystal Si(100) by dip coating, and the specimens were cut into pieces of 1 × 1 cm^2. The thickness of the film was under 1 μm. The thin film samples were calcined separately at 850, 900, and 950 °C for various times with a very fast heating rate of 100 °C s^{-1}. A ramp rate of 100 °C s^{-1} was sufficiently fast to prevent transformation during heating and allowed the direct application of a JMA model[24–27]– for transformation kinetics.

X-ray diffraction (XRD) patterns of powders and thin films of Yb:YAG were characterized using a Philips PW-3710 diffractometer equipped with Cu Kα radiation. The tube current and voltage were 35 mA and 35 kV, respectively. The scan step time was 4 s, and the step size was 0.020. The 2θ range examined was 15–60°. Disk samples for the experiment of infrared transmittance spectra were prepared by mixing Yb:YAG powders with KBr according to the mass ratio 10:100. Infrared spectra of Yb:YAG powders were performed in a Genesis series Fourier transform infrared (FT-IR) made by ATI Mattson, and Raman spectra were finished in a Renishaw Ramanscope system 2000 spectrometer using the helium/neon laser with a laser wavelength of 633 nm and 25 mW power. The examined wavenumber range of IR is from 1000 to 400 cm^{-1}. For Raman spectra, it is in the range of 200–1000 cm^{-1}.

The surface morphology of powders was investigated using XL30 ESEM-FEG. Specimens for transmission electron microscopy (TEM) observation were prepared by briefly dispersing ultrasonically the powders in acetone. One drop of the solution was then placed on a copper grid coated with an evaporated amorphous carbon film. TEM characterization was performed on a Philips CM20 at 200 kV.

3. Results and Discussion

3.1. Crystalline Structure Conversion. 3.1.1. The powders annealed at 800 °C were found to be amorphous, with small crystallites whose size was in the nanoscale. However, the fully crystallized phase was identified as a garnet structure for powders after being heated at 850 °C (JCPDS[28] No. 33-40 for YAG and No. 73-1369 for YbAG). Traditionally, the synthesis temperature high up to 1600 °C is required by solid-state sintering methods. The XRD patterns are shown in Figure 2 A–D respectively for 10, 20, 50, and 100 atomic % Yb:YAG. The maximum line locates at about 2θ of 33.4°. The relative intensity of the peak at 2θ of 18° is about 20%. Apparent structural changes can be found in Figure 2 by comparing them with each other. Typically the relative intensities of two peaks at about 27.8° and 29.6° are seen. The change is dependent on the doped Yb^{3+} molar ratio from 10% and 20% to 50% and then 100% Yb:YAG.

The 2θ angle position change of the maximum line (420) of four Yb-doped YAG powders is shown in Figure 3. They are Kα_1 X-ray peaks, and Kα_2 peaks were stripped. Hence, the cell constants calculated from Figure 3 are 12.023, 11.991, 11.988, and 11.960 Å for 10, 20, 50, and 100 atomic % doped Yb:YAG, separately. These values are greater than what theoretically they should be (a = 11.931 Å for YbAG, JCPDS[28] No. 73-1369, and a = 12.01 Å for YAG, JCPDS No.33-40; thus, we know the cell constant of Yb:YAG lies between 11.931 and 12.01 Å). The reason may be caused by the

---

(10) Patel, F. D.; Honea, E. C.; et al. *IEEE J. Quantum Elect.* **2001**, *37* (1), 135.
(11) Shimada, T.; Ishida, Y.; et al. *Opt. Commun.* **2001**, *194*, 238.
(12) Spühler, G. J.; Paschotta, R.; et al. *Appl. Phys. B* **2001**, *72*, 285.
(13) Raghavan, R. S. *Phys. Rev. Lett.* **1997**, *78*, 3618.
(14) Guerassimova, N.; Garnier, N.; et al. *Chem. Phys. Lett.* **2001**, *339*, 197.
(15) Antonini, P.; Belogurov, S.; et al. *Nucl. Instrum. Methods Phys. Res. A* **2002**, *486*, 799–802.
(16) Antonini, P.; Belogurov, S.; et al. *Nucl. Instrum. Methods Phys. Res. A* **2002**, *488*, 591–603.
(17) Saikawa, J.; Kurimura, S.; et al. *Opt. Mater.* **2002**, *19*, 169–174.
(18) Qiu, H.; Yang, P.; et al. *Mater. Lett.* **2002**, *55*, 1–7.
(19) Zhou, Y.; Thai, Q.; et al. *Opt. Commun.* **2003**, *219*, 365–367.
(20) Manalert, R.; Rahaman, M. N. *J. Mater. Sci.* **1996**, *31* (13), 3453.
(21) Paz Vaqueiro, M.; López-Quintela, A. *J. Mater. Chem.* **1998**, *8* (1), 161.
(22) Veith, M.; Mathur, S.; et al. *J. Mater. Chem.* **1999**, *9* (12), 3069.
(23) Wang, H. M.; Simmonds, M. C.; Rodenburg, J. M. *Mater. Chem. Phys.* **2003**, *77*, 802–807.
(24) Avrami, M. *J. Chem. Phys.* **1940**, *8*, 212.
(25) Avrami, M. *J. Chem. Phys.* **1941**, *9*, 177.
(26) Marotta, A.; Buri, A.; Valenti, G. L. *J. Mater. Sci.* **1978**, *13*, 2483.
(27) Znidarsic, V.; Kolar, P. O. *J. Mater. Sci.* **1991**, *26*, 2490.
(28) PCPDFWIN, Version 2.1, JCPDS ICDD International Centre for diffraction Data, June 2000.

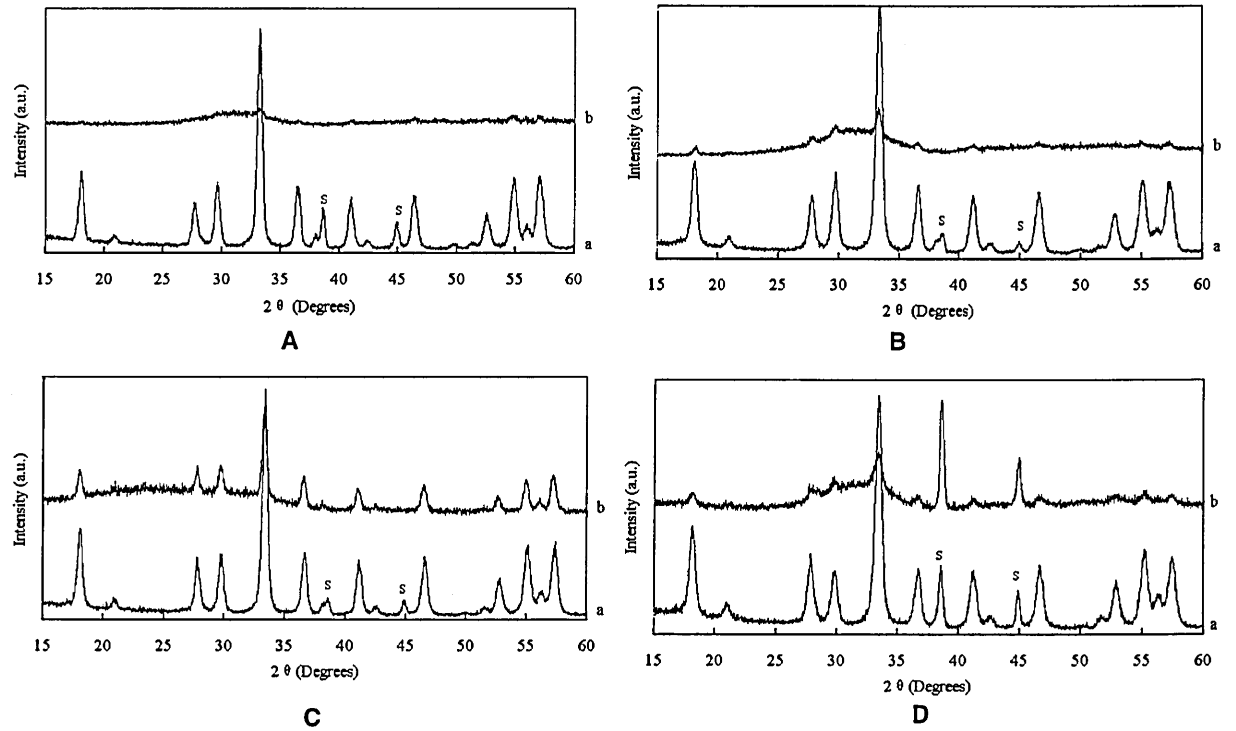

Figure 2. XRD patterns of Yb:YAG powders: (A) 10 atomic %; (B) 20 atomic %; (C) 50 atomic %; (D) 100 atomic %.

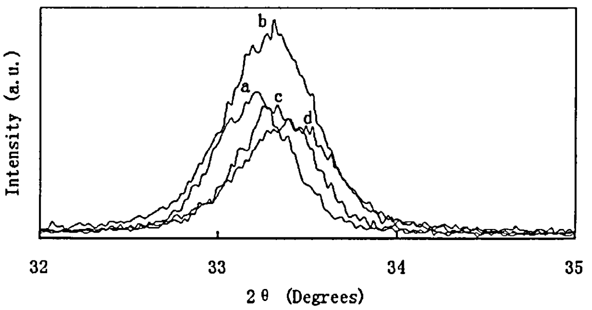

Figure 3. XRD peaks at about 33.5° (420) of the Yb-doped YAG: (a) 10 atomic %; (b) 20 atomic %; (3) 50 atomic %; (d) 100 atomic %.

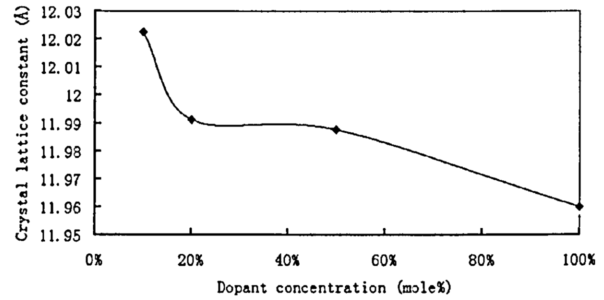

Figure 4. Plot of the lattice constant with Yb doping concentrations in YAG.

powder consisting of nanoparticles, which results in the lattice expansion.[29,30] Thus, with the increase in time or temperature of the calcination, the cell lattice will become close to the theoretical value as the particle size increases. The relationship between the lattice parameters and the Yb concentration then is shown in Figure 4. It does not present the linear relationship. Because the effective radius of Yb^{3+} (0.86)[31] is smaller than that of Y^{3+} (0.89), doping Yb into YAG garnets will decrease the crystal lattice constant and lead to the structure deformation. When the Yb^{3+} doping concentration is below 20 atomic %, the lattice constant decreases sharply. However, there is almost no change of the lattice constant between the doping concentrations of 20 and 50 atomic %. Then, the lattice constant decreases smoothly again from 50 to 100 atomic %. Clearly, these changes are dominated by the distribution of the occupied positions of Yb^{3+} in YAG.

3.1.2. Typical XRD patterns of 100 atomic % Yb:YAG thin films on Si substrates that were heated at 850 °C for various times are shown in Figure 5. A structure composed of very fine nanocrystallites and an amorphous phase are observed (850 °C for 1 h). Only a single phase (garnet) is shown in Figure 5. The intensities of all peaks increased with the increment in the calcination time until they reached a saturation level. When the peak intensities of thin film XRD patterns at various heat-treatment conditions are compared, e.g., the thin film sample at 850 °C for 23 h in Figure 5 to that of the powder XRD patterns in Figure 2, it was found that the crystal growth in thin films exhibits highly preferred orientation growth. Especially, it is seen that the relative intensity of the (211) peak at 2θ of about 18° is enhanced from 45% at 850 °C for 1 h of calcination to 85% at 850 °C for 23 h of heat treatment. This percentage value is much higher than about 20% for powders heated at 850 °C for 11 h: 37.24% for YAG (JCPDS[28]

---

(29) Ayyub, P.; Multani, M.; et al. *J. Phys. C: Solid State Phys.* **1988**, *21*, 2229.

(30) Lamber, R.; Wetjen, S.; Jaeger, N. I. *Phys. Rev. B* **1995**, *51*, 10968.

(31) Klein & Hulburt, *Manual of Mineralogy*, 20th ed.; 1985.

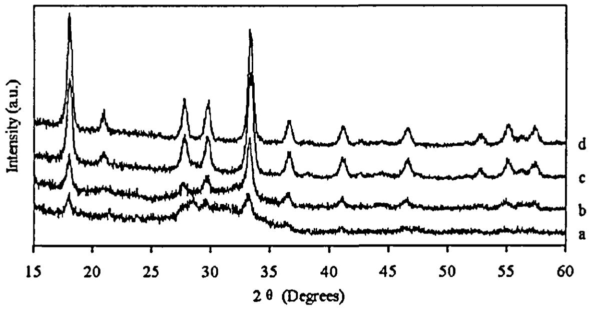

Figure 5. XRD patterns of 100 atomic % Yb-doped YAG thin films on Si. Heat treatment at 850 °C: (a) 1 h; (b) 3 h; (c) 8 h; (d) 23 h.

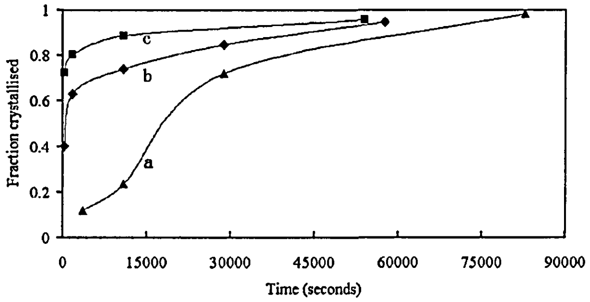

Figure 6. Combined plot of the crystallized fracture via the change of time for 100 atomic % Yb:YAG thin films: (a) 850 °C; (b) 900 °C; (c) 950 °C.

No. 33-40) and 65.37% for YbAG (JCPDS No. 73-1369). The same result of the preferred orientation of Yb:YAG was found at other heating temperatures. An unknown peak at 2θ of 16.9° shown in the initial stage is due to the fast heating rate, but it disappeared upon further calcination. Hence, the texture maximum is the (211) peak, which can be used to stand for the amount or degree of thin film crystallization.

3.2. Activation Energy of Crystalline Growth in the Thin Films. The Johnson–Mehl–Avrami equation, shown below, was used to model the isothermal growth data.[24–27]

$$x(t) = 1 - \exp[-(kt)^n] \tag{1}$$

It can be rearranged as

$$\ln \ln[1 - x(t)]^{-1} = n \ln k + n \ln t \tag{2}$$

where $x(t)$ is the volume fraction of the transformed phase, t the heating time, and n a morphology index, which is related to the crystallization mechanism, and k could follow as the Arrhenius equation

$$k(T) = k_0 \exp(-E_a/RT) \tag{3}$$

Thus,

$$\ln k = \ln k_0 - E_a/RT \tag{4}$$

where k_0 is a constant, T is the temperature, R is the gas constant (8.314 J mol^{-1}), and E_a is the activation energy associated with nucleation and growth. Figure 6 shows the results corresponding to the isothermal growth experiments at 850, 900, and 950 °C. The figure was built up as follows. The integrated intensity of the texture maximum (211) in the XRD patterns increased until they reached a saturation level. The integrated intensity of the (211) peak, normalized to this saturation value, was used to monitor the crystalline fraction of the film, $x(t)$. Thus, each curve point corresponds to the integrated intensity of the (211) line, at that time and temperature, divided by the saturation value. Here, it should be reasonable that we use the integrated intensity of the texture maximum (211) because it increased much faster than other increased peaks in XRD patterns with the increment in the calcination time and, on the other hand, we do no expect any sintering to occur under the relatively low calcination temperatures used here.

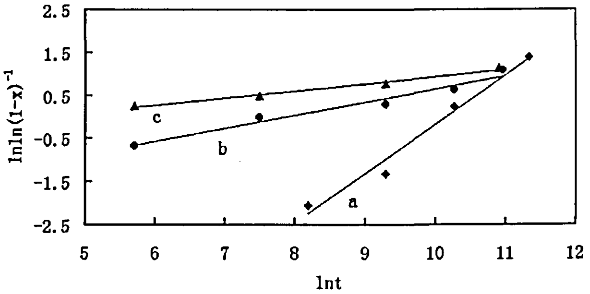

Figure 7. Plot of ln ln(1 − x)$^{-1}$ versus ln(t) of 100% Yb:YAG thin films: (a) 850 °C; (b) 900 °C; (c) 950 °C.

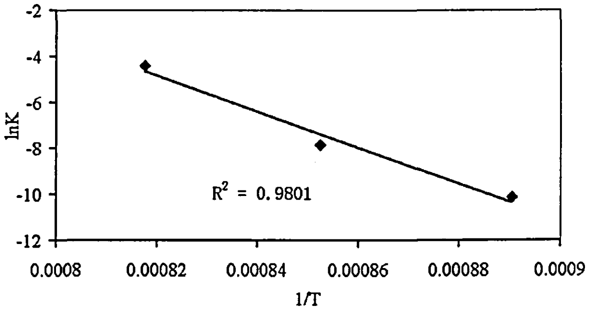

Figure 8. Relationship curve of ln K and $1/T$ of 100 atomic % Yb:YAG thin films.

Linear regression analysis of the plots ln ln[1 − $x(t)$]$^{-1}$ versus ln(t) according to eq 2 is shown in Figure 7. We can obtain three rate constants by the three intercepts with the vertical axis of the plots. Using eq 4, the relationship of ln K and T^{-1} is shown in Figure 8. The correlation coefficient is 0.98. From the slope of the line, the activation energy can be calculated as 653 ± 10 kJ/mol. Other parameters such as the Avrami exponent n and the reaction rate k are all tabulated in Table 1. Within the framework of a proposed classification of diffusion-controlled transformations,[32] an exponent n greater than 2 indicates that the transformation is nucleation limited. The activation energy can be related to nucleation energy. In contrast, values of n of less than 1 indicate that the crystal growth dominates. The average exponent n calculated from our experiments is 0.5379, and this indicates that the crystal growth dominates. However, three values of exponents are dispersion. Especially, at 850 °C the exponent value n is 1.1428 greater than 1. This means that the mechanism of crystallization at this temperature could be

---

(32) Rao, C.; Rao, K. *Phase transformation in solids;* W & J Mackay Ltd.: Chatham, U.K., 1978.

Table 1. Crystallization Kinetics Parameters for 100% Yb:YAG Films

sample	*n*	*k*	k_0	E_a (kJ/mol)
100% Yb-doped YAG garnet films	850 °C, 1.1428	3.93×10^{-5}	8.03×10^{25}	653 ± 10
	900 °C, 0.3029	3.87×10^{-4}		
	950 °C, 0.168	1.23×10^{-2}		
	average: 0.5379			

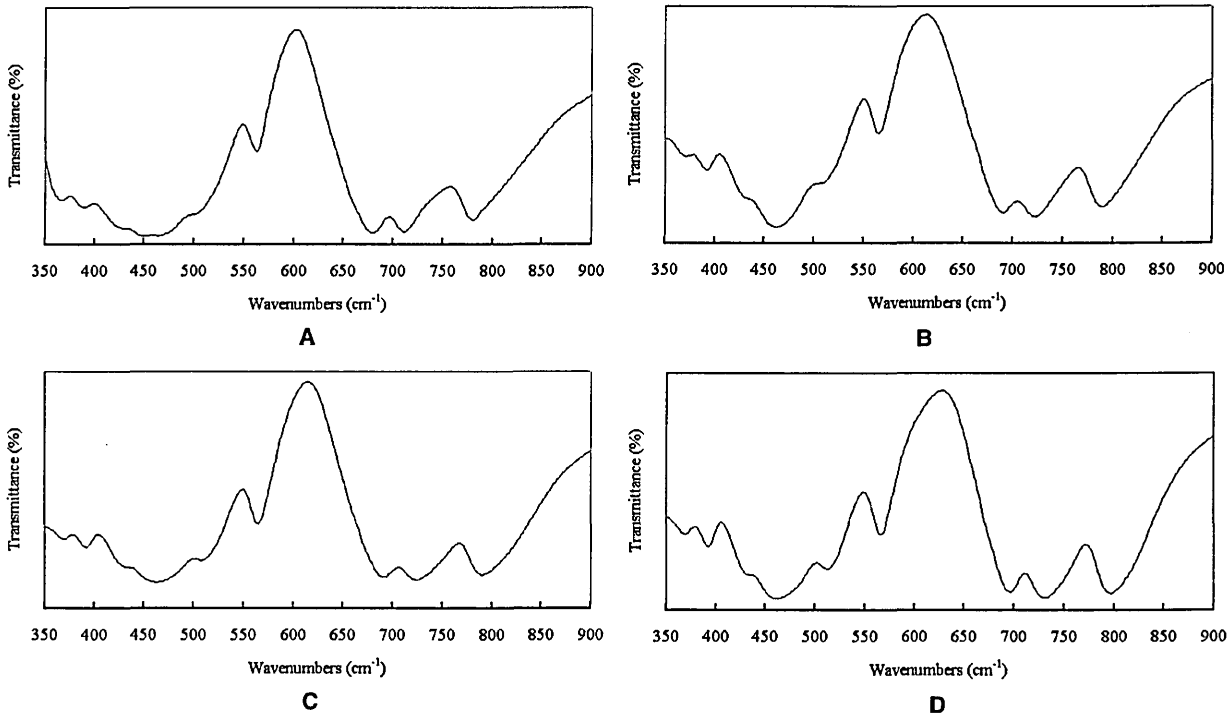

Figure 9. Infrared spectra of Yb-doped YAG powders: (A) 10 atomic %; (B) 20 atomic %; (C) 50 atomic %; (D) 100 atomic %.

nucleation together with the crystal growth limitation. At high temperature, overcoming the nucleation barrier becomes easier. This conclusion is in agreement with our experimental observations by XRD that show a very fast nucleation at the initial stage at high-temperature heat treatment. The results of this part of the work are very close to the studies of crystallization kinetics reported by Johnson and Kriven[33] recently. However, Johnson and Kriven used the sample that was prepared by the rapidly (at approximately 250 °C/s) quenched YAG glass beads from a melting temperature of 2200 °C. The crystallization kinetics was carried out by using differential thermal analysis exotherms. The YAG composition glass beads were populated by the nanoscale crystals of YAG. The material crystallized directly into stoichiometric YAG at temperatures as low as 840 °C. The nanoscale crystals in the glass beads are studied most likely as seeds for subsequent crystal growth. Their obtained activation energy for crystallization was 437 kJ/mol. In general, crystallization in thin films has a higher activation energy than that in bulk materials.

3.3. FT-IR and Raman Spectra. IR transmittance spectra of Yb-doped YAG powders are shown in Figure 9A–D. They are in very good agreement with rare-earth aluminum garnets.[34] A comparison of the IR spectra of the Yb-doped YAG is given in Table 2. There are not any other phase infrared vibration peaks in the IR spectra apart from aluminum garnets (e.g., Y_2O_3, Yb_2O_3, Al_2O_3, or $YAlO_3$). In Table 2, the peak at ~566 cm^{-1} is relatively stable and some other peaks will shift according to the Yb-doped concentration in the YAG matrix. The wavenumber shift value is very small between 20 and 50 atomic % Yb: YAG garnets (e.g., 790 → 790, 723 → 725, and 690 → 692 cm^{-1}). However, the wavenumber change is relatively large from 10 to 20 atomic % and from 50 to 100 atomic % Yb:YAG (e.g., 781 → 790 and 790 → 798 cm^{-1}). The changing tendency is in agree-

Table 2. Comparison of IR Vibrational Frequencies of the Yb:YAG Powders

Yb:YAG				
10%	20%	50%	100%	ref data[34]
781	790	790	798	794
711	723	725	732	726
680	690	692	698	691
563	566	566	566	567
				532
501	510	510	513	522
458	462	462	462	463
428	430	430	430	432
390	392	392	392	396

---

(33) Johnson, B. R.; Kriven, W. M. *J. Mater. Res.* **2001**, *16*, 1795–1805.

(34) Hofmeister, A. M.; Campbell, K. R. *J. Appl. Phys.* **1992**, *72*, 638.

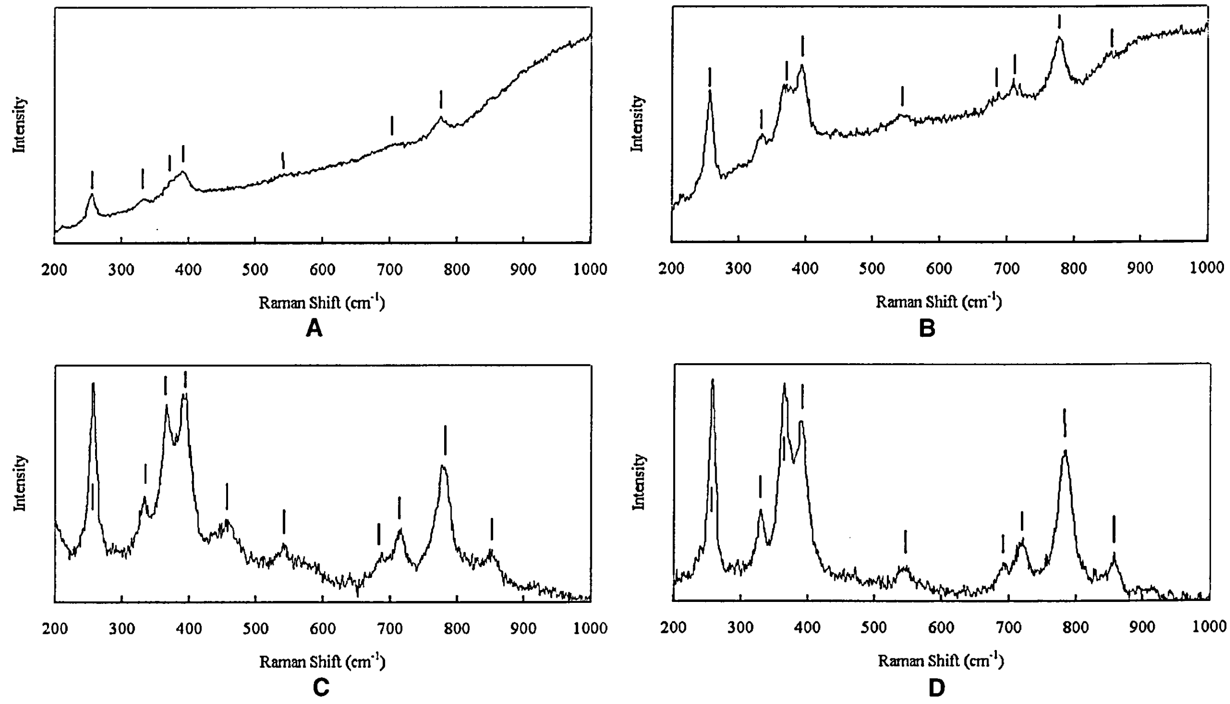

Figure 10. Raman spectra of Yb-doped YAG powders: (a) 10 atomic %; (b) 20 atomic %; (c) 50 atomic %; (d) 100 atomic %.

Table 3. Comparison of Raman Active Vibrational Frequencies of the Yb-Doped YAG Powders

10%	20%	50%	100%
	850	850	857
777	778	779	785
712	713	714	720
	688	689	695
541	541	542	548
		459	
391	394	393	390
372	368	366	365
335	335	333	330
256	257	257	258

ment with the lattice deformation we discussed in section 3.1.1.

Raman spectra of Yb-doped YbAG powders are shown in Figure 10a–d: (i) 7 Raman active vibrational modes are observed in Figure 10a for 10 atomic % Yb:YAG particles; (ii) 9 Raman active vibrational modes are found in Figure 10b for 20 atomic % Yb:YAG particles; (iii) 10 Raman modes are observed in Figure 10c for 50 atomic % Yb:YAG particles; (iv) 9 Raman modes can be seen in Figure 10d for 100 atomic % Yb:YAG particles, which are all indicated by the vertical solid line in the figures. A comparison of Raman vibrational frequencies of the Yb-doped YAG powders is given in Table 3. The lines of the observed Raman active vibrational modes are in good agreement with the experimental and calculated Raman mode frequencies of YAG or rare-earth aluminum garnets.[35,36] Some frequency and intensity changes of the Raman vibrational lines are found. The changing tendency presents the same way with the IR spectra and the cell constant. For instance, the frequency of the line, which is at 711 cm^{-1} for 10 atomic % Yb:YAG particles, increases to almost the same 723 and 725 cm^{-1} at 20 and 50 atomic % Yb:YAG powders (Figure 10b,c) and then becomes 732 cm^{-1} in 100 atomic % Yb:YAG powders (Figure 10d). Especially, a distinctive change can be observed in the comparison of the relative intensities of the two lines, the frequencies of which are located at about 365 and 390 cm^{-1}. The intensity of the line at about 365 cm^{-1} is smaller than that of the line at about 390 cm^{-1} in the former three samples (Figure 10a–c). However, the intensity of the line at 365 cm^{-1} becomes greater than that of the line at 390 cm^{-1} for 100 atomic % Yb:YAG.

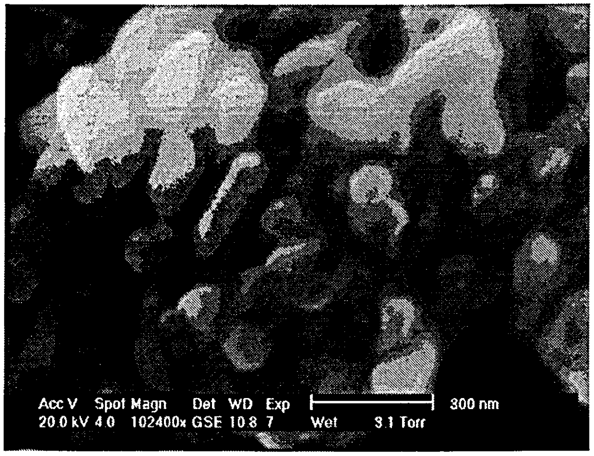

Figure 11. Typical scanning electron micrographs of Yb-doped YAG powders.

The structural changing tendency is now confirmed again by the observed Raman spectra. This explains that the doped Yb^{3+} affects the lattice vibration modes, which is related to the doping concentration and the

---

(35) Hurrell, J. P.; Porto, S. P. S.; et al. *Phys. Rev.* **1968**, *173*, 851.
(36) Papagelis, K.; Kanellis, G.; et al. *Phys. Status Solidi B* **2001**, *223*, 343–347.

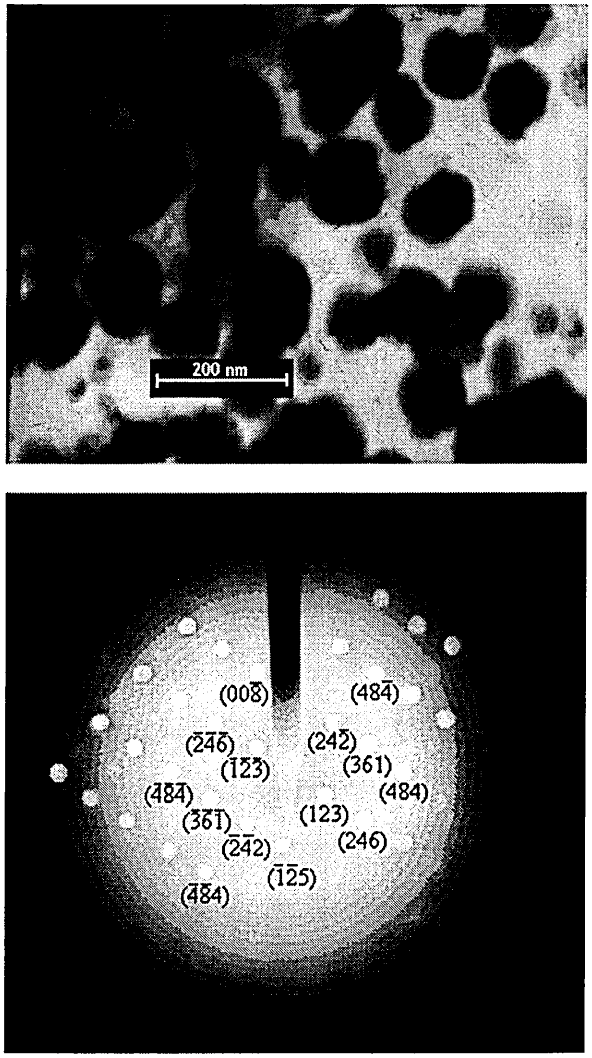

Figure 12. (a) Bright-field transmission electron image of Yb-doped YAG powders. (b) Micro area electron diffraction pattern of Yb:YAG crystals.

distribution of the occupied positions of Yb^{3+} cations in the garnet structure. However, this change could be divided into three circumstances according to the doping concentration of Yb^{3+}, i.e., 1–20, 20–50, and 50–100 atomic %. The changes of lattice vibrations will influence the interaction between the Yb^{3+} ion and the host YAG. These changes will at last have some effect on the spectra and the laser and scintillation performance of Yb:YAG materials. This could be one of the causes why these materials present better laser and scintillation properties that have been studied by many researchers[12,16,17] in about 20 atomic % Yb:YAG crystals.

3.4. Morphologies of Nanosized Yb-Doped YAG Powders. A typical scanning electron micrograph of Yb-doped YAG powders is shown in Figure 11. The morphologies of various concentrations of Yb-doped YAG are the same and show no differences with the change of the Yb-doped concentration in YAG. It can be observed that the particles do not have very regular shape. They exhibit generally lengthened, rounded irregular shape. Some particles are aggregated but mainly are still dispersed. The particle size is well distributed, and the uniform size is about 100 nm.

A bright-field TEM image of Yb-doped YAG is shown in Figure 12a. A micro area electron diffraction pattern of a Yb:YAG crystal is shown in Figure 12b, correspondingly. The shape and size of the particles are the same as those with the results of the scanning electron micrograph. The diffraction patterns were identified as the garnet structure. The corresponding crystal plane indexes were all labeled in the picture. The axis of the zone is of the indice $[\bar{2}, 1, 0]$.

4. Conclusions

Powders and thin films of Yb-doped YAG with nanosized crystallites were prepared by sol–gel methods at significantly lower temperature than the traditional method. The crystal transformation in thin films on Si(100) shows a strong preferred texture (211) growth. The crystallization kinetics was studied by the Avrami model, and the activation energy was 653 ± 10 kJ/mol. The crystallization mechanism is mainly dominated by the crystal growth. The studies of XRD, IR, and Raman spectra of Yb:YAG with various doped concentrations show the crystal lattice deformation, and the phonon vibration changes according to the Yb^{3+}-doped concentration in YAG, which could be divided into three ranges of Yb^{3+} mole concentration (i.e., 1–20, 20–50, and 50–100 atomic %). This could, in part, explain why about 20 atomic % Yb:YAG crystals generally present the better laser and scintillation properties that have been studied by many other researchers.

Acknowledgment. H.M.W. acknowledges the help of Dr. Christopher Sammon in MRI of Sheffield Hallam University to finish the Raman spectra experiments.

CM021248L

ELSEVIER

Materials Chemistry and Physics 77 (2002) 802–807

MATERIALS CHEMISTRY AND PHYSICS

www.elsevier.com/locate/matchemphys

Manufacturing of YbAG coatings and crystallisation of the pure and Li_2O-doped Yb_2O_3–Al_2O_3 system by a modified sol–gel method

H.M. Wang*, M.C. Simmonds, J.M. Rodenburg

Materials Research Institute, Sheffield Hallam University, City Campus, Sheffield S1 1WB, UK

Received 7 January 2002; received in revised form 5 March 2002; accepted 21 March 2002

Abstract

In addition to their widespread use as optical scintillators, recent research has shown that garnet structures, such as YAG ($Y_3Al_5O_{12}$), may be promising candidates as thermal barrier coatings (TBCs), or as oxidation or erosion resistant materials. We report here for the first time the fabrication of YbAG ($Yb_3Al_5O_{12}$) garnet coatings via a relatively low temperature sol–gel technique. Crystallisation under the firing temperature up to 800 °C of a pure and Li_2O-doped Yb_2O_3–Al_2O_3 system was investigated on single crystal Si(1 0 0) and steel substrates. A single-phase polycrystalline YbAG garnet film was manufactured for the first time at the comparatively low temperature of 700 °C. This is in contrast with traditional sintering methods that require at least a temperature of 1600 °C to produce YbAG garnet ceramics. When coated on a hardened steel substrate, a mesoporous surface with a relatively high hardness is produced. The thermal behaviour of the processing method was analysed by DTA and the structure of coatings was characterised by XRD, SEM and XPS. Such films may have widespread application as a wear-resistant TBC.

Keywords: Sol–gel; YbAG garnet; Coating; Yb_2O_3–Al_2O_3 system

1. Introduction

Ytterbium is rare earth element in the lanthanide series and belongs to the same group as yttrium in the periodic table. Hence the compounds that they form often have similar applications and properties. For example, Y_2O_3 or Yb_2O_3 is a commonly used dopant to stabilise ZrO_2 ceramic films that are widely used as thermal barrier coatings (TBCs). Yttrium oxide or ytterbium oxide is also an addition to self-reinforce silicon nitride ceramics [1]. Neodymium-doped YAG is presently the most widely used solid-state laser material, and ytterbium-doped YAG is one of the most promising laser-active materials and is more suitable for diode-pumping than the traditional Nd-doped crystals. Highly ytterbium-doped YAG (concentration up to 100%) thin films also show promise for various laser waveguide applications in photonic devices and they can be produced by many methods, one of which is where amorphous thin films were prepared at 400 °C using pulsed laser deposition and then heat treated for 3 h at a temperature of 1000 °C to obtain epitaxially grown films [2]. More recently, it has been shown [3,4] that garnet structural ceramic coatings are promising as TBCs, or as oxidation and erosion resistant materials that could, for example, be used in military and commercial gas turbine engines. Because of their utility, much research has been done in the Y_2O_3–Al_2O_3 system by sol–gel techniques. Phase development was studied for the sol–gel method by Lo and Tseng [5]. The reported lowest temperature of producing single-phase YAG by sol–gel synthesis is 900 °C at present [6]. Generally, higher calcination temperatures are required to realise the crystallisation of YAG thin films.

According to the phase diagram of Yb_2O_3–Al_2O_3 binary system [7], ytterbium sesquioxide, Yb_2O_3, has a cubic structure below 1870 °C and it is used as a catalyst in the petrochemical industry [8]. At higher temperatures it exists as both monoclinic and hexagonal phases [9]. However, formation of $YbAlO_3$ perovskite is not observed and it is extrapolated that ytterbium aluminium garnet (YbAG) theoretically has a smaller lattice parameter than that of YAG [10] because the radius of Yb^{3+} (0.86 Å) is smaller than that of Y^{3+} (0.89 Å).

The published papers and applications of YbAG garnet in the Yb_2O_3–Al_2O_3 system are relatively rare. As far as we are aware, the synthesis of a thin film coating of YbAG via the sol–gel method has not been reported in the literature. We present here a novel low temperature synthesis technique

---

* Corresponding author.

E-mail address: h.wang@shu.ac.uk (H.M. Wang).

0254-0584/02/$ – see front matter © 2002 Elsevier Science B.V. All rights reserved.
PII: S0254-0584(02)00142-6

for YbAG, which is facilitated by the addition of lithia and an inorganic–organic polymer agent. The technique offers a route for coating metal alloys at relatively low temperature in order to produce novel high-temperature thermal insulation and oxidation resistance ceramic materials [4]. It may also be of use in the synthesis of optically active coating materials.

2. Experimental

2.1. Preparation of sol

Aluminium sol was prepared from the precursor $AlCl_3$ (99.985%, Alfa). A small quantity of an inorganic–organic hybrid solvent (abbreviation AOS) with a polymer-like structure was used to stabilise and strengthen the network structure of the sol. For reasons of commercial sensitivity, we are unable to reveal the exact details of the AOS. The addition of the AOS solvent into the sol was found to be beneficial for improving film adhesion with metal substrates and for obtaining thick coatings. We have also found that the addition of lithia as a precursor significantly lowers the temperature required for crystallisation. Fig. 1 shows a schematic representation of the processing steps. For comparison, four different composition sols were produced according to the following molar ratios. They are: (1) sample I: $Al_2O_3/Yb_2O_3 = 1{:}1$, with no lithia doping and no AOS solvent; (2) sample II: $Al_2O_3/Yb_2O_3 = 1{:}1$, with 8 mol% lithia doping and no AOS solvent; (3) sample III: $Al_2O_3/Yb_2O_3 = 1{:}1$, with 8 mol% doped lithia and AOS solvent; (4) sample IV: $Al_2O_3/Yb_2O_3 = 5{:}3$, with 4 mol% doped lithia and AOS solvent. The prepared sols were aged 24 h before coating.

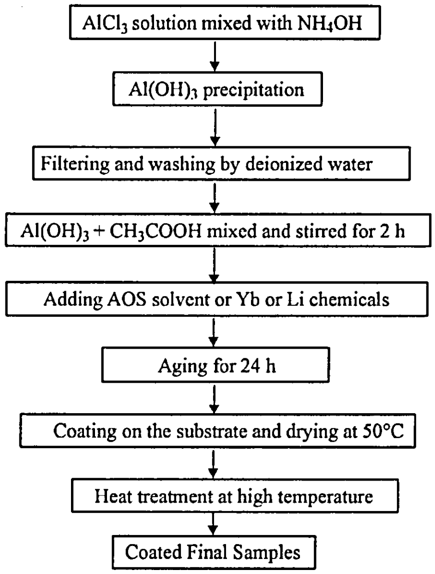

Fig. 1. Flow chart for preparation of samples.

2.2. Preparation of thin films

We have used two substrates to test the coatings: silicon and hardened steel. Si crystals with surface normal orientation [1 0 0] were prepared in $1 \times 1\ \mathrm{cm}^2$ samples. The hardened steel samples consisted of 30 mm diameter coupons which surfaces were polished to within 1 μm. All substrates were cleaned by soap and water and then deionised water, and finally ultrasonically cleaned in ethanol and acetone.

The sol was dropped directly onto the Si substrates which were kept horizontal at a temperature of 50 °C. The sol dried quickly to form a thin film. The coated samples were heated within three temperature regimes to study the crystallisation: (1) 200 °C for 1 h; (2) 450 °C for 1 h; (3) 500, 600, 700, and 800 °C for 1 h at each temperature. For the hardened steel substrates the coatings were obtained by the multiple dip technique with each layer calcined, respectively, at 400 °C for 30 min. The elevation speed was $3\ \mathrm{cm\,min^{-1}}$. After more than 10 dipping processes and calcination at 450 °C for 2 h, a coating with a thickness of about 10 μm was prepared.

2.3. Thermal analysis

Thermal analysis of the samples was performed by first scratching off the gel thin films which were multicoated on the Si substrates. Thermal analysis was performed with a Perkin-Elmer thermal analyser. DTA curves were recorded over a wide range of temperatures (up to 1000 °C) at a heating rate of $10\ {}^{\circ}\mathrm{C\,min^{-1}}$ in an air atmosphere.

2.4. Characterisation techniques

The X-ray diffractograms of samples I and II were collected in the low-angle mode of a Philips PW1710 diffractometer using Cu Kα radiation. XRD patterns of samples III and IV were obtained in Philips PW3710 diffractometer using Cu Kα radiation. The tube current and voltage were 40 mA and 40 kV, respectively. The scan step time was 4 s and the step size was 0.02°. The 2θ range examined was 15–60°. The peak intensity of the Si substrate is affected by the exact orientation of samples and the thickness of thin films. The surface morphology of the films was examined using Jeol 800 SEM at 20 keV incident beam voltage. Chemical analysis of the surface of sample III was performed after 800 °C and 1 h heating via XPS analysis using a Kratos AXIS 165 instrument with monochromatic Al Kα radiation (1486.6 eV). Survey scans were taken at a pass energy of 80 eV. High resolution scans were taken at a pass energy of 20 eV. In the latter configuration the Ag $3d_{5/2}$ peak has a measured FWHM of around 0.6 eV. The spectra were analysed and the background subtraction was carried out using XPSPEAK software. All the curve fitting was done with 80% Lorentzian and 20% Gaussian curves.

2.5. Hardness tests

Knoop hardness of the coatings on the hardened steel substrate was measured using MVK-H2 Mitutoyo hardness tester with an indentation load of 100 mN.

3. Results and discussion

3.1. Thermal behaviour of the coatings

Fig. 2 shows thermal analysis traces of samples I–IV. The very strong endothermic peaks between 100 and 200 °C in the DTA are due to the removal of residual organic solvent and absorbed structural water. The endothermic peaks between 200 and 600 °C can be attributed to dehydroxylation of the residual hydroxyl groups. The main broad and shallow endotherm centred around 240 and 370 °C for sample I; 300, 337, and 418 °C for sample II; 229, 330, and 479 °C for sample III; and 218, 300, and 467 °C for sample IV. A relatively narrow exothermic peak at around 850 °C was found for sample I. But for samples II and III, a broad exothermic peak were found around 805 and 780 °C. Distinctively, a very broad exotherm of sample IV centred around 700 °C. These different exotherms of samples I–IV illustrate that the samples have different characteristics of crystallisation.

3.2. Phase transformation processes

Table 1 lists the relationship of phases and heat treatment conditions. At a heat treatment temperature of 450 °C all samples had an amorphous structure. Cubic-Yb_2O_3 initially appeared at a temperature of 700 °C for sample I (Al_2O_3/Yb_2O_3 = 1:1, with no doped lithia and no AOS solvent); the associated XRD pattern is shown in Fig. 3.

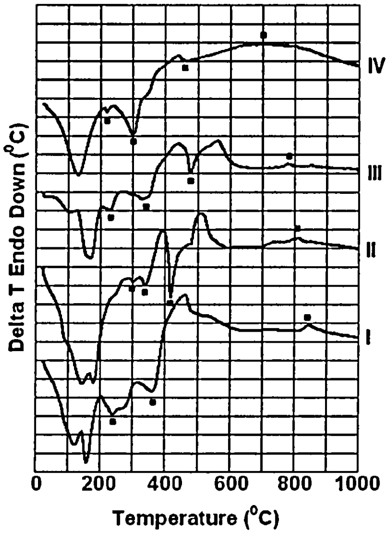

Fig. 2. DTA traces of samples I–IV.

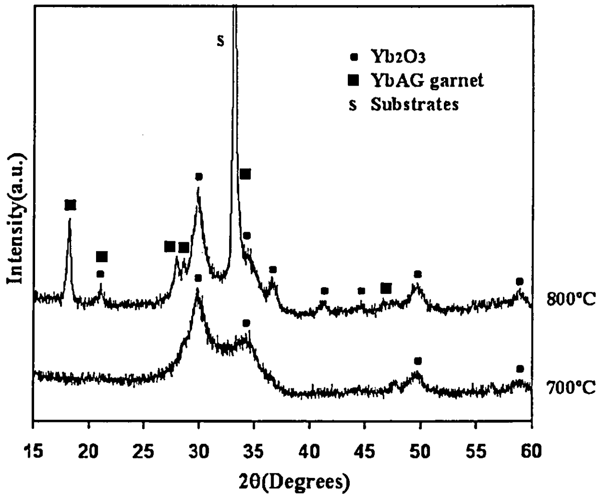

Fig. 3. XRD patterns of sample I.

Cubic-Yb_2O_3 was identified as #43-1037 from the JCPDS database [11]. YbAG garnet peaks (identified by JCPDS as #73-1369) were found at a temperature of 800 °C.

Sample II (Al_2O_3/Yb_2O_3 = 1:1, with 8 mol% doped lithia and no AOS solvent) was found to be amorphous at a temperature of 500 °C and strong cubic-Yb_2O_3 peaks began to be observed at a temperature of 600 °C in the XRD pattern, as shown in Fig. 4. Very small amounts of YbAG garnet appeared at temperature of 800 °C. The weak peaks of YbAG in Fig. 4 imply that it is comparatively difficult to crystallise YbAG without the AOS solvent, although crystallisation is facilitated to some extent by the lithia.

Among these four samples, the lowest temperature at which cubic-Yb_2O_3 appeared was 500 °C in sample III (Al_2O_3/Yb_2O_3 = 1:1, with 8 mol% doped lithia and AOS organic solvent). YbAG garnet formation in sample III was observed at a temperature of 700 °C; the associated XRD

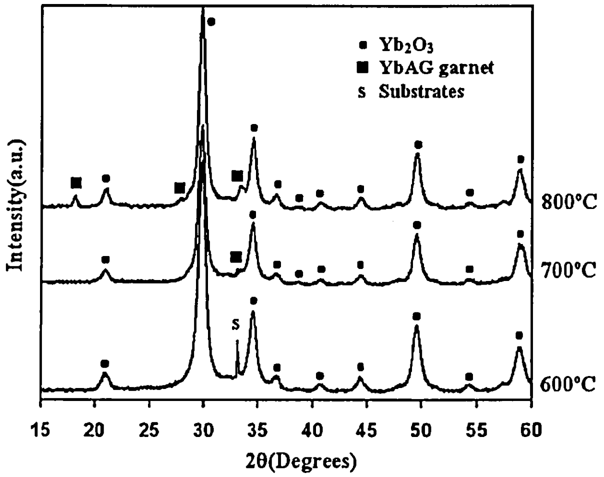

Fig. 4. XRD patterns of sample II.

Table 1
Relationship of crystallisation and heating conditions

Samples	Heat treatment conditions				
	450 °C and 1 h	500 °C and 1 h	600 °C and 1 h	700 °C and 1 h	800 °C and 1 h
I	Amorphous	Amorphous	Amorphous	Cubic-Yb_2O_3	Cubic-Yb_2O_3, $Yb_3Al_5O_{12}$ garnet
II	Amorphous	Amorphous	Cubic-Yb_2O_3	Cubic-Yb_2O_3	Cubic-Yb_2O_3, $Yb_3Al_5O_{12}$ garnet
III	Amorphous	Cubic-Yb_2O_3	Cubic-Yb_2O_3	Cubic-Yb_2O_3, $Yb_3Al_5O_{12}$ garnet	Cubic-Yb_2O_3, $Yb_3Al_5O_{12}$ garnet
IV	Amorphous	Amorphous	Amorphous	$Yb_3Al_5O_{12}$ garnet	$Yb_3Al_5O_{12}$ garnet

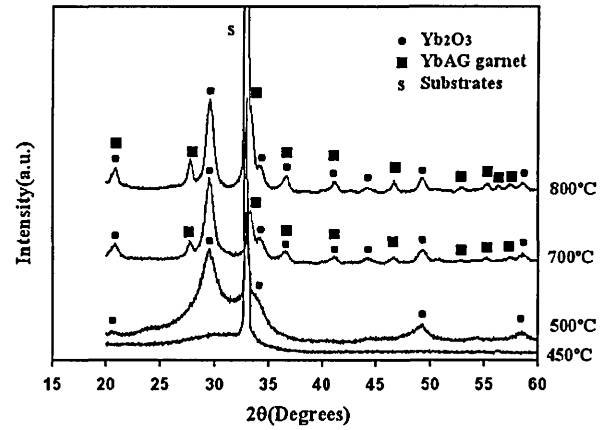

Fig. 5. XRD patterns of sample III.

pattern for sample III is shown in Fig. 5. This result is attributed to the addition of AOS solvent. The promotion of YbAG garnet crystallisation by AOS solvent, at the same time, was confirmed by sample IV ($Al_2O_3/Yb_2O_3 = 5:3$, with 4 mol% doped lithia and AOS solvent). Sample IV is amorphous at a temperature of 600 °C shown in Fig. 6 and the strongest peak of YbAG (at $2\theta = 33.56°$) in the sample seems to be observed but it is very weak. The single-phase YbAG garnet was obtained at the 700 °C low calcination temperature. There were no other phases that can be detected for 25 h calcination at a temperature of 800 °C apart from YbAG. It must be emphasised that this is the first time that the single-phase YbAG film has been manufactured, as far as we are aware, at this very low temperature.

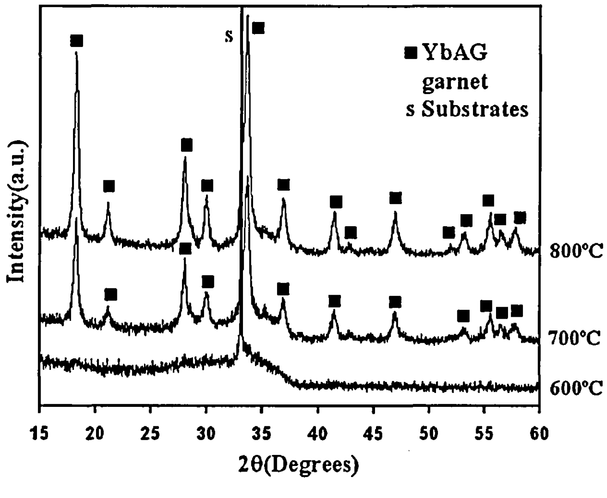

Fig. 6. XRD patterns of sample IV.

3.3. *The effects of lithia and AOS solvent on the crystallisation*

When we compare sample I to sample II, it is evident that the doped lithia has lowered the crystallisation temperature for cubic-Yb_2O_3 by about 100 °C. Similarly, comparison of samples II–IV suggest that the AOS solvent has lowered the crystallisation temperature of YbAG garnet by at least 100 °C.

The exact mechanism of the lowering of the crystallisation temperature is not known, although we can postulate that the sol–gel process may be modified by both the presence of lithia and AOS solvent as follows. It is well known that the gel film has a porous and amorphous network structure. The central cations such as Al^{3+} and Yb^{3+} here are bonded by the bridged oxygen O_b, >Al–O–. The oxygen may also exist as the non-bridge oxygen O_{nb}, H–O–Al<. As the calcination temperature rises, some bridged oxygens may break up and become non-bridged oxygen. This results in the decrease of the bridge oxygen and causes structural changes and subsequent changes in the co-ordination of the cations. However, with further increasing calcination temperature, the non-bridge oxygen transforms back to the bridge oxygen. Thus, cation positions in the oxygen polyhedral also change correspondingly.

The cations Al^{3+} can exist in the oxygen octahedral or tetrahedral sites. However, the radius of Yb^{3+} (0.86 Å) is larger than that of Al^{3+} (0.39 Å). It generally occupies the oxygen octahedral or dodecahedron sites. Yb^{3+} form the basic crystal growth units $[YbO_6]$ octahedral with O and H. In this case, the chain consists of these octahedral units that are bonded through the corner, the edge and the face. The binding between the chains is OH^- and so the crystallisation of Yb_2O_3 is actually the convergence and order arrangement process of Yb oxygen coordination octahedral. The more the number of basic octahedral growth units $[YbO_6]$ are bound together, the easier the crystallisation of Yb_2O_3. However, the problem here is that the hydrogen will be lost due to heat treatment and lead to a decrease in the basic

Table 2
XPS core level binding energies (BE ± 0.1 eV) of sample III (values have been charge corrected for C 1s = 284.8 eV)

O 1s	Al 2p$_{3/2}$	Al 2p$_{1/2}$	Yb 4d$_{5/2}$	Li 1s
530.1	74.4	73.6	185.0	55.7

growth units. Thus, the small radius lithium ion that was added in the sol may replace the hydrogen position to keep the basic growth units at the same number density during the firing process and hence be beneficial to the formation of cubic-Yb_2O_3 and to catalyse the Yb_2O_3 crystallisation. Furthermore, chemically it might form a very unstable intermediate phase $Yb_2O_3{\cdot}XLi_2O$ which is then decomposed very quickly to yield Yb_2O_3 and Li_2O. A high molar concentration of Li_2O on the very top surface has been confirmed by the XPS experiments described below.

The YbAG garnet structure consists of [AlO_4] tetrahedral, [AlO_6] octahedral and [YbO_8] dodecahedron. A perfect oxygen coordination polyhedral network structure is significant for the YbAG crystallisation. In other words, increasing the amount of O_b will promote the YbAG crystallisation. The AOS solvent decreases the amount of non-bridge oxygen and enhanced the network structure by its

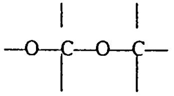

$$-\mathrm{O}-\underset{|}{\overset{|}{\mathrm{C}}}-\mathrm{O}-\underset{|}{\overset{|}{\mathrm{C}}}-$$

bonding with cations. Hence, this may account for the observed temperature decrease of 100 °C for the YbAG crystallisation.

3.4. XPS spectra

The XPS wide scan spectra of sample III after heated for 1 h at 800 °C in the range 0–1200 eV was obtained and the major features were identified. The most intense peak at 530 eV corresponds to the O 1s peak. The Li 1s and Al 2p peaks appear at 48–62 and 70–80 eV, respectively. The Yb 4d peaks occur at 176–213 eV. High resolution spectra were performed for all the elements and the deconvoluted Al, Yb and Li peaks spectra are shown in Fig. 7. The binding energy (BE) data are shown in Table 2. The Al 2p in Fig. 7a has been deconvoluted into two peaks (73.6 and 74.4 eV for $p_{3/2}$ and $p_{1/2}$, respectively), which show reasonable agreement with that expected for an oxidised form which have reported values of around 74.0 eV [12]. The somewhat lower peak value may be as a result of aluminium atoms sitting in the YbAG structure. There is no obvious evidence of aluminium occupying tetrahedral and octahedral sites. The differences in binding energies are probably too small to result in separate peaks. The Yb 4d spectra in Fig. 7b have five peaks between 185 and 210 eV which can be attributed to a Yb_2O_3 type phase. The BE of the principal $4d_{5/2}$ peak is 185.0 eV which shows good agreement with reported values of 185.2 for Yb_2O_3 by Uwamino et al. [13]. The Li 1s spectra (Fig. 7c) has a well-resolved peak at around 55.7 eV which shows good agreement with reported value of 55.6 eV for Li_2O [14]. The Li spectra has a weak diffuse peak below the principal peak (not shown in Fig. 7) which may be due to Li-doped into Y_2O_3 or YbAG phase which exists as interstitial cations. Further research is required to identify the exact Li^+ sites in the structure. The detailed studies about this and YbAG finer structural features will be discussed elsewhere.

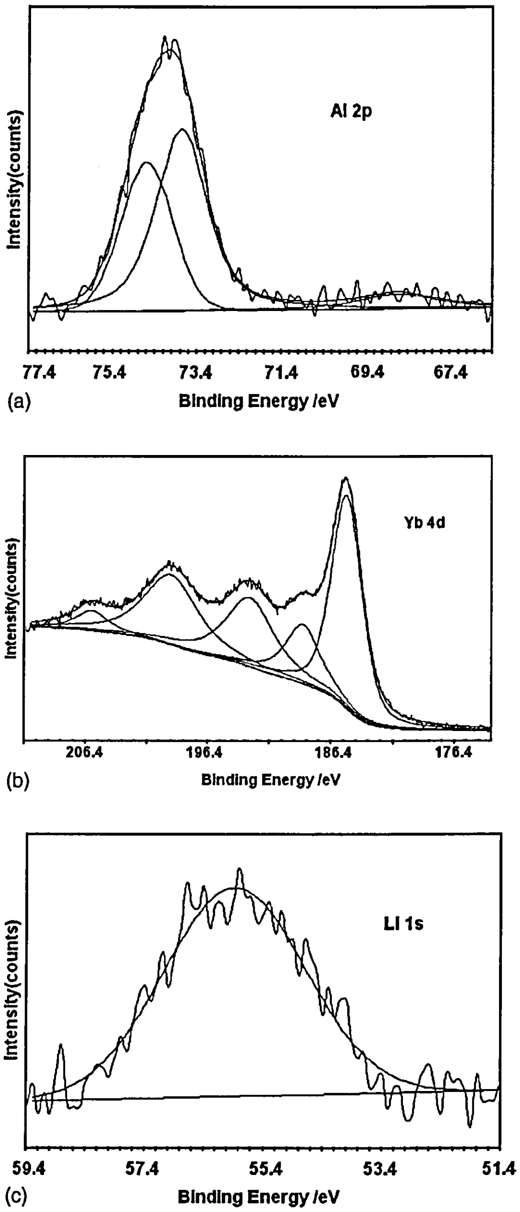

Fig. 7. High resolution XPS spectra of Al, Yb, and Li.

3.5. Coating surface characterisation and hardness

The coating surface structure was observed by SEM. Figs. 8 and 9 show the surface structure of coatings on Si(1 0 0) and hardened steel substrates, respectively. The

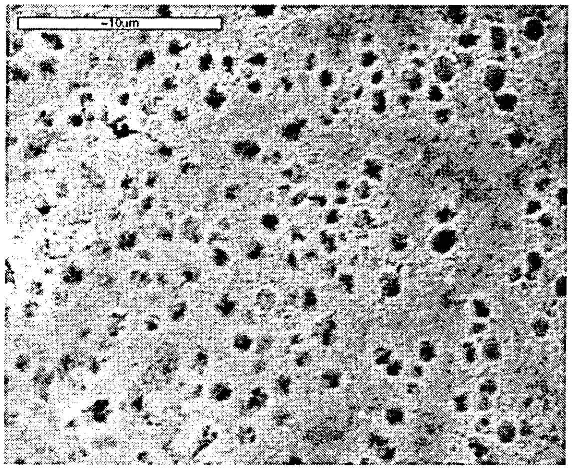

Fig. 8. Surface structure of thin films on the Si substrate.

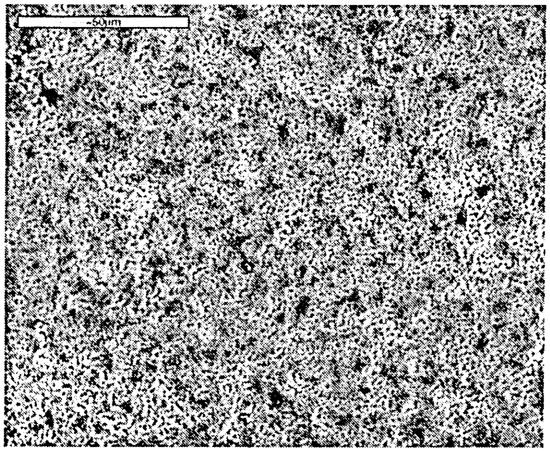

Fig. 9. SEM characterisation of the coating on the harden steel substrate.

coating on the hardened tool steel substrate was heated at 450 °C for 2 h. There is an even distribution of pores which have a mean diameter of about 1–2 μm for both coatings.

Hardness tests were performed on the coating on the hardened steel substrate. The average Knoop hardness was 1024 kg mm^{-2}. These results lay the foundation for potential future application of garnet ceramic coating as a thermal barrier, or oxidation and erosion resistant material.

4. Conclusions

Single-phase YbAG garnet polycrystalline films were produced first time and at very low heat treatment temperature by a modified sol–gel method. In the Yb_2O_3–Al_2O_3 system, when the mole ratio of Al_2O_3/Yb_2O_3 is 1:1, doped lithia promotes the cubic-Yb_2O_3 crystallisation. Adding the AOS inorganic–organic hybrid solvent has been found effectively to lower the crystallisation temperature of YbAG garnet by at least 100 °C and to be beneficial to the adhesion with the coated metal substrates. DTA traces have shown different thermal behaviour of these different samples crystallised at the temperature range of 600–800 °C. A porous and thick coating can be obtained on hardened steel substrate by multiple dip technique. The coating possesses a relatively high hardness even when in the amorphous phase produced via heat treatment at 450 °C. We conclude that porous coatings of considerable hardness and easy, low temperature manufacturing can be produced by the sol–gel method. The low thermal conductivity of garnet and the thermal stability of the phases produced suggest that a coating of garnet ceramic structure may be a good prospective candidate as a hard, corrosion-resistant TBC.

Acknowledgements

The authors would like to thank Dr. N. Bricklebank for several helpful discussions.

References

[1] Y.S. Zheng, K.M. Knowles, J.M. Vieira, A.B. Lopes, F.J. Oliveira, Microstructure, toughness and flexural strength of self-reinforced silicon nitride ceramics doped with yttrium oxide and ytterbium oxide, J. Microsc., Part 2 201 (2001) 238–249.

[2] T. Shimoda, Y. Ishida, K. Adachi, M. Obara, Fabrication of highly ytterbium doped YAG thin film by pulsed laser deposition, Opt. Commun. 194 (2001) 175–179.

[3] N.P. Padture, P.G. Klemens, Low thermal conductivity in garnets, J. Am. Ceram. Soc. 80 (4) (1997) 1018–1020.

[4] T. Yasushi, Corrosion-resistant composite oxide material, European Patent 1 013 623 (2000).

[5] J.R. Lo, T.Y. Tseng, Phase development and activation energy of the Y_2O_3–AL_2O_3 system by a modified sol–gel process, Mater. Chem. Phys. 56 (1998) 56–62.

[6] Y. Liu, Z.F. Zhang, B. King, J. Halloran, R.M. Laine, J. Am. Ceram. Soc. 79 (1996) 385.

[7] M. Mizuno, T. Noguchi, Yogyo Kyokaishi 88 (1980) 322.

[8] H. Arakawa, Technol. Jpn. 21 (1988) 32.

[9] P. Kofstad, Nonstoichiometry, Diffusion and Electrical Conductivity in Binary Metal Oxides, Wiley, New York, 1972.

[10] V.I. Chani, A. Yoshikawa, H. Machida, T. Fukuda, Mater. Sci. Eng. B 75 (2000) 53–60.

[11] PCPDFWIN, Version 2.1, JCPDS ICDD International Centre for Diffraction Data, June 2000.

[12] See www.srdat.nist.gov/xpsand references therein.

[13] Y. Uwamino, Y. Ishizuka, H. Yamatera, J. Electron. Spectrosc. 34 (1984) 69.

[14] J.P. Contour, A. Salesse, M. Froment, M. Garreau, J. Thevenin, D. Warin, J. Microsc. Spectrosc. Electron. 4 (1979) 483.